Nonlinear Optical Effects in Weyl Semimetals and Other Strongly Correlated Materials

by

Elizabeth A. Drueke

A dissertation submitted in partial fulfillment
of the requirements for the degree of
Doctor of Philosophy
(Physics)
in the University of Michigan
2021

Doctoral Committee:

Assistant Professor Liuyan Zhao, Chair
Professor Steven Cundiff
Professor Jennifer Ogilvie
Associate Professor Kai Sun
Professor Herbert G. Winful

Elizabeth A. Drueke

edrueke@umich.edu

ORCID-iD: 0000-0001-5204-9533

DEDICATION

For Nick and for my parents

ACKNOWLEDGEMENTS

There are many people without whose contributions, help, and encouragement this thesis would not have been possible. First, my advisor, Liuyan Zhao, has been incredibly supportive and helpful to me from the moment I began working in her group. Her thoughtful comments and willingness to teach are never in short supply, and her understanding and recognition that students' personal lives must sometimes take precedent has been crucial to my success in this program. Rachel Owen and Matthew Day have also been invaluable friends, colleagues, collaborators, and coffee mates. Both their scientific and personal support have been integral to my success as a graduate student.

Many other professors have helped and supported me along the way. Our theory discussions with Kai Sun and experimental collaborations with Steve Cundiff, Lu Li, and Dong Sun have been incredibly helpful to this scientific undertaking. I thank Jennifer Ogilvie and Herbert Winful for serving on my committee and for their kind words of encouragement and openness to discussion. In addition, I thank our collaborators who fabricated our samples– Junjie Yang, Sang-Wook Cheong, Henchang Lei, and Adam Tsen – for always providing us with samples of the highest quality and caliber. I also thank the NSF-GRFP program for my funding the last three years (grant no. DGE-1256260), and the Physics Department for my first year fellowship.

I also thank my fellow group members past and present – Wencan Jin, Hongchao Xie, Youngjun Ahn, Kara Mattioli, Siwen Li, Rachel Owen, Xiangpeng Luo, and Xiaoyu Guo – for their hard work and dedication to their projects and to the lab. Each one of them has, at least once,

carved a day or two out of their busy schedules to show me an alignment procedure or helped me to get data on a new experimental setup. Thank you as well to Austin Kaczmarek, who never worked with us in the official capacity of a graduate student, but still managed to fully fill that role. I would also like to recognize the many undergraduate students I have had the pleasure of working with over the years – Shannon Gray, Ian Blackman-Staves, Zhibo Kang, Samia Sabir, Yuanhao Meng, DJ Imoehl, Lauren Weinberg, Zijia Cheng, Yanyu Jia, Charlotte Albunio, and Laura Zichi. I have very much enjoyed working with each one of them and watching them learn and grow as students and as scientists. I wish them all the best in their futures.

Last but certainly not least, I thank my family for their never-ending support and encouragement. We have all been through a lot these last several years, but our support for each other has only made us stronger. I want to especially thank my parents for teaching me when I was small that I could be anything I wanted to be and for instilling in me a solid work ethic and a capacity for resiliency. In every way, they set me up for success today by constantly thinking ahead when I was younger. I must also thank Nick. It takes a special kind of man to put up with the late nights of experiments, the hours of coursework, and the constant stress I inevitably brought home. I cannot wait to see what the next chapter of our lives brings.

TABLE OF CONTENTS

CHAPTERS

LIST OF FIGURES

beam into n orders of beams. Here, the first order beams only are shown. A block is then used to stop all but one of the first order beams. This grating and the block are also on an automatic rotating mount to ensure that the incoming polarization is locked to the plane of incidence. The beam then passes through two dichroic mirrors (DM1 and DM2) which are each at a 45 ◦ angle to the incident beam and normal to each other. Then it passes through an achromatic doublet (AC1) which focuses the beam to the sample location. The reflected SHG is then picked up by DM2 after passing back through AC1 and directed to DM3, which reflects the SHG to a polarizer which acts as an analyzer for the experiment. This polarizer is also on an automatic rotation mount to ensure that the polarization of the measured SHG is locked to the incoming polarization. It then passes through a color filter set consisting of one bandpass (BP) and two shortpass (SP) filters to ensure that only the 400 nm light is measured at the CCD. Once filtered, the light is focused to the detector. Not pictured is a white light imaging system which allows us to place the beam at the desired location on the sample and helps with focusing and an optional neutral density (ND) filter placed before the WP.   56

wavelength of 800 nm. Both pump and probe beams pass through their own telescopes (pump telescope L1, L2 and probe telescope L3, L4), where the probe beam is expanded and the pump is decreased in size to ensure proper overlap, with the pump beam larger than the probe beam, at the sample site. The pump beam is further chopped by an optical chopper at a frequency of 8 kHz which serves as a reference for the lock-in detector. The probe then passes through an automatic translation stage which allows for the tuning of the time delay between the pump and probe pulses. It also passes through a waveplate (WP1) to allow for polarization resolution. It is then picked up and directed parallel to the pump beam, which also passes through a waveplate (WP2), before both are focused down (L5) to the sample. The probe beam comes in at a slightly oblique angle due to it being incident slightly off the center of the L1 optic. As a result, it is spatially separated from the pump upon reflection and can be easily be picked up and directed to the silicon photodiode with a mirror. Further color filtering is performed to eliminate any remaining pump scatter before the probe is focused down (L6) to the detector. 73

Figure IV.9 – An illustration of the optical beam path for the photocurrent generation setup. The incoming beam first goes through a telescope to expand the beam (L1, L2). At the focal point of L1, an optical chopper chops the beam to allow for a reference for a lock-in amplifier. The beam is then incident on either a QWP or HWP. There are two experimental geometries illustrated depending on the orientation of the flip mirror M1. In the case that M1 is not in the optical beam path, the light will be focused down normally onto the sample by lens L3. In the case that M1 is in the beam path, a series of mirrors will direct the beam to focus through L4 at an oblique incidence onto the sample. Not pictured is the initial ND filtering used to set the power of the beam at the sample sight or the white light imaging arm used for alignment purposes. 75

Figure IV.10 – Several images of the photocurrent setup. (Top Left) An image of a sample in a chip carrier in the cryostat. The chip carrier is inserted into two 8-pin connectors, one on either side, to transfer the electrical signal from the sample to the cryostat port. (Top Right) The chip carrier and sample together with the shielding necessary to cool the sample down with the cryostat. (Bottom Left) The BNC box built in collaboration with Austin Kaczmarek designed to transfer the electrical signals from the sample to the lock-in amplifier. Each labeled BNC port has the ability to connect with one of the pads on the sample via the 8-pin connectors. Each port also has a switch to control the signal and ground output of the BNC. Here, we can see that a BNC cable is plugged into port 3 and that the switch of port 4 is set to shield grounding. All other switches are flipped up. This means that we are measuring the current across pads 3 and 4 on the sample. (Bottom Right) The sample and chip carrier on their mount which is typically used with the cryostat, together with the cryostat port used to transfer the electrical signal from the cryostat to the lock-in amplifier, which is in ambient conditions. Here, the copper mount and cryostat port have been removed from the cryostat itself for a scanning measurement, discussed in the next section. 78

Figure IV.11 – An illustration of the operating principle behind using the motorized scanning mirror (left) and of the resulting scanning SHG setup (right). Both images are provided by Austin Kaczmarek. 80

Figure IV.12 – Pictures of the glovebox-based 2d fabrication setup in the lab in the sub-basement of Randall Laboratory. (Left) The 4-glove Purelab HE from Inert. (Right) The Olympus microscope setup for the stacking procedure inside the glovebox. Two motorized stages from Thorlabs are shown to allow lateral movement of the sample within the focal plane. Atop these

circularly polarized light is incident on the sample, electrons will be excitely selected on only one side of the WP, yielding a nonzero CPGE. 135

Figure VI.8 – Photocurrent data for the y-component of the (100) crystal facet. The raw data are shown for the HWP in blue solid dots and for the QWP in red solid dots, together with the fit to the data from Equations VI.8 and VI.9 displayed as solid curves of the appropriate color. A microscope image of the (100) crystal face with the gold pads and wires is included to the left. The photocurrent data was obtained using a laser spot location indicated by the solid red dot and was taken between the two leads highlighted in open red circles. 137

Figure VI.9 – Photocurrent data from the (111) facet of the CoSi crystal. The plots to the right indicate the dependence of the photocurrent response on the waveplate angle from vertical for the case of a HWP (top) and a QWP (bottom). In each plot, the raw data are indicated by open circles and the fits to the oblique incidence data are included as solid curves using functional forms from Equations VI.10, VI.11, and VI.12. The data which is not fit comes from the normal incidence geometry. A microscope image of the (111) crystal facet with the gold pads and the wires is included to the left. The solid red circle indicates the location of the beam for the data in the plots to the right. The lead circled in black is used in both the x- and y-component measurements, and the lead used with the black lead for x is shown in red and for y is shown in blue. 139

Figure VI.10 – Scanning photocurrent data taken on the (111) CoSi crystal facet with different lead combinations in an oblique incidence geometry at a peak in the polarization-resolved data with a QWP. A microscope image of the facet with the scanned area indicated by a purple box is included in the bottom right. All three scanning images have the same color scale, which is given in units of nA. The height and width of each pixel in the scanning photocurrent images is 30 μm. 141

Figure VI.11 – Scanning photocurrent data taken on the (111) CoSi crystal facet with different lead combinations in a normal incidence geometry at a peak in the polarization-resolved data with a QWP. A microscope image of the facet with the scanned area indicated by a purple box is included in the bottom right. The color bar for each image is included and are given in units of nA. The height and width of each pixel in the scanning photocurrent images is 30 μm. 142

Figure VI.12 – Scanning photocurrent data filtered to provide the LPGE and CPGE signal for each pixel from the FFT of the data over all WP angles. This data follows the lower left scanning photocurrent data from Figure VI.11 taken on the (111) CoSi crystal facet at normal incidence with a QWP. The location of the beam used to obtain the data from Figure VI.9, where a pure CoSi photocurrent response is expected, is circled in red. The height and width of each pixel is 30 μm. 144

Figure VI.13 – Scanning photocurrent data filtered to provide the LPGE and CPGE signal for each pixel from the FFT of the data over all WP angles. This data follows the lower left scanning photocurrent data from Figure VI.11 taken on the (111) CoSi crystal facet at oblique incidence with a QWP. The area of the sample used to take the data from Figure VI.9, where a pure CoSi photocurrent response is expected, is circled in red. The height and width of each pixel is 30 μm. 145

LIST OF TABLES

LIST OF APPENDICES

APPENDIX

LIST OF COMMON ABBREVIATIONS

A/B   linear polarization at a $\pm 45°$ angle to the optical table

ARPES   angle-resolved photoemission spectroscopy

BBO   beta-barium borate [crystal]

CCD   charge-coupled device

CPGE   circular photogalvanic effect

CW   continuous wave [laser]

DC   direct current

DECP   displacive excitation of coherent phonons

DFT   density functional theory

ED   electric dipole

EFISH   electric field induced second harmonic

EM   electromagnetic

EQ   electric quadrupole

FFT   fast Fourier transform

H   linear polarization parallel to the optical table

hBN   hexagonal boron nitride

HWP   half-waveplate

ISRS   impulsive stimulated Raman scattering

L   left-handed circularly polarized light

LPGE	linear photogalvanic effect
MD	magnetic dipole
ND	neutral density
NLAHE	nonlinear anomalous Hall effect
NOPA	nonlinear optical parametric amplifier
P	linear polarization parallel to the plane of incidence
PGE	photogalvanic effect
PMT	photomultiplier tube
QWP	quarter-waveplate
R	right-handed circularly polarized light
RA-SHG	rotational anisotropy of the second harmonic generation [experiment]
S	linear polarization perpendicular to the plane of incidence
SHG	second-harmonic generation
SIS	spatial-inversion symmetry
SOC	spin-orbit coupling
TEM	transmission electron microscopy
TMDC	transition metal dichalcogenide
TR-MOKE	time-resolved magneto-optical Kerr effect
TRS	time-reversal symmetry
TTM	two-temperature model
V	linear polarization perpendicular to the optical table
VISIR	visible to infrared [wavelength]
WP	Weyl Point *or* waveplate

WSM   Weyl semimetal

ABSTRACT

The study of Weyl semimetals has been of interest since their first prediction in pyrochlore iridates in 2011 and their experimental discovery in TaAs in 2015. Since then, several classifications of Weyl semimetals have been identified, including electronic and magnetic, type-I and type-II, chiral, and multifold. In addition, the nonlinear optical properties of these materials have stood out as being particularly remarkable. This is due in part to the topological nature of Weyl semimetals, which affects the strength of the nonlinear properties and yields the potential for quantization, and in part due to the symmetry properties of Weyl semimetals, which dictates the anisotropy of these effects.

Second harmonic generation and the photogalvanic effect have both been shown to be of particular interest in Weyl semimetals. A strong second harmonic response has already been identified in type-I Weyl semimetals even at optical wavelengths. However, there is still some discussion as to whether this is directly attributable to the topological nature of the type-I semimetal band structure. Photocurrent measurements, and particularly the circular photogalvanic effect, have also stood out as a potential probe of the topology of the Weyl semimetal band structure. Yet experiments to date have attributed photocurrent generation to multiple physical origins, including the linear and circular photogalvanic effects, photon drag, and the photothermal, photoelectric, and photovoltaic effects.

In this thesis, we present a survey of a variety of nonlinear optical studies on several Weyl semimetals. In particular, we study the second harmonic responses of the type-II Weyl semimetals

T_d-WTe$_2$ and T_d-MoTe$_2$ and of the chiral Weyl semimetal CoSi. We look at the rotational anisotropy of those responses and use point-symmetry analyses to attribute that anisotropy to the symmetries of the crystalline structures of these materials. We also characterize the sizes of the responses in these materials. Although we cannot identify with certainty a topological contribution to the strength of the second harmonic, our analysis suggests that the topology of these materials may play some role in the outsized responses observed.

We further present information on impulsive stimulated Raman scattering in the type-II Weyl semimetal T_d-WTe$_2$, which is observed through excitations of the 0.25 THz shear mode in a time-resolved optical reflectivity experiment. By analyzing the phase of the excitation of this mode, we also see indications of the shear displacement through the Pockels effect. Additionally, the asymmetric Fano line shape of this mode suggests possible coupling to the Weyl fermion quasiparticle excitations in this material.

We also study photocurrent generation in the chiral Weyl semimetal CoSi. We survey several facets of this crystal and use a point-symmetry analysis to pin down the origins of both a linear and circular photogalvanic effect in this material. Spatially resolved photocurrent measurements suggest that the experimental geometry used can potentially cause extraneous polarization-dependent photocurrent responses in the case of laser illumination of the electronics on the sample surface.

Finally, one of the defining characteristics which allows for the existence of the Weyl semimetal state is strong spin-orbit coupling. Thus, I end by presenting a study of the second harmonic response in another strongly correlated material, the complex oxide $RbFe(MoO_4)_2$. Investigating the structural phase transition of this material, we identify for the first time a

ferrorotational ordering, and offer a point-symmetry analysis to identify potential coupling fields

for this new electronic state.

CHAPTER I

Introduction

Condensed matter systems are remarkably complicated physical playgrounds. A simple sheet of aluminum you can hold in your hand actually consists of billions of quintillions of atomic nuclei, and even more electrons. Remarkably, despite the large number of particles involved, many materials can be modeled well with the assumption that all particles are independent, or at least that all electrons are independent from one another and exist in a regularly patterned potential that can be written down mathematically in only a few terms. One important class of materials in which this assumption breaks down is strongly correlated materials. In strongly correlated materials, the interactions between the degrees of freedom of the electrons cannot be ignored. These strong correlations dramatically complicate mathematical modelling, but also lead to unique electronic and magnetic properties [1, 2].

One electronic structure made possible by strong correlations in materials is known as the Weyl semimetal (WSM). These materials have received much attention since their first theoretical description and prediction in pyrochlore iridates [3]. They are defined by topologically protected crossing points in the bulk band structure at the Fermi energy. These points, known as Weyl points (WPs), each have a distinct chirality and always come in pairs, with each WP in the pair having opposite chirality [4, 5]. These bulk topological features result in surface states, known as Fermi arcs, which are accessible through angle-resolved photoemission spectroscopy (ARPES) experiments. The first experimental confirmation of a WSM state in TaAs using ARPES in 2015

[6, 7] stimulated a wide-spread effort to identify the WSM state in other materials. Outside of the identification of these states, work has also been done to identify distinctions between electronic and magnetic WSMs depending on their symmetry properties and between type-I and type-II WSMs depending on the tilt of the band structure around the WPs [8]. A further class of chiral WSMs characterized by paired WPs occurring at different energies has been discovered in WSMs lacking mirror symmetries [9-11]. In addition, a number of different applications have been predicted which utilize the unique band structure and high electron mobility in WSMs to develop everything from broadband photodetection devices to novel lasing methods [12, 13].

As this field of research has grown, some of the most stunning features of WSMs identified have been their nonlinear optical responses. The field of nonlinear optics spans the study of any property in which a material response is determined by more than one copy of or by multiple incoming electric or magnetic field(s). In [14], it was found that the second harmonic generation (SHG) of TaAs is orders of magnitude larger than that of GaAs. Further studies have shown a strong anisotropic photocurrent response [15, 16], the nonlinear Hall effect [17, 18], and the chiral anomaly [19, 20], among others, in a variety of these materials. In this work, I will focus primarily on exploring SHG and photocurrent generation in WSMs and look at spatial and temporal variations in these effects. I will also look at nonlinear optical properties of one other strongly correlated system, $RbFe(MoO_4)_2$, using nonlinear optics to probe new ferroic orders.

The outline for this work is as follows. Chapters II and III provide background information for our experiments. Chapter II establishes a thorough definition of a Weyl semimetal. This chapter serves as a basic background chapter on condensed matter physics and the roles that symmetry and topology play in it. In particular, I will start with a review of symmetry in crystalline systems, discussing crystal classifications as well as some of the basic applications of group theory in

condensed matter physics. Then, I will move on to descriptions of band structure and topology, both vital to understanding what makes WSMs such unique materials. Finally, I will describe WSMs in this framework, discussing their unique band structure and topological properties and including some history into their prediction and discovery. Chapter III provides some theoretical background for nonlinear optics. In particular, I will begin by establishing a basic definition of nonlinear optics and providing some examples in WSMs. Then, I will expand on the definition by building up a mathematical foundation for the study of second harmonic generation and the photogalvanic effect, which are the primary effects studied in the experimental chapters. I will also include how these effects relate to both symmetry and to topology and give a review of past results from literature to form a foundation for our work.

Chapter IV describes our experimental development. Several optical setups are described, including an experiment to study the rotational anisotropy of the second harmonic generation (RA-SHG), an experiment to study the photocurrent responses of materials, a time-resolved optical reflectivity experiment, a scanning SHG setup, and a glovebox-based fabrication system. In addition, some information on basic data analysis and modelling of results for each optical setup is presented for use as reference material in future chapters.

Chapters V through VII present our experimental results. In particular, Chapter V presents second harmonic and time-resolved optical reflectivity results on two type-II WSMs, WTe_2 and $MoTe_2$ [8, 21, 22]. Chapter VI introduces chiral WSMs and presents experimental results on the second harmonic and photocurrent responses of the chiral WSM CoSi [23-25]. Chapter VII expands our discussion to other strongly correlated systems by discussing the discovery of a ferrorotational ordering in the complex oxide $RbFe(MoO_4)_2$. We conclude in Chapter VIII with a quick summary of our work and suggest new directions for continuing these studies in the future.

3

CHAPTER II

Background

Perhaps the broadest material class into which we can place WSMs is the class of crystalline materials. In contrast to liquids and gases, solid crystalline materials consist of atoms regularly spaced in a lattice structure. Because of this, symmetry plays a particularly vital role in the study of crystalline materials. We can use symmetry operations to build full crystalline lattice structures from a handful of atomic positions, and the symmetry properties of a given crystal dictate the phenomena which can be realized in that material. Symmetry plays an even more vital role in the study of WSMs, which require that either time reversal symmetry (TRS) or spatial inversion symmetry (SIS) be broken. WSMs are unique in that their symmetries allow them to host certain condensed matter analogues of high energy phenomena. In particular, quasiparticle excitations in these materials act as Weyl fermions of particle physics, massless spin-1/2 particles first predicted by Hermann Weyl in 1929 [26]. This appearance of high energy physics phenomena in condensed matter systems arises because the dispersion relation in WSMs is well-described by the Weyl Hamiltonian [27, 28]. This potentially allows for the first studies of Weyl fermions, which have not yet been experimentally observed in vacuum in high energy systems.

One of the main themes of the study of WSMs is the interplay between symmetry and topology. We have already mentioned the fundamental role played by SIS and TRS in WSMs. At the same time, the unique WSM band structure has topologically protected crossing points, meaning that they cannot be gapped out by perturbations. This leads to some interesting questions:

which physical characteristics of these materials are dictated by the symmetry properties and which by the topological properties? And how does the interplay between symmetry and topology effect the properties of these materials? In this chapter, I will describe the roles that symmetry and topology play in condensed matter systems, building up to a definition of a WSM, and review the history of the prediction and experimental confirmation of the WSM state.

Symmetry Operations in Crystalline Materials

A symmetry of a physical system is an operation under which the system is invariant. Classically, we can find symmetries by looking at how the Lagrangian of a system varies with changes in generalized coordinates. In particular, if a generalized coordinate q_i is a symmetry of a system described by Lagrangian $\mathcal{L}$, then it is required that

$$\frac{\partial \mathcal{L}}{\partial q_i} = 0 .$$

II.1

The corresponding canonical momentum $p_i = \frac{\partial \mathcal{L}}{\partial \dot{q}_i}$ must then be constant in time. That is, the symmetry of the system q_i leads to a conserved physical quantity p_i. The same holds true in quantum mechanics, where most of the underlying mathematical formalism comes from unitary operators[1] acting on quantum systems. If such an operator $\mathcal{M}$ is a continuous symmetry of a system, then it can be written as

$$\mathcal{M} = 1 - \frac{i\varepsilon}{\hbar} G$$

II.2

where G is the Hermitian generator of $\mathcal{M}$, and ε is taken to be infinitesimally small. Further, it will be true that $[G, H] = 0$, so G must be a conserved quantity of the system [29].

---

[1] A unitary operator U satisfies $U^\dagger = U^{-1}$, where $U^\dagger$ is the matrix formed by taking the complex conjugate of the transpose of U [29].

In crystalline systems, we are primarily interested in discrete symmetries. This is because the primitive unit cell of a crystal structure has a well-defined size. Any translation by a primitive lattice vector must a symmetry of the system. That is to say, any such translation necessarily brings one primitive unit cell back onto itself. Similarly, certain rotations, inversions, and mirrors can exist in the lattice which will also leave the system undisturbed. Because the unit cell which defines the basic block of the system has a finite size, any symmetry of the system must be discretely defined (eg. n translations along a primitive lattice vector, where $n \in \mathbb{N}$).

Mathematically, we can describe this construction using group theory, which is reviewed in Appendix A. Here, we define the set of translations by linear combinations of the primitive lattice vectors as a group with the operation of addition. Elements of the group take the form $T_{\vec{X}}$, where $\vec{X} = n_1\overrightarrow{a_1} + n_2\overrightarrow{a_2} + n_3\overrightarrow{a_3}$ for primitive lattice vectors $\overrightarrow{a_1}, \overrightarrow{a_2}, \overrightarrow{a_3}$ and $n_1, n_2, n_3 \in \mathbb{Z}$. It is clear that such a group is closed under addition. Further, because the addition of integers is commutative, it is necessary that $T_{\vec{X}}T_{\vec{Y}} = T_{\vec{X}+\vec{Y}} = T_{\vec{Y}+\vec{X}} = T_{\vec{Y}}T_{\vec{X}}$ for all $T_{\vec{X}}, T_{\vec{Y}}$ in the group of translations. Thus, the group of translations is also commutative, meaning it is abelian. This is a special property of the translation group since generally symmetry groups in physics, such as rotation groups, are not abelian.

In crystals, the group of all rotations, reflections, inversions, and their combinations under which the system is invariant is known as the point group of that crystal. Including translations as well yields the space group of the crystal. In general, there are several different types of elements which may be included in a point group:

- The identity 1

- Rotations C_n, describing rotation along an axis by $2\pi/n$

- Spatial Inversion/Parity I, which takes the spatial coordinates $x, y, z \rightarrow -x, -y, -z$

- Mirror reflections σ_{ij}, where ij defines the mirror plane

- Rotations followed by mirror reflections perpendicular to the rotating axis $S_n = \sigma C_n$

A full overview of crystalline point groups is presented in Appendix B.

In addition to the symmetry operations discussed above, it is often useful to look at how physical systems respond under TRS [30]. Essentially, when we think about how physical systems behave under TRS, we picture going from time t to time $-t$. For example, in statistical mechanics we are taught that the entropy of the universe naturally increases over time. Thus, the state of the universe is not invariant under TRS because entropy would decrease under the operation that takes $t \rightarrow -t$. Table II.1 provides information on how several common physical properties behave under the TRS operation.

Under $t \rightarrow -t$, physical quantity a is invariant ($a \rightarrow a$, or a is even under TRS)	Under $t \rightarrow -t$, physical quantity a is not conserved ($a \rightarrow -a$, or a is odd under TRS)
Position $\vec{x}$	Velocity $\vec{v}$
Acceleration $\vec{a}$	Momentum $\vec{p}$
Force $\vec{F}$	Magnetic Vector Potential $\vec{A}$
Electric Field $\vec{E}$	Magnetic Field $\vec{B}$
Electric Polarization $\vec{P}$	Magnetization $\vec{M}$
Energy E	
Electric Potential V	

Table II.1 – A table of examples of how some physical properties behave when acted on by the time reversal operator.

Topology of the Band Structure

Having now presented a review of basic symmetry operations and how they are applicable in the study of crystalline materials, we move on to discuss topology, which is another fundamental tool used in the study of materials. Topology plays a vital role in the band structure of WSMs. The concept of band structure and some basic examples are shown in Appendix C. Band structure is

important because it helps us to determine transport properties of the material, among other things. With knowledge of the Fermi energy, the maximum energy of an electron in a system, the band structure can be used to quickly identify materials as conductors or insulators as shown in Figure II.1. In particular, if the Fermi energy occurs mid-band, the material is a conductor, and the intersected band is known as the conduction band. If it occurs in a gap between two bands, the material is an insulator and the band immediately below the Fermi energy is the valence band. In a WSM, the band structure will show that the Fermi energy occurs at a crossing point of the conduction and valence bands, which each exhibit a linear dispersion. This structure will be discussed in more detail in the Defining Weyl Semimetals section below.
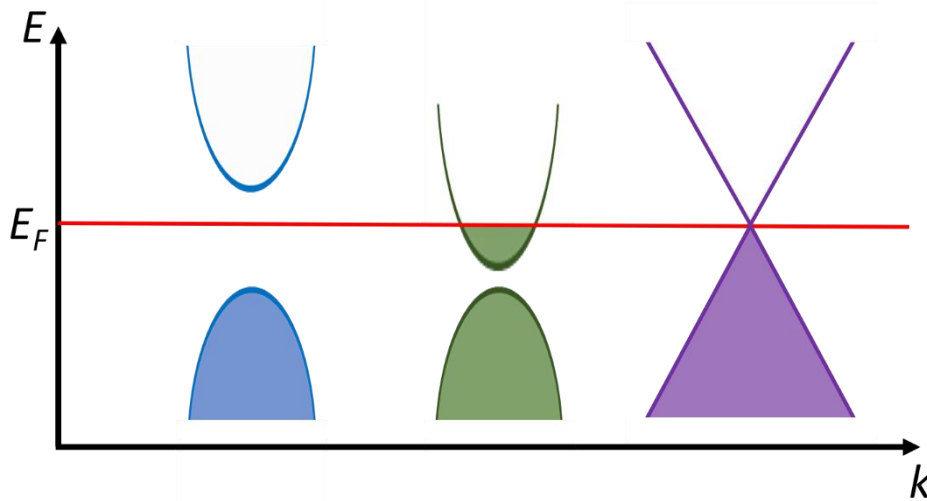
Figure II.1 – An illustration of various types of band diagrams. In the insulator (blue), the conduction band lies above the Fermi energy, so electrons can only exist in the valence band. Because this band is full, there is no conduction in an insulator. In the conductor (green), the conduction band is intersected by the Fermi energy, so there can be a flow of electrons because there are both occupied states and available unoccupied states in the conduction band. The third example (purple) is that of a Dirac/Weyl semimetal, where the valence and conduction bands meet at the Fermi energy with linear dispersion relationships. In this case, only very small energy perturbations would be required to cause conduction in such a material.

When we talk about topology in condensed matter physics, we typically do so using the formalism developed by Michael Berry in 1984 [31], which deals with the adiabatic evolution of an eigenstate of a Hamiltonian $\vec{H}(\vec{R})$ with slowly varying parameters $\vec{R} = (R_1(t), R_2(t), \cdots)$ which move through a closed loop C in the parameter space. We will label the instantaneous orthonormal eigenbasis as

$$\vec{H}(\vec{R})|n(\vec{R})\rangle = \varepsilon_n(\vec{R})|n(\vec{R})\rangle. \tag{II.3}$$

The Berry formalism tells us that a system starting in an eigenstate of this Hamiltonian will remain in that eigenstate and that the eigenstate will return to itself after the loop is precessed in the parameter space. However, it will pick up an extra geometrical, gauge-invariant phase factor known as the Berry phase.

The existence of a phase factor in such a situation was known before Berry through the adiabatic approximation of quantum mechanics [29]. Berry's contribution came in identifying that the phase was geometric – that is, dependent only on the path taken through the parameter space. In particular, Berry found that this phase can be written as

$$\gamma_n = \oint_C d\vec{R} \cdot \overrightarrow{A_n}(\vec{R}) \tag{II.4}$$

where

$$\overrightarrow{A_n}(\vec{R}) = i \left\langle n(\vec{R}) \left| \frac{\partial}{\partial \vec{R}} \right| n(\vec{R}) \right\rangle \tag{II.5}$$

is known as the Berry connection. This description, with the help of the generalized Stokes' theorem, indicates that in fact the Berry phase can be written as the flux of a field $\overrightarrow{B_n}(\vec{R})$, known as the Berry curvature, which is derived from the Berry connection as

$$\overrightarrow{B_n}(\vec{R}) = \nabla_R \times \overrightarrow{A_n}(\vec{R}) \tag{II.6}$$

through any surface bounded by the path taken through the parameter space.

Equation II.4 is very similar in form to Cauchy's Residue Theorem, which states that the integral of a function over a simple closed path in complex space is equal to the sum of the residues of the function contained in the path up to some factor [32]. Similarly, because the integral defining the Berry phase is over a closed curve in the parameter space, it must be an integer multiple of 2π. This integer multiple is known as the Chern number and defines the topology of the system, which is discussed below.
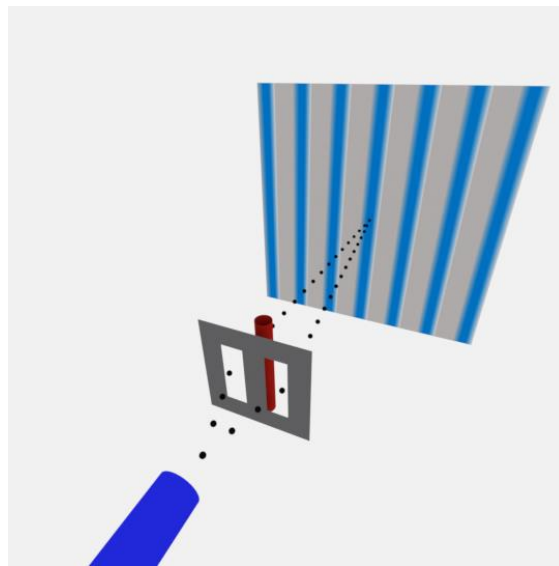
Figure II.2 – The Aharonov-Bohm effect. In this effect, electrons are emitted from a source (blue cylinder) and sent through a double slit. On the other side of the slit, they go around a region of nonzero magnetic field (red). Even though the electrons do not pass through the magnetic field directly, they are affected by the nonzero magnetic vector potential along their path, causing an interference pattern on the screen.

A useful analogy to help us understand the Berry formalism is the Aharonov-Bohm effect [33]. In this phenomenon, electrons travel through free space near to, but not through, a magnetic field. It is required that the magnetic vector potential be continuous over all space. Thus, even though the magnetic field in the space traversed by the electron is zero, it does have a nonzero

vector potential. Physically, this nonzero vector potential causes the electrons to pick up a phase shift, which can be observed as an interference pattern on a screen, as shown in Figure II.2. Here, the phase factor picked up by the electrons is like the Berry phase. In both cases the phase is physical and measurable. The magnetic vector potential and magnetic field are like the Berry connection and curvature, respectively, having the same mathematical relationship to each other and to the phase [29, 34].

The Berry formalism is how we relate condensed matter systems to the mathematical concept of topology. Mathematically, topology is the study of how manifolds depend on operations such as twisting and bending. Any two manifolds that can be deformed into one another by some means besides cutting or gluing are considered to be topologically equivalent. Each class of topologically equivalent manifolds can be described by its Chern number, or its topology, which is determined by the number of holes in the manifolds. In Figure II.3, we demonstrate several examples of topological manifolds with topologies of zero, one, and two.

Figure II.3 – Examples of different topological manifolds. The sphere, cube, and cylinder can all be continuously deformed one into another and so are considered topologically equivalent. They

have a topology of 0. In contrast, a cut would need to be made in order to realize the torus or the double-torus, which have topologies of 1 and 2, respectively.

We can also consider the topology of a crystalline material. If we consider the vacuum to be an insulator with a conduction band (electrons), valence band (positrons), and an energy gap (for pair production), then materials that can undergo a metal-insulator transition by means of perturbations to the band structure are considered topologically equivalent to the vacuum. We say that this class of insulators has a Chern number of zero. However, not all materials can undergo such a transition with small perturbations. The simplest counterexample is that of an integer quantum Hall state. Such a state exists when a thin sheet of metal is placed in a magnetic field oriented perpendicular to its surface. An otherwise free electron in such a system is subject to a Hamiltonian

$$H = \frac{\hbar^2}{2m}(-i\partial_x)^2 + \frac{1}{2m}\left(-i\hbar\partial_y - \frac{e}{c}Bx\right)^2 \qquad \text{II.7}$$

where the material lies in the xy-plane with a magnetic field $\vec{B} = B\hat{z}$, and where we have chosen the Landau gauge for our magnetic vector potential, $\vec{A} = (0, Bx, 0)$. This reduces to the Hamiltonian for a quantum harmonic oscillator in the y-component, yielding quantized energy levels

$$E_{n,k_y} = \left(n + \frac{1}{2}\right)\hbar\omega = \left(n + \frac{1}{2}\right)\frac{eB\hbar}{cm} \qquad \text{II.8}$$

for some integer n. We can treat this as a band structure with flat bands for each n, as shown in Figure II.4. However, now the gaps in this band structure are topologically protected, meaning that perturbations to the system or to the field will not change the fact that the gaps exist. The only effect perturbations can have on the bands is to change the distance between them [35].

To see this, consider that in order to transition from one insulating state to the next, you must necessarily go through a metallic phase. This is similar to a "tear" in the manifold in the mathematical definition of topology. Another way to think about this is to consider that the Landau levels are quantized and that this quantization is intrinsically related to the Chern number. This arises from the fact that the Hall conductivity is the total Berry curvature of the system. Due to the fact that they can be well-described using the Berry formalism and because they have a nonzero topology, Hall insulators are known as topological insulators.
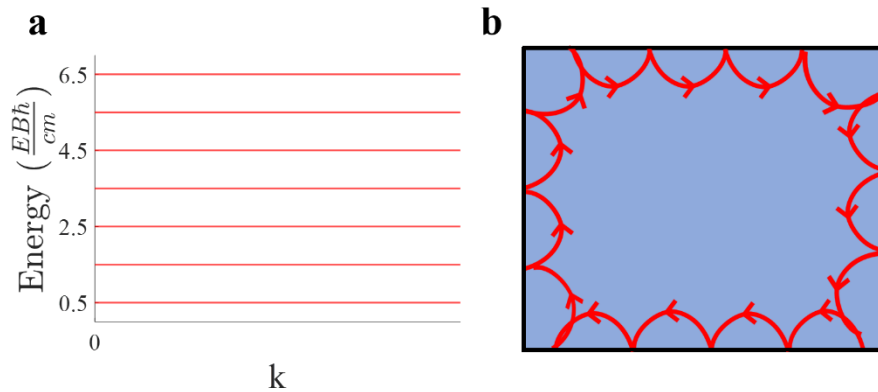
Figure II.4 – Hall Effect illustrations. (a) The "band structure" resulting from the Hall effect. It is clear that the bands are flat and evenly spaced, and so the sweeping the Fermi energy would require transitions from insulating to metallic to insulating states. (b) A cartoon illustration of the chiral edge states which arise due to the topology in such a Hall system.

Earlier, we mentioned that the vacuum is an insulator with a trivial topology. Taking this into account, if we place a Hall insulator in vacuum, we must necessarily go from a trivial to a nontrivial topology. According to our mathematical definition, this requires a "tear" in the topological manifold. The way this "tear" manifests physically is in a conducting edge state where current flows in one direction around the edges of the system, as shown in Figure II.4. We can also picture this in terms of the classical view of electrons in the plane of the material orbiting in a

13

cyclotron motion due to the external magnetic field. At the edges of the material, the electrons would not be able to fully complete their orbit and would thus flow in one direction around the edge of the material. Importantly, this edge state is robust against impurities in the system. Such topological edge states are typical of topological materials and are often used as a detection mechanism for these systems [6, 7].

Defining Weyl Semimetals

In WSMs, the Fermi energy occurs at a touching point of the conduction and valence bands and the dispersion near this touching point is both linear and protected topologically against perturbations. In these systems, the touching point is known as a Weyl Point (WP). Suppose for the sake of illustration that this WP occurs at momentum $\vec{k_0}$,[2] where we are now working in three dimensions. Then we can expand the momentum-space Hamiltonian around this point as

$$H(\vec{k}) = \pm\hbar v_F(\vec{k} - \vec{k_0}) \cdot \vec{\sigma},$$ II.9

where v_F is the Fermi velocity and $\vec{\sigma} = (\sigma_x, \sigma_y, \sigma_z)$ is a vector of the Pauli matrices

$$\sigma_x = \begin{pmatrix} 0 & 1 \\ 1 & 0 \end{pmatrix}, \qquad \sigma_y = \begin{pmatrix} 0 & -i \\ i & 0 \end{pmatrix}, \qquad \sigma_z = \begin{pmatrix} 1 & 0 \\ 0 & -1 \end{pmatrix}.$$ II.10

We know that this should model the dispersion near the WP because it is indeed linear in the wave vector as is required by the definition of a WSM. An investigation of this Hamiltonian shows that small perturbations of $\vec{k_0}$ and E_0 do not create a gap at the location of the WP (ie. the existence of the WP persists despite small perturbations). Instead, the WP is moved around in momentum space. Similarly, perturbations of v_F change the slope of the dispersion at the WP without eliminating the WP altogether. This is the first indication that the WP is protected [4].

---

[2] We will define the energy at which this crossing point occurs as the zero potential.

There are two concepts that we would like to emphasize here. The first is that the WP is intrinsically describing a crossing point in a 3d bulk band structure – that is, a 3d cone. This distinction is vital to the protection of the WP. If the crossing point occurred only at a cross-section of the band structure (that is, in two dimensions of the available three), then a perturbation in the third dimension could easily gap out the crossing point [36]. The second is that such crossing points can only occur in materials which break one of either TRS or SIS. This is because the preservation of both of these symmetries in a material causes the band structure to be doubly degenerate, such that two WPs would perfectly overlap in momentum space [4]. This is the case for Dirac semimetals, which will not be discussed in this work but are described further in [37].

The Hamiltonian presented in Equation II.9 is independently known as the Weyl Hamiltonian [26], which was first predicted by Hermann Weyl in 1929. Solutions to the Weyl Hamiltonian are a left- and right-handed spinors, each of which has the general form

$$\psi(\vec{r}, t) = \begin{pmatrix} \gamma_1 \\ \gamma_2 \end{pmatrix} e^{-i(\vec{k} \cdot \vec{r} - \omega t)}. \qquad \text{II.11}$$

These solutions are known as Weyl fermions, which are massless particles with a distinct chirality. Interestingly, quasiparticles which occur in WSMs as a result of excitations around the WPs have properties identical to the Weyl fermions of high energy physics. As such, WSMs, and type-I WSMs in particular, have been proposed as a means by which to explore the properties of the high-energy Weyl fermions, have not yet been experimentally realized [38-40].

More than this, it can be shown that the crossing points in the bulk band structure of the WSMs are topologically protected. To see this, we can compute the Berry curvature of our Weyl Hamiltonian to obtain the relation [4]

$$\vec{\Omega}(\vec{k}) = \pm \frac{\vec{k}}{\left|\vec{k} - \vec{k_0}\right|^3}. \qquad \text{II.12}$$

15

This relation requires that the Berry curvature must have singularities at the WP. This implies that the WPs serve as sources and sinks of Berry curvature [4, 36] and must correspond to a nonzero Berry phase. They have a nonzero Chern number and therefore must be topologically protected. An illustration of what this field might look like is shown in Figure II.5. Further, the Nielsen-Ninomiya No-Go theorem then says that all WPs must come in pairs of opposite chirality [41]. Figure II.5 indicates a space consisting of two WPs – one of positive and the other of negative chirality.
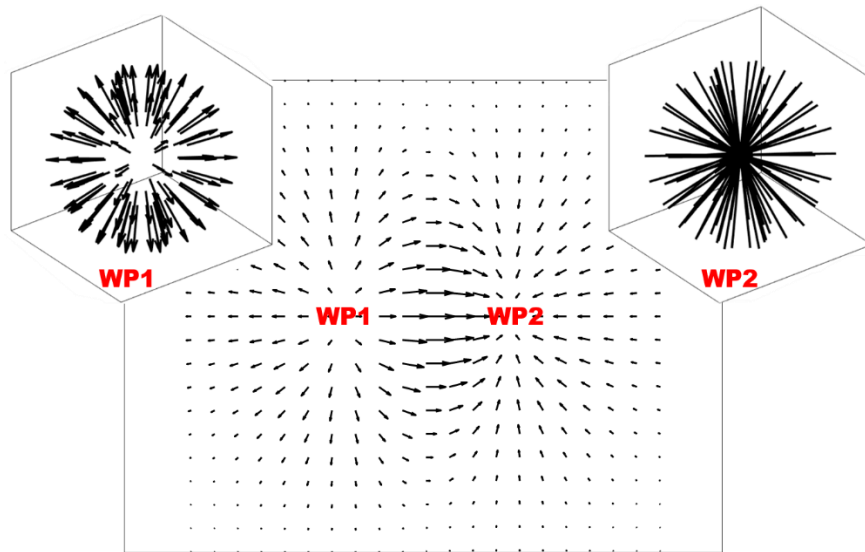
Figure II.5 – An illustration of the Berry curvature field in the simplest case of a WSM consisting of two WPs with opposing chirality in the bulk. Shown is a 2d vector representation of the field, with WP1 (positive chirality) and WP2 (negative chirality) indicated. The insets show the 3d effect of the singularities at WP1 and WP2, such that they serve as a source and sink of Berry curvature, respectively.

Because there is a requirement that either SIS or TRS be broken, WSMs are typically classified as either magnetic (broken TRS) or electronic (broken SIS). The existence of a WSM state was first described and predicted to exist in pyrochlore iridates, which are magnetic WSMs

16

[3]. However, the first successful experimental confirmation of a WSM state in a material was in an electronic WSM. In particular, WSM states were first predicted to exist in the TaAs class of materials in [27, 28] and were first experimentally observed in TaAs using ARPES [6, 7] in 2015. In ARPES experiments, photons are directed at the sample with a known energy and momentum, and electrons emitted from the material through photoemission are then detected using a detector sensitive to both energy and momentum. By comparing the initial and final particles in the photoemission process and requiring energy-momentum conservation, the energy and momentum of the electron in the material can be calculated. Ultimately, this provides the band structure on the surface of the material. This allows for the detection of the WSM state because of its topology, which results in surface states detectable in ARPES measurements. In WSMs, these surface states connect the WPs and are known as Fermi arcs. Since the confirmation of TaAs as a WSM, several other WSMs have also been predicted and experimentally confirmed. Some examples of these are shown in Table II.2.
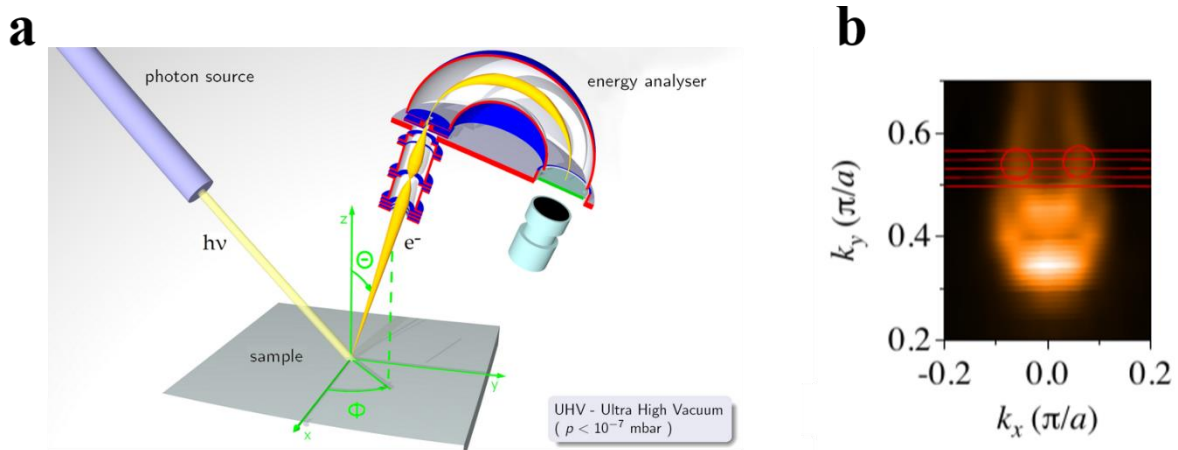
Figure II.6 – Experimental discovery of WSM in TaAs. (a) A schematic of an ARPES setup from Wikipedia. (b) ARPES data on TaAs at the Fermi energy around one of the Weyl points. The Fermi arc surface states are clear from the data [6].

TaAs falls into a class of what is known as electronic type-I WSMs, which contrasts with the electronic type-II WSMs predicted in [8]. The distinction between the type-I and type-II classes of WSMs arises from a subtlety of Equation II.9, which is that the zero-potential definition of the system is somewhat arbitrary. We can imagine an offset in energy by some E_0 which is a function of the momentum $\vec{k}$, which changes our expression of the Weyl Hamiltonian to the Dirac equation

$$H(\vec{k}) = E_0(\vec{k})\sigma_0 \pm \hbar v_F(\vec{k} - \vec{k_0}) \cdot \vec{\sigma},\qquad \text{II.13}$$

where σ_0 is the identity matrix. In most cases, this E_0 term can be Taylor expanded in a way which includes a term linear in $\vec{k}$ such that

$$H(\vec{k}) = \hbar\widetilde{v_F}(\vec{k} - \vec{k_0})\sigma_0 \pm \hbar v_F(\vec{k} - \vec{k_0}) \cdot \vec{\sigma}.\qquad \text{II.14}$$

The distinction between type-I and type-II WSMs then comes from a comparison between v_F and $\widetilde{v_F}$. TaAs and other type-I WSMs satisfy $v_F > \widetilde{v_F}$, but if $v_F < \widetilde{v_F}$ we have a type-II WSM where the two bands overlap in energy yielding electron and hole pockets around the WP [4]. An example of these electron and hold pockets are shown in Figure II.7.
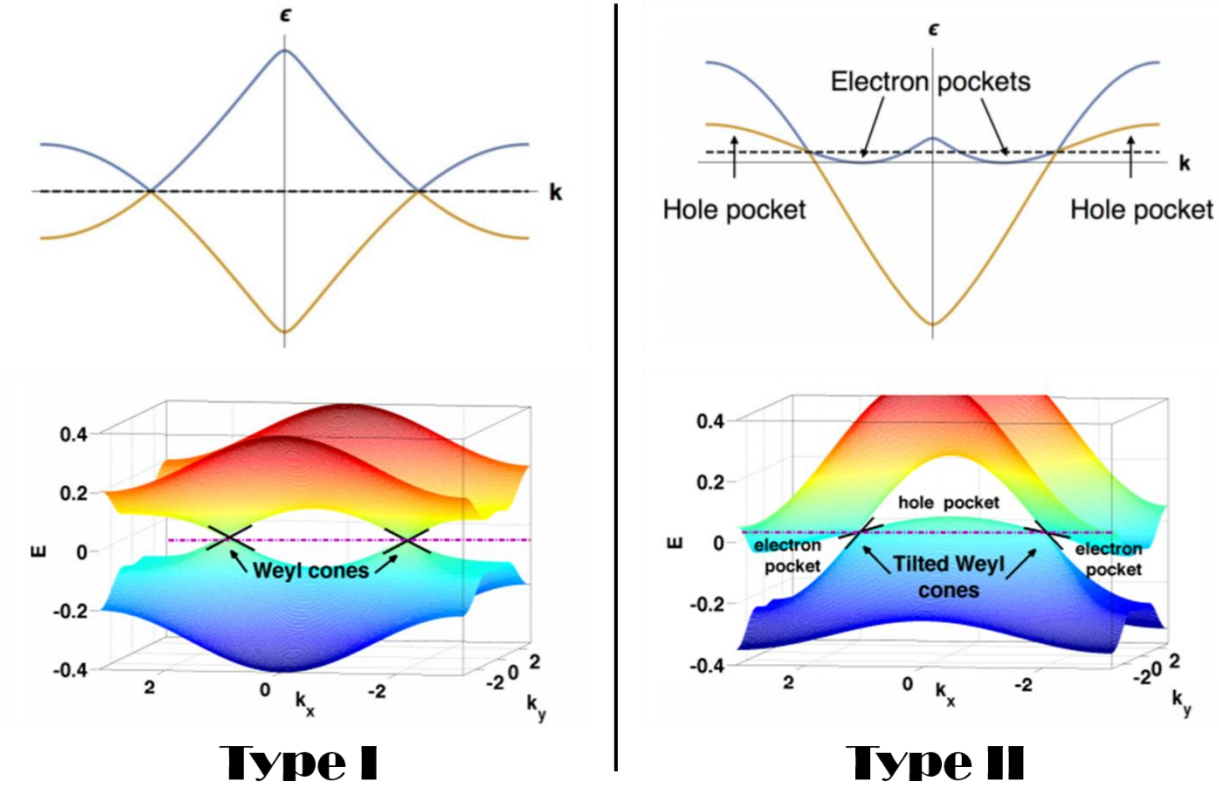
Figure II.7 – An illustration of the differences between type-I and type-II WSMs. In particular, the type-II WSMs are defined by electron and hole pockets right at the WPs in the bulk band structure. These figures are adapted from [4, 40].

In addition, WSMs commonly have mirror symmetries, but these symmetries are not required for the existence of the WSM state. However, when a WSM does have mirror symmetries, it restricts the band structure in such a way that the corresponding WPs must share the same energy. This makes direct optical studies of the topology of these points challenging because it means that accessing one WP necessarily accesses the WP of the opposite chirality, and the net Chern number of such a process is zero. However, in the absence of mirror symmetries, it is possible for corresponding WPs to exist at different energies in the band structure. This means a clever choice of wavelength can optically access one WP and not the other, allowing for the potential to probe

19

topological features of the material. These WSMs with non-degenerate WPs are known as chiral WSMs [42].

Type of WSM	Description	Example Materials	References
Magnetic	TRS broken	Pyrochlore Iridates	[3, 43]
		Mackay-Terrones crystals	[44]
		YbMnBi$_2$ (type-II)	[45]
		Magnetically doped superlattice	[46]
Electronic	SIS broken	Quantum Spin-Hall state	[47]
Type-I	WSMs with minimal tilting of Weyl cones	TaAs	[6, 7]
		TaP	[48, 49]
		NbAs	[50]
		NbP	[51]
Type-II	WSMs with electron and hole pockets at the WPs	T$_d$-MoTe$_2$	[22, 52, 53]
		T$_d$-WTe$_2$	[8, 54-56]
		LaAlGe	[57]
Chiral	Electronic WSMs lacking mirror symmetries	RhSi, CoSi	[25, 42, 58-60]

Table II.2 – A summary of the various types of WSM states known and predicted today, together with their descriptions and a selection of example materials for each category.

The unique topological band structure and symmetry requirements of WSMs leads to several unique physical phenomena, including nonlinear optical properties, which will be discussed in Chapter III.

Spin-Orbit Coupling and Strong Correlations

The last topic we will discuss in this chapter is the importance of spin-orbit coupling (SOC) and strong electron-electron correlations in WSMs. Generally, SOC refers to coupling between the spin and angular momentum of a particle while strong electron-electron correlations refer to

interactions between electrons in a material. This latter effect is in direct contradiction to the Drude theory of solids, which assumes that there are no electron-electron interactions and that instead electrons can only interact with the underlying lattice structure [61, 62]. As early as 1937, de Boer and Verwey discussed that this assumption of the Drude theory did not lead to accurate predictions in all real material systems [63]. Later work by Mott and Hubbard fully developed the inclusion of an electron-electron correlation term into the Hamiltonian and identified its role in metal-insulator transitions [64]. The Mott and Hubbard model was particularly crucial for modeling 3d transition metal oxides and determining how electron-electron correlations contributed to effects such as quantum criticality and unconventional superconductivity in these materials [65-67].

SOC, on the other hand, arises due to the fact that electrons are moving charged particles in electric fields, which means that electrons experience an effective magnetic field $\overrightarrow{B_{eff}} \propto \vec{v} \times \vec{E}$. When this field interacts with the spin of the electron, a term in the Hamiltonian $H_{LS} \propto \vec{L} \cdot \vec{S}$ arises, for $\vec{L}$ the orbital angular momentum and $\vec{S}$ the spin [29]. SOC is particularly common in heavy elements, and a good deal of work has been done to study its effect particularly in materials with filled f-orbits [68] and in topological insulators [67]. The effects of SOC and strong correlations can both be seen commonly in 4d and 5d orbital material systems, where the interplay between the two can lead to novel transport phenomena like the anomalous Hall effect and control of spin currents. Additionally, SOC and strong correlations can lead to the onset of topological phases of matter [2]. An example illustration of a phase diagram for such a material is shown in Figure II.8.

In this phase diagram, we can see that the WSM state lies in the area of the parameter space where electron-electron correlations and SOC are both relatively strong. This emphasizes the point that the inclusion of spin-orbit coupling is necessary to identify materials as WSMs [23]. However, there is a wide variety of other physical systems which also fall into this area of the parameter

21

space. The last experimental chapter of this thesis will be devoted to one particularly interesting

material, the complex oxide $RbFe(MoO_4)_2$, which fall into this category of strongly correlated,

strong SOC materials which are not WSMs.
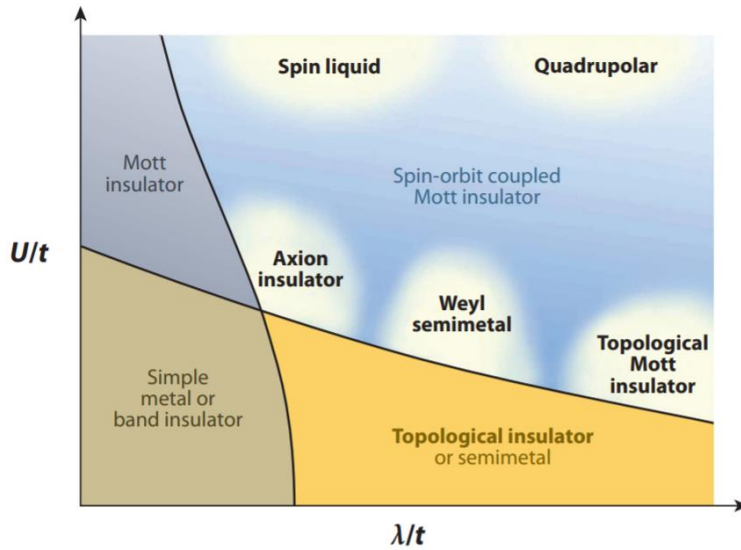
Figure II.8 – Generic band diagram of a material experiencing both SOC, with strength given by λ, and strong electron-electron correlations, with strength given by U, taken from [67]. Here, t described the hopping amplitude, or the probability that an electron will move from one lattice site to an adjoining lattice site, which is a fundamental property of the Hubbard model.

CHAPTER III

Nonlinear Optics

We have so far discussed broadly the materials we are interested in for the study of this thesis, and, in the process, we have developed a robust definition for the WSM state. In this chapter, we will introduce the experimental methods we used to complete our studies. The primary tools are derived from nonlinear spectroscopic techniques. In the most basic sense, nonlinear optical processes occur when a system undergoes a change due to the application of light which is not linearly proportional to the field of the applied light. All materials have the potential to experience nonlinear optical effects, but the strength of those effects is highly material- and geometry-dependent. For example, light transmitted through plexiglass is unlikely to undergo a strong nonlinear process regardless of experimental geometry. In contrast, beta-barium borate (BBO) crystals are well-known for their second harmonic, or frequency doubling, effects, but the strength of those effects is dependent on the cut of the crystal as well as the orientation of the crystal relative to the wavevector and polarization of the incident light. More specifically, this dependence on the experimental conditions requires the wavevectors of the incoming fields add to exactly the wavevector of the nonlinear field generated in the material to maximize the SHG response, a phenomenon known as phase matching. At perfect phase matching, the dipoles within the material line up such that their fields can be summed coherently, yielding the largest possible nonlinear response [69].
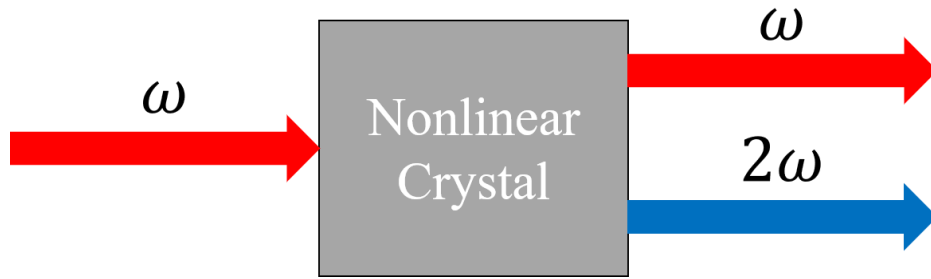
Figure III.1 – An illustration of the frequency doubling process which occurs in a BBO. Light of frequency ω is incident on the BBO and light of frequency 2ω is emitted after it interacts with the nonlinear crystal.

The nonlinear optical response is a material property intricately related to the symmetry and topology of the material under investigation, as will be discussed throughout this chapter. In particular, we will begin with a brief review of previous experiments studying nonlinear optical processes in WSMs to motivate our use of nonlinear probes in our studies of these materials. Then we will move on to the two nonlinear optical processes in which we are most interested – SHG and the photogalvanic effect, or photocurrent generation. For each of these, we will present a mathematical foundation and a more in-depth look into the roles played by symmetry and topology in the manifestation of these effects in WSMs. We also note here that the EE^* formalism developed in this chapter to study photocurrent generation in materials is unique to our work, and was created jointly by myself and my advisor, Liuyan Zhao.

Nonlinear Optical Effects in Weyl Semimetals

Because of their unique symmetry and topology, the study of the nonlinear optical properties of WSMs is of particular interest. Already, WSMs have been shown to exhibit strong nonlinear optical effects, including SHG [14, 70, 71], photocurrent generation [9-11, 15, 16, 72-75], the nonlinear Hall effect [17, 18, 76, 77], the chiral anomaly [78], and others [79]. A summary

of some specific nonlinear optical effects observed in WSMs is presented in Table III.1. We will focus on SHG and photocurrent generation in the following sections and chapters. However, it is worthwhile to take a moment to describe two additional nonlinear phenomena – the chiral anomaly and the nonlinear Hall effect – and the role they play in WSMs.

Nonlinear Effect	Material Observation	Reference
Chiral Anomaly	TaAs	[80]
Nonlinear Hall Effect	$TaIrTe_4$	[81]
	WTe_2	[17]
SHG	TaAs	[14, 70]
Photogalvanic Effect	TaAs	[9, 82]
	$MoTe_2$, WTe_2	[83]
	RhSi	[10, 11, 58, 60]

Table III.1 – A summary of several nonlinear optical effects and references to studies on specific WSMs.

The chiral anomaly is a perfect example of a high energy physics phenomenon being realized in a material system, appearing as the triangle anomaly in the decay of the neutral pion in high energy physics experiments [5, 38, 80]. This effect is nonlinear in that it relies on both incoming electric and magnetic fields. In particular, when these incoming fields are parallel, they can cause unequal populations of electrons in the Weyl cones. Because each cone is chiral, a nonzero chiral current can emerge which causes an increase in the conductivity of the material with increased magnetic field [5]. One of the ways that this physically manifests in measurements is through a negative longitudinal magnetoresistance [39], which is when the resistivity of the material decreases with increasing magnetic field. This effect has been reported in TaAs [80]. The connection between the nonzero chiral current and the topology is intuitive. We recall from our discussion in Chapter II that the chirality of the Weyl cones is described by the Chern number, calculated by integrating the flux of the Berry curvature. The Chern number determines the

topology of the system and the chiral current resulting from the unequal populations of the Weyl cones is a direct manifestation of this topology.

The nonlinear Hall effect is another process directly related to the topology of the WSM state. The linear Hall effect has already been discussed in some detail in Chapter II. The basic idea is that if a metal with a current traveling through it is placed into a magnetic field perpendicular to the direction of the current, then that field will cause the charge carriers to curve a particular direction. This leads to an accumulation of charge on the edges of the conductor which contribute to a voltage difference across the device perpendicular to both the current and the applied magnetic field [84]. This effect requires the breaking of TRS. However, the nonlinear Hall effect, which is a higher-order analogue of the linear Hall effect is still symmetry-allowed in electronic WSMs. In this case, an electric field is applied to cause a current in the material, and the Hall conductivity is proportional to two copies of this field [85]. The nonlinear Hall effect has already been observed in several WSMs, including the type-II WSMs $TaIrTe_4$ [81] and WTe_2 [17].

One of the most important features of the linear and nonlinear Hall effects is quantization. The quantization of the linear Hall effect can be modeled using the Berry curvature. Such a calculation shows that the Hall conductivity is the integral of the Berry curvature over occupied states [86]. This means that the Chern number is the root cause of the quantized effect observable through linear Hall measurements. The nonlinear Hall effect is similarly related to the topology because the interband transitions can be modeled as the first-order integral of the Berry curvature, known as the Berry curvature dipole [18, 75, 87].

The nonlinear Hall effect is a particularly useful illustration for a theme which will emerge throughout this work. Symmetry considerations dictate whether this phenomenon can occur in a material at all, and what form the material response will take. But the strength of the response is

given by the quantization, which is related to the topology of the material. Throughout this work, we will try to draw comparisons between the allowance and anisotropy of an effect and the symmetries of the system, and the size of the effect and its topology.

Mathematical Foundations of Nonlinear Optics and Second Harmonic Generation

The most generic experiment we can do when studying nonlinear optical properties of materials is to direct light at a material and measure the response. The light source we use is a pulsed laser, the details of which are presented in Chapter IV. Laser light is polarized and has a particular wavelength. Such a light source can be represented as

$$\tilde{E}(\vec{x}, t) = \vec{E} e^{i(\vec{k} \cdot \vec{x} - \omega t)} + c.c., \qquad \text{III.1}$$

where $\vec{E}$ describes the amplitude and polarization of the light, $\vec{k}$ is the wavevector, ω is the frequency, and $c.c.$ stands for taking the complex conjugate of the first term (that is, a monochromatic plane wave will consist of light of frequency ω and $-\omega$) [69].

To the lowest approximation, when light shines onto a material, it will induce a change in the electronic polarization of that material given by

$$\tilde{P}(\vec{x}, t) = \epsilon_0 \chi \tilde{E}(\vec{x}, t), \qquad \text{III.2}$$

for $\epsilon_0 = 8.854 \times 10^{-12}$ F/m, a fundamental constant known as the permittivity of free space, and for χ the optical susceptibility of the material. The full effect of the electric field on the material polarization, however, is given by a Taylor expansion in terms of that field

$$P_i(\vec{x}, t) = \epsilon_0 (\chi_{ij}^{(1)} E_j(\vec{x}, t) + \chi_{ijk}^{(2)} E_j(\vec{x}, t) E_k(\vec{x}, t) + \cdots), \qquad \text{III.3}$$

where now we are using the Einstein summation notation typical when working with tensors. We can see that Equation III.2 above is simply the first term of this expansion – the linear term. The

additional terms are nonlinear in the electric field and are thus the basis for the field of nonlinear optics [69].

We will be primarily focused on second-order effects, and so we will begin by exploring the second order nonlinear optical response in a bit more detail. We know from Equation III.3 that the second order response can be written as $\tilde{P}^{(2)}(\vec{x}, t) = \epsilon_0 \chi^{(2)} \tilde{E}^2(\vec{x}, t)$. We can write this out explicitly using the form of $\tilde{E}$ from Equation III.1 as

$$\tilde{P}(t) = \epsilon_0 \big(2\chi^{(2)} E E^* + \chi^{(2)} E^2 e^{-2i\omega t} + \chi^{(2)} (E^*)^2 e^{2i\omega t}\big), \qquad \text{III.4}$$

where E^* indicates the complex conjugate. By looking at the exponentials, we can immediately see that we have terms of two different frequencies, neither of which is the original frequency ω. In particular, the first term has a frequency of zero. That is, it is a direct current (DC) term. The second and third terms have frequency 2ω. These are the contributions to SHG, also aptly known as frequency doubling. In this calculation, we have assumed that the mixing fields have the same frequency, but it is also possible to mix two fields of different frequencies within the material. In this case, the DC term will correspond to difference frequency generation[3] and the SHG term to sum frequency generation [69].

χ^{NL} and Crystal Symmetry

Up until now, we have discussed the effect of the incoming laser field on the nonlinear response of the material. To see how the nonlinear response relates to the material properties, however, we must use the nonlinear optical susceptibility tensor, χ^{NL}. This tensor is a material-dependent property which obeys the point symmetries of the crystal. This means that we can use

---

[3] In the case of the mixing of fields of different frequencies, this term will no longer be a DC effect but rather a low-frequency effect obeying $\omega_1 - \omega_2$ for ω_1, ω_2 the frequencies of the two incoming fields.

the nonlinear response of the crystal to study its symmetry properties. As a simple example, we can consider the $\chi^{(2)}$ tensor (ie. the second-order nonlinear response tensor) for a centrosymmetric material. We know that such a tensor must obey

$$P_i(\vec{x}, t) = \epsilon_0 \chi^{(2)}_{ijk} E_j(\vec{x}, t) E_k(\vec{x}, t). \qquad \text{III.5}$$

However, because we are working with a centrosymmetric material, this equation must remain invariant in the case that we apply the spatial inversion operator to it. In particular, applying spatial inversion to the polarization will require $P_i \rightarrow -P_i$ and $E_i \rightarrow -E_i$. This means that Equation III.5 will become

$$-P_i(\vec{x}, t) = \epsilon_0 \chi^{(2)}_{ijk} (-E_j(\vec{x}, t))(-E_k(\vec{x}, t)). \qquad \text{III.6}$$

The only way that Equations III.5 and III.6 will hold simultaneously in all of space and time is if $\chi^{(2)} = 0$ for all tensor elements. That is, there is no second order SHG response in centrosymmetric crystals.
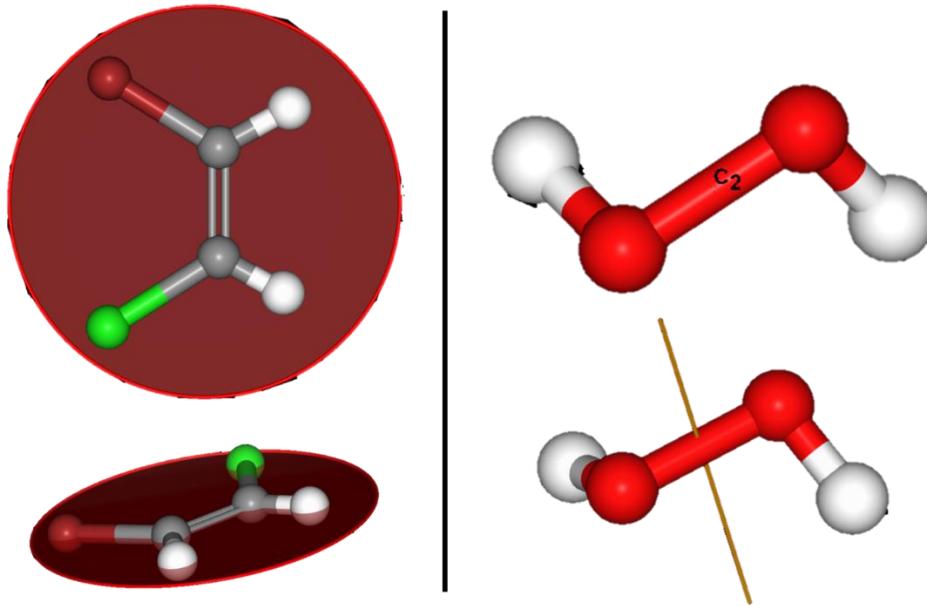
Figure III.2 – (Left) An example of a molecule obeying the m point group, ethylene-BrCl. The singular mirror is highlighted by the plane of the red circle. (Right) an example of a molecule

obeying the C_2 point group, hydrogen peroxide. The C_2 axis is indicated by the line in the lower image and is out of plane in the top image. All illustrations are adapted from and drawn using [88].

In actuality, the relationship between the crystal symmetry and the nonlinear susceptibility tensor goes farther than dictating whether or not an effect occurs. In fact, we can use the crystal symmetry to derive the general form of the nonlinear susceptibility tensor by, as above, requiring that Equation III.5 remain invariant when it is operated on by any symmetry operation of the point group of the crystal. As a simple example, let us consider the m point group, which consists of one mirror plane. An illustration of a molecule obeying this point symmetry is shown in Figure III.2. We will arbitrarily choose the mirror to lie in the xz-plane. In this case, there is one symmetry operator for the point group, given by

$$M_{xz} = \begin{pmatrix} 1 & 0 & 0 \\ 0 & -1 & 0 \\ 0 & 0 & 1 \end{pmatrix}. \tag{III.7}$$

For the case of the linear response, the $\chi^{(1)}$ tensor will have the generic form of

$$\chi^{(1)} = \begin{pmatrix} \chi_{xx}^{(1)} & \chi_{xy}^{(1)} & \chi_{xz}^{(1)} \\ \chi_{yx}^{(1)} & \chi_{yy}^{(1)} & \chi_{yz}^{(1)} \\ \chi_{zx}^{(1)} & \chi_{zy}^{(1)} & \chi_{zz}^{(1)} \end{pmatrix}. \tag{III.8}$$

We can apply M_{xz} to $\chi^{(1)}$ to find

$$\chi^{(1)\prime} = M_{xz}^{-1} X^{(1)} M_{xz} = \begin{pmatrix} \chi_{xx}^{(1)\prime} & -\chi_{xy}^{(1)\prime} & \chi_{zx}^{(1)\prime} \\ -\chi_{yx}^{(1)\prime} & \chi_{yy}^{(1)\prime} & -\chi_{yz}^{(1)\prime} \\ \chi_{xz}^{(1)\prime} & -\chi_{zy}^{(1)\prime} & \chi_{zz}^{(1)\prime} \end{pmatrix}. \tag{III.9}$$

Because M_{xz} is a symmetry, we require that Equations III.8 and III.9 be equal, which means that, for m, $\chi^{(1)}$ must have the general form

$$X^{(1)} = \begin{pmatrix} \chi_{xx}^{(1)} & 0 & \chi_{zx}^{(1)} \\ 0 & \chi_{yy}^{(1)} & 0 \\ \chi_{xz}^{(1)} & 0 & \chi_{zz}^{(1)} \end{pmatrix}.$$

<div align="right">III.10</div>

We can similarly consider the form of $\chi^{(2)}$ for the m point group. The general form of this higher-order tensor is

$$X^{(2)} = \begin{pmatrix} \begin{pmatrix} \chi_{xxx}^{(2)} \\ \chi_{xxy}^{(2)} \\ \chi_{xxz}^{(2)} \end{pmatrix} & \begin{pmatrix} \chi_{xyx}^{(2)} \\ \chi_{xyy}^{(2)} \\ \chi_{xyz}^{(2)} \end{pmatrix} & \begin{pmatrix} \chi_{xzx}^{(2)} \\ \chi_{xzy}^{(2)} \\ \chi_{xzz}^{(2)} \end{pmatrix} \\ \begin{pmatrix} \chi_{yxx}^{(2)} \\ \chi_{yxy}^{(2)} \\ \chi_{yxz}^{(2)} \end{pmatrix} & \begin{pmatrix} \chi_{yyx}^{(2)} \\ \chi_{yyy}^{(2)} \\ \chi_{yyz}^{(2)} \end{pmatrix} & \begin{pmatrix} \chi_{yzx}^{(2)} \\ \chi_{yzy}^{(2)} \\ \chi_{yzz}^{(2)} \end{pmatrix} \\ \begin{pmatrix} \chi_{zxx}^{(2)} \\ \chi_{zxy}^{(2)} \\ \chi_{zxz}^{(2)} \end{pmatrix} & \begin{pmatrix} \chi_{zyx}^{(2)} \\ \chi_{zyy}^{(2)} \\ \chi_{zyz}^{(2)} \end{pmatrix} & \begin{pmatrix} \chi_{zzx}^{(2)} \\ \chi_{zzy}^{(2)} \\ \chi_{zzz}^{(2)} \end{pmatrix} \end{pmatrix}.$$

<div align="right">III.11</div>

When we act M_{xz} on $\chi^{(2)}$ as $\chi_{ijk}^{(2)\prime} = M_{im}^{xz} M_{jn}^{xz} M_{kl}^{xz} \chi_{mnl}^{(2)}$ and require that $\chi_{ijk}^{(2)\prime} = \chi_{ijk}^{(2)}$, we find that, for the m point group, $\chi^{(2)}$ takes the form

$$X^{(2)} = \begin{pmatrix} \begin{pmatrix} \chi_{xxx}^{(2)} \\ 0 \\ \chi_{xxz}^{(2)} \end{pmatrix} & \begin{pmatrix} 0 \\ \chi_{xyy}^{(2)} \\ 0 \end{pmatrix} & \begin{pmatrix} \chi_{xzx}^{(2)} \\ 0 \\ \chi_{xzz}^{(2)} \end{pmatrix} \\ \begin{pmatrix} 0 \\ \chi_{yxy}^{(2)} \\ 0 \end{pmatrix} & \begin{pmatrix} \chi_{yyx}^{(2)} \\ 0 \\ \chi_{yyz}^{(2)} \end{pmatrix} & \begin{pmatrix} 0 \\ \chi_{yzy}^{(2)} \\ 0 \end{pmatrix} \\ \begin{pmatrix} \chi_{zxx}^{(2)} \\ 0 \\ \chi_{zxz}^{(2)} \end{pmatrix} & \begin{pmatrix} 0 \\ \chi_{zyy}^{(2)} \\ 0 \end{pmatrix} & \begin{pmatrix} \chi_{zzx}^{(2)} \\ 0 \\ \chi_{zzz}^{(2)} \end{pmatrix} \end{pmatrix}.$$

<div align="right">III.12</div>

We can take this example just one step further to illustrate the power of nonlinear optics in identifying the symmetries of crystal structures by examining the C_2 point group. An illustration of a molecule obeying this point group is also found in Figure III.2. Like m, C_2 is a monoclinic

point group. It consists also of one symmetry operation – a two-fold rotation about one axis, which we will take to be the y-axis. This symmetry operation can thus be represented by the matrix

$$C_{2,y} = \begin{pmatrix} -1 & 0 & 0 \\ 0 & 1 & 0 \\ 0 & 0 & -1 \end{pmatrix}.$$

III.13

Applying this transformation to the general form of $\chi^{(1)}$ and requiring that the matrix obey the C_2 symmetry leads to a form of $\chi^{(1)}$ for C_2 of

$$X^{(1)} = \begin{pmatrix} \chi_{xx}^{(1)} & 0 & \chi_{zx}^{(1)} \\ 0 & \chi_{yy}^{(1)} & 0 \\ \chi_{xz}^{(1)} & 0 & \chi_{zz}^{(1)} \end{pmatrix}.$$

III.14

A comparison of Equations III.10 and III.14 shows that the form of these linear tensors is the same for both point groups, despite their different symmetry operations. In fact, this holds true across the different crystal classes – the linear optical susceptibility tensors can generally distinguish between different crystal classes[4]. However, it is necessary to go to higher order tensors, and thus to nonlinear optical effects, to make distinctions between different point groups within a particular crystal class. Here, for example, the form of $\chi^{(2)}$ for the C_2 point group is

$$X^{(2)} = \begin{pmatrix} \begin{pmatrix} 0 \\ \chi_{xxy}^{(2)} \\ 0 \end{pmatrix} & \begin{pmatrix} \chi_{xyx}^{(2)} \\ 0 \\ \chi_{xyz}^{(2)} \end{pmatrix} & \begin{pmatrix} 0 \\ \chi_{xzy}^{(2)} \\ 0 \end{pmatrix} \\ \begin{pmatrix} \chi_{yxx}^{(2)} \\ 0 \\ \chi_{yxz}^{(2)} \end{pmatrix} & \begin{pmatrix} 0 \\ \chi_{yyy}^{(2)} \\ 0 \end{pmatrix} & \begin{pmatrix} \chi_{yzx}^{(2)} \\ 0 \\ \chi_{yzz}^{(2)} \end{pmatrix} \\ \begin{pmatrix} 0 \\ \chi_{zxy}^{(2)} \\ 0 \end{pmatrix} & \begin{pmatrix} \chi_{zyx}^{(2)} \\ 0 \\ \chi_{zyz}^{(2)} \end{pmatrix} & \begin{pmatrix} 0 \\ \chi_{zzy}^{(2)} \\ 0 \end{pmatrix} \end{pmatrix},$$

III.15

---

[4] In fact, the form of the linear optical susceptibility tensor is the same for two different groupings of crystal classes – the tetragonal, trigonal, and hexagonal classes and the cubic and isotropic classes [69].

which is distinct from the form of $\chi^{(2)}$ for m in Equation III.12. We will be using this method of deriving the χ^{NL} tensors for various crystal symmetries to predict the anisotropy of nonlinear optical responses throughout the experimental chapters.

SHG in Weyl Semimetals

The SHG response of the type-I WSM TaAs was one of the first experimental indications the physics community had that studying the nonlinear optical effects of WSMs was worth pursuing. In particular, in 2016, it was found that the strength of the SHG response of TaAs was at least one order of magnitude larger than that of GaAs, which is typically used as a reference sample in SHG experiments because it has such a large and robust second-order response [14]. A sample of the data taken is shown in Figure III.3. This study followed the approach of [77] to link this large SHG response with the Berry formalism and thus with the topology of the Weyl nodes. However, this topological explanation is not the only one which has been offered. A subsequent study in 2018 has suggested that this large response may be due simply to resonance effects [70].
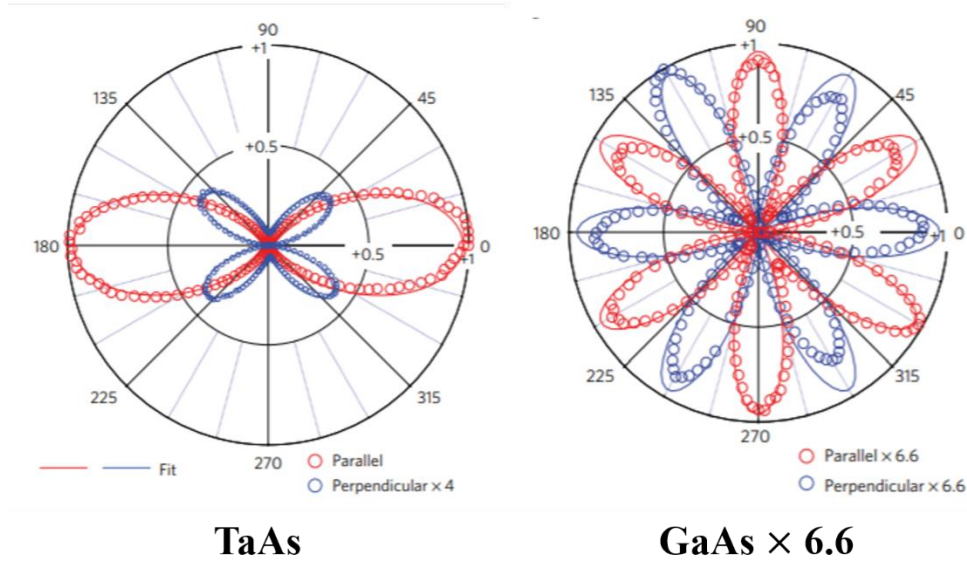
Figure III.3 – An illustration of the RA-SHG data taken on TaAs (left) and GaAs (right) in [14] in two different polarization channels. Both plots are normalized to the same value of +1, but the GaAs data is multiplied by a factor of 6.6, indicating the relative strength of the TaAs response compared with GaAs.

Beyond this initial study, little literature exists studying the SHG response of other WSMs. SHG is used as a tool to study other effects in some type-II WSMs [89, 90], but typically the strength of the response is not estimated, and so the topological connection is not exploited. In addition, many of these studies are on thin materials, which may not access the bulk Weyl cone band structure. This lack of additional information on the strength of the SHG response in WSMs will motivate many of our SHG studies in subsequent chapters.

Mathematical Foundations of the Photogalvanic Effect

Referring to Equation III.4, we recall that the 2ω terms resulted in a second harmonic response. There is also a DC response, which indicates the existence of the photogalvanic effect (PGE) [91]. This PGE is the second-order photocurrent response in a material, where photocurrent

34

is defined as the generation of current in a material without an applied external voltage due to exposure to light [15][5]. Photocurrent generally comes from excitations of the electrons of the material due to the energy imparted on them by the light. But the PGE, as a nonlinear response, is highly dependent on the crystalline symmetries of the material under exploration. For example, just as with SHG, PGE cannot contribute to the photocurrent response in materials possessing a center of inversion symmetry. The existence and form of the PGE will also be dependent on the point group symmetry of the material under study.

The photogalvanic effect is defined as

$$\vec{J} = \eta_{ijk} E_j E_k^*, \qquad\qquad \text{III.16}$$

where η_{ijk} is a complex rank-3 tensor.[6] Requiring $\vec{J}$ be real necessarily requires $\eta_{ijk} = \eta_{ikj}^*$. That is, η_{ijk} is Hermitian in its last two indices. Typically, contributions to the photocurrent from the real and imaginary components of η_{ijk} are considered separately from one another. Indeed, the two have distinct physical origins. The imaginary part contributions known as the circular PGE (CPGE), will change sign with the helicity of the incoming light while the real part contributions, known as linear PGE (LPGE), are independent of helicity [91]. The distinction between these two effects can be seen purely using symmetry arguments.

To highlight the different chiral dependencies of the LPGE and CPGE, we will here show that only the LPGE can contribute to the photocurrent response if the light incident on the material is linearly polarized. To do this, we note that we can write $\eta_{ijk} = A_{ijk} + iB_{ijk}$ for A_{ijk} symmetric

---

[5] In this section, we will focus on DC photocurrent effects.

[6] The $\eta^{(2)}$ tensor has similar symmetry properties to the $\chi^{(2)}$ tensor, but the two are unique. In fact, a similar expansion of the photocurrent response can be performed using η as was done for the induced polarization using χ in Equation III.3.

in the last two indices and B_{ijk} antisymmetric in the last two indices, a requirement for a physical

(real) photocurrent measurement. For linearly polarized light, we have

$$\vec{J} = A_{ijk}E_j E_k^* + iB_{ijk}E_j E_k^*. \qquad \text{III.17}$$

Because linearly polarized light is purely real, we must have

$$A_{ijk}E_j E_k^* + iB_{ijk}E_j E_k^* = A_{ijk}E_k E_j^* + iB_{ijk}E_k E_j^* \qquad \text{III.18}$$

or

$$A_{ijk}E_j E_k + iB_{ijk}E_j E_k = A_{ikj}E_j E_k - iB_{ijk}E_j E_k. \qquad \text{III.19}$$

Because B_{ijk} is antisymmetric in its last two indices, Equation 5 will only hold if B_{ijk} does not

contribute to the photocurrent. Thus, only the real part of η_{ijk} (LPGE) will contribute to the

photocurrent response for linearly polarized light.

In the literature, it is common to see CPGE represented as a rank-2 tensor β_{ij} multiplying

the cross product of E and E^* (eg. [10]). Recalling that CPGE arises only due to contributions from

the imaginary part of η_{ijk}, we can explicitly write out the ith component of the CPGE response as

$$J_i^{CPGE} = i(B_{i11}E_1 E_1^* + B_{i12}E_1 E_2^* + B_{i13}E_1 E_3^* + B_{i21}E_2 E_1^* + B_{i22}E_2 E_2^*$$
$$+ B_{i23}E_2 E_3^* + B_{i31}E_1 E_3^* + B_{i32}E_3 E_2^* + B_{i33}E_3 E_3^*). \qquad \text{III.20}$$

Because B_{ijk} is antisymmetric, we must have that $B_{ijj} = 0$. Simplifying, we can say

$$J_i^{CPGE} = i\left(B_{i12}(E_1 E_2^* - E_2 E_1^*) + B_{i13}(E_1 E_3^* - E_3 E_1^*) + B_{i23}(E_2 E_3^* - E_3 E_2^*)\right)$$

$$= \frac{i}{2} B_{ilm}(E_l E_m^* - E_m E_l^*)$$

$$= \frac{i}{2} B_{ilm}(\delta_{la}\delta_{mb} - \delta_{lb}\delta_{ma})E_a E_b^*$$

$$= \frac{i}{2} B_{ilm}\varepsilon_{jlm}\varepsilon_{jab}E_a E_b^*$$

$$= \frac{i}{2} B_{ilm}\varepsilon_{jlm}\left(\vec{E} \times \overrightarrow{E^*}\right)_j$$

$$= \beta_{ij}\left(\vec{E} \times \overrightarrow{E^*}\right)_j$$

III.21

where we have defined $\beta_{ij} = \frac{i}{2}B_{ilm}\varepsilon_{jlm}$ for ε_{ijk} the levi-civita tensor. Because A_{ijk} is symmetric

in the last two indices, we can write this even more generically as $\beta_{ij} = \frac{1}{2}\eta_{ilm}\varepsilon_{jlm}$.

One subtlety in the discussion of CPGE and LPGE which can easily be overlooked is that it is possible to have LPGE contributions when the incident light is circularly polarized. While this can be proved through a direct computation, it is more illustrative to investigate how CPGE and LPGE come into play with a generic polarization of the incident light. Doing so will allow us not only to show LPGE contributions from purely circular light, but also to draw some broader conclusions about the roles of LPGE and CPGE in photocurrent responses.

The most generic photocurrent experiment typically consists of light normally incident on an optical component such as a waveplate (WP), designed to rotate the polarization of the incoming light before it illuminates the sample. We will assume without loss of generality that the slow axis of the WP is aligned along the x-direction and the fast axis along the y-direction in the lab frame. We can represent such a component in the Jones calculus with a 2×2 matrix

$$M = \begin{pmatrix} e^{-in_s\frac{\omega}{c}l} & 0 \\ 0 & e^{-in_f\frac{\omega}{c}l} \end{pmatrix}, \qquad\qquad \text{III.22}$$

where n_s, n_f are the slow and fast indices of refraction, respectively, and l is the thickness of the component. From there, we can define two phase factors, φ and Γ, such that

$$\varphi = (n_s + n_f)\frac{\omega}{c}l, \qquad \Gamma = (n_f - n_s)\frac{\omega}{c}l. \qquad\qquad \text{III.23}$$

Doing this, we see

$$M = \begin{pmatrix} e^{i(\Gamma-\varphi)/2} & 0 \\ 0 & e^{-i(\Gamma+\varphi)/2} \end{pmatrix} = e^{i(\Gamma-\varphi)/2}\begin{pmatrix} 1 & 0 \\ 0 & e^{-i\Gamma} \end{pmatrix}. \qquad\qquad \text{III.24}$$

For our purposes the overall phase of the incident light is not important, and so we will ignore the prefactor to M in the rest of the discussion [92].

In an experiment, the optical component represented by M is typically rotated about its z-axis. After such a rotation, we would transform $M \to M(\theta)$ for θ the angle of rotation clockwise about the z-axis, given by

$$M(\theta) = \begin{pmatrix} \cos^2(\theta) + e^{-i\Gamma}\sin^2(\theta) & \frac{1}{2}\sin(2\theta)\left(1 - e^{-i\Gamma}\right) \\ \frac{1}{2}\sin(2\theta)\left(1 - e^{-i\Gamma}\right) & \sin^2(\theta) + e^{-i\Gamma}\cos^2(\theta) \end{pmatrix}. \qquad\qquad \text{III.25}$$

If the light incident normally on such a component and was initially horizontally polarized, we would have an electric field polarization of $\begin{pmatrix} \cos^2(\theta) + e^{-i\Gamma}\sin^2(\theta) \\ \frac{1}{2}\sin(2\theta)\left(1 - e^{-i\Gamma}\right) \end{pmatrix}$ after it was transmitted through the waveplate.

For the purposes of illustration, we can now create a tensor representing EE^* as

EE^*

$$= \begin{pmatrix} \cos^4(\theta) + \sin^4(\theta) + \sin^2(2\theta)\cos(\Gamma) & \frac{1}{4}\sin(4\theta)\left(1 - \cos(\Gamma)\right) + \frac{i}{2}\sin(2\theta)\sin(\Gamma) \\ \frac{1}{4}\sin(4\theta)\left(1 - \cos(\Gamma)\right) - \frac{i}{2}\sin(2\theta)\sin(\Gamma) & \frac{1}{2}\sin^2(2\theta)\left(1 - \cos(\Gamma)\right) \end{pmatrix}. \qquad \text{III.26}$$

We then have that nonzero photocurrent must arise from coupling between the real part of η_{ijk} and the symmetric part of EE^*, or the imaginary part of η_{ijk} and the antisymmetric part of EE^*. In other words, the real part of EE^* will contribute to LPGE and the imaginary part to CPGE. As an example, if we had an experiment in which our horizontally polarized light was normally incident on a half-waveplate (HWP), we would have that $\Gamma = \pi$, so

$$EE^* = \begin{pmatrix} \cos^4(\theta) + \sin^4(\theta) - \sin^2(2\theta) & \frac{1}{2}\sin(4\theta) \\ \frac{1}{2}\sin(4\theta) & \sin^2(2\theta) \end{pmatrix}. \qquad \text{III.27}$$

We immediately see that the antisymmetric part of EE^* goes to zero, verifying that, as expected, purely linear light does not give any CPGE contribution to the photocurrent.

CPGE is typically studied using a quarter-waveplate (QWP) to convert pure linear light to pure circular light. For an experiment with horizontally polarized light incident on a QWP, we have that $\Gamma = \frac{\pi}{2}$ and

$$EE^* = \begin{pmatrix} \cos^4(\theta) + \sin^4(\theta) & \frac{1}{4}\sin(4\theta) + \frac{i}{2}\sin(2\theta) \\ \frac{1}{4}\sin(4\theta) - \frac{i}{2}\sin(2\theta) & \frac{1}{2}\sin^2(2\theta) \end{pmatrix}. \qquad \text{III.28}$$

We can immediately see from Equation III.28 that the antisymmetric part of EE^*, which determines the CPGE, has a $\sin(2\theta)$ dependence. This is distinct from the symmetric components of EE^*, which has a 4θ dependence. In fact, this 2θ versus 4θ distinction is true regardless of the type of WP used, assuming that the CPGE term survives, as evidenced in Equation III.26. This angular dependence can thus be used in experiments to distinguish between the LPGE and CPGE contributions to the photocurrent response.

Continuing with the QWP example, we have that pure linear light occurs at $\theta = \frac{n\pi}{2}$ for integers n, simplifying EE^* further to

$$EE^* = \begin{pmatrix} 1 & 0 \\ 0 & 0 \end{pmatrix}, \qquad\qquad \text{III.29}$$

which indicates that all of the photocurrent response arises due to LPGE. In contrast, pure circular light occurs at $\theta = \frac{\pi}{4} + \frac{n\pi}{2}$, so EE^* becomes

$$EE^* = \begin{pmatrix} \dfrac{1}{2} & \pm\dfrac{i}{2} \\ \mp\dfrac{i}{2} & \dfrac{1}{2} \end{pmatrix}. \qquad\qquad \text{III.30}$$

This reflects contributions from both CPGE and LPGE, proving that an LPGE response can arise in conjunction with the CPGE response in materials even for pure circular incident light polarizations.

More than just distinguishing the LPGE and CPGE contributions to the photocurrent, however, there is a further subtlety in identifying different physical contributions to the LPGE. In particular, another look at Equation III.27 reveals that the entirety of the $\cos(4\theta)$ dependence of the LPGE comes from the diagonal elements of EE^*, while the off-diagonal elements contain the $\sin(4\theta)$ dependence. It is clear from the comparison between pure linear light and pure circular light that it is only possible to access the off-diagonal elements if there is some degree of ellipticity. Thus, we can identify the $\cos(4\theta)$ dependence with the "linear contribution to the LPGE" and the $\sin(4\theta)$ dependence with the "elliptical/circular contribution to the LPGE".[7]

One peculiarity with this identification is that, for pure circular light, we have no contribution from the "elliptical contribution to LPGE". Noting that, for a QWP, pure circular light occurs at $\theta = \frac{\pi}{4}$, it is clear the $\sin(4\theta)$ term will go to zero and the $\cos(4\theta)$ term will reach a nonzero minimum for pure circular light ($\theta = \frac{\pi}{4} + \frac{n\pi}{2}$). Meanwhile, the CPGE term behaves as

---

[7] Note that here we are working with light incident normally on the sample surface. This assignment will break down when we introduce an oblique incidence geometry in subsequent sections and chapters.

expected - maximized/minimized depending on the helicity of the polarization. To investigate this apparent inconsistency further, we investigate EE^* for a generic polarization state $E_G = \begin{pmatrix} \cos(\alpha) \\ e^{i\delta} \sin(\alpha) \end{pmatrix}$. This has the benefit that now we can focus on how the variables in play effect the polarization directly, and so we can say that any and all ellipticity in the polarization will come from our δ term.

With E_G, we can compute our EE^* tensor

$$E_G E_G^*$$

$$= \begin{pmatrix} \cos^2(\alpha) & \frac{1}{2}\cos(\delta)\sin(2\alpha) + \frac{i}{2}\sin(\delta)\sin(2\alpha) \\ \frac{1}{2}\cos(\delta)\sin(2\alpha) - \frac{i}{2}\sin(\delta)\sin(2\alpha) & \sin^2(\alpha) \end{pmatrix}. \quad \text{III.31}$$

Here, we can see directly that the ellipticity of the polarization contributes only to the off-diagonal terms. And, in particular, the imaginary part of the ellipticity contributes to the antisymmetric component (CPGE) and the real part to the symmetric component (LPGE). Comparing to Equation III.27, we see that these correspond to the $\sin(2\theta)$ and $\sin(4\theta)$ contributions, respectively. Meanwhile linear contributions come from the diagonal elements, which correspond to the $\cos(4\theta)$ contributions from Equation III.27.

This picture also illustrates why the linear contribution to LPGE seems to dominate for purely circular light. We can see from Equation III.31 that the elliptical contributions alternate between contributions to LPGE and CPGE, such that when CPGE is maximized, elliptical contributions to LPGE are minimized. This is evident by the dependence of the elliptical LPGE contributions on $\cos(\delta)$ and the CPGE contributions on $\sin(\delta)$.

Symmetry Considerations for the Photogalvanic Effect

To this point, all of the statements made have been completely general and independent of the crystal structure, assuming that the crystal is noncentrosymmetric so that the second order photocurrent response is allowed. Now, we will start thinking about how certain crystal symmetry operations might also affect the photocurrent response. Throughout this discussion, we will refer to tensor elements of $\eta = A + iB$, such that elements of A take the form a_{ijk} and elements of B take the form b_{ijk}, and to current $\vec{J} = (J_x, J_y, J_z)$. As discussed previously, symmetries of crystalline materials besides inversion take the form of either mirror planes or axes of rotation or some combination of the two. Thus, we will begin by exploring a simple example of each of these symmetries, and then we will discuss some common material point groups to look at how these considerations play out in real materials.

Our first consideration will be for a crystal with one mirror plane. The inclusion of such a symmetry would place restrictions on η_{ijk}. We will consider first a mirror along the propagation direction (z) of the incoming light. Without loss of generality, as in our SHG discussion, we will assume that the mirror lies in the xz-plane, which takes $y \rightarrow -y$. In this case, η_{ijk} will be zero for any element with an odd number of y indices, taking a form similar to that of $\chi^{(2)}$ of Equation III.13. Thus, for an experiment with horizontally polarized light normally incident on a QWP, we find a photocurrent response of

$$J_x = \frac{1}{4}\left(3a_{xxx} + a_{xyy}\right) + \frac{1}{4}\cos(4\theta)\left(a_{xxx} - a_{xyy}\right),$$

$$J_y = \frac{1}{2}a_{yyx}\sin(4\theta) - b_{yyx}\sin(2\theta), \qquad\qquad \text{III.32}$$

$$J_z = \frac{1}{4}\left(3a_{zxx} + a_{zyy}\right) + \frac{1}{4}\cos(4\theta)\left(a_{zxx} - a_{zyy}\right).$$

That is, only linear contributions to the LPGE survive along axes parallel to the mirror and only circular contributions – to LPGE and CPGE – survive normal to the mirror. This can be physically motivated by the fact that any linear contribution along the y-axis will have an equal and opposite contribution along the y-axis from the operation $y \rightarrow -y$, while circular contributions along the y-axis will propagate along opposite directions but will not be equal because of the helicity dependence. In the xz-plane, however, which contains the mirror, the symmetry will eliminate the helicity component of the light, thus disallowing circular contributions of any form.

This contrasts with the situation in which the mirror is normal to the propagation direction of the light ($z \rightarrow -z$). In this case, we find a photocurrent response of

$$J_x = \frac{1}{4}\left(3a_{xxx} + a_{xyy}\right) + \frac{1}{4}\left(a_{xxx} - a_{xyy}\right)\cos(4\theta) + \frac{1}{2}a_{xyx}\sin(4\theta)$$
$$- b_{xyx}\sin(2\theta),$$

$$J_y = \frac{1}{4}\left(3a_{yxx} + a_{yyy}\right) + \frac{1}{4}\left(a_{yxx} - a_{yyy}\right)\cos(4\theta) + \frac{1}{2}a_{yyx}\sin(4\theta)$$
$$- b_{yyx}\sin(2\theta),$$

$$J_z = 0.$$

III.33

Here, we see that we now have all contributions to LPGE and CPGE in-plane (J_x and J_y), but no second-order nonlinear photocurrent along the direction of propagation (J_z). This is because now there is no requirement on the propagation direction or helicity in-plane, but out of plane both the helicity and propagation directions must be equal and opposite, and so no current is allowed.

As the simplest example of an axis of rotation, we consider a two-fold rotational axis (C_2) about the z-axis. Such a rotation would take $x \rightarrow -x$ and $y \rightarrow -y$, and so we would expect η_{ijk} to vanish for elements with odd numbers of indices of x and y, similar to the $\chi^{(2)}$ tensor presented in Equation III.16. With this symmetry operation, we see a complete reversal of the case presented

in Equation III.33 for a mirror normal to the propagation direction. That is, we have photocurrent contributions of

$$J_x = 0,$$

$$J_y = 0,$$

$$J_z = \frac{1}{4}(3a_{zxx} + a_{zyy}) + \frac{1}{4}(a_{zxx} - a_{zyy})\cos(4\theta) + \frac{1}{2}a_{zyx}\sin(4\theta)$$

$$- b_{zyx}\sin(2\theta).$$

III.34

This is due to the fact that now along both the x- and y-axes the current must be equal and opposite for linearly polarized light $(x \to -x, y \to -y)$ as in the case of a single mirror along the z-axis, while now this double restriction is enough to force equal contributions from opposite chiralities for circular light as well. In contrast, for a C_2 axis in-plane, we would expect that the requirement for linear current normal to the axis would still hold (that is, there would be no linear contributions normal to the axis). However, the requirement for the circular contributions is lifted because the direction of propagation relative to the rotational axis has changed. Along the C_2 axis, however, the chiralities of the circular contributions would be equal and opposite while the linear terms should be allowed. For example, if we had a C_2-axis about the x-axis, we have photocurrent contributions of

$$J_x = \frac{1}{4}(3a_{xxx} + a_{xyy}) + \frac{1}{4}(a_{xxx} - a_{xyy})\cos(4\theta),$$

$$J_y = \frac{1}{2}a_{yyx}\sin(4\theta) - b_{yyx}\sin(2\theta),$$

III.35

$$J_z = \frac{1}{2}a_{zyx}\sin(4\theta) - b_{zyx}\sin(2\theta).$$

That is, we now have linear contributions only along the x-axis and circular contributions only along the y- and z-axes, as expected.

Photocurrent in Real Materials

Equipped now with our symmetry arguments, we can consider some real materials. The first material we will consider is Bi_2Se_3, a Dirac semimetal. The QWP experiment discussed in the previous section has already been reported for Bi_2Se_3 [74]. While bulk Bi_2Se_3 belongs to the D_{3d} point group, which possesses a center of inversion symmetry, it is possible to get second-order surface photocurrent contributions because the surface belongs to the C_{3v} point group, which does not possess inversion symmetry. The C_{3v} point group consists of an out of plane three-fold rotational axis C_3 and three mirror planes related to one another by that rotation. Using these symmetries, and taking one of the mirror planes to lie in the yz-plane, we can impose restrictions on the elements of η_{ijk} such that

$$\eta = \begin{pmatrix} \begin{pmatrix} 0 \\ -a_{yyy} \\ a_{yzy} - ib_{yzy} \end{pmatrix} & \begin{pmatrix} -a_{yyy} \\ 0 \\ 0 \end{pmatrix} & \begin{pmatrix} a_{yzy} + ib_{yzy} \\ 0 \\ 0 \end{pmatrix} \\ \begin{pmatrix} -a_{yyy} \\ 0 \\ 0 \end{pmatrix} & \begin{pmatrix} 0 \\ a_{yyy} \\ a_{yzy} - ib_{yzy} \end{pmatrix} & \begin{pmatrix} a_{yzy} + ib_{yzy} \\ 0 \\ 0 \end{pmatrix} \\ \begin{pmatrix} a_{zyy} \\ 0 \\ 0 \end{pmatrix} & \begin{pmatrix} 0 \\ a_{zyy} \\ 0 \end{pmatrix} & \begin{pmatrix} 0 \\ 0 \\ a_{zzz} \end{pmatrix} \end{pmatrix}, \qquad \text{III.36}$$

to find an expected in-plane photocurrent response of

$$J_x = -\frac{1}{2} a_{yyy} \sin(4\theta),$$

$$\qquad \text{III.37}$$

$$J_y = -\frac{a_{yyy}}{2} (\cos(4\theta) + 1).$$

That is, we expect circular contributions to LPGE along the x-axis and linear contributions to LPGE along the y-axis.

However, it is possible to lift some of these symmetry restrictions on observable photocurrent responses by sending the light in at an oblique incidence. The experiment in [74] did just this – sending in light obliquely incident in the xz-plane and observing j_y. Letting ξ be our angle of incidence with this experimental geometry, we now have an electric field polarization of

$$E = \begin{pmatrix} \cos(\xi)\left(\cos^2(\theta) - i\sin^2(\theta)\right) \\ \frac{1}{2}(1+i)\sin(2\theta) \\ -\sin(\xi)\left(\cos^2(\theta) - i\sin^2(\theta)\right) \end{pmatrix} \qquad \text{III.38}$$

for a QWP and a photocurrent contribution j_y of

$$j_y = \frac{1}{4}\Big(a_{yyy}(1 - \cos(4\theta) - \cos^2(\xi)(3 + \cos(4\theta))) - 4b_{yzy}\sin(2\theta)\sin(\xi)$$

$$\qquad\qquad \text{III.39}$$

$$- 2a_{yzy}\sin(4\theta)\sin(\xi)\Big).$$

In other words, we expect both LPGE and CPGE contributions to the photocurrent response. The data and fit using a functional form of Equation III.39 are shown in Figure III.4 [74].
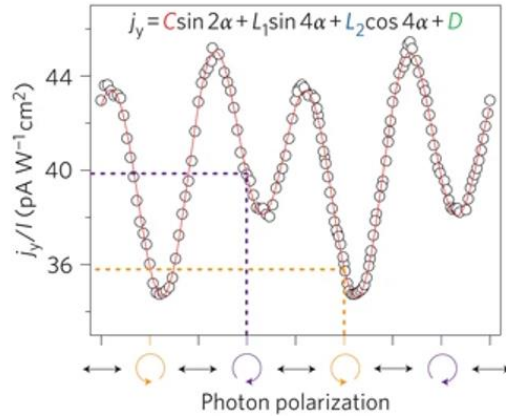
Figure III.4 – Photocurrent data and fit using the CPGE and LPGE contributions on Bi$_2$Se$_3$ taken in an oblique incidence experimental geometry. This figure is adapted from [74].

Photocurrent in Weyl Semimetals

The photocurrent response in WSMs has also garnered much interest in recent past, and so we will consider now the expected photocurrent response in the type-I WSM TaAs, which belongs to point group C_{4v}. C_{4v} has both a C_2 and a C_4 rotation about the z-axis and mirror planes in both the xz- and yz-planes. These symmetries require

$$\eta = \begin{pmatrix} \begin{pmatrix} 0 \\ 0 \\ a_{yzy} - ib_{yzy} \end{pmatrix} & \begin{pmatrix} 0 \\ 0 \\ 0 \end{pmatrix} & \begin{pmatrix} a_{yzy} + ib_{yzy} \\ 0 \\ 0 \end{pmatrix} \\ \begin{pmatrix} 0 \\ 0 \\ 0 \end{pmatrix} & \begin{pmatrix} 0 \\ 0 \\ a_{yzy} - ib_{yzy} \end{pmatrix} & \begin{pmatrix} 0 \\ a_{yzy} + ib_{yzy} \\ 0 \end{pmatrix} \\ \begin{pmatrix} a_{zyy} \\ 0 \\ 0 \end{pmatrix} & \begin{pmatrix} 0 \\ a_{zyy} \\ 0 \end{pmatrix} & \begin{pmatrix} 0 \\ 0 \\ a_{zzz} \end{pmatrix} \end{pmatrix}. \qquad \text{III.40}$$

For light normally incident along the z-axis then, we have a photocurrent response of

$$j_x = 0,$$

$$j_y = 0, \qquad \text{III.41}$$

$$j_z = \frac{1}{4}\left(a_{zyy}(3 + \cos(4\theta)) + 2a_{zyy}\sin^2(2\theta)\right).$$

That is, there is no in-plane second-order photocurrent response.

It is possible to adjust the angle of incidence of the light in order to force non-zero in-plane contributions as we did for Bi$_2$Se$_3$, but another option for TaAs is to send the light normally incident to a different facet of the crystal. So far, all of our hypothetical experiments have assumed that the (001) face of the crystal was normal to the plane of incidence (ie. the c-axis of the crystal is along the z-axis in the lab frame). Now, we will explore the case for TaAs in which the (010) axis is aligned along the z-axis of the lab frame. This can be simulated by rotating η_{ijk} by $90°$

about the x-axis of the lab frame. With this rotated photocurrent tensor, we have a photocurrent response of

$$j_x = b_{yzy} \sin(2\theta) - a_{yzy} \sin(4\theta),$$

$$j_y = \frac{1}{4}\Big(\big(a_{zzz} - a_{zyy}\big)\cos(4\theta) - 3a_{zyy} - a_{zzz}\Big), \qquad \text{III.42}$$

$$j_z = 0.$$

That is, now we expect a non-zero in-plane response even at normal incidence.

Several photocurrent experiments have been performed in the geometries presented in Equations III.41 and III.42, but the results of these experiments seem contradictory both to the symmetry arguments presented here and to one another. For example, in [9], a CPGE response only is measured along the j_x direction for the (010) face at normal incidence. While the arguments presented above rule out linear contributions to LPGE along this direction, circular contributions to LPGE are not symmetry-forbidden, so we would still expect some 4θ dependence in the observed photocurrent response. Another relevant example is presented in [82], where experiments performed with light incidence on the (001) face see non-zero in-plane response in direct contradiction to the symmetry arguments presented here while experiments with light incident on the (010) face pick out the LPGE components predicted above but do not see any CPGE contributions.

We will discuss some of these discrepancies in greater detail in Chapter VI, where we present our own experimental LPGE and CPGE studies on the chiral WSM CoSi. In chiral WSMs, the strength of the CPGE response plays a particularly important role. As discussed in Chapter II, chiral WSMs are typically electronic WSMs which do not possess mirror symmetries. In many other WSMs, these mirror symmetries restrict the paired Weyl cones to occur at the same energy in the band structure of the material. However, the lack of mirrors in the chiral systems means that

the Weyl cones of opposite chirality can occur at different energies. This means that, through wavelength selection, the incident light can be used to populate only one of the paired Weyl cones. This leads to the expectation of quantized effects, where the quantization is given by the Chern number of the populated Weyl cone [93]. In fact, the photocurrent response can be written directly in terms of the Berry curvature and Berry phase regardless of whether we are looking at the chiral WSMs [77]. However, even though this connection between the topology and the photocurrent response exists in all WSMs, the quantization is easiest to experimentally detect in these special chiral material systems. In particular, the quantization of the photocurrent response has been reported already in the chiral WSM RhSi using direct photocurrent measurements and THz generation techniques [10, 11, 58, 60].

CHAPTER IV

Experimental Development

To this point, we have discussed both the broad material class in which we are interested and the probe of nonlinear optics we wish to use to explore the symmetry and topology of these materials. We now turn our attention to the specific experimental construction which goes into this study. In particular, throughout this chapter, we will discuss the optical setups of our RA-SHG measurements, time-resolved optical reflectivity measurements, photocurrent measurements, and scanning measurements which will be used in subsequent chapters. At the end of this chapter, we will also outline the development of a glovebox-based fabrication setup for the purposes of building a multi-lab collaboration to study 2d materials.

We note here the contributions to each of these experiments by myself and other group members. All group members have been responsible for alignment of the NOPA systems which serve as the light sources for our experiments. However, I have taken a particularly active role and have served several times to teach other newer members of the lab the alignment procedure. The RA-SHG experiment was first constructed in our lab by Wencan Jin and Kara Mattioli. I have worked on significant realignment in the years since then. I was solely responsible for the design and construction of both time-resolve optical reflectivity and photocurrent generation setups. Austin Kaczmarek and I were both responsible for the creation of the sample mount and electronic detection system for the photocurrent setup. The scanning SHG setup was designed and created by Austin Kaczmarek, although I did help with troubleshooting problems he encountered along

the way in my role supervising summer undergraduate students. Members of the team which designed the glovebox-based 2d fabrication setup included Ziji Xiang, who took the lead in ordering the glovebox, myself, who ordered the microscope and designed and built the interactions of the relevant components for the scanning and stacking procedures, Liuyan Zhao, Lu Li, Steve Cundiff, Hui Deng, Jason Horng, Albert Liu, Hanna Ruth, and Spencer Batalden. Since the initial construction, Ian Blackman-Staves, Samia Sabir, Laura Zichi, and Shannon Gray have all worked on the searching and scanning component of this project.

All of the optical experiments we will discuss are ultrafast optical experiments. Ultrafast optics are studies involving lasers which have a pulsed output rather than a continuous output. These pulses are typically on the order of picoseconds to femtoseconds[8] in length and repeat at frequencies on the order of kHz to MHz. Ultrafast optics is a particularly useful tool because it allows for time resolution which is not possible with continuous wave (CW) lasers and the possibility of spatial resolution down to the diffraction limit. In addition, because the intensity of the laser field is inversely proportional to the pulse duration, ultrafast laser sources result in high intensity fields which can be used to probe nonlinear optical effects, which are typically too weak to observe with continuous wave lasers [95].

Spirit NOPA-VISIR

In all studies presented here, the light source used is the Spirit NOPA-VISIR system from Spectra Physics [96]. The laser, known as the Spirit, is an industrial-grade femtosecond pulsed laser with a repetition rate of 200 kHz and an output power of 16 W at 1040 nm. The output beam from the Spirit is split three directions. 1 W of power is sectioned off for experiments at 1040 nm

---

[8] In fact, the shortest pulse duration so far was achieved in 2017 – 43 attoseconds (10^{-18}s) [94].

and for diagnostics which must be performed directly on the Spirit. The other 15 W is split in half, with each half fed into a nonlinear optical parametric amplifier (NOPA). The purpose of the NOPA is to allow a flexible tuning of the wavelength of the light used for experiments. Using this Spirit NOPA-VISIR system, we can generate light at any wavelength from 650 nm to 900 nm or from 1200 nm to 2500 nm for use in experiments with a pulse width of < 350 fs without a prism compressor and typically < 70 fs with a prism compressor. Because we have two NOPAs, we can perform multiple experiments simultaneously at different wavelengths or use two wavelengths with one experiment. The specifics of the wavelengths used in a given setup will be discussed in more detail as the experiments are introduced below. Images of the Spirit NOPA-VISIR system in the lab are shown in Figure IV.1.
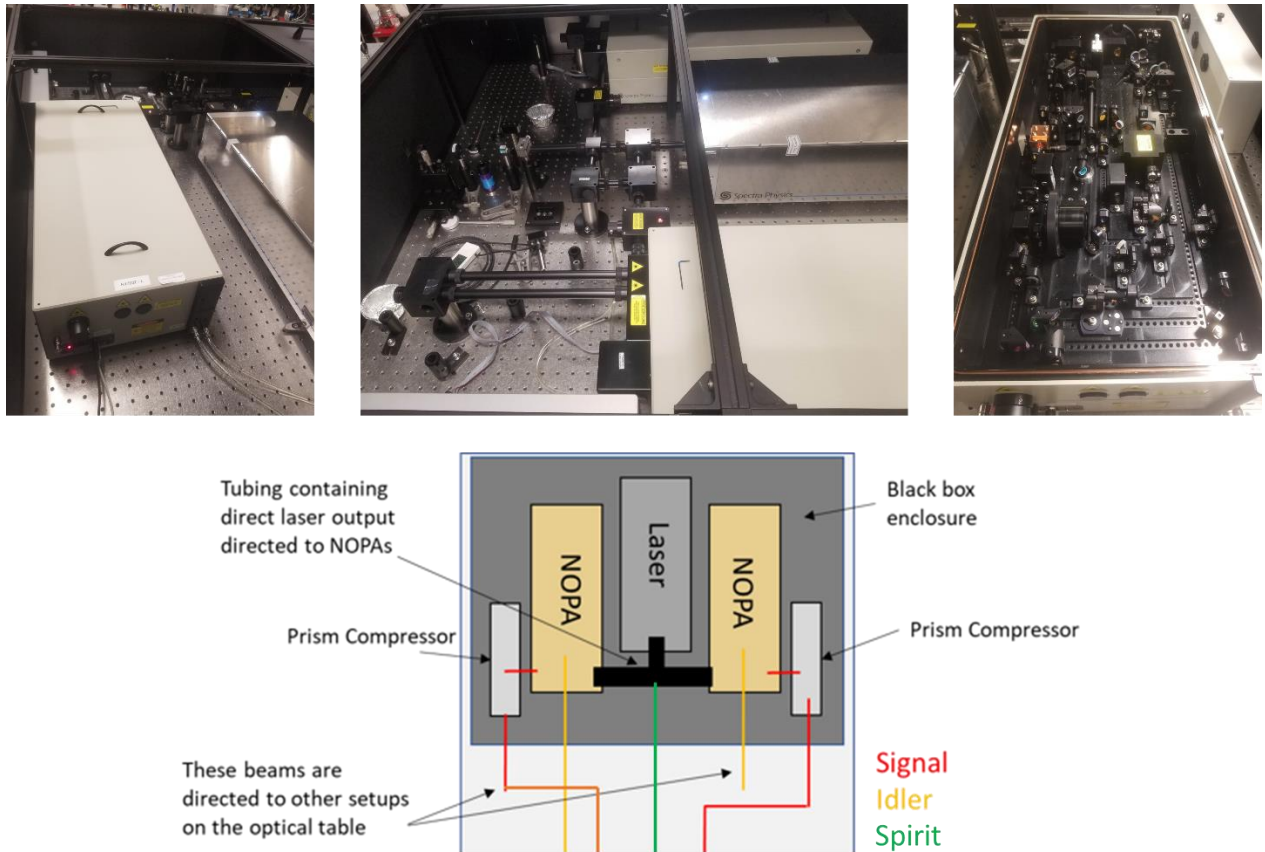
Figure IV.1 – (Top) Pictures of the Spirit NOPA-VISIR setup on the optical table in the lab. (Left) the externals of the NOPA (beige) and the Spirit (silver). (Center) Another image of the externals, this time showing both NOPAs with the Spirit between them. Also pictured is the covered optical beam path taking the output light of the Spirit to the NOPAs. The light output from the NOPAs to their prism compressors is uncovered so that it may be used to monitor the power output of the NOPA directly when necessary. (Right) An image of the internal optical components of the NOPAs. Also pictured in the upper right is the external of the prism compressor used for the output of the NOPA. (Bottom) A cartoon of how the setup looks from above on the table for clarification. The entirety of the Spirit NOPA-VISIR system is enclosed in a black box on the optical table to protect users in the lab from potential stray beams and to protect the laser system from fluctuations of the temperature and humidity in the lab.

The internal schematics of the NOPA are shown in Figure IV.2. Generally, there are three steps to adjust the wavelength of the light within the NOPA. First, 100 mW – 200 mW are sent to a nonlinear crystal to generate a white light continuum. This white light continuum provides the basis for the tunability of the wavelength because white light by definition contains a range of

wavelengths within one beam. The remaining 1040 nm light is meanwhile frequency doubled to 520 nm. The white light continuum is then temporally dispersed such that the shorter wavelengths arrive after the longer ones, allowing for the selection of a particular wavelength through sum-frequency generation by temporally overlapping the desired wavelength within the continuum with ~400 mW of the 520 nm beam within a nonlinear crystal, referred to as the first amplification stage. The output of this first amplification stage serves as the seed for the second amplification stage, where it is spatially and temporally overlapped within a second nonlinear crystal with the remaining 520 nm light to increase the power of the desired wavelength to ~400 mW, which is then sent out of the NOPA as the signal beam.

A	– iris aperture	L	– lens	RP	– rotator of polarization
BB	– beam blocker	M	– mirror	SHG	– harmonic generation crystal
BS	– beam splitter	NC	– nonlinear crystal	SP	– spectrometer mirror
BRM	– beam routing mirror	P	– polarizer	WLD	– temporal dispersion medium
CL	– collimating lens	PBM	– pump blocking mirror	WLG	– white light generation substrate
DM	– dichroic mirror	PIM	– pump interception mirror	WS	– wavelength separator
ICMP	– idler compressor				

Figure IV.2 – The internal schematics of the NOPA system, taken from [96]. Each optical component is labeled, and the various wavelengths present throughout the system are traced in different colors. The pink beam is the initial 1040 nm pumped by the Spirit, the white is the white light continuum resulting from the white light generation crystal, the green is the 520 nm beam used to amplify the first and second stages, the yellow is the seed from the first stage amplification,

the orange is the signal from the second stage amplification, and the purple is the idler, which can be separated from the signal output and used for longer wavelength experiments.

Upon exiting the NOPA, the signal pulse duration can be up to 350 fs. However, because we are interested in nonlinear optics, which is typically associated with a low signal level, we wish to decrease the pulse duration as much as possible so as to increase the total electric field available at the sample locations of our setups. Thus, the final step is to send the signal to a prism compressor, shown in Figure IV.1, which uses a two-prism system to compress the pulse duration back to ~70 fs when the system is fully optimized. It is this compressed beam which is then directed to the experimental setups.

RA-SHG

The first experimental setup we will discuss which will be used throughout the remaining chapters of this thesis is an optical setup which measures the rotational anisotropy of the second harmonic response of a material, fondly referred to from here on as the RA-SHG setup. It was first proposed in [97, 98], and was initially constructed in our lab by Wencan Jin and Kara Mattioli. The basic idea is that light of frequency ω illuminates a sample at either a normal or oblique angle of incidence, and the intensity of the reflected SHG is measured as a function of angle. Neumann's principle states that any symmetry under which a crystal structure is invariant must also dictate the response of any other physical properties of that crystal [99]. This together with our understanding of the relationship between the nonlinear optical susceptibility and the crystalline point group outlined in Chapter III motivates the idea that we can use this RA-SHG technique to gather information on the symmetry properties of the crystal we are studying.
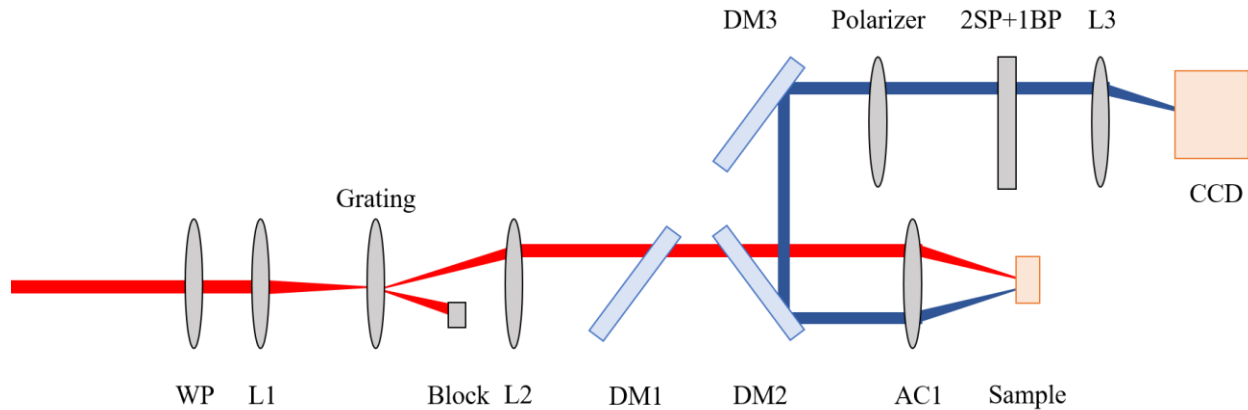
Figure IV.3 – An illustration of the optical beam path for the RA-SHG setup. The beam first passes through a WP which is on an automatic rotating mount to allow for polarization resolution of the incoming beam. It then passes through a telescope comprised of lenses L1 and L2. In the case of an oblique incidence geometry, as shown, a grating is placed at the focal point of L1 to split the beam into n orders of beams. Here, the first order beams only are shown. A block is then used to stop all but one of the first order beams. This grating and the block are also on an automatic rotating mount to ensure that the incoming polarization is locked to the plane of incidence. The beam then passes through two dichroic mirrors (DM1 and DM2) which are each at a 45˚ angle to the incident beam and normal to each other. Then it passes through an achromatic doublet (AC1) which focuses the beam to the sample location. The reflected SHG is then picked up by DM2 after passing back through AC1 and directed to DM3, which reflects the SHG to a polarizer which acts as an analyzer for the experiment. This polarizer is also on an automatic rotation mount to ensure that the polarization of the measured SHG is locked to the incoming polarization. It then passes through a color filter set consisting of one bandpass (BP) and two shortpass (SP) filters to ensure that only the 400 nm light is measured at the CCD. Once filtered, the light is focused to the detector. Not pictured is a white light imaging system which allows us to place the beam at the desired location on the sample and helps with focusing and an optional neutral density (ND) filter placed before the WP.

An illustration of the optical setup for the RA-SHG experiment is shown in Figure IV.3. In a typical experiment, the light enters the setup collimated with vertical polarization and with a central wavelength of 800 nm. It first passes through an ND filter set, which is used to control the power of the light incident on the sample. Then it passes through a HWP, which is set on a motorized rotation stage so that it can be used to rotate the polarization of the light incident on the sample. In this experiment, the light is always linearly polarized. After the HWP, it passes through a telescope with lens 1 and lens 2 focal lengths in ratio 1:3, which is used to expand the beam size

56

and recollimate the beam. From there, it goes through two dichroic mirrors (Thorlabs DMLP425) which are oriented at 45° from the beam path. They are set up such that the reflective dichroic coating is on the transmission side of the optic relative to the incoming fundamental beam. Then, the beam is focused onto the sample with an achromatic doublet. As the system has been described so far, the angle of incidence is 0° (ie. normal incidence). An oblique incidence geometry will also be discussed below.

The light will at this point interact with the sample and undergo both linear and nonlinear optical processes which will be reflected back along the initial beam path due to the normal incidence geometry. However, this time, the first dichroic mirror that the reflected SHG encounters (DM2) will reflect the frequency doubled 400 nm light to a third dichroic mirror (DM3) which will send the beam to a polarizer on a motorized rotating mount used to select only certain orientations of the polarization of the reflected beam for the experiment. This now analyzed light will then pass through two shortpass filters (Thorlabs FESH0450) and a bandpass filter (Thorlabs FBH400-40) to remove any remaining fundamental light which was not filtered by the reflection off the dichroic mirror. The shortpass filters each transmit 3.07×10^{-4} percent of the fundamental 800 nm light and 98.53% of the reflected 400 nm light, and the bandpass filter transmits 2.82×10^{-5} percent of the fundamental 800 nm light and 96.71% of the reflected 400 nm light, according to their specifications on the Thorlabs website. This means that we expect a total transmission to the CCD of no more than 2.66×10^{-16} percent of the reflected fundamental light from the sample to the CCD and 93.89% of the reflected SHG. This is in addition to the filtering provided by the dichroic mirrors. Once the light passes through these filters, it will be focused down onto a single-photon sensitive Andor iXon Ultra 897 camera, a CCD camera with EM Gain [100].

The Andor camera is one of the few detection systems available which is sensitive enough to measure the very small reflected SHG, which is typically on the order of femtowatts for incident power in the hundreds of microwatts range, and thus is worthy of some additional discussion. A CCD pixel is basically a piece of biased silicon. When a photon comes in, it creates an electron-hole pair through the photoelectric effect, and this pair is separated by the bias present in the system to prevent recombination. Once the accumulation is completed (ie. the shutter of the camera is open for a set amount of time), the charge is moved into the readout register to be converted into a digital signal which is sent to the computer. With the EMCCD of the Andor camera, all of this remains the same, but the readout register is extended to include a multiplication register, where with some small probability each electron in the register might create an additional electron [100]. This occurs by using more voltage than necessary to move the charges through the register, thus giving them more energy and effectively increasing the chances that the excitation of another electron will occur as the signal moves through the material of the register. This is known as impact ionization. This technique is used because it is not sensitive to electronic noise and can thus be used to amplify the signal above that noise which is inherent in all CCDs [100].
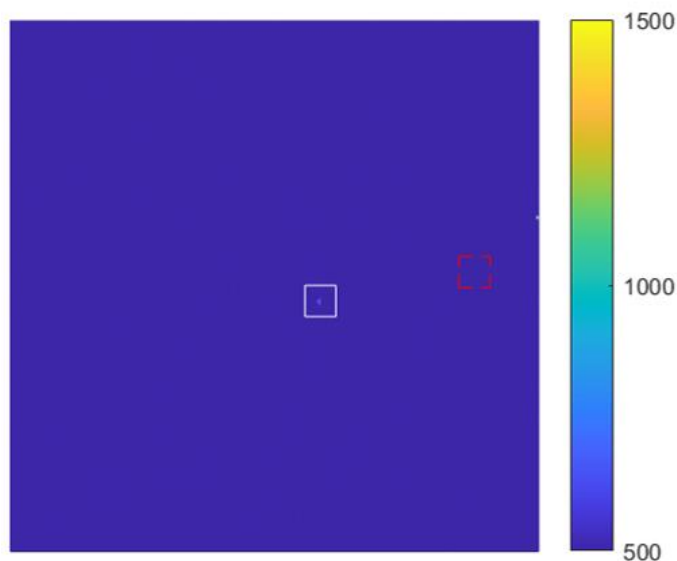
Figure IV.4 – An example of an image taken using the Andor camera on the RA-SHG setup. In this case, the material being investigated was the (100) face of the chiral WSM CoSi. The experiment was performed in a normal incidence geometry. Here, the white box contains the laser point of the reflected SHG from the sample. The red box, which is the same size as the white box, is used to subtract the background from the data. The color bar indicates the uncorrected photon count recorded over the experimental accumulation time by the Andor camera and is given in arbitrary units. The total acquisition time was 40 s. This image would correspond to one data point in an RA-SHG polar plot.

An example of an image of the reflected SHG obtained using the Andor camera is shown in Figure IV.4. It is clear that there is a small spot of light being picked up on the CCD, as expected when the SHG is focused down by the lens after the polarizer. To obtain signal photon count measurements, we integrate a small area of pixels around the beam and then subtract the background level by integrating a square of equal size on a random area of the screen, shown in Figure IV.4 in white and red, respectively. Of course, as evidenced by Equation III.3, the physical quantity relevant to many of our measurements will be the reflected SHG intensity or the reflected SHG field rather than the photon count on the CCD camera, taken by opening the shutter for a selected amount of time, known as the acquisition, exposure, or integration time. We can convert this photon count to the SHG power at the CCD as

$$P_{2\omega} = p.c.\frac{hc}{\lambda\tau_{int}}, \qquad\qquad\qquad \text{IV.1}$$

where $p.c.$ is the photon count, h is Planck's constant, c is the speed of light in vacuum, λ is the wavelength of the reflected SHG, and τ_{int} is the integration time of the camera. However, we are working with a pulsed laser system, which means we will need to work with the maximum power at the CCD rather than the average power, given by Equation IV.1. To convert average power to peak power for a pulsed laser, it is necessary to divide by $f_{rep}\tau$, where f_{rep} is the repetition rate of the laser and τ is the pulse duration at the sample site. From there, we can calculate the electric field of the SHG as

$$E_{2\omega} = \sqrt{\frac{2P_{2\omega,peak}}{\pi r_{2\omega}^2 \cdot c\epsilon_0}}, \qquad\qquad \text{IV.2}$$

for $r_{2\omega}$ the spot size of the SHG beam on the CCD (typically ~60 μm). Of course, we must account as well for the EM Gain and other multiplication used by the Andor camera to increase the sensitivity enough to detect the SHG beam. This correction is done by multiplying the photon count by the sensitivity of the camera and then dividing by the quantum efficiency and the EM gain used in the experiment [100]. To further increase the accuracy of our measurements, we also account for the efficiency of the optics used to direct the SHG beam from the sample to the CCD using the specifications for each optic listed on the Thorlabs website.
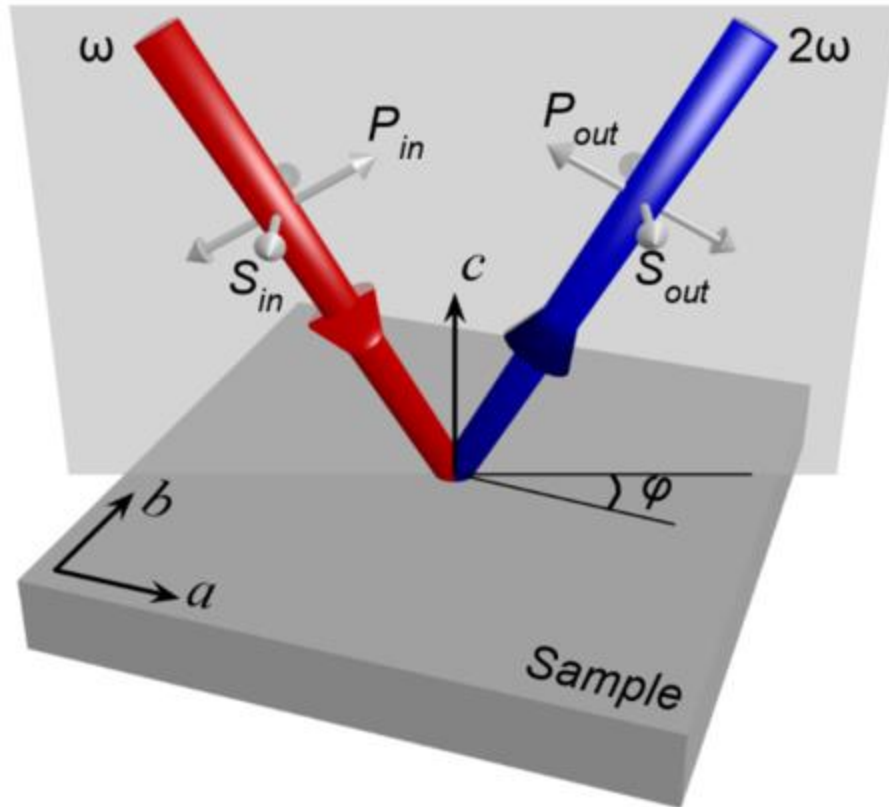
Figure IV.5 – An illustration of the beam orientations for the RA-SHG experiment at oblique incidence (incoming red beam makes angle θ with c-axis of crystal). The a- and b-axes of a hypothetical sample are shown in the lower left corner. The plane of incidence is rotated by angle ϕ about the c-axis of the crystal (the z-axis of the lab frame) to get angle-resolved SHG intensity measurements. Four polarization channels are shown using combinations of P/S$_{in/out}$ [101].

The polarization of the incoming fundamental and reflected SHG light is one of the key features of this experimental setup. As mentioned above, these are controlled respectively by a HWP and a polarizer, both of which are mounted on automatic rotation mounts. During the operation of this experiment, the polarization of the incoming light is set to be either vertical (S) or horizontal (P) and the polarizer is set to transmit either S or P light as well. This yields four different polarization channels, aptly labeled S-S, S-P, P-S, and P-P, as shown in Figure IV.5. While taking data, these two components are rotated together clockwise by angle ϕ in usually

either 5° or 10° increments and, at each new angle, a picture is taken with the CCD. This results in an angle- and polarization-resolved collection of SHG intensities which can be analyzed according to Equation III.5.

Let us take a moment to look a little more closely at this data analysis procedure by using the orthorhombic D_2 point group as an example. This point group consists of C_2 rotations about the x-, y-, and z-axes, and thus has a $\chi^{(2)}$ tensor of the form

$$\chi^{(2)}_{D_2} = \begin{pmatrix} \begin{pmatrix} 0 \\ 0 \\ 0 \end{pmatrix} & \begin{pmatrix} 0 \\ 0 \\ \chi^{(2)}_{xyz} \end{pmatrix} & \begin{pmatrix} 0 \\ \chi^{(2)}_{xzy} \\ 0 \end{pmatrix} \\ \begin{pmatrix} 0 \\ 0 \\ \chi^{(2)}_{yxz} \end{pmatrix} & \begin{pmatrix} 0 \\ 0 \\ 0 \end{pmatrix} & \begin{pmatrix} \chi^{(2)}_{yzx} \\ 0 \\ 0 \end{pmatrix} \\ \begin{pmatrix} 0 \\ \chi^{(2)}_{zxy} \\ 0 \end{pmatrix} & \begin{pmatrix} \chi^{(2)}_{zyx} \\ 0 \\ 0 \end{pmatrix} & \begin{pmatrix} 0 \\ 0 \\ 0 \end{pmatrix} \end{pmatrix},$$

IV.3

which can be calculated using the procedure outlined in Chapter III. Because we are working with SHG, we can further simplify this by requiring that $\chi^{(2)}_{ijk} = \chi^{(2)}_{ikj}$ because the two fields which are mixing to create the nonlinear effect are identical. In this case, Equation IV.3 becomes

$$\chi^{(2)}_{D_2} = \begin{pmatrix} \begin{pmatrix} 0 \\ 0 \\ 0 \end{pmatrix} & \begin{pmatrix} 0 \\ 0 \\ \chi^{(2)}_{xzy} \end{pmatrix} & \begin{pmatrix} 0 \\ \chi^{(2)}_{xzy} \\ 0 \end{pmatrix} \\ \begin{pmatrix} 0 \\ 0 \\ \chi^{(2)}_{yzx} \end{pmatrix} & \begin{pmatrix} 0 \\ 0 \\ 0 \end{pmatrix} & \begin{pmatrix} \chi^{(2)}_{yzx} \\ 0 \\ 0 \end{pmatrix} \\ \begin{pmatrix} 0 \\ \chi^{(2)}_{zyx} \\ 0 \end{pmatrix} & \begin{pmatrix} \chi^{(2)}_{zyx} \\ 0 \\ 0 \end{pmatrix} & \begin{pmatrix} 0 \\ 0 \\ 0 \end{pmatrix} \end{pmatrix}.$$

IV.4

We can simulate the SHG pattern expected given the rotation of the beam by instead rotating the $\chi^{(2)}$ tensor, which is equivalent to rotating the sample itself. In fact, this type of angle-resolved SHG experiment was traditionally done by rotating the sample directly rather than by rotating the

polarization of the beam. However, rotating the sample can easily lead to drift of the beam location

which causes each data point to be taken at a different location on the sample, yielding inconclusive

data in spatially nonuniform samples (of which there are many). The first implementation of this

technique in which the beam is rotated rather than the sample was in [97, 98]. The key ingredient,

so-to-speak, was the use of the DM1 in Figure IV.3 to account for the change in polarization caused

by the insertion of DM2, which is necessary to collect the reflected SHG.

In our case, if we rotated $\chi^{(2)}$ about the z-axis by angle ϕ, we find a tensor of the form

$$\chi_{D_2}^{(2)}(\phi) =$$

$$\begin{pmatrix}
\begin{pmatrix} 0 \\ 0 \\ -\left(\chi_{xzy}^{(2)} + \chi_{yzx}^{(2)}\right)\cos(\phi)\sin(\phi) \end{pmatrix} & \begin{pmatrix} 0 \\ 0 \\ \chi_{xzy}^{(2)}\cos^2(\phi) - \chi_{yzx}^{(2)}\sin^2(\phi) \end{pmatrix} & \begin{pmatrix} -\left(\chi_{xzy}^{(2)} + \chi_{yzx}^{(2)}\right)\cos(\phi)\sin(\phi) \\ \chi_{xzy}^{(2)}\cos^2(\phi) - \chi_{yzx}^{(2)}\sin^2(\phi) \\ 0 \end{pmatrix} \\
\begin{pmatrix} 0 \\ 0 \\ \chi_{yzx}^{(2)}\cos^2(\phi) - \chi_{xzy}^{(2)}\sin^2(\phi) \end{pmatrix} & \begin{pmatrix} 0 \\ 0 \\ \left(\chi_{xzy}^{(2)} + \chi_{yzx}^{(2)}\right)\cos(\phi)\sin(\phi) \end{pmatrix} & \begin{pmatrix} \chi_{yzx}^{(2)}\cos^2(\phi) - \chi_{xzy}^{(2)}\sin^2(\phi) \\ \left(\chi_{xzy}^{(2)} + \chi_{yzx}^{(2)}\right)\cos(\phi)\sin(\phi) \\ 0 \end{pmatrix} \\
\begin{pmatrix} -2\chi_{zyx}^{(2)}\cos(\phi)\sin(\phi) \\ \chi_{zyx}^{(2)}\cos(2\phi) \\ 0 \end{pmatrix} & \begin{pmatrix} \chi_{zyx}^{(2)}\cos(2\phi) \\ \chi_{zyx}^{(2)}\sin(2\phi) \\ 0 \end{pmatrix} & \begin{pmatrix} 0 \\ 0 \\ 0 \end{pmatrix}
\end{pmatrix}. \quad \text{IV.5}$$

From here, we can use Equation III.5 to calculate the induced polarization for all four polarization

geometries. Noting that the incoming fundamental fields take the form

$$\overrightarrow{E_P} = (1,0,0), \qquad \overrightarrow{E_S} = (0,1,0), \qquad\qquad \text{IV.6}$$

we can compute $P_i = \chi_{ijk}^{(2)} E_j E_k$ for each possible incoming field orientation:

$$P_{P_{in},x} = \chi^{(2)}_{xjk}E_{P,j}E_{P,k} = 0$$

$$P_{P_{in},y} = \chi^{(2)}_{yjk}E_{P,j}E_{P,k} = 0$$

$$P_{P_{in},z} = \chi^{(2)}_{zjk}E_{P,j}E_{P,k} = -2\chi^{(2)}_{zyx}\cos(\phi)\sin(\phi)$$

$$P_{S_{in},x} = \chi^{(2)}_{xjk}E_{S,j}E_{S,k} = 0$$
$$\text{IV.7}$$

$$P_{S_{in},y} = \chi^{(2)}_{yjk}E_{S,j}E_{S,k} = 0$$

$$P_{S_{in},z} = \chi^{(2)}_{zjk}E_{S,j}E_{S,k} = \chi^{(2)}_{zyx}\sin(2\phi)$$

These must then be converted to an intensity so as to model the photon count accessible at the CCD detector. To do this, we approximate the polarization as the reflected SHG field. Then

$$I^{2\omega}_{P-P}(\phi) = P^2_{P_{in},x} = 0$$

$$I^{2\omega}_{P-S}(\phi) = P^2_{P_{in},y} = 0$$

$$I^{2\omega}_{S-P}(\phi) = P^2_{S_{in},x} = 0$$
$$\text{IV.8}$$

$$I^{2\omega}_{S-S}(\phi) = P^2_{S_{in},y} = 0$$

From Equation IV.8, it is apparent that, in all four polarization channels, there will be no signal detected at the CCD. In fact, even for point groups which do exhibit a nonzero SHG pattern for this experimental geometry, the P-P and S-S channels yield identical results and the P-S and S-P channels also yield identical results[9]. This is because, at normal incidence, we are restricted to being sensitive to only a subset of the nonzero $\chi^{(2)}$ tensor elements. However, we can overcome this downfall by sending the beam in at an oblique incidence, rather than a normal incidence. To accomplish this, we insert a diffraction grating at the focal point of the telescope and block all but one of the first order beams, as shown in Figure IV.3. This means that the beam incident on the

---

[9] For this reason, with a normal incidence geometry, we refer to the S-S and P-P channels jointly as the parallel channel and the S-P and P-S channels jointly as the crossed channel.

sample will be incident on the achromatic doublet used to focus the beam at an off-axis location, and so will be incident on the sample at an oblique angle θ. In our experimental setup, the first order beam is removed from the center of the doublet by about ~5.5 mm. Thus, for a focal length of 25.4 mm, we have an angle of $\theta \approx 7°$. Further, we place the grating as well on a rotation mount so that the incident beam can be rotated about the z-axis of the lab frame and the polarization is permanently parallel to (P) or perpendicular to (S) the plane of incidence of the beam.

In this case, we will now have

$$\overrightarrow{E_P} = (-\cos(\theta), 0, \sin(\theta)), \qquad \overrightarrow{E_S} = (0,1,0), \tag{IV.9}$$

and we can redo the calculations from Equation IV.7 as

$$P_{P_{in},x} = \chi_{xjk}^{(2)} E_{P,j} E_{P,k} = 2\left(\chi_{xzy}^{(2)} + \chi_{yzx}^{(2)}\right) \cos(\theta)\cos(\phi)\sin(\theta)\sin(\phi)$$

$$P_{P_{in},y} = \chi_{yjk}^{(2)} E_{P,j} E_{P,k} = -2\cos(\theta)\sin(\theta)\left(\chi_{yzx}^{(2)}\cos^2(\phi) - \chi_{xzy}^{(2)}\sin^2(\phi)\right)$$

$$P_{P_{in},z} = \chi_{zjk}^{(2)} E_{P,j} E_{P,k} = -2\chi_{zyx}^{(2)}\cos(\phi)\sin(\phi)\cos^2(\theta)$$

$$\tag{IV.10}$$

$$P_{S_{in},x} = \chi_{xjk}^{(2)} E_{S,j} E_{S,k} = 0$$

$$P_{S_{in},y} = \chi_{yjk}^{(2)} E_{S,j} E_{S,k} = 0$$

$$P_{S_{in},z} = \chi_{zjk}^{(2)} E_{S,j} E_{S,k} = \chi_{zyx}^{(2)}\sin(2\phi)$$

This yields intensity calculations at the CCD of

$$I_{P-P}^{2\omega}(\phi) = \left(P_{P_{in},x}\cos(\theta)\right)^2 + \left(P_{P_{in},z}\sin(\theta)\right)^2$$

$$= 4\left(\left(\chi_{xzy}^{(2)} + \chi_{yzx}^{(2)}\right)^2 + \chi_{zyx}^{(2)\,2}\right)\cos^4(\theta)\cos^2(\phi)\sin^2(\theta)\sin^2(\phi)$$

$$I_{P-S}^{2\omega}(\phi) = P_{P_{in},y}^2 = 4\cos^2(\theta)\sin^2(\theta)\left(\chi_{yzx}^{(2)}\cos^2(\phi) - \chi_{xzy}^{(2)}\sin^2(\phi)\right)^2 \qquad \text{IV.11}$$

$$I_{S-P}^{2\omega}(\phi) = \left(P_{S_{in},x}\cos(\theta)\right)^2 + \left(P_{S_{in},z}\sin(\theta)\right)^2 = \chi_{zyx}^{(2)\,2}\sin^2(\theta)\sin^2(2\phi)$$

$$I_{S-S}^{2\omega}(\phi) = P_{S_{in},y}^2 = 0$$

The RA-SHG patterns from Equation IV.11 are shown in Figure IV.6 for $\chi_{xyz}^{ED} = 1$ pm/V, $\chi_{yzx}^{ED} = 2$ pm/V, and $\chi_{zxy}^{ED} = 3$ pm/V for an angle of incidence of $\theta = 7°$. In each image, the two-fold rotation is apparent in the calculated flower pattern.
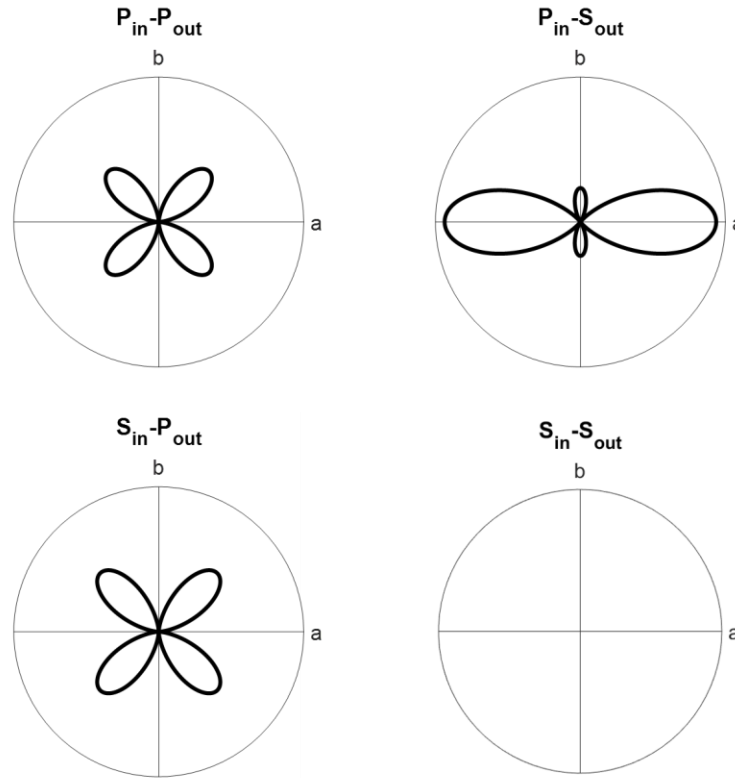
Figure IV.6 – Models of the RA-SHG patterns for the D_2 point group in each of the four polarization channels for an oblique incidence angle of $\theta = 7°$. These models are obtained

assuming arbitrary values of $\chi_{xyz}^{ED} = 1$ pm/V, $\chi_{yzx}^{ED} = 2$ pm/V, and $\chi_{zxy}^{ED} = 3$ pm/V. All four plots are normalized to the same value.

Estimating the Strength of the SHG Response with the RA-SHG Experiment

Throughout the experiments presented here, we will be interested not only necessarily in what the SHG response of the material can tell us about the symmetries of the materials being investigated, but also about the size of that response. As discussed in Chapter III, this is due to the link between the topology of the WSM band structure and the strength of the nonlinear optical responses of the material.

Ordinarily, the strength of the SHG response of a material is quoted as the size of the optical susceptibility tensor elements. From Equation III.5, we can see that, if we want to access the size of $\chi^{(2)}$, it will be necessary to know the strength of the incoming electric field and the strength of the nonlinear polarization induced in the material. The strength of the incoming electric field is certainly the easier of the two to explore. We can describe the intensity of the fundamental field as

$$I^\omega = \frac{c\epsilon_0 n}{2}\left|\vec{E}\right|^2 = \frac{P}{\pi r^2},$$

<div align="right">IV.12</div>

where n is the index of refraction of the fundamental light, P is the power, and r is the radius of the fundamental beam at the sample location (typically ~15 μm). Recalling that we are working with a pulsed laser and thus that the relevant power is the peak power rather than the average power, we can say that

$$\left|\vec{E}\right| = \sqrt{\frac{2P_{peak}}{\pi r^2 c\varepsilon_0 n}}.$$

<div align="right">IV.13</div>

The more challenging aspect of estimating the strength of the SHG response comes from putting a numerical value on the nonlinear polarization. In our simulations of the RA-SHG experiment, we made the approximation that the nonlinear polarization is given by the reflected

SHG at the CCD detector, but this approximation only works if we are interested in the shape of the RA-SHG pattern and does not work if we are interested in a more accurate description of the size of that response. This is because the index of refraction of the material is typically different than that of air. In order to accurately estimate the size of the response, we must work with the nonlinear Fresnel coefficients of the material. In effect, we must consider the air/vacuum-material interface and calculate the transmitted and reflected light at that interface.
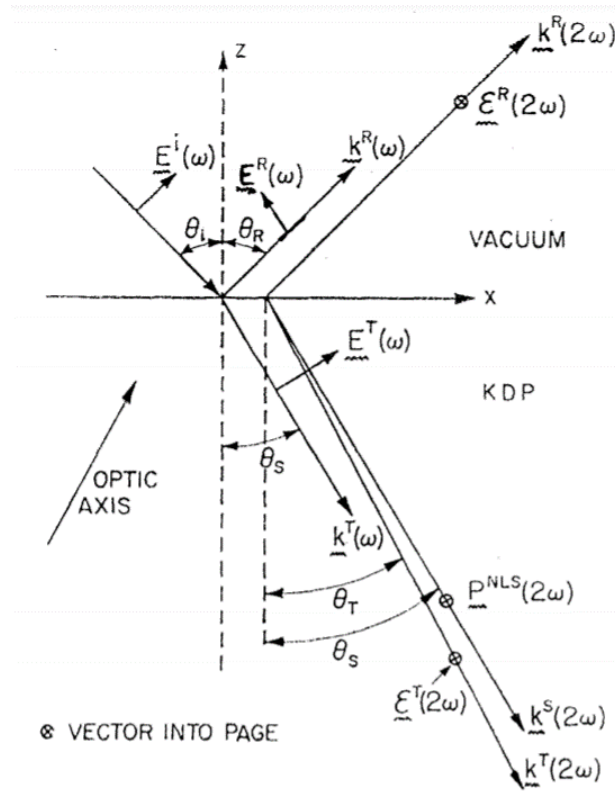
Figure IV.7 – An illustration of the basic setup of the boundary value problem which much be considered for the derivation of the nonlinear Fresnel corrections to the calculation of the magnitude of the $\chi^{(2)}$ tensor elements, taken from [102]. In this diagram, monochromatic light $\overrightarrow{E^i(\omega)}$ is incident at angle θ_i to a crystal (in this case, a KDP crystal). The linear reflected light $\overrightarrow{E^R(\omega)}$ and refracted light $\overrightarrow{E^T(\omega)}$ are shown at angles θ_R and θ_S to the normal with wavevectors $\overrightarrow{k^R(\omega)}$ and $\overrightarrow{k^T(\omega)}$, respectively. The refracted light wave induces a nonlinear polarization $\overrightarrow{P^{NLS}(2\omega)}$, also at angle θ_S and with wave vector $\overrightarrow{k^S(2\omega)}$. This induces a transmitted

68

electric field through the crystal at 2ω of $\overrightarrow{E^T(2\omega)}$ with wavevector $\overrightarrow{k^T(2\omega)}$ and out of the crystal of $\overrightarrow{E^R(2\omega)}$ with wavevector $\overrightarrow{k^R(2\omega)}$.

The derivation of the linear Fresnel coefficients is familiar, but we will go through it briefly as a demonstration to give us the tools necessary to access the nonlinear Fresnel coefficients later. The basic setup of the problem is shown in Figure IV.7, which will also be used as the reference figure for the nonlinear Fresnel discussion below. In essence, a monochromatic plane wave is incident on a boundary between two media. In our case, the incidence medium is either vacuum or air, but this setup works just as well for any two media. When the light hits the interface, some portion is refracted through the material and some portion is reflected. We are interested in knowing what those proportions are.

We can imagine first the case in which the incident light is S-polarized. That is, the light is polarized perpendicular to the plane of incidence. In this case, we can place boundary conditions on the electric $\vec{E}$ and magnetic $\vec{B}$ fields involved in the system by requiring that the fields be continuous across the interface

$$E_i(y = 0) + E_r(y = 0) = E_t(y = 0)$$

$$-B_i(y = 0)\cos(\theta_i) + B_r(y = 0)\cos(\theta_r) = -B_t(y = 0)\cos(\theta_t)$$

IV.14

where the i subscript indicates the incident field, the r subscript indicates the reflected field, and the t subscript indicates the transmitted field. Noting that $\theta_i = \theta_r$ and that Snell's law ($n_i \sin(\theta_i) = n_t \sin(\theta_t)$) holds, and using the fact that $B = \frac{nE}{c}$, we can solve this system of equations for the reflection r_s and transmission t_s coefficients

69

$$r_S = \frac{E_{0r}}{E_{0i}} = \frac{n_i \cos(\theta_i) - n_t \cos(\theta_t)}{n_i \cos(\theta_i) + n_t \cos(\theta_t)}$$

$$t_S = \frac{E_{0t}}{E_{0i}} = \frac{2 n_i \cos(\theta_i)}{n_i \cos(\theta_i) + n_t \cos(\theta_t)}$$

IV.15

We can similarly solve for the case that the incident light is P-polarized as

$$r_P = \frac{n_i \cos(\theta_t) - n_t \cos(\theta_i)}{n_i \cos(\theta_t) + n_t \cos(\theta_i)}$$

$$t_P = \frac{2 n_i \cos(\theta_i)}{n_i \cos(\theta_t) + n_t \cos(\theta_i)}$$

IV.16

However, we are working with a nonlinear medium. This problem was first addressed in [102], and we shall go through it briefly here. The basic setup is shown in Figure IV.7. We want to calculate the nonlinear Fresnel coefficients in order to convert between the nonlinear polarization in the media and the reflected SHG field, which we can then use to estimate the size of the nonlinear response using Equation III.5 and our RA-SHG experiment. The derivation presented here makes the assumption that there will be one refracted ray in the nonlinear medium. In fact, in most cases, there are two refracted rays in such medium. However, the assumption of one will hold true for cubic and uniaxial crystals or for any crystal studied using the normal incidence geometry. We take the interface between the vacuum and the nonlinear media to be at $z = 0$ and the plane of incidence to be at $y = 0$. The wavevector of the incident light is taken to be $\vec{k_i^1}$ and of the refracted wave is $\vec{k_t^1}$, where the 1 indicates that these refer to the fundamental wavelength. Subsequently, an index of 2 will be used to indicate the frequency doubled wavelength. We can use the Fresnel laws in Equations IV.15 and IV.16 to determine the refracted ray $\vec{E_t^1}$. We can also explicitly write out Equation III.5 with the appropriate indices and variables as

70

$$\overrightarrow{P^{NL}} = \chi^{(2)} \overrightarrow{E_t^1 E_t^1} e^{i(\overrightarrow{k_s} \cdot \vec{r} - 2\omega t)} \tag{IV.17}$$

for $\overrightarrow{k_s}$ the wavevector for the nonlinear polarization $\overrightarrow{k_s} = 2\overrightarrow{k_t^2}$.

We will be working with plane wave solutions to Maxwell's equations, given by

$$\overrightarrow{E_r^2} = \hat{e}_r E_r^2 e^{i(\overrightarrow{k_r^2} \cdot \vec{r} - 2\omega t)}$$

$$\overrightarrow{H_r^2} = \frac{c}{2\omega} \left(\overrightarrow{k_r^2} \times \hat{e}_r \right) E_r^2 e^{i(\overrightarrow{k_r^2} \cdot \vec{r} - 2\omega t)} \tag{IV.18}$$

for $\hat{e}_r$ the unit vector in the direction of $\overrightarrow{E_r^1}$, E the magnitude of field $\vec{E}$, and $\vec{H}$ the magnetic field. As in our discussion of the linear Fresnel coefficients, we will impose boundary conditions that the tangential components of $\vec{E}$ and $\vec{H}$ be continuous everywhere, which means that the individual frequency components at ω and 2ω must be separately continuous across the boundary. This sets the requirements that

$$k_{i,x}^1 = k_{r,x}^1 = k_{t,x}^1$$

$$2k_{t,x}^1 = k_{s,x}^2 = k_{r,x}^2 = k_{t,x}^2 \tag{IV.19}$$

and gives us a nonlinear equivalents of Snell's law

$$\sin(\theta_r^2) = \frac{k_{r,x}^2}{\left|\overrightarrow{k_r^2}\right|} = \frac{k_{i,x}^1}{\left|\overrightarrow{k_r^1}\right|} = \sin(\theta_i)$$

$$\sin(\theta_t^2) = \frac{k_{t,x}^2}{\left|\overrightarrow{k_t^2}\right|} = \epsilon^{-\frac{1}{2}}(2\omega) \sin(\theta_i) \tag{IV.20}$$

$$\sin(\theta_s) = \epsilon^{-\frac{1}{2}}(\omega) \sin(\theta_i)$$

where ϵ is the dielectric constant of the material.

Because the vacuum is dispersionless, the reflected SHG field will go in the same direction as the reflected fundamental field. The nonlinear polarization will also go in the same direction as the transmitted fundamental, but the transmitted SHG field will generally go in a slightly different

direction depending on the difference between $\epsilon(\omega)$ and $\epsilon(2\omega)$ unless working with a normal incidence geometry.

When we calculate the strength of the nonlinear susceptibility tensor elements, we apply these requirements and boundary conditions specifically for the point group at hand and then use the experimental values to do the calculations because it is difficult to get a nice analytic solution for all experimental conditions. We also restrict ourselves to doing this computation for the normal incidence geometry RA-SHG experiment so that the assumption of a single nonlinear refracted ray holds true. An example code written for Mathematica is included in Appendix E.

Time-Resolved Optical Reflectivity Measurements

In addition to the RA-SHG experiment, we have constructed a time-resolved optical reflectivity experiment, or a pump-probe experiment, which can be used to probe the time dynamics of various material systems. The optical components of this setup are shown in Figure IV.8. In this setup, there are two beams which serve as input – one from each NOPA. The pump beam is at 720 nm and passes through a telescope of lens focal length ratio 3:1 to shrink the beam slightly before being focused down to the sample using a lens at a normal incidence angle. The probe, on the other hand, is at 800 nm and starts by passing through a telescope of lens focal length ratio 1:3 to expand the beam slightly before being sent to a translation stage which can tune the time at which the probe pulse arrives at the sample location. The expansion and shrinking of the probe and pump beams, respectively, helps to ensure that the diameter of the probe beam will be smaller than that of the pump when they are focused down onto the sample surface. The probe is then picked up by a small mirror and sent parallel to the pump beam to be focused onto the sample with the same lens as the pump, but at a slightly oblique angle of incidence. The reflected probe

beam is then sent to a color filter and a lens which focuses the signal down to a silicon photodiode (Hamamatsu S5972).
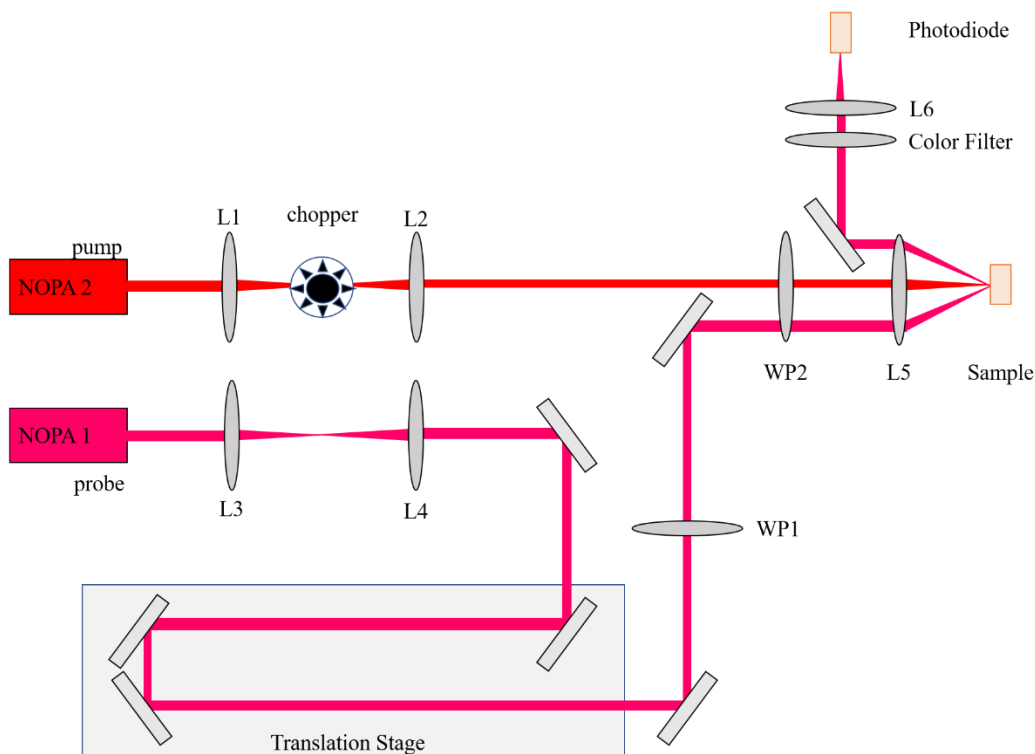
Figure IV.8 – An illustration of the beam path of the time-resolved optical reflectivity, or pump-probe, setup. Here, the pump beam has a center wavelength of 720 nm and the probe has a center wavelength of 800 nm. Both pump and probe beams pass through their own telescopes (pump telescope L1, L2 and probe telescope L3, L4), where the probe beam is expanded and the pump is decreased in size to ensure proper overlap, with the pump beam larger than the probe beam, at the sample site. The pump beam is further chopped by an optical chopper at a frequency of 8 kHz which serves as a reference for the lock-in detector. The probe then passes through an automatic translation stage which allows for the tuning of the time delay between the pump and probe pulses. It also passes through a waveplate (WP1) to allow for polarization resolution. It is then picked up and directed parallel to the pump beam, which also passes through a waveplate (WP2), before both are focused down (L5) to the sample. The probe beam comes in at a slightly oblique angle due to it being incident slightly off the center of the L1 optic. As a result, it is spatially separated from the pump upon reflection and can be easily be picked up and directed to the silicon photodiode with a mirror. Further color filtering is performed to eliminate any remaining pump scatter before the probe is focused down (L6) to the detector.

At the focal point of the pump telescope is an optical chopper which chops the beam at 8 kHz and serves as the reference signal for a lock-in amplifier (Stanford Research SR830) which collects the signal from the photodiode and converts it to a current. This current is transmitted via a BNC cable to a variable resistor (Thorlabs VRT2) which is typically set to 5 kΩ, allowing for detection of a voltage at the lock-in amplifier. During the operation of this experiment, the delay of the probe pulse is tuned so that the pump and probe pulses temporally overlap at the time-zero location, and then so that the probe arrives after the pump at various time delays.

The beam diameters of the pump and probe on the sample are ~50 μm and ~30 μm, respectively, which are measured using the razor blade method. In this measurement, a razor blade is placed on a translation stage at the sample location and used to incrementally cut the beam. A power meter records how quickly the beam is cut, and that power distribution is fit with a Gaussian profile to extract the beam diameter from the fit.

Photocurrent Setup

As discussed in Chapter III, we are also interested in the photocurrent generation in WSMs. This experiment is unique to others in our lab in that the detected signal is not optical but electronic in nature. This means that the samples measured must be prepared beforehand with the placement of leads and wires on the sample surface. The sample must be physically wired to our lock-in detector in order to measure the current produced. Here, I will describe first the optical setup necessary to generate photocurrent in our samples, and then I will describe the electronics which were built in order to collect and record that current.

The optical beam path of the photocurrent setup is shown in Figure IV.9. The beam first passes through a telescope with lens focal length ratio 1:3 to expand the beam and thus decrease the spot size on the sample. At the focal point of the telescope, an optical chopper is placed,

typically at 820 Hz, to chop the beam. This means that the otherwise DC effect of photocurrent

generation will occur instead at the chopping frequency, which is used as a reference for a lock-in

amplifier (Stanford Research SR830). The beam then passes through a waveplate. Depending on

the experiment, it may be a HWP (LPGE) or a QWP (CPGE). In either case, the waveplate is

placed on an automatic rotation stage which allows for computerized control of the incoming beam

polarization.

Figure IV.9 – An illustration of the optical beam path for the photocurrent generation setup. The incoming beam first goes through a telescope to expand the beam (L1, L2). At the focal point of L1, an optical chopper chops the beam to allow for a reference for a lock-in amplifier. The beam is then incident on either a QWP or HWP. There are two experimental geometries illustrated depending on the orientation of the flip mirror M1. In the case that M1 is not in the optical beam path, the light will be focused down normally onto the sample by lens L3. In the case that M1 is in the beam path, a series of mirrors will direct the beam to focus through L4 at an oblique incidence onto the sample. Not pictured is the initial ND filtering used to set the power of the beam at the sample sight or the white light imaging arm used for alignment purposes.

Importantly, as discussed in Chapter III, the angle of incidence is important for certain

materials. Thus, this experimental setup was designed for easy switching between normal and

oblique incidence ($\theta \approx 45°$) geometries. While we may have opted to achieve this flexibility with

a grating as in the RA-SHG setup, here a flip mirror was chosen in order to allow for a larger

possible angle of incidence. The flip mirror is labeled as M1 in Figure IV.9. For a normal incidence geometry, the mirror is flipped down and out of the optical beam path. For an oblique incidence geometry, the mirror is flipped up and a series of mirrors directs the beam to another lens, which focuses it down to the sample at an oblique angle. Razor blade tests performed on the beams at the sample location indicated a normal beam FWHM of ~33 μm. The oblique incidence beam becomes elliptical at the sample sight and the major axis of that ellipse was measured to have a FWHM of ~460 μm.

As mentioned above, the signal in this case is not a reflected beam from the sample surface, but instead an electrical signal generated in the sample. Thus, it is necessary to design a way to collect that signal and direct it to the lock-in amplifier where it can be measured. For air-sensitive materials or materials that need to be cooled, that electrical signal may additionally have to pass through a cryostat. The method developed for this is as follows: the sample is placed in and wired to a chip carrier (Chelsea Technology SB008AK959-1 for 8-pin or Chelsea Technology SB016L086-1 for 16-pin). These chip carriers are then inserted into two 8-pin connectors (Digikey S7041-ND) which are wired directly to 16 pins of a 22-pin cryostat port. This cryostat port is vital to holding the vacuum of the cryostat while feeding the electrical signals from our sample to the lock-in amplifier, which is in ambient conditions, to be measured.

A BNC box was built in collaboration with Austin Kaczmarek which separates each of the signals from the 16 pins of in the cryostat each to its own BNC cable. Each cable has a two-way switch which allows for the signal and ground of the BNC to be either separated or electrically connected. The grounds of all of the BNCs are connected together and can be either floated, connected to the BNC box, or connected to an external ground to allow for biasing. In a typical experiment, we are interested in the photocurrent across two leads on a sample, corresponding to

two pins on the chip carrier. We will refer to these leads as lead 1 and lead 2. To measure the photocurrent response across lead 1 and lead 2, all of the BNC switches are switched up to electrically separate the signals from the BNC common ground except that of lead 2, which is grounded to the BNC box. This sets the ground of the BNC for lead 1 to the signal of lead 2. Then, the photocurrent across these two leads is measured by attaching the lead 1 BNC to a terminator (Thorlabs VT2) which is used as the signal to the lock-in amplifier. That is, the photocurrent is measured as the voltage difference across lead 1 and lead 2 through a BNC whose ground is connected to lead 2 and whose signal is connected to lead 1. An illustration of this setup is shown in Figure IV.10.

Figure IV.10 – Several images of the photocurrent setup. (Top Left) An image of a sample in a chip carrier in the cryostat. The chip carrier is inserted into two 8-pin connectors, one on either side, to transfer the electrical signal from the sample to the cryostat port. (Top Right) The chip carrier and sample together with the shielding necessary to cool the sample down with the cryostat. (Bottom Left) The BNC box built in collaboration with Austin Kaczmarek designed to transfer the electrical signals from the sample to the lock-in amplifier. Each labeled BNC port has the ability to connect with one of the pads on the sample via the 8-pin connectors. Each port also has a switch to control the signal and ground output of the BNC. Here, we can see that a BNC cable is plugged into port 3 and that the switch of port 4 is set to shield grounding. All other switches are flipped up. This means that we are measuring the current across pads 3 and 4 on the sample. (Bottom Right) The sample and chip carrier on their mount which is typically used with the cryostat, together with the cryostat port used to transfer the electrical signal from the cryostat to the lock-in

amplifier, which is in ambient conditions. Here, the copper mount and cryostat port have been removed from the cryostat itself for a scanning measurement, discussed in the next section.

Scanning

As discussed earlier, using a small spot size to obtain high spatial resolution allows for scanning measurement implementations of the various techniques discussed above. In scanning measurements, signal of a given quantity (usually either SHG or photocurrent) is measured at various points across a sample surface in order to observe spatial variations in that signal. For example, a scanning system was implemented on the photocurrent setup by using automated motorized translation stages for the sample stage which could be programmed to move the sample at fixed intervals to create a photocurrent image for a given polarization. However, there are several downsides to this method of physically moving the sample when taking a scanning measurement. For one, when the cryostat is mounted vertical to the table, creating a platform on which the motorized stages can support the weight of the cryostat is difficult and costly. This severely limits the samples which can be measured using this setup to only those which are not air-sensitive (a picture of this is shown in Figure IV.10). Further, the repeatability of the measurement is subject to the minimum repeatable step size of the motors used. While this is not a significant hindrance for the larger beam size of the photocurrent setup, it can be a problem in setups where the beam is significantly smaller, which is necessary especially for smaller samples.
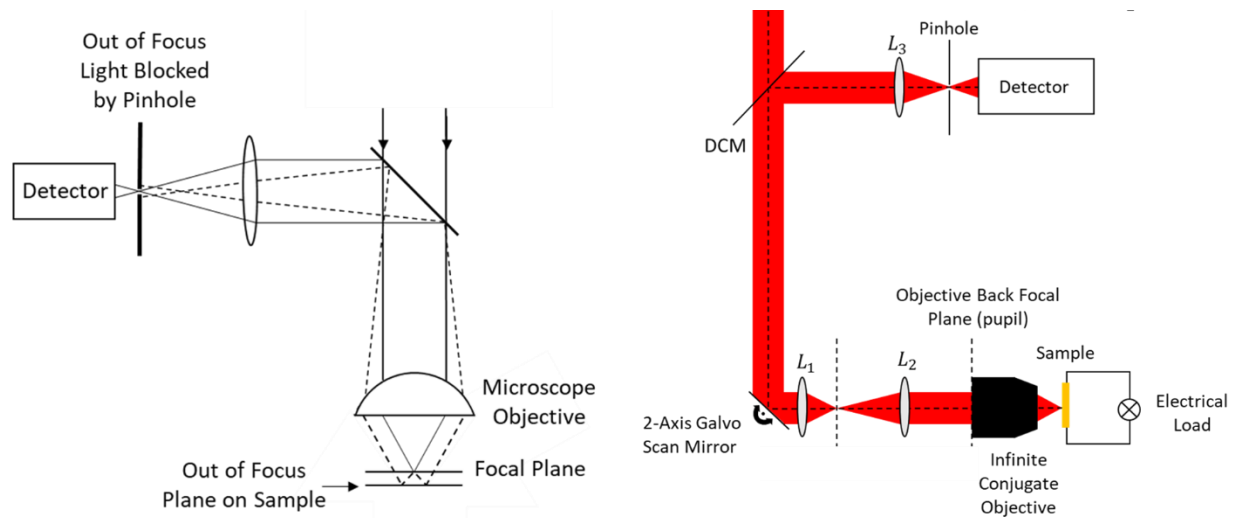
Figure IV.11 – An illustration of the operating principle behind using the motorized scanning mirror (left) and of the resulting scanning SHG setup (right). Both images are provided by Austin Kaczmarek.

The necessity of performing RA-SHG experiments near the diffraction limit for micron-length samples where the ~30 μm spot size of the fundamental beam is too large and of implementing scanning SHG for such small samples led to the development of our scanning SHG setup by Austin Kaczmarek. To obtain a diffraction limited spot size, an infinite focal plane objective from Edmund Optics (#89350) was used to focus the beam to the sample after a telescope which expanded the beam by approximately a factor of 3, yielding a spot size ~3-5 μm. Because this runs into the minimum repeatable distance of the Thorlabs motorized translation stages, it was also necessary to develop an alternative scanning technique, illustrated in Figure IV.11. This technique utilizes a scanning mirror controlled by two Galvo motors connected to an Arduino. The beam direction is changed slightly by the scanning mirror, and then redirected to the sample using a telescope comprised of two standard corrective lenses. When the beam hits the focusing objective to the sample, it is slightly off the center of the optic. Thus, a scanning plane is formed just beyond the normal focal plane of the objective. The use of the telescope helps to ensure that larger steps

of the Galvo motors will lead to smaller scanning increments, thus minimizing the uncertainty due to the minimal repeatable distance of the motors.

Dichroic mirrors direct the reflected SHG, in a method similar to that on the RA-SHG setup, to a PMT with a peak sensitivity in the 400 nm range (Hamamatsu H10720-210). This PMT is connected to a lock-in amplifier (Zurich Instruments MFLI 500 kHz lock-in amplifier) which takes as a reference the 200 kHz signal from the Spirit. This setup does have capabilities similar to that of the RA-SHG setup in that the polarization of the incoming light is tuned by a HWP and an analyzer is before the PMT detector. However, due to difficulties involved with implementing an oblique incidence geometry option with the scanning capabilities and the need for the objective, data can only be taken on this setup at normal incidence.

Glovebox-Based 2d Fabrication Setup

Motivated by the growing interest in the field of 2d materials, which began with the discovery of the scotch tape method of exfoliating graphene from graphite [103] and progressed to similar exfoliation of TMDCs [104], current 2d material research relies heavily on being able to stack n-layer materials of various types and at different angles, such as magic-angle graphene [105], which has unconventional superconductive properties, and moiré superlattices and other 2d heterostructures [104, 106, 107]. The study of these materials is related to WSMs in that topologically protected features may occur in the band structure of these synthetically constructed samples, and in some cases even Dirac cones and flat band structures may be present. Further, several TMDCs, such as $MoTe_2$ and WTe_2, are type-II WSMs in their bulk form [8, 108].

Yet the construction of these thin materials is incredibly challenging due to the air-sensitive nature of the constituent components. To this end, a collaborative team of scientists across the

physics department became interested in creating a system which could hold these air-sensitive samples in a nitrogen environment to avoid contamination during the exfoliation procedure. It was also necessary to be able to stack heterostructures in this enclosed environment to prevent oxygen and other dirt from lodging between the stacked layers, and to be able to load and unload these samples to a vacuum chamber, such as a cold-finger cryostat, for transport to optical setups. These requirements constituted the need for a glovebox, which had to be large enough to contain a microscope which could be used for the fabrication procedure as well as motorized stages which were sensitive enough to allow for the delicate stacking to procedure to be performed. It also needed a large enough antechamber to hold our cryostat. Further, we needed a sensitive enough microscope to be able to search for thin flakes of material suitable for stacking and which had a large enough focal plane to be able to visualize the stacking procedure.

Figure IV.12 – Pictures of the glovebox-based 2d fabrication setup in the lab in the sub-basement of Randall Laboratory. (Left) The 4-glove Purelab HE from Inert. (Right) The Olympus microscope setup for the stacking procedure inside the glovebox. Two motorized stages from Thorlabs are shown to allow lateral movement of the sample within the focal plane. Atop these lateral stages is a Thorlabs rotation stage, on which is an aluminum sample mount with a thermal heating pad. Also pictured is the three-axis stage used to hold the microscope slide with the top stack for the stacking procedure.

The full glovebox-based fabrication setup is shown in Figure IV.12. The glovebox unit selected was the 4-glove Purelab HE from Inert. This system is large enough to hold a high-quality imaging microscope, the BX63 from Olympus. We also attached a large antechamber to the glovebox which can hold the necessary cryostat. The BX63 was adapted so that the focusing operation is performed via motion of the objectives rather than of the stage. This allows the top and bottom stacked layers to be held in the same position while the focal plane moves up and down between them. Several objectives were selected – 20x, 50x, 100x – to ensure wide view when searching for flakes to be used in the stacking procedure and a narrow, detailed view when

performing the stacking. All objectives have a long focal length to allow room for the stacking procedure.

Importantly, all components necessary to stack heterostructures of 2d materials are motorized and can be automated. Motorized linear stages from Thorlabs form the basis for the sample stage, allowing for linear lateral motion to reach a desired point on a sample. In addition, an automatic rotation stage from Thorlabs is placed atop the linear stages, on which is mounted a sample mount, to allow the sample to be rotated to a specific angle. Aluminum was chosen as the material for the sample mount because of its ease of use and good thermal transfer properties. This means that the sample can be easily heated using a thermocouple placed on the aluminum stand. This heating is necessary for the stacking procedure, as the "stickiness" of the sample is controlled by its temperature.

The general outline of the stacking procedure is as follows. First, a 2d flake is identified using the microscope which will serve as the bottom layer and another is identified for the top layer. The top layer is placed on the bottom of a transparent microscope slide held by a motorized stage so that the top layer is vertically directly over the bottom layer. The microscope stage is used to ensure that the top layer is transparent enough that the focal plane of the microscope can be adjusted to focus on the both the top and bottom layers as needed. The microscope has both a manual coarse adjustment and a motorized fine adjustment capability. Safety stops are put in place for the fine adjustment to prevent damage to the top and bottom layers during the procedure which might be caused by accidentally moving them too quickly or too close together. The temperature of the bottom stack is then varied along with the height of the top stack above the bottom stack to allow the two layers to bond.

Further, the motorized stages allow for us to scan for material flakes. In a typical exfoliation process, the bulk material is exfoliated multiple times onto a silicon subtrate which is typically on the order of a couple of cm^2 in area at least. As a result, the silicon substrate is covered in exfoliated flakes of bulk and n-layered material, but only very few flakes of a material are useful for a particular experiment. These monolayer, bilayer, trilayer, etc. flakes of material typically only have lateral dimensions of $\sim10\mu m$ at most, and so finding them on the silicon substrate can be a long and arduous process. Over the course of the last couple of years, I have worked with several undergraduate students (Ian Blackman-Staves, Samia Sabir, Shannon Gray, and Laura Zichi) to automate the scanning procedure for the glovebox system and search for and find flakes which are useable for experiments. Our latest efforts have included implementing machine learning to identify microscope images of high-quality usable flakes, which is ongoing.

CHAPTER V

Nonlinear Optical Measurements on type-II Weyl Semimetals

As discussed in Chapter II, a type-II WSM is a WSM in which the WP occurs at the intersection of an electron and a hole pocket. The layered TMDC WTe_2 was the first predicted electronic type-II WSM [8]. This material had previously attracted much interest due to the observation of extremely large positive magnetoresistance at low temperatures [109] and of superconductivity [110, 111]. Like many layered TMDCs, it can exist in several different polytypes, including the T_d, 1T', and 2H phases. Of these, only the T_d phase is noncentrosymmetric and hosts the WSM state. However, unlike other layered TMDCs, WTe_2 exists in the T_d phase even at room temperature. The T_d phase is a distorted 1T' structure belonging to space group (point group) $Pmn2_1$ (C_{2v}) [75]. An illustration of the crystal structure of T_d-WTe_2 can be found in Figure V.1. It possesses a two-fold screw axis along the c-axis, a mirror in the bc-plane, and a glide mirror in the ac-plane.
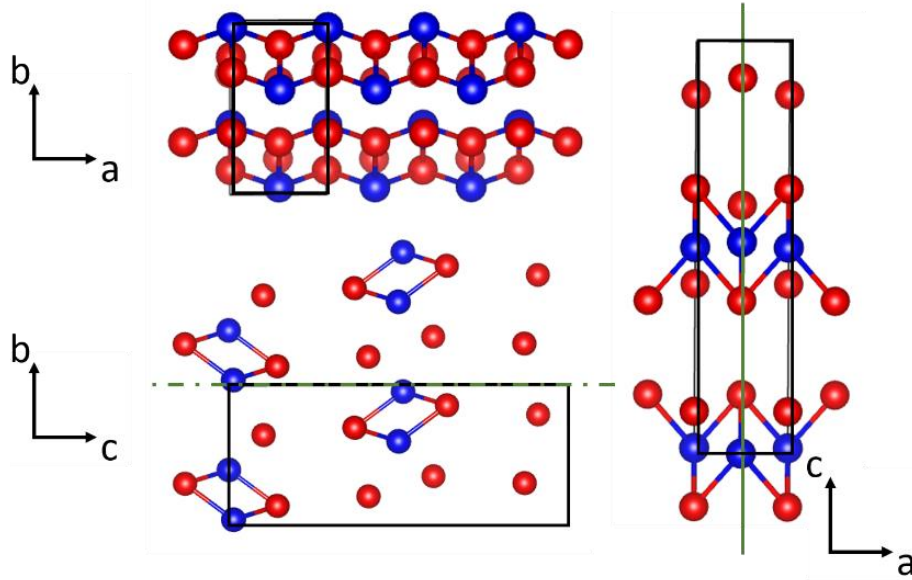
Figure V.1 – The crystal structure of T_d-WTe_2 drawn using VESTA software and crystallographic information from [112] along the *a*-, *b*-, and *c*-axes. Here, the Te atoms are indicated in red and the W atoms in blue. The mirror in the bc-plane (solid green) and the glide mirror in the ac-plane (dashed green) are indicated, and the unit cell is boxed in each orientation. The coordinates next to each plane indicate the crystal axes.

Following the prediction of the WSM band structure in T_d-WTe_2, there was a flurry of experimentation looking to confirm the topological state. Multiple ARPES studies were performed to investigate the surface Fermi arcs [113-115], and studies of the Shubnikov-de Haas oscillations similarly tried to pin down the Fermi arcs near electron and hole pockets [116], but such experiments were not immediately conclusive due to the slightly larger separation between the Fermi energy and the predicted WPs compared with TaAs and other confirmed WSMs. To compensate, some studies using time-resolved ARPES were performed to first excite the electrons up to the Weyl cone and then look at the Fermi arcs [117], but even these studies proved inconclusive when calculations came out predicting that observed Fermi arcs might arise without a topological origin [54, 55, 118]. Since then, several other studies have come out providing strong evidence for a type-II WSM state in T_d-WTe_2. These include ARPES [56, 119], time-resolved

ARPES [120], Xray-ARPES [121], spin-resolved ARPES [122], scanning tunneling microscopy [123], and transport measurements [20]. Due to this evidence, the existence of a type-II WSM state in T_d-WTe$_2$ is now widely accepted in the condensed matter community.

Shortly after the prediction of the WSM state in T_d-WTe$_2$, a type-II WSM state was predicted as well in the similar layered TMDC, T_d-MoTe$_2$ [124]. MoTe$_2$, however, exists in the 1T' phase at room temperature and undergoes a structural phase transition to the T_d phase at 250K [125, 126]. This 1T' phase belongs to space group (point group) $P2_1/m$ (C_{2h}) [89, 127]. The crystal structures of the 1T' and T_d polytypes of MoTe$_2$ are shown in Figure V.2. Like the T_d polytype, the 1T' polytype has a mirror in the bc-plane. Unlike the T_d polytype, the 1T' phase possesses a C_2 skew axis along the a-axis and is inversion symmetric. The energy separation between the Fermi energy and the WPs in this material is less than that in T_d-WTe$_2$, and so experimental confirmation of the WSM band structure through observation of the Fermi arcs with ARPES was achieved with less controversy [22, 52, 53, 108, 128, 129].
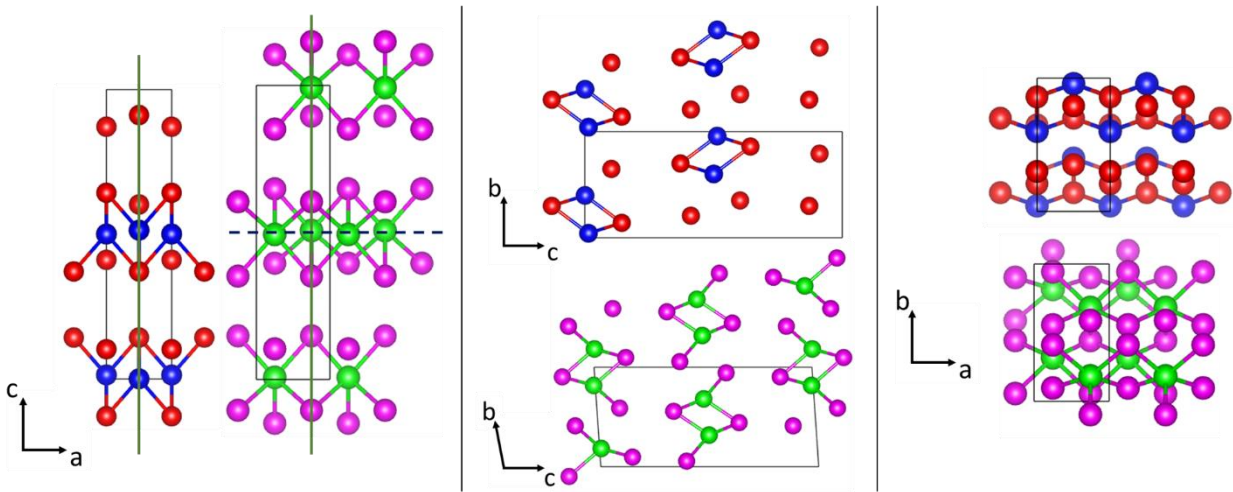
Figure V.2 – An illustration of the MoTe$_2$ crystal structure for both the T_d (blue Te and red Mo) and 1T' (pink Te and green Mo) polytypes. The mirror plane consistent across both polytypes in the bc-plane is indicated as solid green lines and the C_2 skew axis along the a-axis specific to the 1T' polytype is indicated as a dashed blue line. The unit cell in each case is indicated in black. The

coordinates next to each plane indicate the crystal axes. We note here that the b-axis is slightly tilted when viewed in the bc-plane when for the 1T' phase, and so each phase has a coordinate indicator for this plane. These images were drawn using the VESTA software with crystal structure files from [112, 130].

Nonlinear effects including SHG [71], photocurrent generation [72], the nonlinear Hall effect [18], and higher order effects [79] have all been observed in type-II WSMs, but they are often studied in few- or mono-layer materials rather than in bulk. The study of n-layer T_d-MoTe$_2$ and T_d-WTe$_2$ has been a fertile field of research in the last several years after the discovery of the scotch-tape method of exfoliation of graphene [103]. Like graphite, the layers of these TMDCs are held together with weak van-der Waals interactions, making fabrication procedures relatively simple and inexpensive. Yet the topological WPs and Weyl cones are bulk phenomena, and so the study of nonlinear effects in bulk-like thick type-II WSMs is warranted [89, 90].

In this chapter, we will present several experimental studies of second order nonlinear optical effects in the bulk type-II WSMs T_d-WTe$_2$ and bulk-like MoTe$_2$. First, we examine the SHG response of this material and estimate the size of the nonlinear optical susceptibility tensor, which we compare to other nonlinear crystals. Next, we use polarized time-resolved optical reflectivity spectroscopy to study the coherent oscillations of the optical phonons in this material. We identify the excitation mechanism of the lowest-frequency mode, the 0.25 THz shear mode, as the nonlinear process of Impulsive Stimulated Raman Scattering (ISRS), distinct from other observed phonons excited through the Displacive Excitation of Coherent Phonons (DECP). We find the strength of this nonlinear ISRS response to be large compared with the DECP response of the other modes. The 0.25 THz mode is further identified with an observation of the linear electro-optical effect. We use point-symmetry-based analyses to study the anisotropic behavior of both the SHG and ISRS responses to the incoming light polarization. We use fluence-dependent

measurements to verify our identified excitation mechanisms and to study the electron-phonon coupling. We will also present a brief study of the SHG response of few-layer MoTe$_2$ and look at how that response varies as we evolve from thin to bulk samples as well as from the 1T' to T$_d$ phases. We note here that I performed all measurements and completed all analysis for the T$_d$-WTe$_2$ studies and Austin Kaczmarek and I took the measurements for the MoTe$_2$ studies while I performed the analysis. Both studies were completed under the supervision of Liuyan Zhao. Adam Tsen and Archana Tiwari provided the MoTe$_2$ devices and Junjie Yang provided the WTe$_2$ samples.

Material Preparation

T$_d$-WTe$_2$ samples were synthesized using a self-flux method. 0.2 g of WTe$_2$ powder and 10 g of Te (99.999%) were loaded into an alumina crucible, which was sealed in a quartz tube under vacuum. A small amount of quartz wool was later added on top of the alumina crucible to act as a filter to separate the flux from the crystals in a later step. The tube was then heated to 825°C, held for 24 hours, and then slowly cooled to 525°C over 150 hours. At 525°C the flux was separated from the crystals by centrifuging. The WTe$_2$ crystals were then put into another vacuum sealed quartz tube and annealed at 415°C for two days. Before measurements were taken, the sample was cleaved using scotch tape in ambient conditions and immediately transferred to vacuum to prevent oxidation [131]. It was kept at room temperature in a vacuum better than 2×10^{-6} hPa.

All MoTe$_2$ crystals were also grown using the flux method with a Te solvent. Mo (Alfa Aesar, 99.9%) and Te (Alfa Aesar, 99.99%) powders were ground and placed into an alumina crucible in a 1:25 ratio and sealed in a quartz ampoule. The quartz ampoule was first heated to

1050°C and held for two days. Then, it was cooled to 900°C over 120 hours and centrifuged. Shiny, plate-like crystals with lateral dimensions of up to several millimeters were obtained.

The construction procedure for the $MoTe_2$ devices presented at the end of this chapter is as follows. 45 nm Au and 5 nm Ti electrodes were pre-patterned in a circular geometry on Si wafers with a 285 nm oxide layer using conventional photolithography and electron-beam deposition. The graphene (Coorstek), hBN (HQ graphene), and $MoTe_2$ flakes were all exfoliated inside of a nitrogen-filled glovebox system (Inert PureLab HE) using scotch tape onto blank SiO_2/Si wafers. After the desired flakes were identified using an optical microscope (Olympus), a polydimethylsiloxane polymer stamp coated with polycarbonate was used to pick up the full hBN/graphene/hBN/MoTe2/hBN heterostructure. This avoided contamination between the layers. The heterostructure was then aligned and transferred onto the pre-patterned electrodes. The full exfoliation and transfer process was performed in the nitrogen-filled glovebox to avoid degradation.

Second Harmonic Response of T_d-WTe$_2$

As with all noncentrosymmetric materials, we expect an electric-dipole SHG response from T_d-WTe2, as discussed in Chapter III. We can simultaneously confirm the symmetry of the sample and investigate its SHG response by performing RA-SHG experiments [97, 98]. Working with an 800 nm incoming fundamental light source, we expect that we will not be sensitive to the translational symmetries of the space group because they are relevant on the length-scale of the lattice constants, which are only a few angstroms, and thus several orders of magnitude smaller than the wavelengths used in our experiments. Thus, we typically derive the relevant point group of a material for experiments at 800 nm by eliminating the translational symmetries of the space

group. For the $Pmn2_1$ space group of T$_d$-WTe$_2$, this corresponding point group must consist of mirrors in the ac- and bc-planes (ie. eliminating the translational symmetries of the glide mirror yields a mirror) and a C_2-rotation about the c-axis (ie. eliminating the translational symmetries of the skew axis yields a rotation). These point symmetries correspond to the C_{2v} point group. We can derive χ^{ED} using these point symmetries. Doing so, we find seven nonzero elements, five of which are independent. These are

$$\chi^{ED}_{xzx} = \chi^{ED}_{xxz}; \chi^{ED}_{yzy} = \chi^{ED}_{yyz}; \chi^{ED}_{zxx}; \chi^{ED}_{zyy}; \chi^{ED}_{zzz}. \hspace{2cm} \text{V.1}$$

Figure V.3 shows the reflected SHG intensity as a function of polarization angle at a selection of normal and oblique incidence polarization channels[10] [132]. We see that there is a nonzero response even in the normal incidence experimental geometry, and that there is a large anisotropy in that response. However, the out-of-plane C_2-axis of C_{2v} strictly forbids any SHG response at normal incidence. This contradiction between our measurements and the point-group-based prediction can be reconciled by the fact that this C_2-axis in reality is a skew axis, or a rotation operation followed by a half unit cell translation along the out-of-plane direction (ie. the incident light wavevector direction). The RA-SHG response of T$_d$-WTe$_2$ differentiates the skew axis from C_2-rotation and thus demonstrates a nonzero SHG response even at normal incidence.

We therefore model the RA-SHG response of T$_d$-WTe$_2$ using the symmetries of the m point group, which is a subgroup of $Pmn2_1$ containing only one mirror in the bc-plane. The ED susceptibility tensor for this point group has 14 nonzero elements, of which 10 are independent. These are

$$\chi^{ED}_{xyx} = \chi^{ED}_{xxy}; \chi^{ED}_{xzx} = \chi^{ED}_{xxz}; \chi^{ED}_{yxx}; \chi^{ED}_{yyy}; \chi^{ED}_{yzy} = \chi^{ED}_{yyz}; \chi^{ED}_{yzz}; \chi^{ED}_{zxx}; \chi^{ED}_{zyy}; \chi^{ED}_{zyz}$$
$$\hspace{6cm} \text{V.2}$$
$$= \chi^{ED}_{zzy}; \chi^{ED}_{zzz}.$$

---

[10] See Chapter III for a description of the various polarization channels accessible with the RA-SHG experiment.

Using this tensor, we can compute the expected forms of the RA-SHG data in both the parallel and

crossed normal incidence polarization channels as

$$I^{2\omega}_{parallel}(\phi) = \left(\chi^{ED}_{yyy} \sin^3(\phi) + \left(2\chi^{ED}_{yxy} + \chi^{ED}_{yxx}\right) \cos^2(\phi) \sin(\phi)\right)^2$$

$$I^{2\omega}_{crossed}(\phi) = \cos^2(\phi) \left(\chi^{ED}_{yxx} \cos^2(\phi) + \left(\chi^{ED}_{yyy} - 2\chi^{ED}_{xyx}\right) \sin^2(\phi)\right)^2.$$

V.3

Similar results can also be derived for the oblique incidence polarization channels as

$$
\begin{aligned}
I^{2\omega}_{S-S}(\phi) &= \left(\chi^{ED}_{yyy} \cos^3(\phi) + 2\left(\chi^{ED}_{xyx} + \chi^{ED}_{yxx}\right) \cos(\phi) \sin^2(\phi)\right)^2, \\
I^{2\omega}_{S-P}(\phi) &= \cos^2(\theta) \sin^2(\phi) \left(\left(\chi^{ED}_{yyy} - 2\chi^{ED}_{xyx}\right) \cos^2(\phi)\right. \\
&\qquad \left. + \chi^{ED}_{yxx} \sin^2(\phi)\right)^2 \\
&\qquad + \sin^2(\theta) \left(\chi^{ED}_{zyy} \cos^2(\phi) + \chi^{ED}_{zxx} \sin^2(\phi)\right)^2, \\
I^{2\omega}_{P-S}(\phi) &= \left(\chi^{ED}_{yzz} \cos(\phi) \sin^2(\theta)\right. \\
&\qquad + \cos(\phi) \cos^2(\theta) \left(\chi^{ED}_{yxx} \cos^2(\phi)\right. \\
&\qquad \left. + \left(\chi^{ED}_{yyy} - 2\chi^{ED}_{xyx}\right) \sin^2(\phi)\right) \\
&\qquad \left. - \left(\chi^{ED}_{xzx} - \chi^{ED}_{yzy}\right) \cos(\theta) \sin(\theta) \sin(2\phi)\right)^2, \\
I^{2\omega}_{P-P}(\phi) &= \left(-\chi_{yzz} \sin^2(\theta) \sin(\phi) - \cos^2(\theta) \sin(\phi) \left(\left(2\chi^{ED}_{xyx}\right.\right.\right. \\
&\qquad \left.\left. + \chi^{ED}_{yxx}\right) \cos^2(\phi) + \chi^{ED}_{yyy} \sin^2(\phi)\right) \\
&\qquad \left. - 2 \cos(\theta) \sin(\theta) \left(\chi^{ED}_{xzx} \cos^2(\phi) + \chi^{ED}_{yzy} \sin^2(\phi)\right)\right)^2 \\
&\qquad + \sin^2(\theta) \left(\chi^{ED}_{zzz} \sin^2(\theta) + \chi^{ED}_{zzy} \sin(2\theta) \sin(\phi)\right. \\
&\qquad \left. + \cos^2(\theta) \left(\chi^{ED}_{zxx} \cos^2(\phi) + \chi^{ED}_{zyy} \sin^2(\phi)\right)\right)^2.
\end{aligned}
$$

V.4

We then use the signal strength of the RA-SHG measurements to estimate the strength of

the SHG response.[11] This estimation is a crucial step towards understanding the strong nonlinear

optical effects in type-II WSMs by allowing for comparison of the nonlinear responses across other

materials. From Chapter IV, we know that we must use the refractive index of bulk T_d-WTe$_2$ to

adjust for the nonlinear Fresnel coefficients [102]. To our knowledge, this quantity has not been

experimentally determined, but Density Functional Theory (DFT) calculations have recently been

---

[11] See Chapter IV for details on this procedure.

performed [133]. Using these calculated parameters, we find nonlinear susceptibility tensor elements of $\chi^{ED}_{xyx} \approx 300$ pm/V, $\chi^{ED}_{yxx} \approx 350$ pm/V, and $\chi^{ED}_{yyy} \approx 200$ pm/V, which are up to two orders of magnitude larger than previously reported measurements on non-topological polar metals [14, 134, 135].
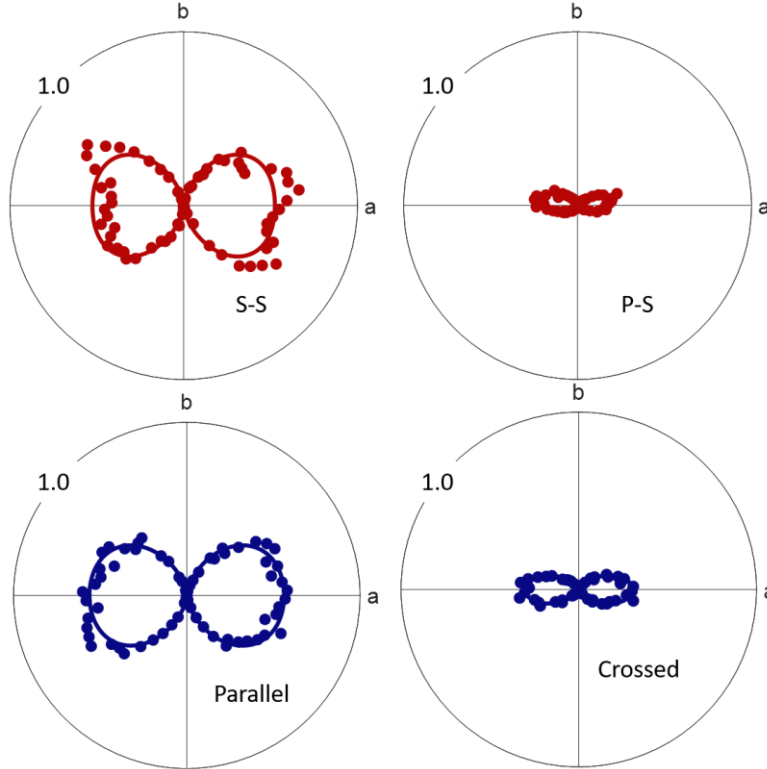
Figure V.3 − RA-SHG data (dots) and corresponding fits (solid curve) taken in the oblique S-S and P-S polarization channels (top, red) and in the corresponding parallel and crossed normal incidence polarization channels (bottom, blue). The models are taken from Equations V.3 and V.4 using the electric-dipole response of the m point group. The plot is normalized such that 1.0 corresponds to 17.4 fW.

The nonlinear susceptibility tensor elements of the type-I WSM TaAs have already been determined to be ~7200 pm/V.[12] This was found to be an order of magnitude larger than the

---

[12] Specifically, this is the χ^{ED}_{zzz} susceptibility tensor element which accesses the polar c-axis in this material.

response in GaAs at 800 nm, which is a material typically used to calibrate SHG measurements [14]. In contrast, our estimation for the SHG response in T_d-WTe$_2$ is about half that of GaAs. There are several possible explanations for this difference in strength between the type-I and type-II WSM second harmonic responses. One explanation could be that the experimental geometry used in the TaAs measurements accessed the polar c-axis, while the experimental geometries shown in Figure V.3 do not because of the differing point symmetries between these materials. However, the strength of the SHG response is pretty consistent between both the normal and oblique incidence geometries and so it is unlikely that this is the cause of the discrepancy. Further, the layered structure of T_d-WTe$_2$ means that the van der Waals bonds between layers along this polar c-axis will be significantly weaker than the ionic bonds along the TaAs polar c-axis. This would naturally yield a weaker out-of-plane second harmonic response.

Another second possible explanation for the discrepancy between our T_d-WTe$_2$ experiment and previous TaAs experiments is that the wavelength of our fundamental light is farther from resonance than measurements taken on TaAs [70]. Although absorption measurements have not been performed on T_d-WTe$_2$, optical conductivity measurements and DFT calculations on T_d-WTe$_2$ at room temperature do both indicate that the band edge is several orders of magnitude lower than either the fundamental (800 nm) or SHG (400 nm) wavelengths used in this experiment, and that there are no additional features in the optical conductivity [133, 136].

A third possible explanation is that the discrepancy in the strength of the SHG response is more directly related to the Weyl physics through carrier screening effects which might occur due to the presence of the electron and hole pockets present in the band structure of type-II WSMs at the WPs which are not present in the type-I band structure. Such an effect occurs in metals, where the multitude of free carriers effectively screens the incoming fundamental electric field, thus

95

reducing the SHG response. The electron and hole pockets near the WP of type-II WSMs, including T_d-WTe$_2$, might allow for more free carriers in these materials than in type-I WSMs. In any case, further study is certainly needed to pin down the exact source of this discrepancy between the type-I and type-II SHG responses.

Time-Resolved Optical Reflectivity Studies on T_d-WTe$_2$

The experimental setup of the time-resolved optical reflectivity experiment is discussed in Chapter IV and is shown in Figure V.4. Here, the horizontal (H) polarization is along the glide mirror direction with an uncertainty of $\pm 10°$ and the vertical (V) polarization is along the mirror direction with an uncertainty of $\pm 10°$. In general, for this material, we will work with 12 different polarization channels. These are the H-H, H-V, V-H, V-V, L-L, L-R, R-L, A-A, A-B, B-A, and B-B channels, where the A and B polarizations are linear polarizations which are 45° rotated from either H or V, and where L and R refer to left- and right-handed circularly polarized light, respectively.
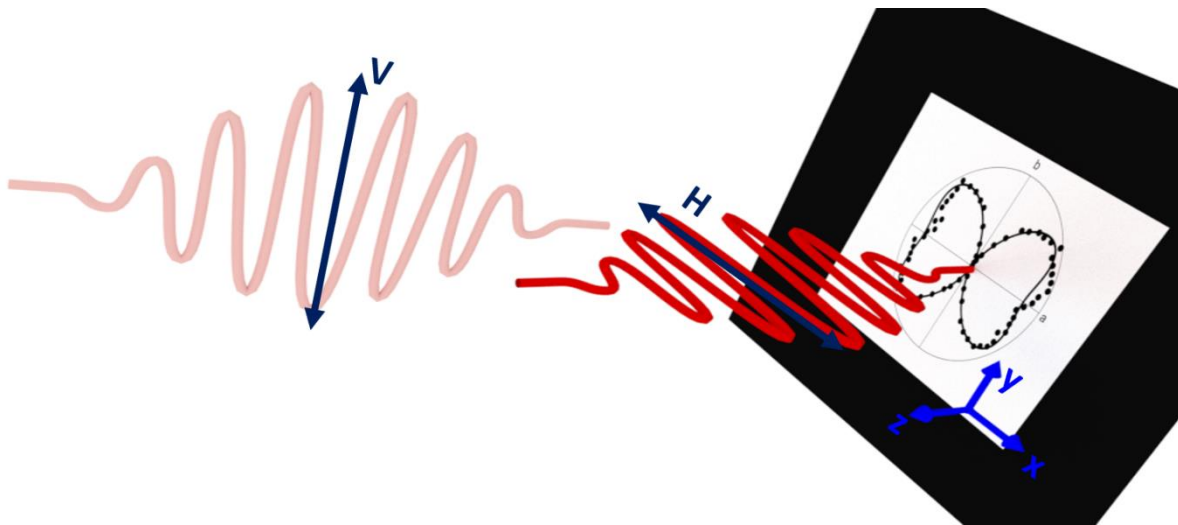
Figure V.4 – The experimental setup for the time-resolved reflectivity measurements. The pump pulse at 720 nm is normally incident on the sample and followed at a time delay by a probe pulse

at 800 nm at a small oblique angle (~7°). The polarization of the pump and probe can be independently tuned into eight different polarization combinations and are shown here in the H-V channel. The lab frame is indicated in blue, and the sample coordinate system is indicated by the RA-SHG pattern.

Raw data obtained in the H-H and H-V polarization channels are shown in Figure V.5. The overall trend for both channels is defined by two key features. The first feature is a dramatic dip in the $\Delta R/R$ value at the temporal overlap point (time-zero) of the pump and probe, which is attributed to the excitation of electrons in the material by the pump pulse, followed by a gradual recovery process. The second feature is the oscillatory behavior in the dynamic response after time-zero, which we associate with coherent excitations of optical phonons. Throughout all of our experiments, six phonon oscillations were observed at 0.25 THz, 2.4 THz, 3.5 THz, 3.9 THz, 4.9 THz, and 6.4 THz. All observed phonons are associated with A_1 modes by comparing their frequencies to previous Raman measurements [131, 137-140].
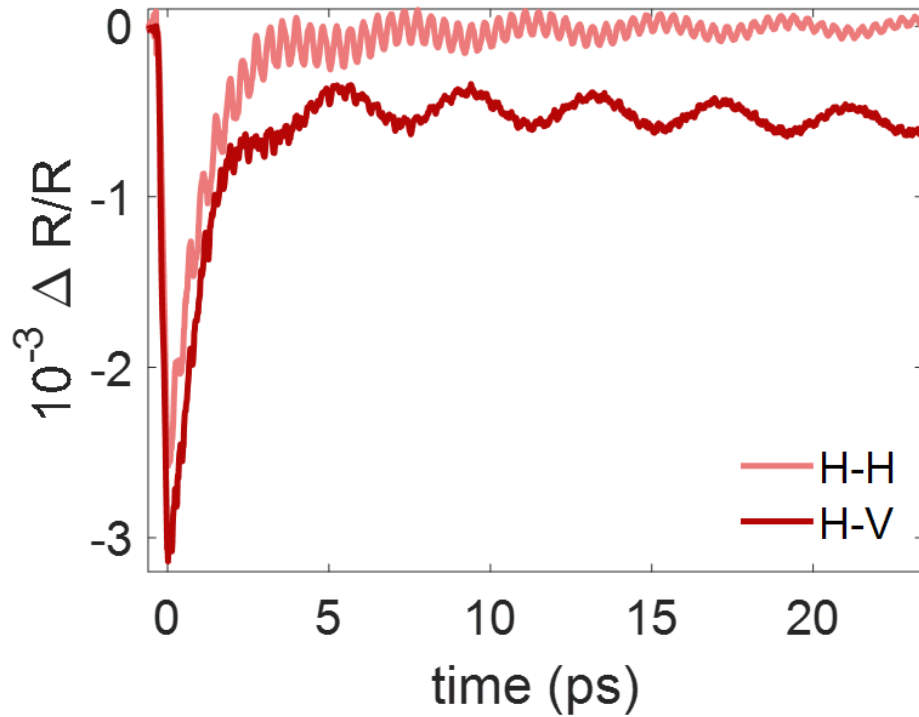
Figure V.5 – Time-resolved reflectivity measurements on T_d-WTe$_2$ for linearly polarized pump and probe in two polarization channels. In both channels, a dip in the change in reflectivity ($\Delta R/R$) is observed at time zero followed by a decay with oscillations dependent on the polarization of the probe pulse.

To extract the frequencies of the phonon modes observed, it is necessary to perform a fit to the time dynamics. We fit the overall time dynamics using two exponential decays convolved with a Gaussian beam profile, as shown in Figure V.6. Throughout our time-resolved optical reflectivity measurements on T_d-WTe$_2$, we find one shorter time constant on the order of 1 ps, which we associate with electron-phonon thermalization, and a longer, weaker decay on the order of 5-10 ps which has previously been associated with phonon-assisted electron-hole recombination [141]. To extract the frequencies of these oscillations, the relaxation dynamics are subtracted from the raw data and a fast-Fourier transform (FFT) is performed on the resulting data set. The oscillatory response of the L-L channel after subtraction of the time dynamics is shown in the lower panel of Figure V.6.
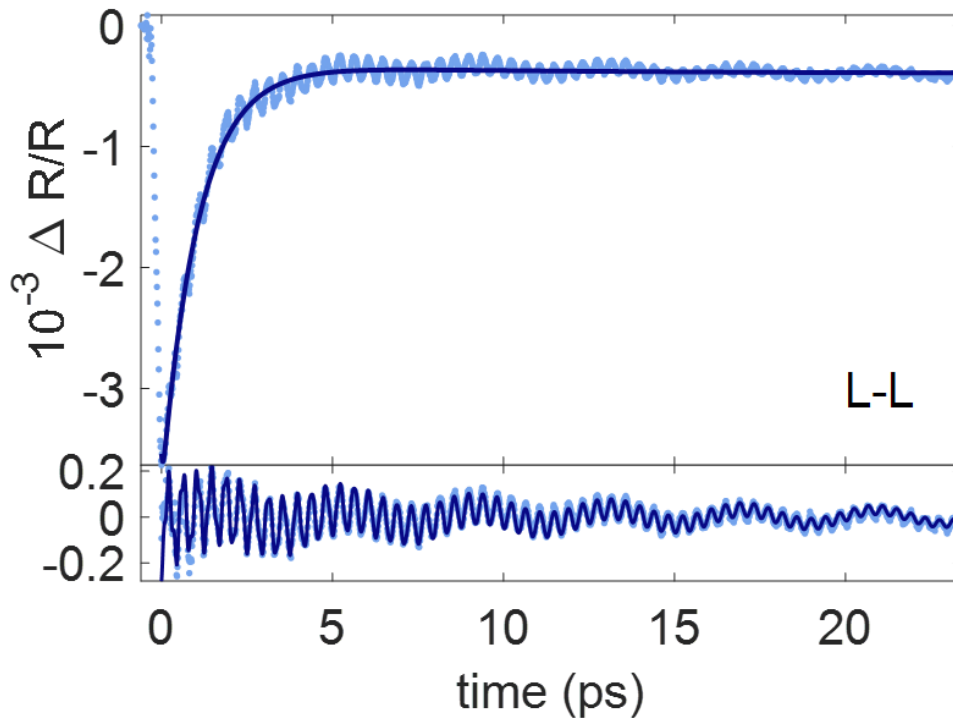
Figure V.6 – An illustration of the fitting procedure used in the data analysis in the case of an L-L dataset. First, the decay dynamics are fit to the sum of two exponential decays convolved with a Gaussian beam. This fit is then subtracted from the data to reveal the underlying phonon oscillations, which are fit individually assuming decaying sinusoidal oscillations.

Figure V.7 shows time-resolved optical reflectivity measurements for circularly polarized pump and probe beams. The same relaxation and oscillatory features can be seen in this data as were observed in the linear polarization channels, although the phonon oscillations seem to be much more consistent for different polarizations than were seen in the linearly polarized data. The purpose of using circularly polarized light is to identify if there is a time-resolved magneto-optical Kerr effect (TR-MOKE) present in the sample. Such measurements are typically taken by using a balanced photodiode but may be accessible to us due to our polarization resolution. In particular, we can calculate the TR-MOKE signal by subtracting the raw data from our L-L and L-R channels. Such a signal would be an indication of the Weyl physics of T_d-WTe$_2$ because left- and right-hand circularly polarized light will populate the Weyl cones differently because of their distinct

chirality. The inset of Figure V.7 illustrates that we find a null result for the TR-MOKE signal under our experimental conditions. This is likely because the pump wavelength will excite electrons far above the chiral WPs to higher bands whose response will dominate over that expected using topological arguments.
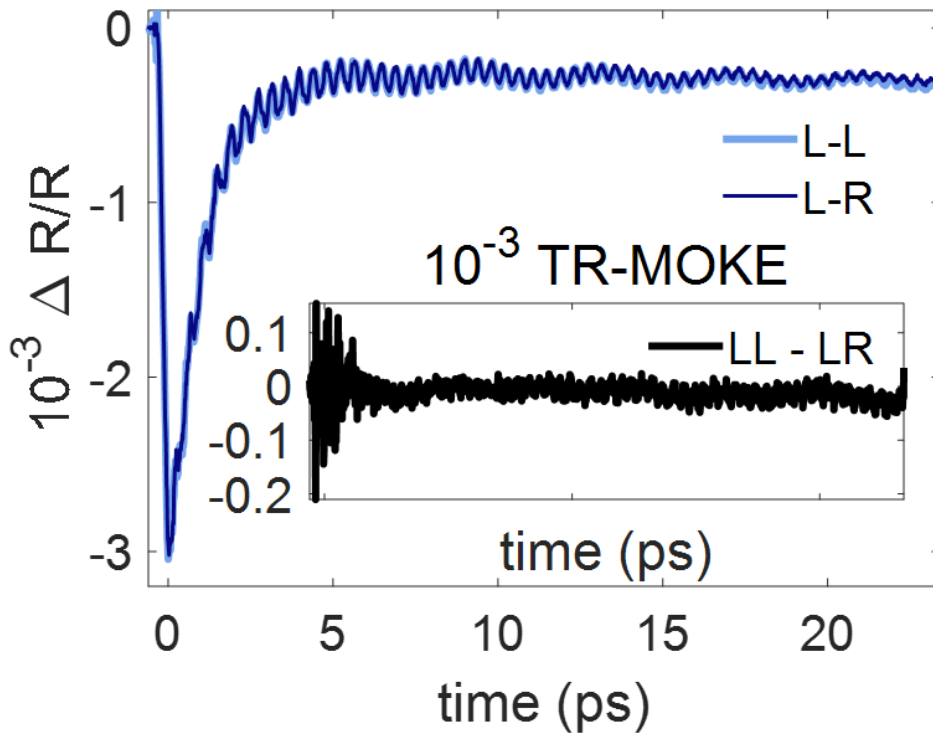
Figure V.7 – Time-resolved reflectivity measurements for circularly polarized pump and probe. The inset illustrates the TR-MOKE signal calculated by subtracting the L-L and L-R polarization channels.

While Figure V.5 and Figure V.7 demonstrate that the oscillations of the phonon modes depend on the polarization channel, Figure V.8 and Figure V.9 show this dependence quantitatively by demonstrating the polarization dependence of the phonon amplitudes and phases, respectively. In Figure V.8, the frequency spectra of the oscillations are shown for all 12 polarization channels. We observe a strong anisotropy in the coherently excited phonons apparent

through the polarization dependence of the amplitudes of the oscillations in the linear polarization channels. This can be seen by comparing the 2.4 THz and the 3.9 THz modes, where we see that the 2.4 THz mode is preferentially sampled with vertically polarized probe while the 3.9 THz mode is preferentially sampled with horizontally polarized probe. In addition, we see that the A-A, A-B, B-A, and B-B channels sample all of the phonon modes accessible in channels with H and V polarized light, but at an intermediate strength. In Figure V.9, the oscillations of the two strongest phonons at 0.25 THz and 2.4 THz are highlighted. We observe that the 0.25 THz mode oscillates sinusoidally and has a phase of π between H and V polarized probe while the 2.4 THz mode oscillates cosinusoidally in all linear polarization channels.
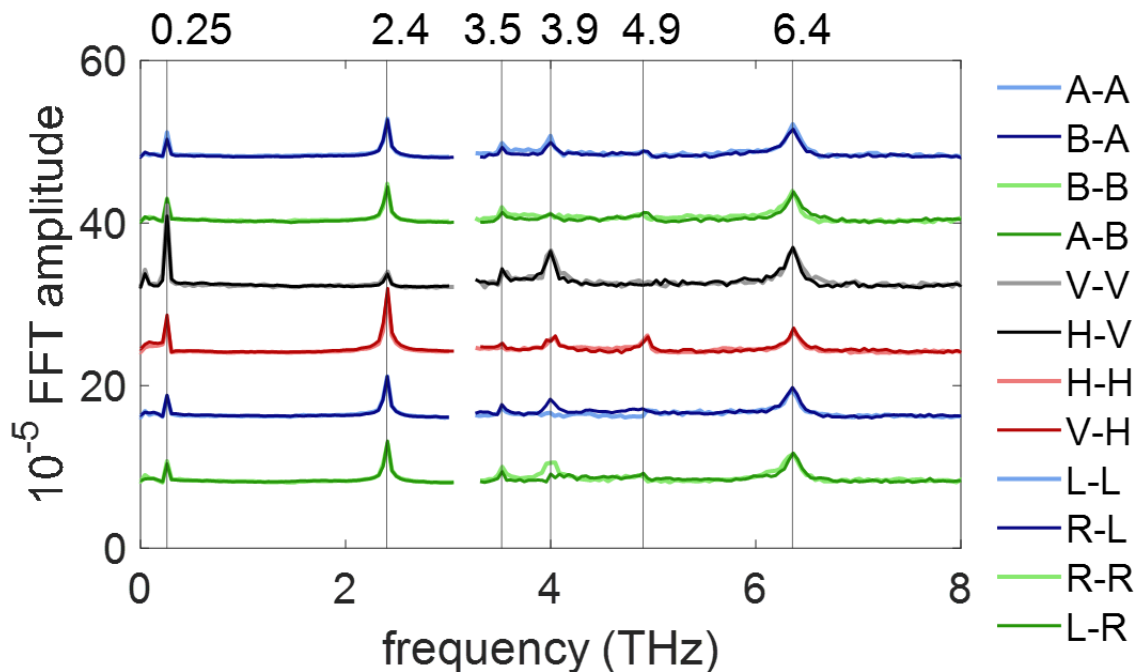
Figure V.8 – The FFT of the raw phonon oscillations for various linear and circular polarization channels, with the spectrum above 3 THz enhanced by a factor of five for clarity. There is a clear dependence of the strength of the observed phonons on the probe polarization.

Determining the polarization dependence of the phase of the oscillations allows us to identify the excitation mechanism of the coherent phonons. The origin of excitations of coherent phonons is typically assigned to either DECP or ISRS. In DECP, the coherent excitation is driven by the perturbations of the electronic distribution by the pump beam and is thus dictated by the potential landscape of the phonons (ie. the band structure) [142]. ISRS, in contrast, is a nonlinear optical effect which makes use of the fact that the pulse spectrum of the pump beam is finite rather than a delta-function. In ISRS, excitations occur at frequencies accessible through difference frequency generation of that pulse spectrum [143]. Important differences exist between the phonons excited by these two mechanisms. For example, in DECP, only fully-symmetric A_1 Raman modes can be excited, and they must have a $\cos(\omega t)$ dependence. In ISRS, in contrast,

modes of any symmetry can be excited but those oscillations will only a $\cos(\omega t)$ dependence when the incoming light is at resonance excitations.

To extract the initial phase of the phonon mode oscillations, we first subtract out the decay dynamics and then fit the remaining oscillatory response to a sum of exponentially decaying sine curves (one for each observed frequency in the FFT). When this fit is performed, we find that the extracted phase of the 2.4 THz mode is 4.524 ± 0.13 rad or $260° \approx 1.45\pi$ rad for the H-H channel and 4.880 ± 0.025 rad or $280° \approx 1.55\pi$ rad for the H-V channel. That is, the 2.4 THz mode obeys a cosine-like oscillation in time (within $10°$). Because our pump laser is at least two orders of magnitude removed from the band edge according to DFT calculations and optical conductivity measurements [133, 136], we can identify its origin as DECP. The oscillations of the higher-frequency phonons are too weak to be directly visualized as in Figure V.9, and fitting them to exponentially decaying sinusoidal functions leads to large uncertainties. However, previous studies have already assigned these higher-frequency phonons to DECP [144, 145].

The identification of the mechanism behind the 0.25 THz mode is slightly more complicated. The phases extracted from the fits for this mode are 5.338 ± 0.05 rad or $305° \approx 1.67\pi$ rad for the H-H channel and 2.373 ± 0.189 rad or $136° \approx 0.76\pi$ rad for the H-V channel. This implies that the oscillations of this phonon mode have a phase which places them almost exactly in-between pure sine and pure cosine behavior. Previous calculations have been performed which indicate that ISRS and DECP are actually two manifestations of the same basic effect, where the dominant part of the dielectric constant of the material dictates the origin of the oscillations [146]. In particular, if the imaginary component of the dielectric constant dominates, then DECP is the main mechanism of generation, and vise versa. We also consider previous experiments which have observed a similar phase difference in the oscillations of phonon modes depending on the

probe polarization. These experiments, largely performed on GaAs, also have a starting phase in-between a pure sine and pure cosine, and still assign the mechanism of generation to ISRS [147-149]. Indeed, a review of literature suggests that DECP is typically assigned when the oscillations are at most ~20° removed from a pure cosine dependence [150]. Thus, despite of the difference in phase from a pure sine oscillation, we believe that the proximity of the phase to a pure sine oscillation taken together with the observation of the surface field effects is sufficient to associate the 0.25 THz mode with ISRS excitations in T_d-WTe$_2$.
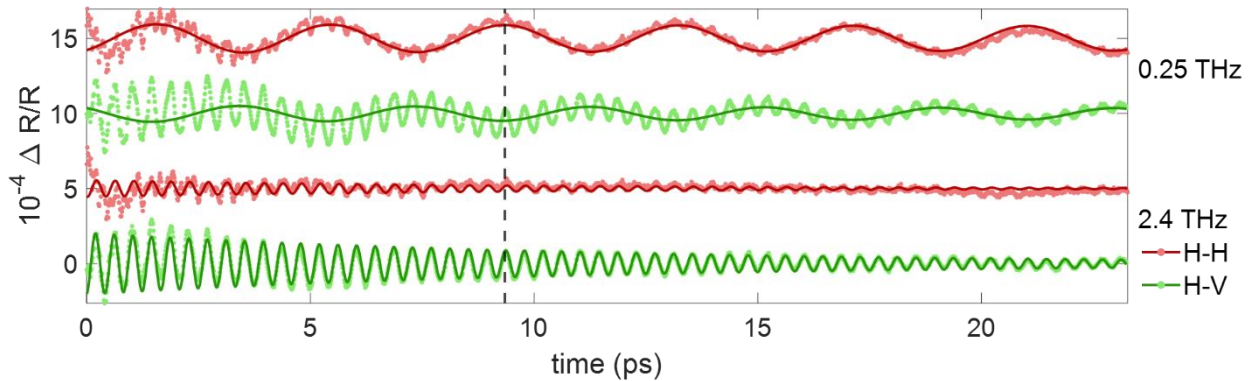
Figure V.9 – An illustration of the oscillations at 0.25 THz and 2.4 THz for the H-H and H-V channels in T_d-WTe$_2$. Using the dashed line as a guide, a phase difference of π between these two channels can be observed for 0.25 THz which is not present in the oscillations at 2.4 THz. This is indicative of the linear electro-optical effect.

Importantly, the determination of the location of time-zero is vital to the identification of the initial phase of the oscillations of the optical phonons and thus to our assignment of the excitation mechanism. Yet this determination can be incredibly challenging. In particular, it is often best accomplished by mirroring the pump-probe spectrum about time-zero by switching the roles of the pump and probe to take a backwards time trace [150, 151]. Here, we assign time-zero to be the minimum location of the dip in the time dynamics. Although this is not optimal from a

theoretical point of view, practically it can be justified with our very small autocorrelation time (~44 fs). The autocorrelation measurement is shown against the time dynamics of the L-L polarization channel in Figure V.10. The autocorrelation for this experiment is found by spatially overlapping the pump and probe beams inside a BBO crystal and then measuring the transmitted SHG power as we scan through the temporal overlap location. Because the experimental settings (ND filtering requiring different amounts of glass in the pump and probe beams) are different between the actual experiment and the autocorrelation measurement, and because the location of time-zero determined in the autocorrelation measurement is heavily reliant on the thickness and tilt of the BBO crystal, we cannot use the precise location of time-zero found in the autocorrelation measurement as the location for the T_d-WTe_2 measurements. However, the size of the autocorrelation is consistent across measurements. If we pessimistically assume that there is an uncertainty in our determination of time-zero from this autocorrelation equal to half of the autocorrelation time, this will correspond to a phase shift of $\sim 2°$ for the 0.25 THz mode and a phase shift of $\sim 19°$ for the 2.4 THz mode. Another possible uncertainty when determining the initial phase of the oscillations comes from subtracting the fit for the decay dynamics before performing the fit to the oscillations, which can lead to some additional oscillations near time-zero. However, it has been our experience that these are typically lower-frequency remnants with a quick decay time. This means that our method of fitting to several periods of oscillation mostly eliminates this problem, with any effect being incorporated in the fit to the uncertainty of the phase.
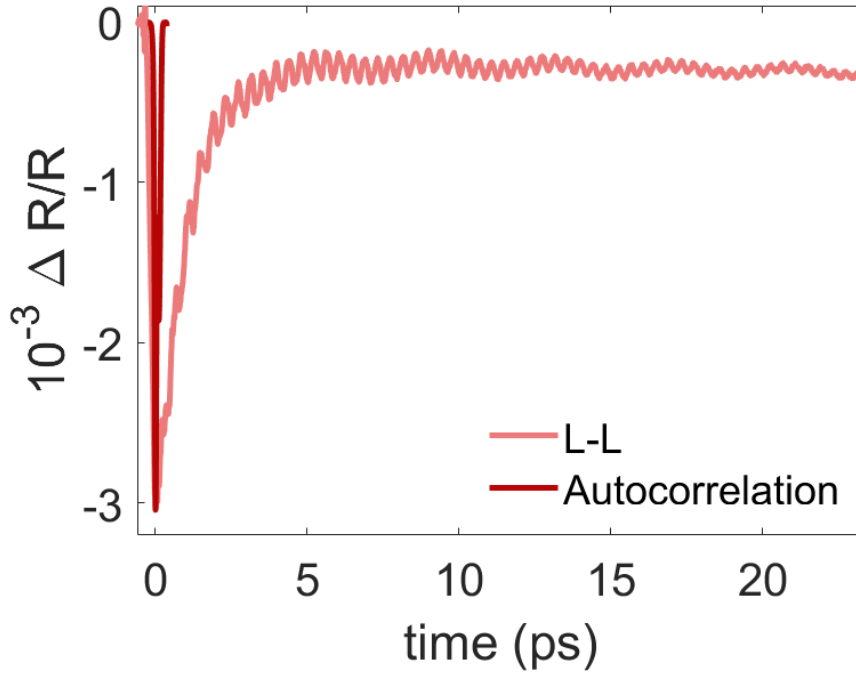
Figure V.10 – A plot of the autocorrelation measurement of the pump-probe setup compared with the time dynamics of the L-L polarization channel.

It is worthwhile at this point to compare the strength of the ISRS excitation to the DECP excitations. The first predictions and observations of DECP suggested that these oscillations are very large, especially compared with ISRS excitations [142, 150]. And indeed, in materials in which both excitation mechanisms are observed simultaneously, the ISRS excitations have been significantly weaker, often to the point of only barely being visible in the FFT spectrum [152]. Theory predictions state that the reason that the DECP response is typically so much stronger than the ISRS response comes from the fact that these two mechanisms are actually two components of the same tensor with different imaginary contributions such that, except when working near an absorption edge or an impurity feature where $|dRe(\epsilon)/d\omega| \ll Im(\epsilon)/\Omega$ does not hold, coherently excited phonons will be displacive in nature [146]. However, DFT calculations on T_d-WTe_2 show that we are not in this special regime and so we would ordinarily expect a stronger DECP response,

which is contrary to what we observe [133]. This raises the possibility that the nonlinear ISRS response is somehow being enhanced by the topological nature of the T_d-WTe$_2$ band structure, but more studies would be needed to prove this conclusively.

There are two subtleties in our identified excitation mechanisms apparent through the polarization dependence of the amplitudes of the excited phonons. First, Figure V.8 illustrates that even though our observed frequencies correspond with A$_1$ modes, they do not all have the same polarization dependence. This is because the strength of the excitation of a mode is proportional to the coupling of the probe polarization and the A$_1$ Raman tensor for C_{2v}, which is

$$A_1 = \begin{pmatrix} a & 0 & 0 \\ 0 & b & 0 \\ 0 & 0 & c \end{pmatrix}.$$ V.5

This means that it is possible for opposite probe-polarization dependencies to result from two A$_1$ modes depending on the strength of the a and b elements for each mode [140, 153]. Second, ISRS typically results in excitations with distinct pump polarization dependencies, which is not apparent in our measurements. To understand this, we can analyze the pump polarizations in the frame of their behavior under C_{2v} group operations.

It is well-known that the polarization induced in the material by ISRS obeys [153]

$$P_{NL} \propto E_{pump}E_{pump}^*E_{probe}.$$ V.6

We can thus form symmetry arguments surrounding our measured polarization dependencies of the coherently excited phonons in our data by deconstructing the polarizations of the pump and probe beams into symmetries of the crystalline point group. The C_{2v} point group of T_d-WTe$_2$ is given in Table V.1. Because the polarizations of the linearly polarized pump and probe beams are aligned with the crystal axes of the sample, we can directly associate horizontally polarized light with B_1 and vertically polarized light with B_2.

C_{2v}	E	C_2	σ_{ac}	σ_{bc}
A_1	1	1	1	1
A_2	1	1	-1	-1
B_1	1	-1	1	-1
B_2	1	-1	-1	1

Table V.1 – The character table for the C_{2v} point group.

The product table for C_{2v} is given in Table V.2. From Equation V.6 above, we know that P_{NL} is proportional to two copies of the pump beam. In either case of linearly polarized light, this will yield an A_1 phonon excitation because $B_1 \times B_1 = A_1$ and $B_2 \times B_2 = A_1$.

$\times$	A_1	A_2	B_1	B_2
A_1	A_1	A_2	B_1	B_2
A_2	A_2	A_1	B_2	B_1
B_1	B_1	B_2	A_1	A_2
B_2	B_2	B_1	A_2	A_1

Table V.2 – The product table for the C_{2v} point group.

Analyzing the phase of the 0.25 THz mode reveals the appearance of the linear electro-optical effect in addition to helping to pin down the excitation mechanism. This effect, also known as the Pockels effect, is apparent through a phase shift between the H and V probe channels as shown in Figure V.9. This phase shift was first reported in time-resolved optical reflectivity measurements on GaAs [147]. From a symmetry perspective, because C_{2v} is an anisotropic point group, the pump will cause inequivalent changes to the indices of refraction along the a- and b-crystal axes which are then sampled by the probe. The fact that this effect is apparent through the 0.25 THz mode can be understood intuitively by recognizing that this mode is a shear mode. In particular, from Figure V.1, it is clear that the unit cell of T_d-WTe$_2$ encompasses two of the van der Waals stacked layers rotated 180° from one another. This 0.25 THz shear mode will cause

intra-layer motion between these two layers of the unit cell. Previous experiments have used THz pumps to excite this mode and use it to drive a transition from the T_d phase to the 1T' phase in WTe$_2$ because the deformations it causes can be so extreme that it serves to establish a pure mirror symmetry in the bc-plane as opposed to the glide mirror present in the T_d phase [90, 144].

Our understanding of the Pockels effect in this material is that the 0.25 THz shear mode will only cause deformations of the crystal along the b-axis, and thus will cause changes in the index of refraction only along this axis. This also explains why we only see a phase difference through the 0.25 THz mode and not through the 2.4 THz mode – the anisotropic changes to the index of refraction must necessarily also occur at the frequency of the shear displacement. Of course, any change to the index of refraction must also be apparent through the overall value of $\Delta R/R$. Indeed, looking at Figure V.5, we see that there is a difference in the maximum dip of the H-H and H-V channels. In particular, the difference in the dips of these channels is 0.762×10^{-3}, which is comparable to the maximum difference in the oscillations between these two channels ($\sim 0.592 \times 10^{-3}$). We would not, however, expect the overall sign of $\Delta R/R$ to change because the total change in reflectivity is caused by both the coherent excitation of the phonons and the incoherent population of electron carriers. At time-zero, the incoherent part, which will not be affected by the birefringence caused by the coherent excitations, will dominate.

We can also explicitly calculate this effect following [92]. The electro-optical tensor r_{ik} for the C_{2v} point group has five independent elements: $r_{13}, r_{23}, r_{33}, r_{42}, r_{51}$. The index ellipsoid can then be written as

$$\left(\frac{1}{n_x^2} + r_{13}E_z\right)x^2 + \left(\frac{1}{n_y^2} + r_{23}E_z\right)y^2 + \left(\frac{1}{n_z^2} + r_{33}E_z\right)z^2 + 2yzr_{42}E_y \qquad \text{V.7}$$
$$+ 2zxr_{51}E_x = 1$$

where n_x, n_y, n_z are the indices of refraction of T$_d$-WTe$_2$ along the principal axes and E_i is the ith component of the surface field. For a horizontally polarized field, this can be simplified to

$$\frac{x^2}{n_x^2} + \frac{y^2}{n_y^2} + \frac{z^2}{n_z^2} + 2zxr_{51}E_x = 1. \tag{V.8}$$

This equation can be diagonalized by a change of basis from $(x, y, z) \rightarrow (x', y, z')$ defined by

$$x = x' \cos\theta - z' \sin\theta \tag{V.9}$$

where

$$\tan 2\theta = \frac{2E_x r_{51}}{\frac{1}{n_x^2} - \frac{1}{n_z^2}}. \tag{V.10}$$

This yields a transformed equation for the index ellipsoid of

$$\left(\frac{1}{n_x^2} + E_x r_{51} \tan\theta\right) x'^2 + \frac{y^2}{n_y^2} + \left(\frac{1}{n_z^2} - E_x r_{51} \tan\theta\right) z'^2 = 1. \tag{V.11}$$

Given that we can define the change in the index of refraction as $dn = -\frac{1}{2}n^3 d\left(\frac{1}{n^2}\right)$, we can define new indices of refraction of

$$n_x' = n_x - \frac{1}{2}n_x^3 E_x r_{51} \tan\theta$$

$$n_y' = n_y \tag{V.12}$$

Because the change in reflectivity $\Delta R \propto \Delta n$, we can see that a horizontal probe will lead to a phase shift in the oscillatory data compared to a vertical probe.

The physical origin of the surface field is worthy of note here. Similar observations of such an effect in GaAs have assigned the field to a surface charge-screening field occurring due to pinning of the Fermi surface at the material-vacuum interface [147-149]. Indeed, such surface field effects have also been reported in Bi$_2$Se$_3$, another van der Waals layered material with a Dirac

semimetal band structure [74]. Therefore, it is not unreasonable to assume such an effect is also occurring here.

Fluence-Dependent Measurements

To further motivate the nonlinear ISRS excitation of the 0.25 THz shear mode in T_d-WTe_2, and to try to understand the strong oscillations of this excitation mechanism compared to other DECP excitations observed, we investigated the pump fluence dependence of the phonon amplitudes, which are shown in Figure V.11. We expect this dependence to be linear because ISRS is reliant on the mixing of two copies of the electric field of the pump at frequencies ω and $\omega + \Omega$ to excite a phonon of frequency Ω. Indeed, we find that the phonon amplitude is linearly dependent on this pump fluence. The amplitudes of the two strongest DECP excitations at 2.4 THz and 6.4 THz are also shown in Figure V.11 to scale linearly with the pump fluence. In the case of DECP, this pump fluence dependence is due to the fact that there is a larger number of excited carriers at higher fluences. That is, the dependence is not indicative of a nonlinear optical process. Interestingly, it seems there is a divergence from the otherwise linear dependence of all three modes after 200 µJ/cm². In similar measurements on $MoTe_2$, such a divergence was indicative of a light-induced change in the lattice symmetry [89]. It is also very possible that the divergence seen here is due to the probe fluence at the lower pump fluence points being larger than that of the pump.
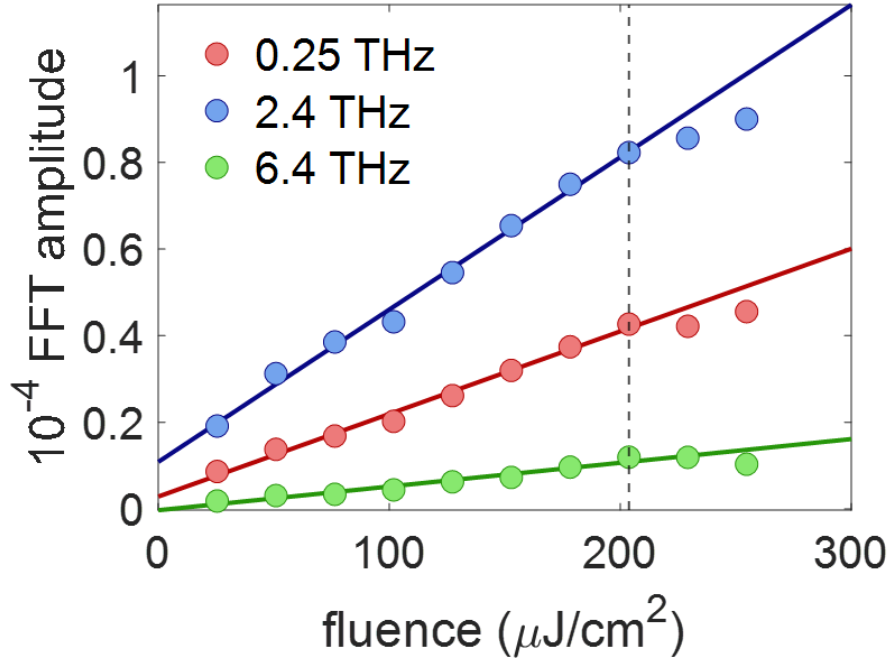
Figure V.11 – Fluence dependence of the FFT amplitudes of the three strongest coherently excited phonons in T_d-WTe2, indicating that all measurements were taken in the linear regime. The solid lines guide the eye for a linear fit to the data. A kink in this linear behavior can be seen for all three oscillations after 200 µJ/cm^2, indicated by the dashed line.

To learn more about the mechanism behind the large ISRS excitation of the 0.25 THz mode, we also investigated the electron-phonon thermalization time, as shown in Figure V.12. We can use this information to extract the electron-phonon coupling constant. This time constant has previously been analyzed for increasing lattice temperature [141]. We performed a two-temperature model (TTM) fit [154-156] assuming a purely thermal effect and using material parameters derived using DFT calculations [133]. In this TTM, we take the electron-phonon thermalization time to be

$$\tau_{e-ph} = \frac{\gamma(T_e^2 - T_l^2)}{2H(T_e, T_l)},$$ V.13

where T_e is the electron temperature, T_l is the lattice temperature, γ is the electron specific heat coefficient, which is used as a heating parameter, and $H(T_e, T_l)$ is a function of T_e and T_l given by

$$H(T_e, T_l) = f(T_e) - f(T_l) \qquad \text{V.14}$$

for

$$f(T) = 4g_\infty \frac{T^5}{\Theta_D^4} \int_0^{\frac{\Theta_D}{T}} \frac{x^4}{e^x - 1} dx \qquad \text{V.15}$$

for Θ_D the Debye temperature, taken to be 133.8 K [141] and g_∞ the electron-phonon coupling constant, the second fitting parameter used in the model. T_e is computed using the lattice temperature and the deposited laser energy density U_l as

$$T_e = \left(T_l^2 + \frac{2U_l}{\gamma} \right)^{1/2}. \qquad \text{V.16}$$

In addition, an adjustment to T_l is made to account for heating by the laser. In particular, we take

$$T_l' = \left(\frac{E_{laser}}{C} + T_l^4 \right)^{1/4} \qquad \text{V.17}$$

for E_{laser} the energy deposited in the material per pulse, C a constant equal to 1.658×10^{-16}, and T_l taken initially to be room temperature [157]. The extracted material parameters using this method are $\gamma \approx 10.2$ mJ mol^{-1}K^{-2} and $g_\infty = 6.79 \times 10^{15}$ Wm^{-3}K^{-1}.
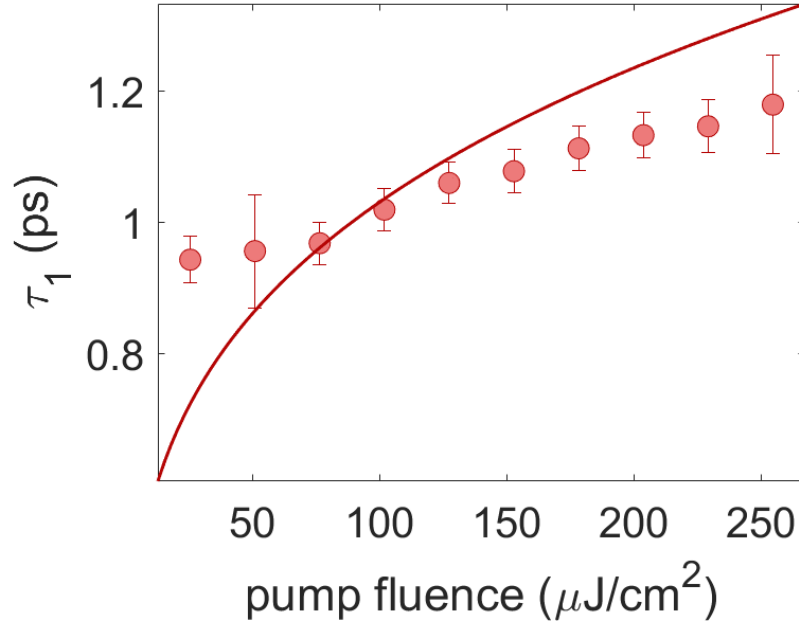
Figure V.12 – The fluence dependence of time constant τ_1 dictating the electron-phonon thermalization time with a TTM fit in T_d-WTe$_2$.

While the TTM fit matches the monotonic trend of the measured fluence dependence, it did not provide an adequate fit to the data, in contrast with previous experiments [141]. This may be because the fluence used here is two orders of magnitude larger than that used in previous measurements and the TTM assumption of a purely thermal response between the lattice and excited electrons breaks down as we move away from the perturbative regime. This is especially because the 720 nm pump excites well above the Fermi energy. Because our fluence-dependent measurements of the FFT amplitude of the phonon modes indicate that we are in the linear regime [142, 158], and because we are well below the previously reported damaged threshold [79], there may be an additional mechanism involved in reaching equilibrium between the electrons and phonons after excitation. One such possibility is interactions between the phonons and Weyl fermion excitations, which has previously been reported in TaAs [159]. Indeed, our FFT spectra

show evidence of a Fano lineshape for the 0.25 THz mode, shown in Figure V.13. This asymmetric

lineshape is typically used as evidence of coupling between the excited phonon mode and a

continuous spectrum of additional particles [159-161].
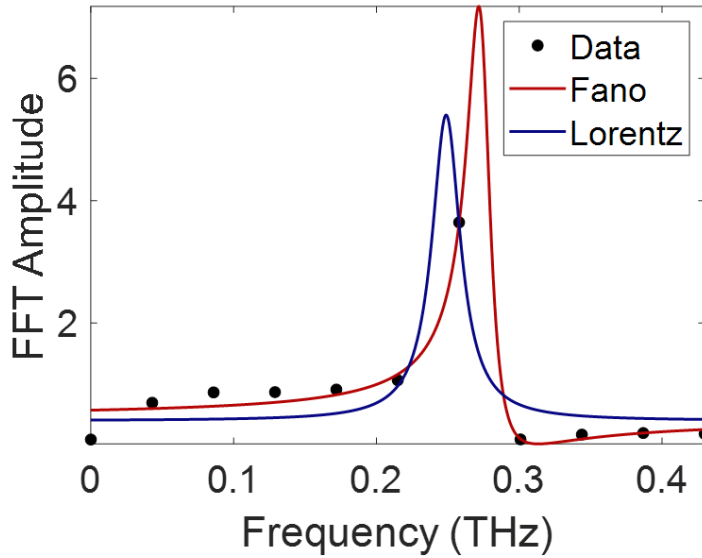
Figure V.13 – Illustration of the asymmetry of the lineshape of the 0.25 THz mode for the L-L channel in T_d-WTe$_2$. Pictured here is the raw data (black circles) together with a fit using a Lorentzian lineshape (blue) and a Fano lineshape (red).

Second Harmonic Response of T_d-MoTe$_2$

In addition to the SHG measurements performed on bulk T_d-WTe$_2$, we have also performed

RA-SHG and scanning SHG measurements on few-layer MoTe$_2$ as part of a collaboration with

Adam Tsen's group at the University of Waterloo. In particular, the Waterloo group was

performing nonlinear anomalous Hall effect (NLAHE) measurements on devices they had created

using a combination of gold and few-layer graphene leads on hexagonal boron nitride (hBN)-

encapsulated MoTe$_2$. An illustration of the device schematic is provided in Figure V.14. They

found an exceptionally large NLAHE effect in these devices, larger than any previous

measurements on other materials. In their paper, which has recently been accepted at Nature Communications, they attributed this large effect to scattering processes at both high and low temperatures. We were tasked with identifying through RA-SHG measurements the crystal axes of the flakes to ensure that their measurements made sense from a symmetry perspective.
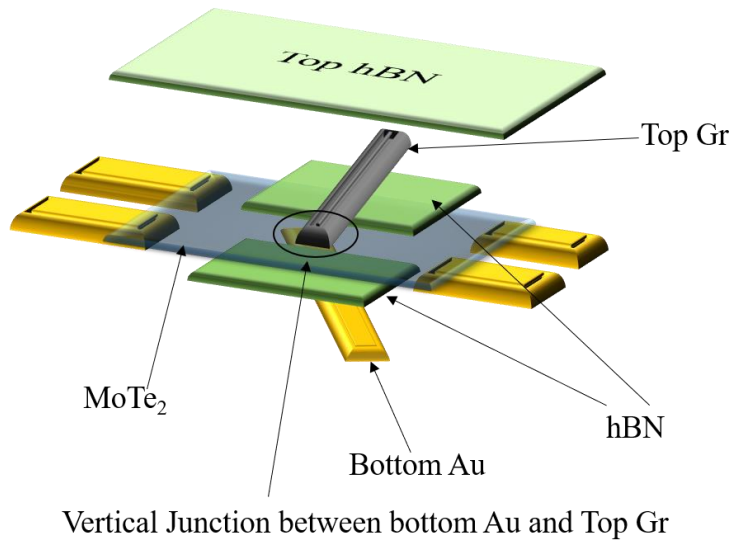
Figure V.14 – An illustration of the basic device schematic used the nonlinear Hall measurements performed by Adam Tsen's group at the University of Waterloo, provided by Archana Tiwari. Gold leads are placed around and below the thin MoTe$_2$ flake, and a top lead of graphene is used to collect vertical Hall measurements. The whole device is encapsulated in hBN.

In particular, we tested three devices, pictured in Figure V.15. Device 1 is a thin device, with an MoTe$_2$ thickness of ~28 nm. Device 2 is of intermediate thickness, with an MoTe$_2$ thickness of ~50 nm, and Device 3 is particularly thick, with an MoTe$_2$ thickness of ~127 nm. This difference in thicknesses has the potential to affect the observable symmetries of the material. In particular, previous reports have indicated a phase transition in this material below ~12 nm, where the crystal structure assumes the T$_d$ phase. This was modeled using the m point group, rather than

the 1T' phase even at room temperature as the thickness of the sample decreases below the critical thickness [127]. Another report suggests that, for thinner samples, the point symmetry depends on the number of layers, alternating between the bulk 1T' phase and the m point group for odd and even numbers of layers, respectively [162]. Thus, in addition to identifying the mirror plane of the MoTe$_2$ devices, it is interesting to look at the SHG response above and below the T$_d$ to 1T' phase transition to see how it evolves, if at all, with both temperature and sample thickness.
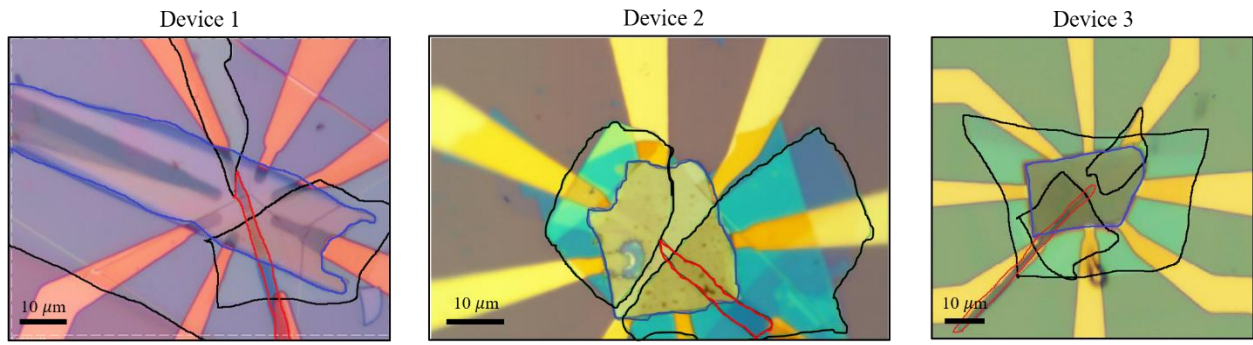
Figure V.15 – Microscope images of the three MoTe$_2$ devices studied, provided by Archana Tiwari. Throughout, the MoTe$_2$ is outlined in blue, the hBN in black, and the graphene in red. Scale bars are included in the lower left corner of each image for reference.

The RA-SHG measurements taken on each of the three devices below the critical temperature is shown in Figure V.16, together with the fit to the data. These RA-SHG scans were taken using the scanning SHG setup, and so all data is collected in the normal incidence geometry. As with the RA-SHG measurements on T$_d$-WTe$_2$, we find that we must model the MoTe$_2$ as obeying the m point group, regardless of sample thickness. However, from the crossed and parallel data shown in Figure V.16, it appears that the mirror is not consistent across different polarizations. This inconsistency is fixed by considering as well the SHG contribution from the thin hBN which encapsulates the MoTe$_2$ devices. hBN belongs to point group D_{3h} [163], which consists of a C_3

axis along the c-axis, three C_2 axes in the ab-plane, three mirrors normal to the ab-plane aligned with the C_2 axes, a mirror in the ab-plane, and an S_3 axis along the c-axis. Applying these symmetries yields a χ^{ED} tensor for hBN with four nonzero elements, of which one is independent. They are

$$\chi_{xxy}^{ED} = \chi_{xyx}^{ED} = \chi_{yxx}^{ED} = -\chi_{yyy}^{ED}. \qquad \text{V.18}$$
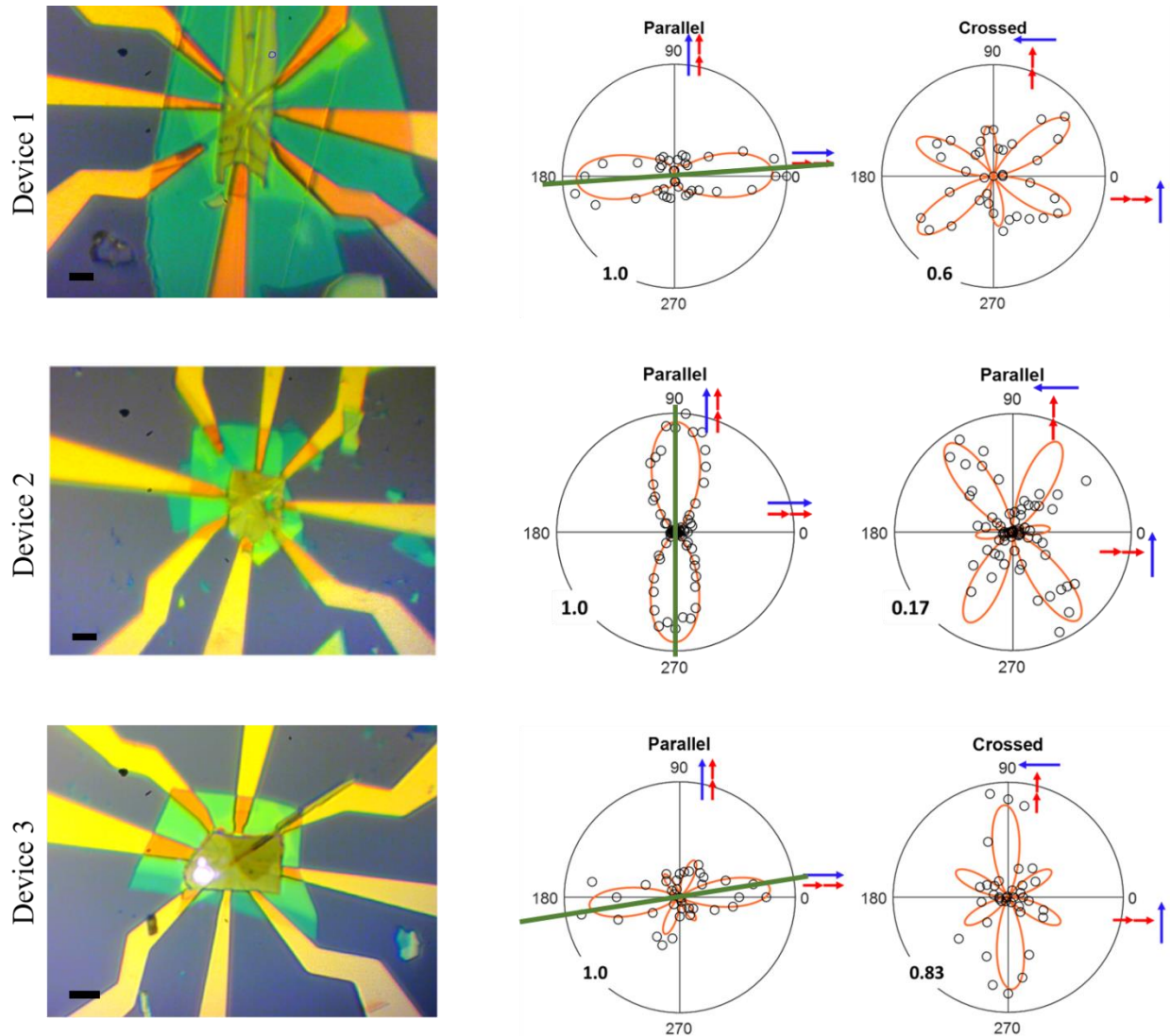
Figure V.16 – A summary of the RA-SHG measurements taken at normal incidence at 80 K in both the crossed and parallel channels for each of the three MoTe₂ NLAHE devices, together with white light imaging pictures taken on the scanning setup during the data collection procedure. In the optical images, 10 μm scale bars are shown in black in the lower left corner. In the RA-SHG

polar plots, the raw data are displayed as open circles and the fit derived using the form of Equation V.19 is shown as a solid orange curve. The mirror plane for MoTe$_2$ extracted using the fit (ie. the extracted value of α) is shown in green on each of the parallel RA-SHG flower patterns. Also shown is the orientation of the polarizations of both the incoming fundamental (red arrows) and reflected SHG (blue arrows) light at both 0° and 90° on the RA-SHG polar plots. The devices are labeled to the left of the row. The RA-SHG polar plots for Device 1 are normalized to 359 fW, for Device 2 to 108 fW, and for Device 3 to 54 fW.

In this case, we expect the SHG fields of both the MoTe$_2$ and the hBN to sum in order to yield a total SHG intensity at the detector location. That is, if we define $P_i = \chi_{ijk}^{ED} E_j E_k$ for each material, we will have $P_{i,tot} = P_{i,MoTe_2} + e^{-i\gamma} P_{i,hBN}$ for some complex phase γ, which is used as a fitting parameter. Doing this, we find fits to the data of

$$I_{parallel}^{2\omega}(\phi) = \left(3\chi_{yxx}^{ED}\cos^2(\alpha - \phi)\sin(\alpha - \phi) + \chi_{yyy}^{ED}\sin^3(\alpha - \phi)\right)^2$$

$$- 2\chi_{hBN}^{ED}\cos(\gamma)\sin(\alpha - \phi)\left(3\chi_{yxx}^{ED}\cos^2(\alpha - \phi)\right.$$

$$+ \chi_{yyy}^{ED}\sin^2(\alpha - \phi)\left.\right)\sin(3(\delta - \phi)) + \chi_{hBN}^{ED}{}^2\sin^2(3(\delta - \phi))$$

$$I_{crossed}^{2\omega}(\phi) = \frac{1}{4}\left(\cos^2(\alpha - \phi)\left(\chi_{yxx}^{ED} - \chi_{yyy}^{ED}\right.\right.$$

$$+ \left(\chi_{yyy}^{ED} - 3\chi_{yxx}^{ED}\right)\cos(2(\alpha - \phi))\right)^2$$

$$+ 4\chi_{hBN}^{ED}\cos(\gamma)\cos(\alpha - \phi)\left(\chi_{yxx}^{ED} - \chi_{yyy}^{ED}\right.$$

$$+ \left(\chi_{yyy}^{ED} - 3\chi_{yxx}^{ED}\right)\cos(2(\alpha - \phi))\right)\cos(3(\delta - \phi))$$

$$+ 4\chi_{hBN}^{ED}{}^2\cos^2(3(\delta - \phi))\left.\right)$$

V.19

for γ the complex phase, α the angle between the MoTe$_2$ sample orientation and the plane of the optical table, δ the angle between the hBN sample orientation and the plane of the optical table, and $\chi_{hBN}^{ED} = \chi_{yyy}^{ED}$ of the hBN nonlinear optical susceptibility tensor of Equation V.18. An illustration of this summed field approach to fitting the RA-SHG patterns is shown in Figure V.17 for Device 3. The extracted value of α for each of the devices corresponded to within 10° of the

identification of the *b*-axis of the crystal structure identified by our collaborators using their

NLAHE measurements.
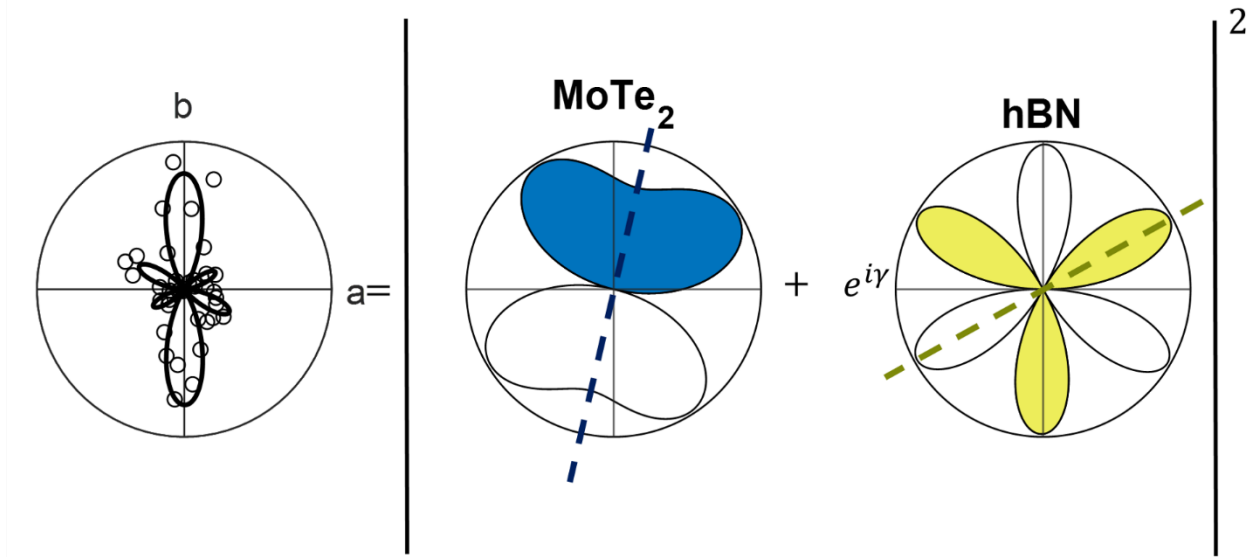
Figure V.17 – An illustration of the incoherent summation of fields used to fit the RA-SHG patterns of Figure V.16 using Equation V.19 for Device 3 at 80 K. The shading indicates the phase of the second harmonic field. The dashed lines indicate the mirrors planes extracted for MoTe$_2$ and hBN using α and δ, respectively. The scaling of the plots is arbitrary.

We can take this analysis a step beyond the requirements of our collaborators by looking

at the evolution of the SHG response in these devices as a function of location and temperature.

We can investigate the SHG response as a function of location on the device by using the scanning

capability of this scanning SHG setup. Scanning SHG images of Devices 1 and 3 are shown in

Figure V.18 at both low temperature and room temperature. From these images, several things are

immediately apparent. The first is the clear enhancement of the SHG signal from both the gold and

graphene leads. RA-SHG patterns taken to survey various locations on the device indicate that the

graphene provides a strong but anisotropic background to the SHG response while the gold seems

to enhance signal from the hBN. Another is that the thinner MoTe$_2$ flakes seem to have the

strongest SHG signal. This is not terribly surprising given the structural transition demonstrated in previous measurements [127, 162]. However, the fact is nicely highlighted particularly in the Device 1 images, where the SHG signal is particularly strong along the edges of the sample where the MoTe$_2$ thickness is presumably smallest.
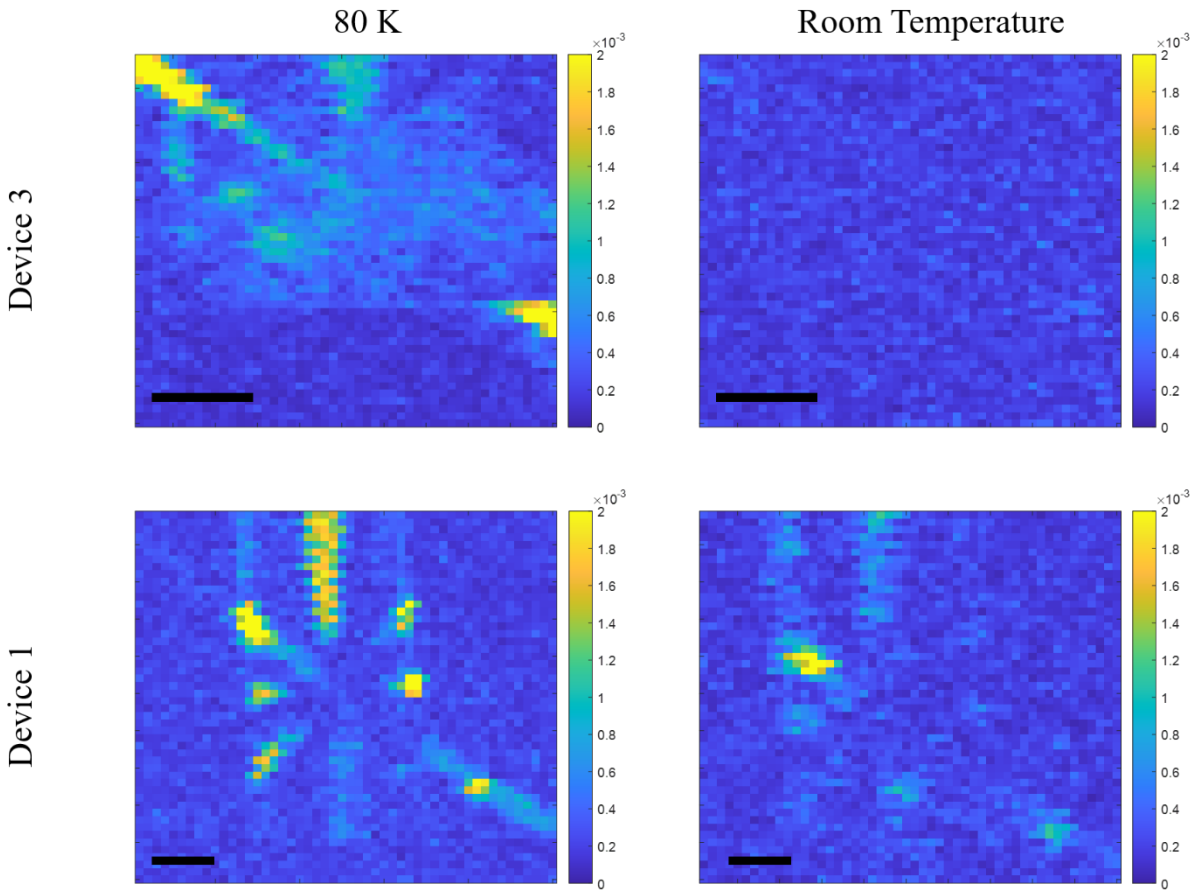
Figure V.18 – Scanning SHG images of Device 3 and Device 1 at both room temperature and 80 K. The color bar for each image is the same and is indicated on the right. The maximum reading of 2×10^{-3} photons/second shown corresponds to 359 fW. A black 10 μm scale bar is included in the lower left corner of each image.

The thickness dependence of the SHG response can be quantified by looking at the extracted sizes of the susceptibility tensor elements obtained using the fit from Equation V.19. The

method of adjusting the lock-in reading to something physically corresponding to the second harmonic field using the PMT of the scanning setup is similar to the procedure outlined in Chapter III for the Andor camera. However, we must now account for the drop in signal upon reflection through the objective (~60%) and the gain used to amplify the signal ($5 \times 10^4 \Omega$ for the measurements on Devices 1 and 3 and $5 \times 10^5 \Omega$ for the measurements on Device 2). A plot illustrating the dependence of the χ_{hBN}^{ED}, χ_{yyy}^{ED}, and χ_{yxx}^{ED} tensor elements on the device thickness is shown in Figure V.19. Overall, we can see that these MoTe$_2$ devices generally have a smaller SHG response than the bulk WTe$_2$ explored earlier in this chapter. We also see that there seems to be a dip in the SHG response going from the thin to bulk-like samples. This corresponds to the decrease in SHG response observed through the scanning images in Figure V.18.
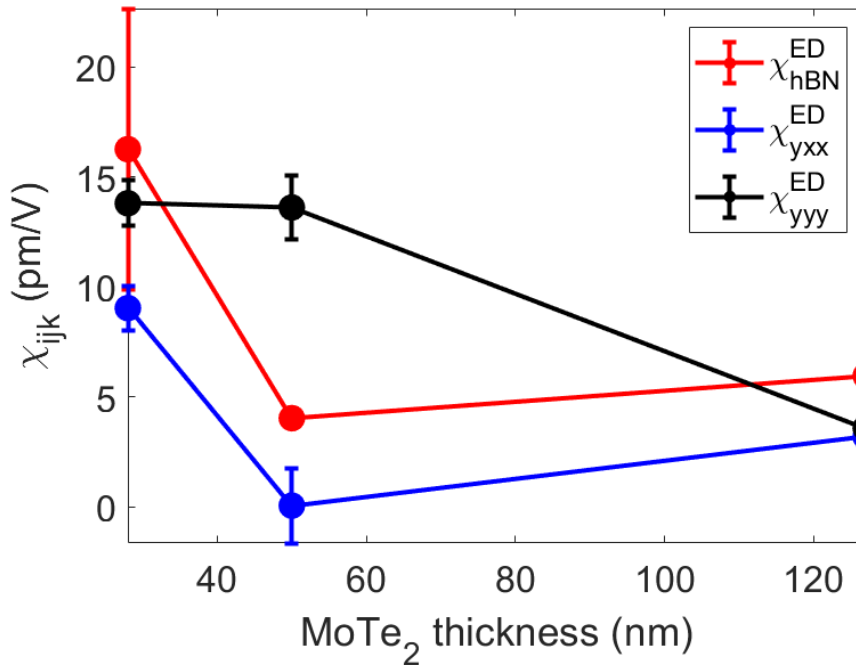
Figure V.19 – A plot of the extracted susceptibility tensor elements using the parallel channel as a function of device thickness at 80 K. Error bars corresponding to uncertainties in the fits are included.

CHAPTER VI

Nonlinear Optical Measurements on a Chiral Weyl Semimetal

To this point, we have provided background information on WSMs and nonlinear optics, using previous literature on type-I WSMs as examples to guide the discussion, and we have presented nonlinear optical studies on two type-II WSMs to try to compare and contrast results between these two species. We now turn our attention to an even more exotic WSM, known as a chiral WSM. In general, a chiral structure is a structure, like DNA, which, when mirrored, cannot be superposed back onto itself [24, 164]. Chiral WSMs are similarly defined by an absence of mirror planes in their crystal structures, which allows for the WPs in these materials to occur at different energies in the band structure. This contrasts with other examples we have seen of WSMs so far, where the mirrors restrict the paired WPs of opposite chirality to occur at the same energy in the band structure. Further, the symmetry of these materials allows for higher-order WPs. That is, WPs with Chern numbers whose absolute value is greater than one, also known as multifold Weyl fermions [165]. Like the tilted Weyl fermions of type-II WSMs, which break Lorentz invariance, these multifold fermions do not have an analogue in high energy physics [166-168].

In this chapter, we will present two nonlinear optical studies on the chiral WSM CoSi. The first is an analysis of the RA-SHG response of this material on different crystal facets and different spot locations. We will use this information, together with ellipsometry data taken by Rachel Owen, to identify the size of the SHG response of this material. We find that it is highly facet-dependent, both in anisotropy and in SHG strength. We also will present photocurrent studies in

which we look for CPGE and LPGE signals on devices built from bulk CoSi samples. We find that we do see that expected two-fold and four-fold angular dependence in our data, corresponding to CPGE and LPGE, respectively, but that the pad and lead placement can give a significant contribution to the observed signal.

We note here the contributions by various lab members to this experiment. Our CoSi samples were provided by Hechang Lei, Chenghe Li, and Shangjie Tian. Sample preparation and gold pad deposition were performed by Rachel Owen. Lu Chen, Ziji Xiang, and Kuan-Wen Chen from Lu Li's group have all helped with wiring the samples to the chip carriers. This project was completed in collaboration with Lu Li and Steve Cundiff. In particular, Steve's group members Matthew Day, Ruixue Zhang, Yiming Gong, Grace Kerber, and Kelsey Bates, as well as visiting researcher Dong Sun, have provided invaluable discussions and experimental collaboration as they have worked to build a similar experiment and perform similar measurements in their lab.

CoSi Crystal and Band Structure

As mentioned above, the particular chiral WSM we will be focused on for these studies is CoSi. CoSi belongs to the space group (point group) $P2_13$ (T), which is a cubic point group [60]. The crystal structure of CoSi is shown in Figure VI.1. The T point group consists of four C_3 axes located along each of the (111) axes and three C_2 axes along the a-, b-, and c-axes. Importantly, the T point group lacks mirror symmetries, making it a chiral point group.

| (100) | (110) | (111) |
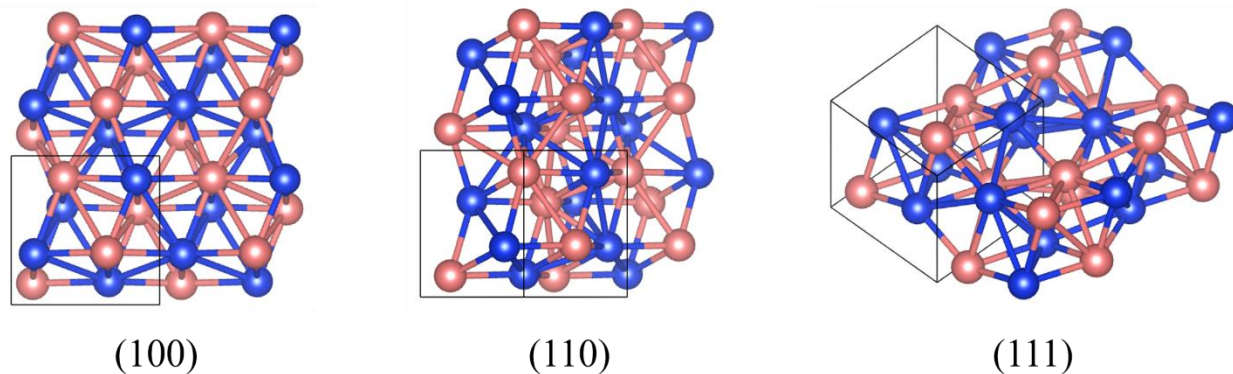
Figure VI.1 – (Top) An illustration of the CoSi crystal structure, drawn using the VESTA software using material information from [169]. Here, the Co are illustrated in pink and the Si in blue. The unit cell is outlined in black. Shown from left to right are the views along the (100), (110), and (111) directions.

The CoSi samples used throughout these studies were prepared according to [24]. Specifically, single CoSi crystals were grown using the chemical vapor transport method. Co and Si powders were placed into a silica tube of length 200 mm with an inner diameter of 14 mm in a 1:1 molar ratio. 200 mg of I_2 was also added as a transport reagent. The tube was then evacuated to a pressure of 10^{-2} Pa and sealed. The tube was then placed into a two-zone horizontal furnace and the temperatures of the source and growth zones were raised over the course of two days to 1173 K and 1273 K, respectively. They were held at these temperatures for seven days. Shiny crystals with lateral dimensions of up to several millimeters were able to be obtained using this method.

RA-SHG Measurements on CoSi

We begin by presenting our results using RA-SHG measurements to survey the CoSi crystals to identify the crystal facet from the observed symmetry of the RA-SHG flower pattern.

125

The T point group results in an electric dipole susceptibility tensor with six nonzero elements, of which one is independent. They are

$$\chi_{xyz}^{ED} = \chi_{xzy}^{ED} = \chi_{yxz}^{ED} = \chi_{yzx}^{ED} = \chi_{zxy}^{ED} = \chi_{zyx}^{ED}.$$ VI.1

We can use the method outlined in Chapter IV to calculate a predicted functional form for the RA-SHG flower pattern obtained for light incident along the c-axis of the crystal (ie. illuminating the [100] crystal face). Doing so, we find

$$
\begin{aligned}
I_{P_{in}-P_{out}}^{2\omega}(\phi) &= 5\chi_{zyx}^{ED}{}^2 \cos^4(\theta)\sin^2(\theta)\sin^2(2\phi) \\
I_{P_{in}-S_{out}}^{2\omega}(\phi) &= 4\chi_{zyx}^{ED}{}^2 \cos^2(\theta)\sin^2(\theta)\cos^2(2\phi) \\
I_{S_{in}-P_{out}}^{2\omega}(\phi) &= \chi_{zyx}^{ED}{}^2 \sin^2(\theta)\sin^2(2\phi) \\
I_{S_{in}-S_{out}}^{2\omega}(\phi) &= 0
\end{aligned}
$$ VI.2

for incident angle θ.

The raw data and fits to that data using Equation VI.2 are shown in Figure VI.2. As expected, there is no clear RA-SHG signal in the oblique $S_{in} - S_{out}$ channel or in either of the two normal incidence channels. There does seem to be some spatial dependence, but that dependence is likely explained by a slight curvature of the sample surface, yielding deviations from a perfectly normal incident beam from one spot to another.
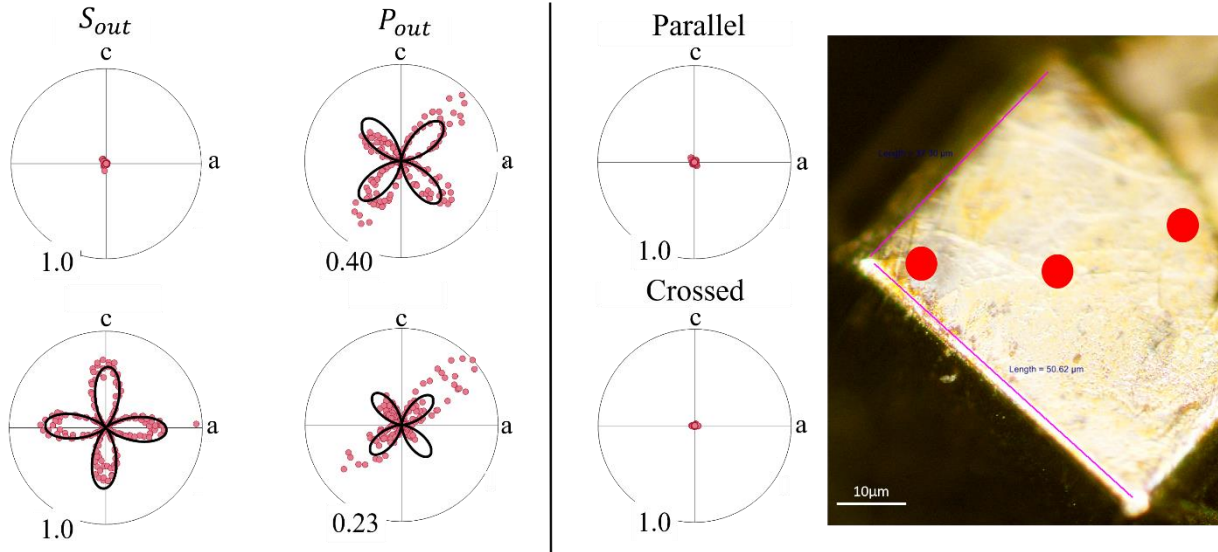
Figure VI.2 – An illustration of the RA-SHG raw data (closed circles) and derived fits using Equation VI.2 for three spots on the (100) crystal face for each of the four oblique incidence polarization channels (left of vertical line) and each of the normal incidence polarization channels (right of vertical line). A microscope image of the facet under investigation, complete with the locations of the four RA-SHG measurements, is shown on the far right. All RA-SHG flower plots are normalized to 15 fW.

We wish to use our RA-SHG method to determine which of the crystal facets we are accessing. To this end, it is necessary to both take RA-SHG measurements on a variety of crystal faces as well as to derive fits similar to those in Equation VI.2 to fit that data. We can do this by rotating the χ^{ED} susceptibility tensor, whose elements are given in Equation VI.1, so that it is oriented along a different axis than the c-axis of the crystal. We must thus begin by deriving the rotation matrix necessary to align the χ^{ED} tensor correctly. Such derivations of rotation matrices are well-known through linear algebra courses, so we will not present in-depth details here because they are not particularly enlightening. However, we will present the results of those derivations. In particular, the rotation matrix to bring the (100) face to the (111) face is given by

$$R_{(100)\rightarrow(111)} = \begin{pmatrix} -\dfrac{1}{\sqrt{2}} & \dfrac{1}{\sqrt{2}} & 0 \\[2mm] -\dfrac{1}{\sqrt{6}} & -\dfrac{1}{\sqrt{6}} & \sqrt{\dfrac{2}{3}} \\[2mm] \dfrac{1}{\sqrt{3}} & \dfrac{1}{\sqrt{3}} & \dfrac{1}{\sqrt{3}} \end{pmatrix}, \qquad \text{VI.3}$$

which yields functional forms for the RA-SHG channels of

$$
\begin{aligned}
I^{2\omega}_{P_{in}-P_{out}}(\phi) &= \frac{1}{3}\chi_{zyx}^{ED\,2}\left(5\cos^4(\theta)\sin^2(\theta) - 4\cos^2(\theta)\sin^4(\theta) + 4\sin^6(\theta)\right. \\
&\quad \left. - 4\sqrt{2}\cos^5(\theta)\sin(\theta)\sin(3\phi) + 2\cos^6(\theta)\sin^2(3\phi)\right) \\
I^{2\omega}_{P_{in}-S_{out}}(\phi) &= \frac{2}{3}\chi_{zyx}^{ED\,2}\cos^4(\theta)\cos^2(3\phi) \\
I^{2\omega}_{S_{in}-P_{out}}(\phi) &= \frac{1}{3}\chi_{zyx}^{ED\,2}\left(\sin^2(\theta) + 2\cos^2(\theta)\sin^2(3\phi)\right) \\
I^{2\omega}_{S_{in}-S_{out}}(\phi) &= \frac{2}{3}\chi_{zyx}^{ED\,2}\cos^2(3\phi)
\end{aligned}
\qquad \text{VI.4}
$$

The RA-SHG raw data and fits for light incident on the (111) face are shown in Figure VI.3.
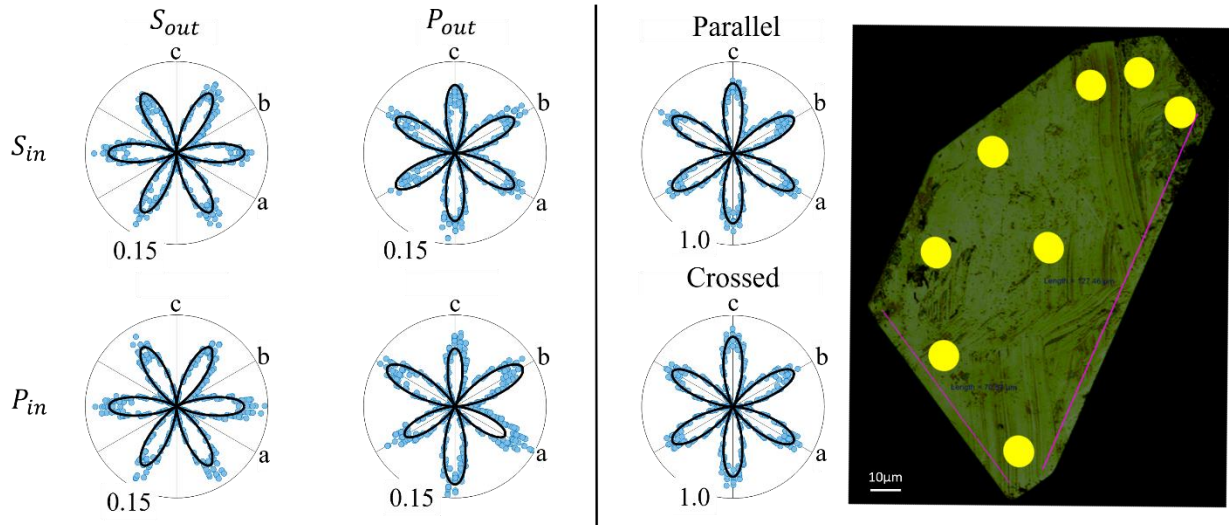
Figure VI.3 – An illustration of the RA-SHG raw data (closed circles) and derived fits using Equation VI.4 for eight spots on the (111) crystal face for each of the four oblique incidence polarization channels (left of vertical line) and each of the normal incidence polarization channels (right of vertical line). A microscope image of the facet under investigation, complete with the

locations of the four RA-SHG measurements, is shown on the far right. All RA-SHG flower plots are normalized to 59 fW.

Similarly, we can derive the rotation matrix to model light incident on the (110) crystal facet. We find

$$R_{(100)\to(111)} = \begin{pmatrix} -\dfrac{1}{\sqrt{2}} & \dfrac{1}{\sqrt{2}} & 0 \\ 0 & 0 & 1 \\ \dfrac{1}{\sqrt{2}} & \dfrac{1}{\sqrt{2}} & 0 \end{pmatrix},$$
VI.5

and

$$
\begin{aligned}
I^{2\omega}_{P_{in}-P_{out}}(\phi) &= \chi_{zyx}^{ED}{}^2 \cos^2(\theta)\left(9\cos^4(\theta)\cos^4(\phi) - 6\cos^2(\theta)\cos^2(\phi)\sin^2(\theta)\right.\\
&\quad \left. + 5\sin^4(\theta)\right)\sin^2(\phi)\\
I^{2\omega}_{P_{in}-S_{out}}(\phi) &= \left(-\frac{1}{4}\chi_{zyx}^{ED}\cos^2(\theta)\left(\cos(\phi)+3\cos(3\phi)\right)\right.\\
&\quad \left. + \chi_{zyx}^{ED}\cos(\phi)\sin^2(\theta)\right)^2\\
I^{2\omega}_{S_{in}-P_{out}}(\phi) &= \frac{1}{4}\chi_{zyx}^{ED}{}^2\cos^2(\theta)\left(1+3\cos(\phi)\right)^2\sin^2(\phi)\\
I^{2\omega}_{S_{in}-S_{out}}(\phi) &= 9\chi_{zyx}^{ED}{}^2\cos^2(\phi)\sin^4(\phi)
\end{aligned}
$$
VI.6

The raw data and fits for the RA-SHG measurements taken on the (110) crystal facet are shown in Figure VI.4.
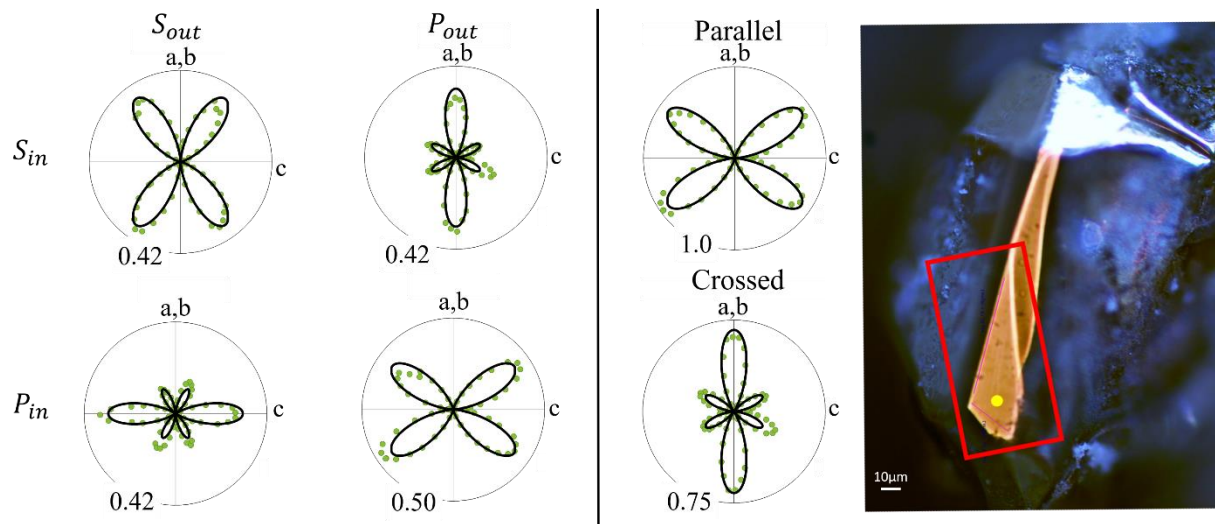
Figure VI.4 – An illustration of the RA-SHG raw data (closed circles) and derived fits using Equation VI.6 for one spot on the (110) crystal face for each of the four oblique incidence polarization channels (left of vertical line) and each of the normal incidence polarization channels (right of vertical line). A microscope image of the facet under investigation, complete with the locations of the four RA-SHG measurements, is shown on the far right. All RA-SHG flower plots are normalized to 59 fW.

Immediately we can note several observations apparent from our RA-SHG survey of the crystal facets of the CoSi sample. First, the polar plots do indeed maintain the symmetry we would expect for a given face. That is, the T point group has a C_2 axis along the c-axis which should be and is apparent in the RA-SHG plots taken incident to the (100) facet, and it has a C_3 axis normal to the (111) facet which should be and is apparent in the RA-SHG plots taken incident to that face. There are no true crystalline symmetries which should exist for light incident on the (110) crystal face. However, there is an apparent two-fold symmetry in our RA-SHG plots. This can be understood by imagining the cuts required to reach the (110) crystal facet from a simple cubic structure, shown in Figure VI.5. Although a two-fold rotation normal to the (110) facet will not bring the CoSi molecules back onto themselves, the cubic crystal structure predicts a two-fold symmetric rectangular cut for the (110) face. This explains the apparent two-fold symmetry in the

(110) RA-SHG polar plots. We can also see that the RA-SHG data taken on multiple spots of each crystal facet are remarkably consistent in terms of both strength and pattern, as discussed above. The orientation of the flower patterns is also consistent from spot to spot across a given crystal facet.
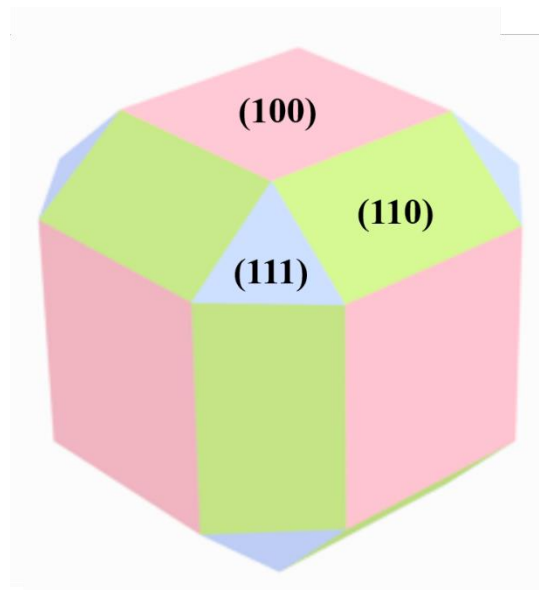
Figure VI.5 – An illustration of the cubic CoSi crystal with imagined cuts corresponding to the (100), (110), and (111) crystal facets.

We wish to further investigate the strength of the SHG response of the CoSi crystal in order to contribute to the current literature values of the susceptibility tensor elements for the type-I WSM TaAs and our previous measurements on T_d-WTe$_2$ in Chapter V. As discussed in Chapter IV, this will require knowledge of the index of refraction at both 400 nm and 800 nm. At the time of this study, measurements of these values had not been performed. Thus, Rachel Owen performed ellipsometry measurements on multiple crystal facets using a Woollam Ellipsometer at the Lurie Nanofabrication Facility on the Engineering Campus at the University of Michigan. The

results of these measurements are shown in Figure VI.6. The CoSi crystal structure is assumed to be isotropic based on the T crystal symmetry. Data was taken on both a (111) and a (100) crystal facet, and the extracted real and imaginary components of the index of refraction was found to be relatively consistent between the two (within 20%).

Taking this index of refraction into account, we find, using an RA-SHG flower pattern obtained in the normal incidence parallel channel for light incident on a (111) crystal facet, that the susceptibility tensor element for CoSi is given by $\chi_{zyx}^{ED} = 1200$ pm/V, which falls between our calculated susceptibility tensor strength for T$_d$-WTe$_2$ and the reported result on TaAs at 800 nm [14, 70]. Because the of the chiral nature of this material, the polar axis arguments presented in Chapter V to explain the SHG strength in T$_d$-WTe$_2$ are not relevant here. We might also expect that there could perhaps be some resonance effects contributing to the strength of the SHG signal at this wavelength. However, optical conductivity measurements have been performed and calculated which indicate no features near either the incoming fundamental or reflected SHG wavelengths [170].
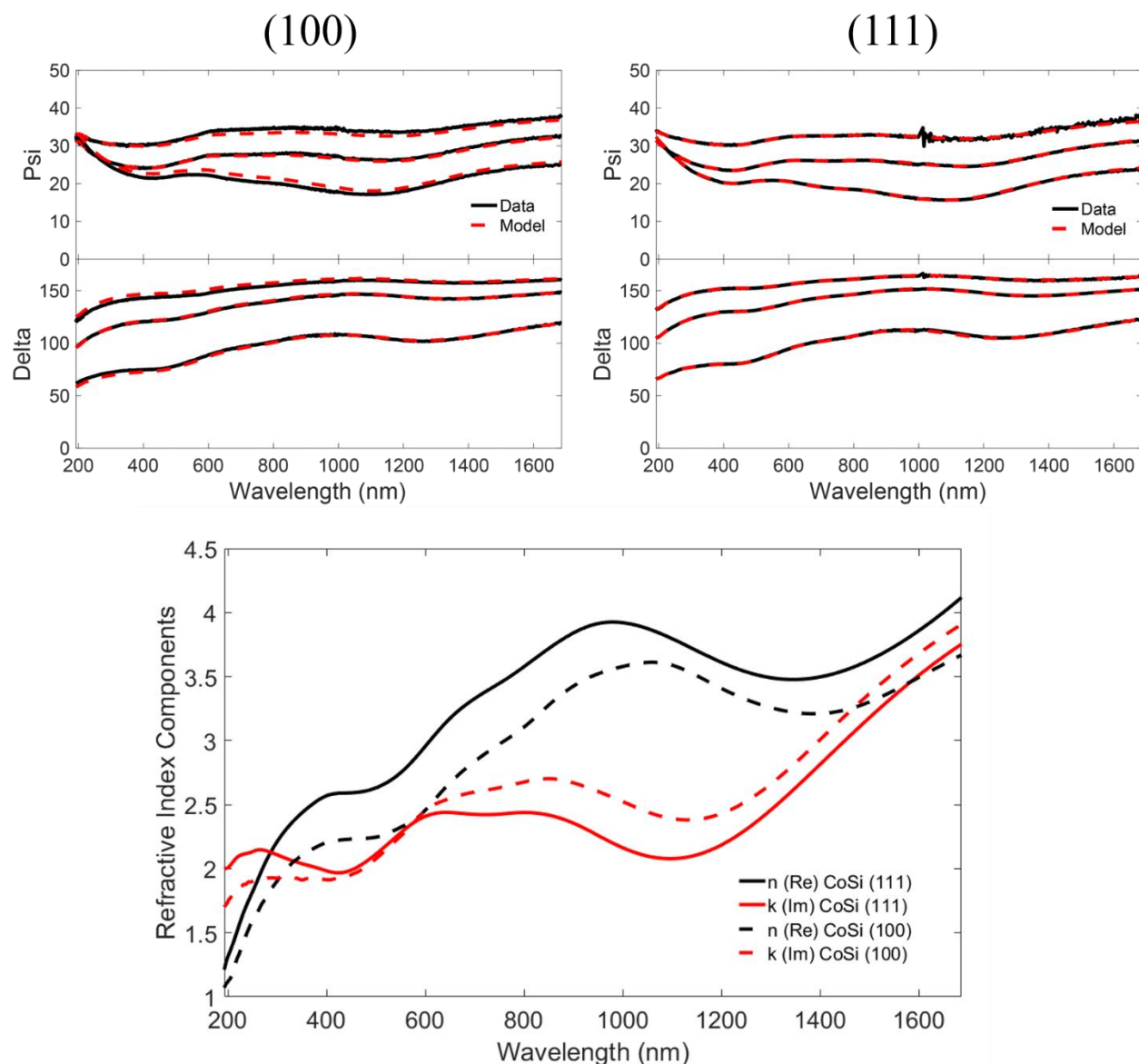
Figure VI.6 – Ellipsometry measurements taken by Rachel Owen. (Top) The raw data and fit derived assuming an isotropic crystal structure on a (100) and a (111) face. (Bottom) The derived components of the index of refraction for both the (100) and (111) crystal faces.

Indeed, it seems that the most consistent explanation for the strength of the SHG response of both the T_d-WTe_2 and this CoSi sample arises from the Weyl physics. In both instances, the 800 nm incoming light for this experiment, corresponding to 1.5 eV, will excite electrons well above the WPs. In the case of CoSi, the chiral WPs seem to lack an electron or hole pocket, which we

argued in the previous chapter might explain the lower SHG strength of the WTe$_2$ compared with TaAs. Thus, we might expect a larger SHG response from the CoSi. However, when we excite with 1.5 eV, we see from Figure VIII.2 that we will access the crossing point at the M-point of the band structure, which looks like it might allow for some screening effects due to the presence of electron and hole pockets and thus a lower SHG response than that of TaAs, as observed.

Photocurrent Studies on CoSi

As discussed briefly in Chapters II and III, photocurrent generation in WSMs has attracted particular interest in recent years due to the unique band structure of these materials. CPGE, in particular, is of interest because of the chiral nature of the Weyl cones. As illustrated in Figure VI.7, circularly polarized light will cause current to flow in a particular direction from either side of the Weyl cone. In type-I and type-II WSMs with mirror symmetries, the tilt of the Weyl cone plays a particular importance because the cones lie at the same energy in the band structure. This means that the tilt will determine whether the flow of current in a particular direction will dominate [9, 15]. However, in the chiral Weyl structure, a good choice of wavelength can be used to excite electrons around one of the two paired Weyl cones of opposite chirality, allowing in theory a strong polarization-dependent response. More than that, this response has been predicted to be quantized in terms of fundamental constants [93]. Several THz emission experiments have been performed particularly on the chiral WSMs RhSi and, to a lesser extent, CoSi [10, 11, 171], which have shown quantization of the photocurrent response in these materials to varying confidence levels. However, to our knowledge, no direct photocurrent measurements have been taken on this class of materials. Here, we present direct photocurrent measurements on various facets of the CoSi crystal.
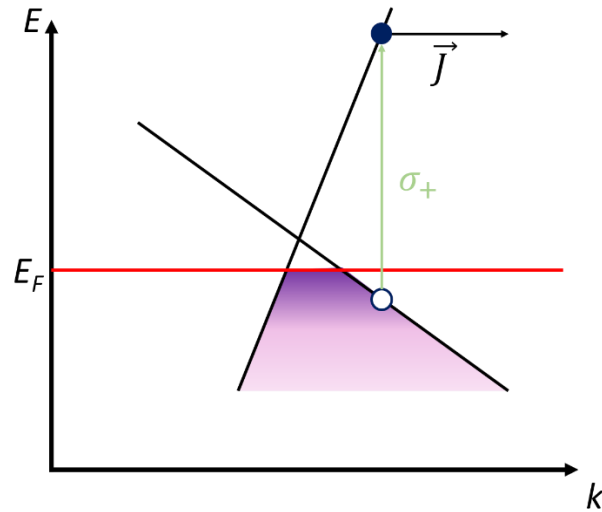
Figure VI.7– An illustration of the chirality-dependent photocurrent response in WSM. Here shown are a 2d representation of the tilted Weyl cone and the Fermi energy. When right-handed circularly polarized light is incident on the sample, electrons will be excitedly selected on only one side of the WP, yielding a nonzero CPGE.

To perform these electrical measurements, gold bonding pads were deposited onto the CoSi sample surface using electron-beam physical vapor deposition with an Angstrom Engineering Evovac Evaporator. The deposited gold layer was around 250 nm. No adhesion layer was deposited to allow easy removal of the gold pads if needed. A transmission electron microscopy copper rectangular mesh grid which was 25 μm thick and had 80 μm bars was used as a shadow mask. The mask was held flush to the sample surface using a custom sample holder which was 0.5 in in height and which attached to the evaporator's mounting platform. This process resulted in rectangular gold bonding pads of area ~530 μm by ~450 μm with between 30 μm and 75 μm separation between each pad. The bonding pads were aligned roughly to the face edges, which our RA-SHG measurements above found to correspond well with the crystal axes. Samples were then placed in chip carriers from Chelsea Technology and the sample bonding pads were connected to

the gold pads of the chip carrier using a 0.001 inch diameter gold wire with an adhesive of silver paste. Wires were anchored to the ceramic edges of the chip carrier using a GE varnish.

The form of the photocurrent tensor η is very similar to that of the χ^{ED} tensor listed above. However, we now are working with complex matrix elements and so must set the requirement that the photocurrent be real in order to derive an appropriate tensor form, as discussed in Chapter III. Applying this requirement and the crystal symmetries of the T crystal structure, we find a tensor form of

$$\eta = \begin{pmatrix} \begin{pmatrix} 0 \\ 0 \\ 0 \end{pmatrix} & \begin{pmatrix} 0 \\ 0 \\ a_{zyx} - ib_{zyx} \end{pmatrix} & \begin{pmatrix} 0 \\ a_{zyx} + ib_{zyx} \\ 0 \end{pmatrix} \\ \begin{pmatrix} 0 \\ 0 \\ a_{zyx} + ib_{zyx} \end{pmatrix} & \begin{pmatrix} 0 \\ 0 \\ 0 \end{pmatrix} & \begin{pmatrix} a_{zyx} - ib_{zyx} \\ 0 \\ 0 \end{pmatrix} \\ \begin{pmatrix} 0 \\ a_{zyx} - ib_{zyx} \\ 0 \end{pmatrix} & \begin{pmatrix} a_{zyx} + ib_{zyx} \\ 0 \\ 0 \end{pmatrix} & \begin{pmatrix} 0 \\ 0 \\ 0 \end{pmatrix} \end{pmatrix}. \qquad \text{VI.7}$$

Thus, for light incident at angle ξ on the (100) crystal face, we expect a photocurrent response of

$$\begin{aligned} J_x &= a_{zyx} \sin(4\theta) \sin(\xi) \\ J_y &= -a_{zyx} \sin^2(2\theta) \sin(2\xi) \\ J_z &= -a_{zyx} \cos(\xi) \sin(4\theta) \end{aligned} \qquad \text{VI.8}$$

for a HWP at angle θ to the vertical and

$$\begin{aligned} J_x &= \left(b_{zyx} + a_{zyx} \cos(2\theta)\right) \sin(2\theta) \sin(\xi) \\ J_y &= -2a_{zyx} \cos^2(\theta) \sin^2(\theta) \sin(2\xi) \\ J_z &= 2\cos(\theta) \left(b_{zyx} - a_{zyx} \cos(2\theta)\right) \cos(\xi) \sin(\theta) \end{aligned} \qquad \text{VI.9}$$

for a QWP at angle θ to the vertical. That is, we expect no in-plane response at all for a normal incidence geometry, and only an in-plane CPGE response along the J_y direction in the case of an oblique incidence geometry.

We note here that there is a subtlety in translating the functional forms of the photocurrent response from Equations VI.8 and VI.9 above to the "linear" vs "circular/elliptical" contributions

to the LPGE discussion presented in Chapter III. Namely, even though Equation VI.8 deals with pure linear light arising from a HWP, we still find a $\sin(4\theta)$ term, which under our EE^* formalism will arise due to an elliptic contribution. Here, however, we are working with light that starts at a vertical polarization rather than a horizontal polarization, which will adjust the location of the zero photocurrent response. Additionally, the oblique incidence geometry can allow us to access off-diagonal elements of the EE^* formalism, whereas before we were working with only the normal incidence response.
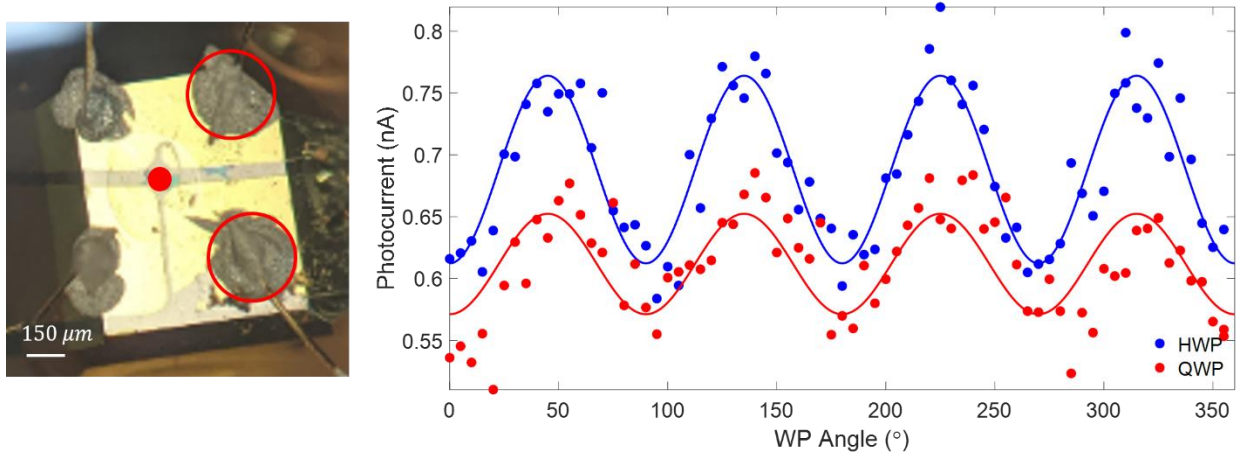
Figure VI.8 – Photocurrent data for the y-component of the (100) crystal facet. The raw data are shown for the HWP in blue solid dots and for the QWP in red solid dots, together with the fit to the data from Equations VI.8 and VI.9 displayed as solid curves of the appropriate color. A microscope image of the (100) crystal face with the gold pads and wires is included to the left. The photocurrent data was obtained using a laser spot location indicated by the solid red dot and was taken between the two leads highlighted in open red circles.

Photocurrent data obtained from the (100) CoSi crystal facet is shown in Figure VI.8. Because of some movement of the TEM grid during the gold pad evaporation and poor electrical contact of the lower left lead, we are only able to investigate experimentally the y-component of this crystal facet. As shown in Equations VI.8 and VI.9, we do not expect any CPGE contribution

137

in this direction. And indeed our data does not indicate any two-fold symmetry. Thus, we claim to see only LPGE contributions using either the QWP or the HWP at oblique incidence as predicted by our models.

Using the rotation matrix from Equation VI.3, we can also compute expected photocurrent responses for the (111) crystal face. We find a response of

$$
\begin{aligned}
J_x &= \frac{1}{\sqrt{3}} a_{zyx}\left(\sqrt{2}\cos(\xi)\sin(4\theta) + \sin^2(2\theta)\sin(2\xi)\right) \\
J_y &= \frac{1}{\sqrt{3}} a_{zyx}\left(\sqrt{2}\cos^2(2\theta)\right. \\
&\quad \left. - 4\sqrt{2}\cos^2(2\theta)\cos^2(\xi)\sin^2(\theta) - \sin(4\theta)\sin(\xi)\right) \\
J_z &= -\frac{1}{4\sqrt{3}} a_{zyx}\left(1 + 3\cos(4\theta) + 6\cos(2\xi)\sin^2(2\theta)\right)
\end{aligned}
$$

VI.10

for a HWP at angle θ from the vertical and

$$
\begin{aligned}
J_x &= \frac{2}{3}\cos(\theta)\sin(\theta)\left(3b_{zyx}\sin(\xi)\right. \\
&\quad \left. + \sqrt{3}a_{zyx}\cos(\xi)\left(\sqrt{2}\cos(2\theta) + \sin(2\theta)\sin(\xi)\right)\right) \\
J_y &= \frac{1}{2\sqrt{3}} a_{zyx}\left(\sqrt{2} + \sqrt{2}\cos^2(2\theta) - 4\sqrt{2}\cos^2(\theta)\cos^2(\xi)\sin^2(\theta)\right. \\
&\quad \left. - \sin(4\theta)\sin(\xi)\right) \\
J_z &= b_{zyx}\cos(\xi)\sin(2\theta) - \frac{1}{8\sqrt{3}} a_{zyx}\left(5 + 3\cos(2\xi) + 6\cos(4\theta)\sin^2(\xi)\right)
\end{aligned}
$$

VI.11

for a QWP at angle θ from the vertical. That is, at normal incidence we should expect to see LPGE in only one in-plane direction with the use of a HWP and we should expect to see CPGE in only one direction and only at oblique incidence when we are using a QWP.

Figure VI.9 – Photocurrent data from the (111) facet of the CoSi crystal. The plots to the right indicate the dependence of the photocurrent response on the waveplate angle from vertical for the case of a HWP (top) and a QWP (bottom). In each plot, the raw data are indicated by open circles and the fits to the oblique incidence data are included as solid curves using functional forms from Equations VI.10, VI.11, and VI.12. The data which is not fit comes from the normal incidence geometry. A microscope image of the (111) crystal facet with the gold pads and the wires is included to the left. The solid red circle indicates the location of the beam for the data in the plots to the right. The lead circled in black is used in both the x- and y-component measurements, and the lead used with the black lead for x is shown in red and for y is shown in blue.

Data obtained from the (111) crystal facet is shown in Figure VI.9 for data along the x- and y-directions using a HWP and a QWP in both the normal and oblique incidence geometries. We immediately notice that we do not observe any polarization dependence at normal incidence. This is possibly because the normal incidence spot size, which is only $\sim 30\ \mu m$, means that the excited photocarriers need to travel too far within the CoSi sample to be picked up efficiently by

the gold pad. The nonzero offset is then caused by the noise floor of the lock-in detection mechanism. We also see a clear four-fold symmetry for data taken with the HWP and a combined four- and two-fold symmetry for data taken with the QWP. However, the models we derive in Equations VI.10 and VI.11 do not fit the data well. In particular, we find that the peak locations should be different for the x- and y- components, which is not observed in our data. This is remedied by considering again the symmetry arguments from our RA-SHG discussions above. There, we discussed that this crystal facet actually is subject to a three-fold symmetry rather than a four-fold symmetry. This means that it will be impossible to use the TEM grid with four-fold symmetry to correctly align the gold pads with the crystal axes. Instead, when we measure the x- and y-components of the photocurrent in the lab frame, we are actually getting components from multiple high-symmetry directions of this crystal facet. Thus, we fit the data in Figure VI.9 with a model derived by weighting the x- and y- components of the photocurrent by some weight w, so that

$$\begin{aligned} J_{x_l} &= wJ_x + (1-w)J_y \\ J_{y_l} &= (1-w)J_x + wJ_y \end{aligned} \qquad \text{VI.12}$$

for each of the HWP and QWP, where x_l and y_l indicate the lab frame components measured. Doing so yields a weight of approximately 0.5 for both the J_x and J_y data. We will focus on this (111) face for the remainder of our discussion.
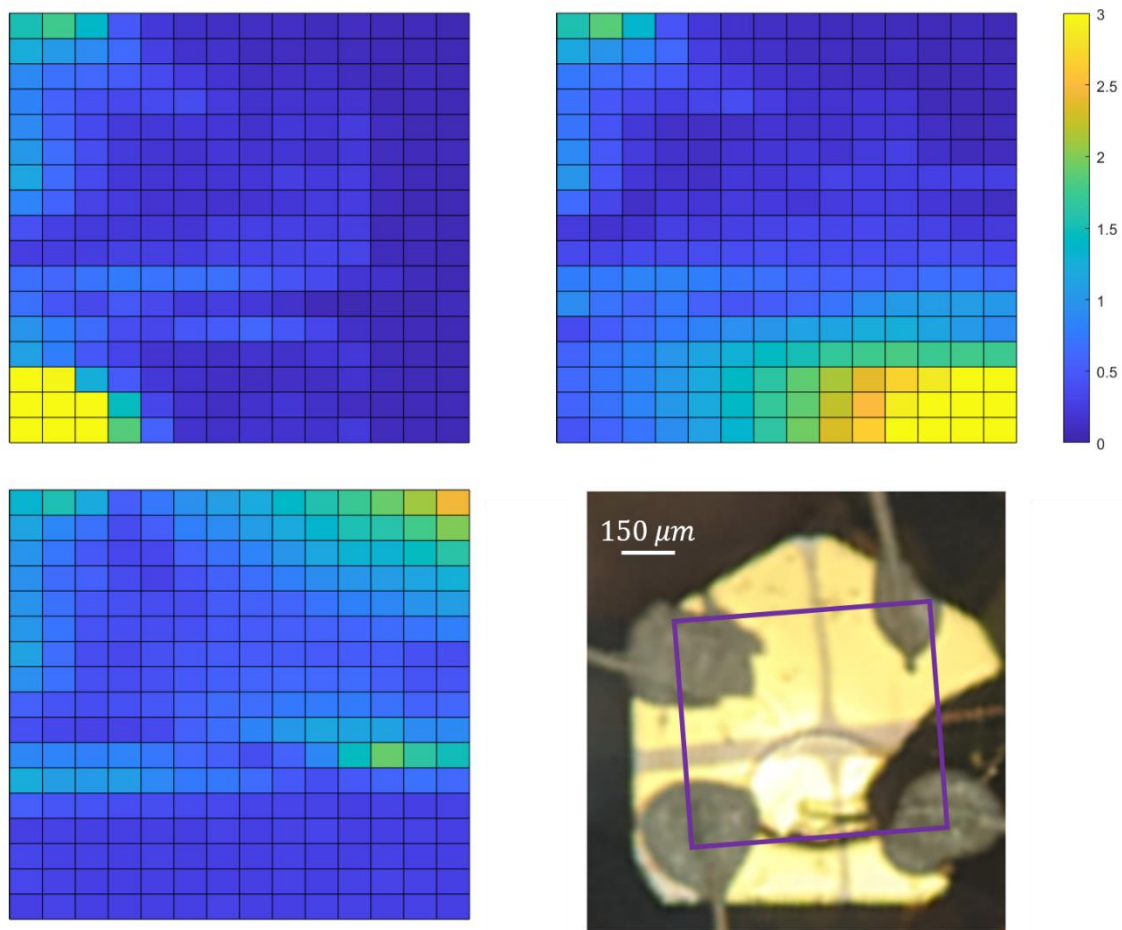
Figure VI.10 – Scanning photocurrent data taken on the (111) CoSi crystal facet with different lead combinations in an oblique incidence geometry at a peak in the polarization-resolved data with a QWP. A microscope image of the facet with the scanned area indicated by a purple box is included in the bottom right. All three scanning images have the same color scale, which is given in units of nA. The height and width of each pixel in the scanning photocurrent images is 30 μm.

The data presented in Figure VI.9 was taken while the laser illuminated only the CoSi sample. However, we are interested to know how the photocurrent response varies over the entire crystal face. With this motivation, we obtained scanning photocurrent angles with multiple experimental geometries and lead combinations. One example of this is shown in Figure VI.10, where we see three different lead combinations in the oblique incidence geometry using a QWP.

We notice immediately that the silver paste attaching the wires to the gold pads for the leads which are used to measure the photocurrent data seem to dominate the overall photocurrent response. This pattern is perhaps even more apparent in the normal incidence geometry, shown in Figure VI.11, where the smaller beam size yields a better spatial resolution.
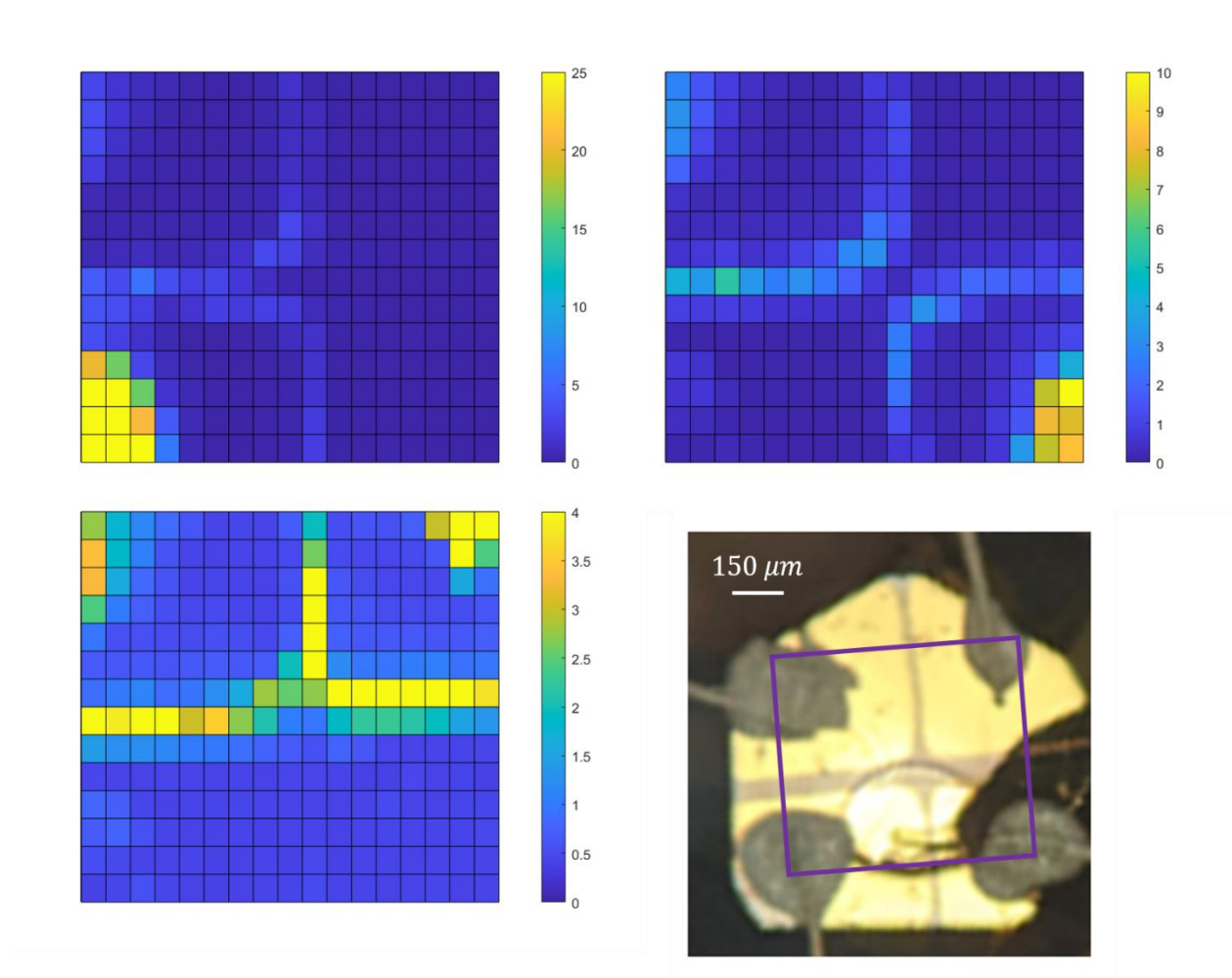
Figure VI.11 – Scanning photocurrent data taken on the (111) CoSi crystal facet with different lead combinations in a normal incidence geometry at a peak in the polarization-resolved data with a QWP. A microscope image of the facet with the scanned area indicated by a purple box is included in the bottom right. The color bar for each image is included and are given in units of nA. The height and width of each pixel in the scanning photocurrent images is 30 μm.

We are interested in pinning down with certainty the source of the photocurrent we see in this material at normal incidence. One possible explanation is that we are seeing a photothermal effect, which would show up as a DC background. There are a couple of features of the normal incidence response which make this unlikely to be the primary factor, however. The first is the spatial distribution of the response. A thermal gradient would be expected to be largest near the leads, but should exhibit a relatively smooth variation between the leads [9]. In our spatial data, however, it is clear that there is a peak in the normal incidence data right along the edges of the gold pads. This means that the normal incidence background does not model what we would expect from a thermal effect. Further, our data presented in Figure VI.9 illustrate that the CoSi response at normal incidence seems to be smaller than that at oblique incidence. However, the scale bars of the scanning photocurrent images in Figure VI.10 and Figure VI.11 indicate that the normal incidence response is larger than the oblique incidence response.

Another possibility is that the large response at normal incidence comes from the CoSi/gold pad interface. The work functions of the gold and CoSi are 5.30 eV [172] and 4.36 eV [173], respectively. This mismatch might be responsible for a potential difference or capacitance effect that could enhance the photocurrent response [174]. Indeed, such an effect might not be visible along the bulk of the gold pad because the deposition thickness of the gold is larger than the penetration depth of the laser. The gold could also be contributing in the form of breaking the symmetry of the system at the surface around the edges of the gold pad. However, it is difficult to tell from the scanning data of one WP angle whether the large response along the edges of the pad is due to this symmetry breaking or some capacitance effect or due instead to the fact that the excited carriers do not need to travel through the CoSi as far to reach the pad and be picked up as a photocurrent response when they are excited near to the pad.
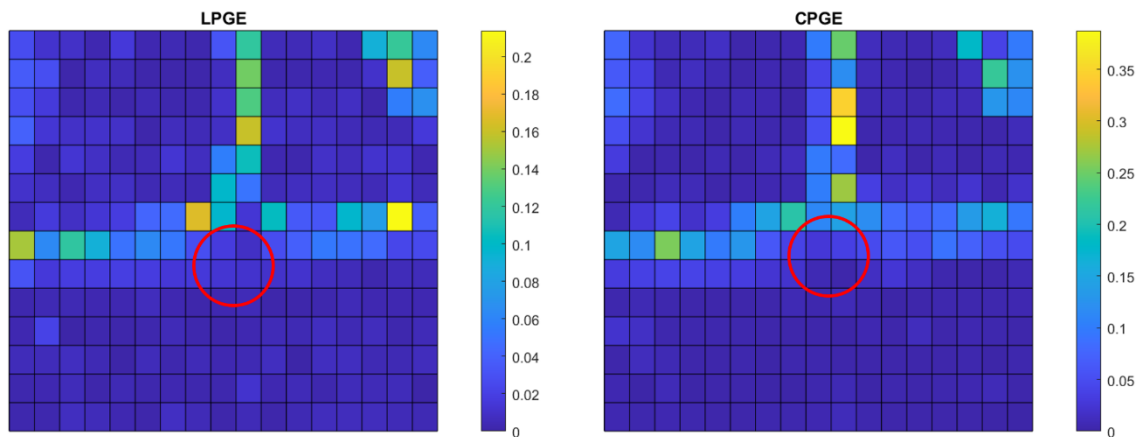
Figure VI.12 – Scanning photocurrent data filtered to provide the LPGE and CPGE signal for each pixel from the FFT of the data over all WP angles. This data follows the lower left scanning photocurrent data from Figure VI.11 taken on the (111) CoSi crystal facet at normal incidence with a QWP. The location of the beam used to obtain the data from Figure VI.9, where a pure CoSi photocurrent response is expected, is circled in red. The height and width of each pixel is 30 μm.

To help answer these questions, we look at the filtered FFT photocurrent scanning data, shown in Figure VI.12 for the lead combination in the lower left scanning photocurrent plot of Figure VI.11. This data was obtained by extracting the polarization dependence of each pixel in the scanning data, performing an FFT on that data, and then filtering for LPGE by extracting the value of the FFT spectrum at $2/\pi$ and for CPGE by taking the value of the FFT spectrum at $1/\pi$. We see that there seems to be a reasonably strong CPGE and LPGE response along the edges of the gold pads. We would not expect a polarization-dependent response from a capacitance enhancement effect, and so our signal is unlikely to come from the mismatch of the work functions of the gold and the CoSi. Further, our symmetry analysis has shown that the CPGE response cannot be coming from the CoSi directly at normal incidence, and so it is reasonable to assume that the symmetry breaking around the edges of the gold pad is contributing not only to the photocurrent

144

response, but also to the polarization-dependent response in the case that the beam illuminates this edge. This conclusion is bolstered by the fact that, in the normal incidence data, the LPGE/CPGE contributions drop off immediately as the pixel location approaches the laser spot location used to take the pure CoSi data presented in Figure VI.9.
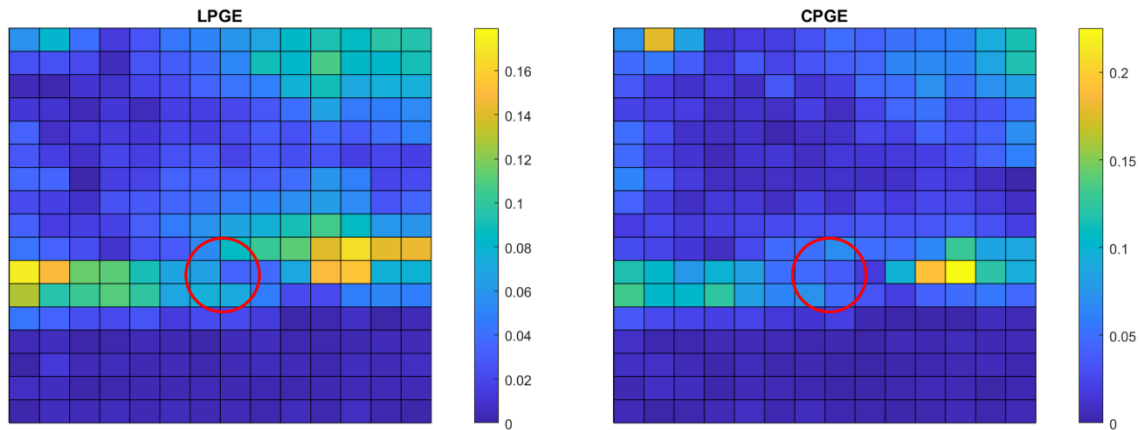
Figure VI.13 – Scanning photocurrent data filtered to provide the LPGE and CPGE signal for each pixel from the FFT of the data over all WP angles. This data follows the lower left scanning photocurrent data from Figure VI.11 taken on the (111) CoSi crystal facet at oblique incidence with a QWP. The area of the sample used to take the data from Figure VI.9, where a pure CoSi photocurrent response is expected, is circled in red. The height and width of each pixel is 30 μm.

In Figure VI.13, we see the filtered data for the same lead combination, but now for an oblique incidence geometry with the QWP. Now we see a much stronger LPGE/CPGE response along the gold/CoSi edge, but we also see that this response continues through the location in the center of the four gold pads which contains only CoSi signal, circled in red. Both the normal and oblique incidence geometries also indicate a polarization-dependent response from the silver paste used to secure the wires to the gold pads. This again is likely due to the decreased symmetry of this region.

These results indicate that the experimental geometry used in the study of real photocurrent effects must be carefully considered. In fact, if the beam illuminates either the edge of the gold pad used to collect the photocurrent signal or the silver epoxy used to attach the wires to the gold, a polarization-dependent photocurrent response similar to the CPGE/LPGE response of the CoSi. This means that the beam size for these experiments must be chosen small enough to not illuminate the electronics on the sample, but large enough to still allow the current to be collected from the material by those electronics.

CHAPTER VII

Nonlinear Probes of Other Strongly Correlated Materials

As discussed near the end of Chapter II, one of the key ingredients to the electronic structure of electronic WSMs is the strong electronic correlations present in these systems. Here, we will discuss another strongly correlated system – RbFe(MoO$_4$)$_2$. In this study, we use the RA-SHG experiment to explore an established structural phase transition in RbFe(MoO$_4$)$_2$ and identify with certainty the point groups above and below the critical temperature T_c. This study is presented as well in [132], and resulted in the establishment of a new type of ferroic ordering – the ferrorotational order – which is characterized by a vector order parameter invariant under both TRS and SIS. As a result, it requires a transition which maintains a center of inversion symmetry. This new ferroic order is important for fundamental physics, adding to the breadth of literature of well-known ferroic orders such as ferroelectricity, ferroelasticity, and ferromagnetism, and also from a device standpoint, as the ferrorotational structure is expected to be the source of multiferroicity in this material below 3.8 K [175]. We note here that Wencan Jin took the data for this study, while I performed the analysis. This project was supervised by Liuyan Zhao. Our samples were provided by Sang-Wook Cheong and Alemayehu Admasu.

Ferroic Ordering

The term "ferroic" was first introduced in 1970 by Aizu, who termed it a crystal which has two or more orientation states in the absence of an external electric, magnetic, or strain fields, and

which can be switched from one to another of those states by application of such an external field [176]. The most common forms of ferroic ordering are ferroelectric and ferromagnetic ordering. In ferroelectric systems, the microscopic dipoles caused by the relationships between electrons and atoms in the crystal are aligned in a particular direction without application of an external field, and their alignment can be switched coherently through application of an external coupling field, in this case the electric field. In ferromagnetic systems, the magnetization vectors of the material are all aligned and can be switched through application of an external magnetic field. Also common is ferroelastic ordering, in which there is a spontaneous strain of the system which can be switched through application of an external force or mechanical stress. Another ferroic ordering, ferrotoroidal ordering, has also been recently observed. This order is characterized by toroidal arrangements of magnetic dipoles [177, 178]. It was first observed in 2007 [177] by using the broken SIS of this system to identify the SHG response, and its conjugate coupling field was found to be $\vec{E} \times \vec{B}$ using hysteretic poling behavior in 2014 [179].

Vital to any discussion of ferroic ordering is the concept of the order parameter. The Landau theory of phase transitions [180, 181] introduces the order parameter as a quantity which gains a non-zero value as the system passes through a phase transition. It can be a scalar [182], a vector [183], or a higher-rank tensor quantity [68] that provides insight into the microscopic origin of its associated phase transition. Often, ferroic systems are classified according to the symmetries of their order parameters. If we consider ferroic orders which have vector order parameters[13], we can create a classification scheme according to how these order parameters behave under SIS and TRS. Doing this, we find that the order parameter for ferroelectricity, the electric dipole moment, is negative under SIS and positive under TRS. The order parameter for ferromagnetism, the

---

[13] Note that this necessarily excludes the ferroelastic order, whose order parameter is a rank-2 tensor which is positive under both SIS and TRS.

magnetic dipole moment, is just the opposite – negative under TRS and positive under SIS. We can also identify the toroidal moment, $\hat{r} \times \vec{M}$, as the order parameter for ferrotoroidal ordering and find that it is negative under both TRS and SIS. This classification scheme is shown in Figure VII.1.
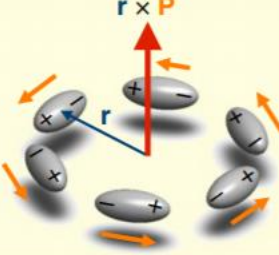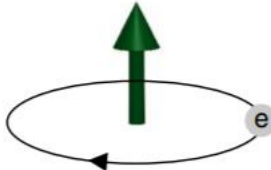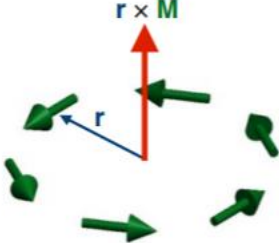
Figure VII.1 – A summary of the four vector order parameters classified by their parities under TRS and SIS operations, with illustrations of typical examples for realizing those order parameters. Here + indicates a parity-even quantity and – indicates a parity-odd quantity. The yellow background highlights the ferrorotational order parameter. This figure is adapted from [132].

We can see from this image that there is a missing piece – a ferroic order with a vector order parameter which is positive under both TRS and SIS. This ordering is known as ferrorotational or ferroaxial ordering and has an order parameter $\hat{r} \times \vec{P}$ [183-185]. It is closely related to a number of phenomena such as polar vortices [186], giant magnetoelectric coupling

[187], and spin-helicity-driven ferroelectricity [175]. Like the ferrotoroidal order, however, it is considerably rarer than the ferroelectric and ferromagnetic orders and has a much more complicated conjugate coupling field.

The ferrorotational order was, however, predicted to be present in complex oxides with structural distortions of uniform oxygen cage rotations [183, 184, 187-190]. To this end, we searched for this ordering in $RbFe(MoO_4)_2$, which consists of stacks of FeO_6 octahedra sharing vertices with MoO_4 tetrahedra, as shown in Figure VII.2. It is an archetype of type-II multiferroic materials and was predicted to host this ferrorotational order below a structural phase transition at $T_C \approx 195$ K in which the octahedra (tetrahedra) rotate counterclockwise (clockwise) about the c-axis [175, 188, 189, 191, 192]. It is also possible to have multiple ferroic domains in this material. A ferroic domain or domain state is a spatial region of the crystal in which the order parameter consists of a particular value. For example, in a ferromagnetic crystal, it is possible to have the microscopic magnetization vectors aligned up in one region of the crystal (domain I – D1) and down in another (domain II – D2). In $RbFe(MoO_4)_2$, it is possible as well to have a second domain state in which the octahedra (tetrahedra) rotate clockwise (counterclockwise) about the c-axis.
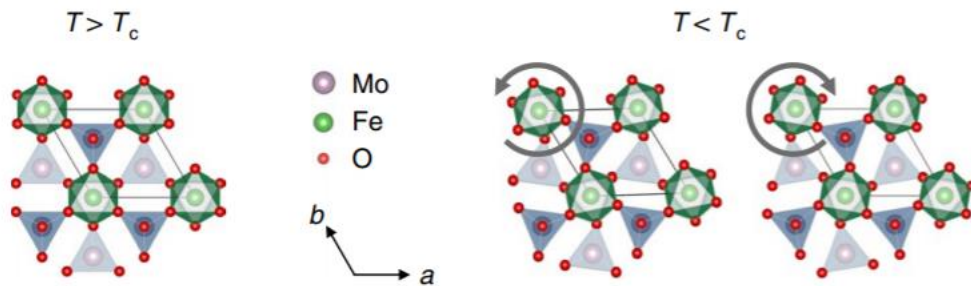
Figure VII.2 – The crystal structure of $RbFe(MoO_4)_2$ as viewed along the c-axis, both above and below the structural phase transition temperature T_c. Two domain states are expected below T_c,

corresponding to counterclockwise and clockwise rotations of the FeO_6 octahedra. This figure is adapted from [132].

It is worth noting that an axial vector invariant under both TRS and SIS must always define the order parameter of the ferrorotational order while the head-to-tail arrangement of electric dipoles shown in Figure VII.1 is just one simple example which can realize the ferrorotational order. That is to say, any ordered phase with an axial vector order parameter invariant under TRS and SIS must belong to the ferrorotational class of ordered phases. With this generalization of this class, the coherent ferroic rotation of oxygen polyhedral is equivalent to the head-to-tail arrangement of electric dipoles. Thus, both phenomena point to ferrorotational ordering because they share the same symmetries.

We can explore this relationship between the oxygen cage rotations and the ferrorotational order both macroscopically and microscopically. Macroscopically, we can argue that the ferrorotational order exists with and is linearly coupled to the coherent oxygen cage rotations in $RbFe(MoO_4)_2$. The coherent rotations will transform as a rotational vector along the c-axis of the crystal, which serves as the order parameter for describing the rotation of the oxygen polyhedral and is an axial vector which preserves both TRS and SIS. It also has the same rank as the ferrorotational order parameter, discussed below. Thus, from the Landau theory of phase transitions, we can say that these two order parameters should be linearly coupled in the free energy expansion.

Microscopically, the rotation of the oxygen polyhedral allows for the development of finite polar vectors looping around the FeO_6 cages, as seen in Figure VII.3. Above the transition, without the oxygen polyhedral rotation, the mirror planes are preserved. If we take the mirror plane

151

highlighted by the red dashed line in Figure VII.3 as an example, we see that, above the transition, all of the ions arrange according to the mirror symmetry, and so a polar vector cannot develop along the c-axis normal to the mirror. Below the transition, however, the red dashed line is no longer a mirror, which allows polar vectors normal to the dashed line to be generated. We can see that the polar vectors generated from either allowed oxygen cage rotation will have opposite orientations because of the clockwise versus counterclockwise motion. Using the three-fold rotational symmetry, we can find the same polar vector components for the other two pairs of oxygen atoms around this Fe atom, which leads to the formation of a loop of six polar vectors around the FeO$_6$ octahedra below T_c, as shown in the head-to-tail arrows in Figure VII.3.
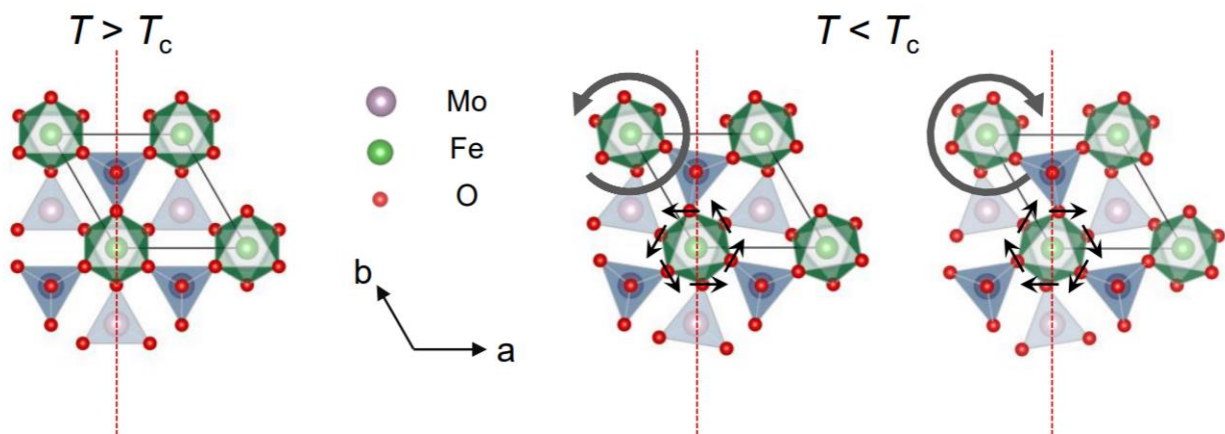
Figure VII.3 – An adaptation of Figure VII.2 which allows for the visualization of the coexistence of the coherent rotation of the oxygen polyhedral and the loop of polar vectors in RbFe(MoO$_4$)$_2$ below the phase transition. The red dashed line highlights one of the three mirrors present above the transition and the dark arrows around the FeO$_6$ cages illustrate the polar vectors which develop from the broken mirrors due to the oxygen polyhedral rotations. This figure is adapted from [132].

RA-SHG on RbFe(MoO₄)₂ at Room Temperature

The discussion presented above hinged on our identifying the structural phase transition of RbFe(MoO$_4$)$_2$ as ferrorotational in order. The point group of the room temperature phase of RbFe(MoO$_4$)$_2$ is known to be $\bar{3}m$ and the point group of the low-temperature phase was likely to be $\bar{3}$, but other possibilities including $3m$ and 32 had also been proposed [189, 191, 193] and needed to be ruled out. Thus, we will here present temperature-resolved RA-SHG data on RbFe(MoO$_4$)$_2$ crystals to pin down the symmetry properties of this material.

Our RbFe(MoO$_4$)$_2$ crystals were synthesized as single crystals by spontaneous crystallization using the flux melt method described in [189]. Powders of Rb$_2$CO$_3$ (Alfa Aesar, 5 N purity), Fe$_2$O$_3$, and MoO$_3$ were thoroughly mixed in the molar ratio 2:1:6. The homogenized mixture was then heated in a platinum crucible at 1100 K for 20 hours in air and cooled at a rate of 2 K per hour to 900 K. At that point, the mixture was cooled at a faster rate of 5 K per hour to room temperature. This process yielded transparent light-yellow to light-green hexagonal platelet crystals with dimensions on the order of $3 \times 3 \times 0.1$ mm^3 which were readily separated from the flux for experiments by dissolving in warm water.

We use the RA-SHG experiment to clearly identify the point group of both phases. To start, the $\bar{3}m$ point group consists of a C_3 axis about the c-axis of the crystal, a C_2 axis along the a-axis of the crystal and then in the ab-plane every $60°$ (three C_2 axes total), a mirror σ_{bc} in the bc-plane of the crystal and two additional mirrors perpendicular to the ab-plane obtained by rotating σ_{bc} by $\pm 60°$ about the c-axis (three mirrors total), an S_6 rotation about the c-axis, and inversion symmetry. Because we are working with a centrosymmetric crystal, we should not expect any electric dipole (ED) SHG response. However, we can explore higher-order terms of the nonlinear expansion of the polarization and see that we can get an electric quadrupole (EQ) contribution to

the SHG from the third-order term. Thus, we start by establishing the EQ contribution as the signal

we see from RbFe(MoO$_4$)$_2$ on our RA-SHG setup.

To do this, it is necessary to look at all four polarization channels in the oblique incidence

geometry. The EQ contribution to the nonlinear polarization is given by

$$P_i^{2\omega} = \chi_{ijkl}^{EQ} E_j^{\omega} \partial_k E_l^{\omega}. \qquad \text{VII.1}$$

Thus, it is necessary to derive χ_{ijkl}^{EQ} using the symmetries of the $\bar{3}m$ point group. The general form

of this tensor is

$$\chi^{EQ}$$

$$= \begin{pmatrix} \begin{pmatrix} xxxx & xxxy & xxxz \\ xxyx & xxyy & xxyz \\ xxzx & xxzy & xxzz \end{pmatrix} & \begin{pmatrix} xyxx & xyxy & xyxz \\ xyyx & xyyy & xyyz \\ xyzx & xyzy & xyzz \end{pmatrix} & \begin{pmatrix} xzxx & xzxy & xzxz \\ xzyx & xzyy & xzyz \\ xzzx & xzzy & xzzz \end{pmatrix} \\ \begin{pmatrix} yxxx & yxxy & yxxz \\ yxyx & yxyy & yxyz \\ yxzx & yxzy & yxzz \end{pmatrix} & \begin{pmatrix} yyxx & yyxy & yyxz \\ yyyx & yyyy & yyyz \\ yyzx & yyzy & yyzz \end{pmatrix} & \begin{pmatrix} yzxx & zyxy & yzxz \\ yzyx & yzyy & yzyz \\ yzzx & yzzy & yzzz \end{pmatrix} \\ \begin{pmatrix} zxxx & zxxy & zxxz \\ zxyx & zxyy & zxyz \\ zxzx & zxzy & zxzz \end{pmatrix} & \begin{pmatrix} zyxx & zyxy & zyxz \\ zyyx & zyyy & zyyz \\ zyzx & zyzy & zyzz \end{pmatrix} & \begin{pmatrix} zzxx & zzxy & zzxz \\ zzyx & zzyy & zzyz \\ zzzx & zzzy & zzzz \end{pmatrix} \end{pmatrix} \qquad \text{VII.2}$$

According to Equation VII.1, because we are working with SHG and so the two mixing fields are

identical, we can require that $\chi_{ijkl}^{EQ} = \chi_{ilkj}^{EQ}$ based on our experimental conditions. This, combined

with enforcing the symmetries of the $\bar{3}m$ point group, yields an EQ susceptibility tensor of

$$\chi^{EQ}$$

$$= \begin{pmatrix} \begin{pmatrix} xyxy + 2xyyx & 0 & 0 \\ 0 & xyyx & -xzxx \\ 0 & -xxzx & yzzy \end{pmatrix} & \begin{pmatrix} 0 & xyxy & -xzxx \\ xyyx & 0 & 0 \\ -xxzx & 0 & 0 \end{pmatrix} & \begin{pmatrix} 0 & -xzxx & yzyz \\ -xzxx & 0 & 0 \\ yzzy & 0 & 0 \end{pmatrix} \\ \begin{pmatrix} 0 & xyyx & -xzxx \\ xyxy & 0 & 0 \\ -xxzx & 0 & 0 \end{pmatrix} & \begin{pmatrix} xyyx & 0 & 0 \\ 0 & xyxy + 2xyyx & xzxx \\ 0 & xzxx & yzzy \end{pmatrix} & \begin{pmatrix} -xzxx & 0 & 0 \\ 0 & xzxx & yzyz \\ 0 & yzzy & 0 \end{pmatrix} \\ \begin{pmatrix} 0 & -zxxx & zzyy \\ -zxxx & 0 & 0 \\ zyzy & 0 & 0 \end{pmatrix} & \begin{pmatrix} -zxxx & 0 & 0 \\ 0 & zxxx & zzyy \\ 0 & zyzy & 0 \end{pmatrix} & \begin{pmatrix} zzyy & 0 & 0 \\ 0 & zzyy & 0 \\ 0 & 0 & zzzz \end{pmatrix} \end{pmatrix}. \qquad \text{VII.3}$$

Using this and Equation VII.1, we can calculate the intensity expected at the Andor CCD detector

as

$$I^{2\omega}_{p-p}(\phi) = \cos^2(\theta)\Big(\sin^2(\theta)\,(zyzy\cos^2(\theta) + (zzzz - 2zzyy)\sin^2(\theta)$$

$$+ zxxx\cos(\theta)\sin(\theta)\sin(3\phi))^2$$

$$+ \big((xyxy + 2xyyx - 2yzzy)\cos^2(\theta)\sin(\theta) + yzyz\sin^3(\theta)$$

$$+ xxzx\cos^3(\theta)\sin(3\phi) - 2zxxx\cos(\theta)\sin^2(\theta)\sin(3\phi)\big)^2\Big) \qquad \text{VII.4}$$

$$I^{2\omega}_{p-s}(\phi) = (xxzx\cos^3(\theta)\cos(3\phi) - 2zxxx\cos(\theta)\cos(3\phi)\sin^2(\theta))^2$$

$$I^{2\omega}_{s-p}(\phi) = \cos^2(\theta)\,(xyxy\sin(\theta) - xxzx\cos(\theta)\sin(3\phi))^2$$

$$+ \sin^2(\theta)\,(zyzy\cos(\theta) - zxxx\sin(\theta)\sin(3\phi))^2$$

$$I^{2\omega}_{s-s}(\phi) = xxzx^2\cos^2(\theta)\cos^2(3\phi)$$

or, more simply,

$$I^{2\omega}_{p-p}(\phi) = (C_1 + C_2\sin(3\phi))^2 + (C_3 + C_4\sin(3\phi))^2$$

$$I^{2\omega}_{p-s}(\phi) = (C_5\cos(3\phi))^2$$

$$I^{2\omega}_{s-p}(\phi) = (C_6 + C_7\sin(3\phi))^2 + (C_8 + C_9\sin(3\phi))^2 \qquad \text{VII.5}$$

$$I^{2\omega}_{s-s}(\phi) = (C_{10}\cos(3\phi))^2$$

for constants $C_1, \dots, C_{10}$ which are linear combinations of the EQ susceptibility tensor elements.

We can use the functional forms of Equation VII.5 to fit our oblique and normal ($\theta = 0$) incidence data, as shown in Figure VII.4. We see that the fit seems to be quite reasonable. However, it is necessary as well to eliminate other possible contributions to the SHG signal, such as electric-field induced SHG (EFISH), surface electric dipole SHG, and bulk magnetic dipole (MD) SHG. To rule out these possibilities, we simulate the expected RA-SHG patterns assuming these physical origins and determine which of the possibilities fits the experimental data best.
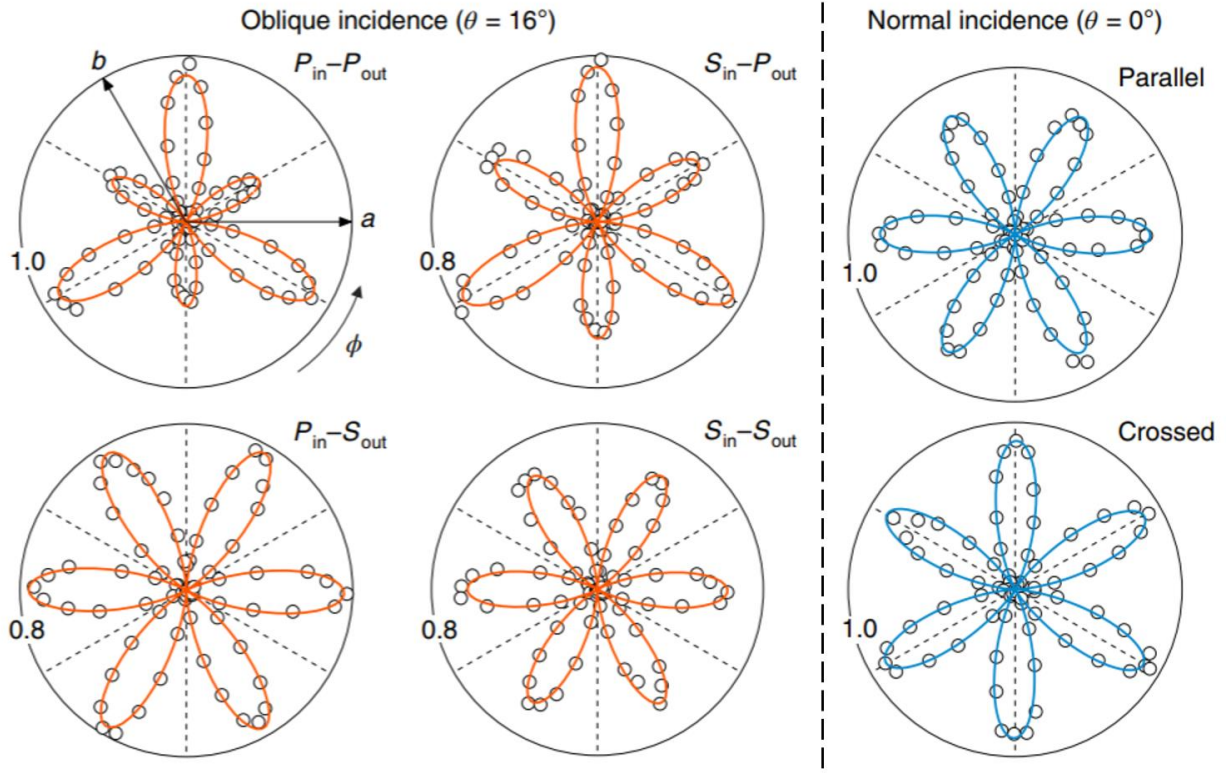
Figure VII.4 – Polar plots of the room temperature ($T = 290$ K) RA-SHG patterns fit with the functional forms derived from the bulk EQ SHG susceptibility tensor under point group $\bar{3}m$ at oblique incidence ($\theta \approx 16°$) in all four polarization channels (left of the dashed line) and at normal incidence in the two unique polarization channels ($\theta = 0°$) (right of the dashed line). Open circles indicate the raw RA-SHG data and the solid curves show the derived fits from Equation VII.5. The crystalline a- and b-axes are labeled in the oblique P-P channel and omitted for the rest. The three vertical mirror planes are indicated by the three dashed radial lines in every plot. All data is plotted on the same intensity scale, with a value of 1.0 corresponding to 22 fW. This figure is adapted from [132].

To start, we can simulate the EFISH contribution for the $\bar{3}m$ point group in the oblique incidence geometry as

$$I^{2\omega}(\phi) = \left| A\hat{e}_i(2\omega)\chi_{ijkl}^{EQ}(\phi)\hat{e}_j(\omega)\vec{E}_{k=z}\hat{e}_l(\omega) \right|^2 I^\omega I^\omega.$$

VII.6

That is, we replace the gradient along the $k = x, y, z$ component of Equation VII.1 with a DC electric field $\vec{E}$ normal to the sample surface. Doing this, we find functional forms for the four polarization channels of

$$I_{p-p}^{2\omega}(\phi) = (zyzy \cos^2(\theta) \sin(\theta) + zzzz \sin^3(\theta))^2$$

$$+ \left(\cos^2(\theta) (yyzy \cos(\theta) \sin(3\phi) - 2yyzz \sin(\theta))\right)^2$$

$$I_{p-s}^{2\omega}(\phi) = (yyzy \cos^2(\theta) \cos(3\phi))^2 \qquad\qquad\qquad \text{VII.7}$$

$$I_{s-p}^{2\omega}(\phi) = (zyzy \sin(\theta))^2 + (yyzy \cos(\theta) \sin(3\phi))^2$$

$$I_{s-s}^{2\omega}(\phi) = (yyzy \cos(3\phi))^2$$

We can compare this to Equation VII.5 and see that they are very similar except for the S-P channel, which EFISH predicts will have six even lobes and bulk EQ SHG predicts will have lobes of alternating size. In Figure VII.5, it is clear that the alternating peak intensities is a better fit for the experimental data.
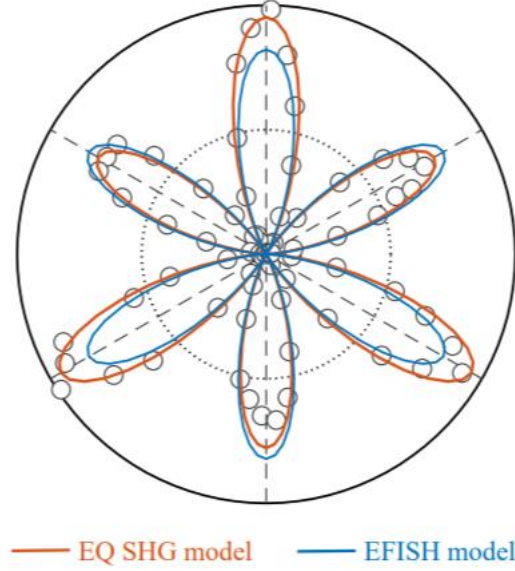
Figure VII.5 – Fits for the room temperature RA-SHG data in the S-P oblique polarization channel using the bulk EQ SHG model of Equation VII.5 and the EFISH model of Equation VII.7. This figure is adapted from [132].

Similarly, we can run simulations of the RA-SHG experiment for a surface ED SHG contribution. At the surface, the $\bar{3}m$ point group reduces to $3m$ due to the absence of inversion symmetry. We can calculate the functional form for the surface ED SHG contribution as

$$I^{2\omega}(\phi) = \left| A\hat{e}_i(2\omega)\chi_{ijk}^{ED}(\phi)\hat{e}_j(\omega)\widehat{e_k}(\omega) \right|^2 I^{\omega}I^{\omega}. \qquad \text{VII.8}$$

Here now we are working with the second-order tensor χ_{ijk}^{ED} for the $3m$ point group. This point group has one C_3 axis along the c-axis of the crystal and three mirror planes aligned with the mirror planes of $\bar{3}m$. Imposing these symmetries as well as the tensor index symmetry for the RA-SHG experiment yields a $\chi^{(2)}$ tensor of

$$\chi^{(2)} = \begin{pmatrix} \begin{pmatrix} 0 \\ -yyy \\ xxz \end{pmatrix} & \begin{pmatrix} -yyy \\ 0 \\ 0 \end{pmatrix} & \begin{pmatrix} xxz \\ 0 \\ 0 \end{pmatrix} \\ \begin{pmatrix} -yyy \\ 0 \\ 0 \end{pmatrix} & \begin{pmatrix} 0 \\ yyy \\ xxz \end{pmatrix} & \begin{pmatrix} 0 \\ xxz \\ 0 \end{pmatrix} \\ \begin{pmatrix} zxx \\ 0 \\ 0 \end{pmatrix} & \begin{pmatrix} 0 \\ zxx \\ 0 \end{pmatrix} & \begin{pmatrix} 0 \\ 0 \\ zzz \end{pmatrix} \end{pmatrix}. \qquad \text{VII.9}$$

This yields functional forms of the SHG intensity for the four polarization channels of

$$I_{p-p}^{2\omega}(\phi) = (zxx \cos^2(\theta) \sin(\theta) + zzz \sin^3(\theta))^2$$

$$+ \cos^4(\theta) (2xxz \sin(\theta) - yyy \cos(\theta) \sin(3\phi))^2$$

$$I_{p-s}^{2\omega}(\phi) = (yyy \cos^2(\theta) \cos(3\phi))^2 \qquad \text{VII.10}$$

$$I_{s-p}^{2\omega}(\phi) = (zxx \sin(\theta))^2 + (yyy \cos(\theta) \sin(3\phi))^2$$

$$I_{s-s}^{2\omega}(\phi) = (yyy \cos(3\phi))^2$$

Similar to our findings using our EFISH simulations, we see here that the surface ED SHG contribution predicts six even lobes for the S-P polarization channel, as show in Figure VII.6 and so this SHG contribution can be ruled out.
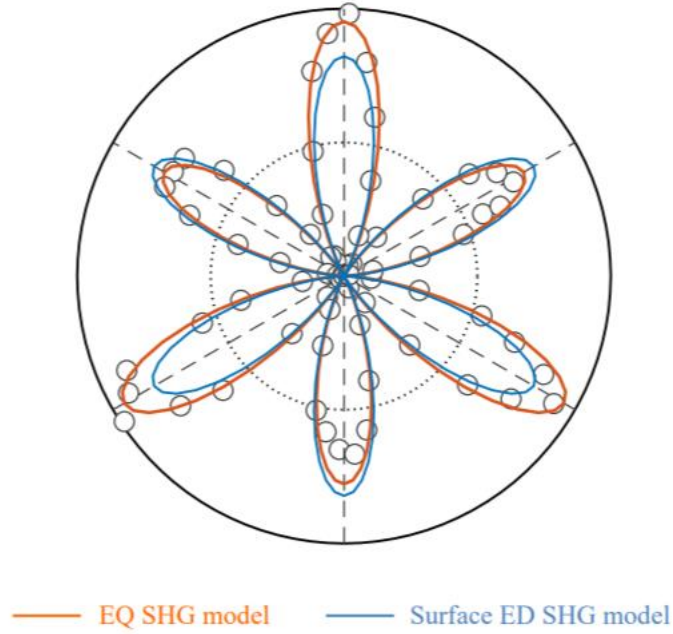
Figure VII.6 – Fits for the room temperature RA-SHG data in the S-P oblique polarization channel using the bulk EQ SHG model of Equation VII.5 and the surface ED SHG model of Equation VII.10. This figure is adapted from [132].

Finally, we look to rule out the bulk MD contribution to the SHG. This MD contribution can be simulated as

$$I^{2\omega}(\phi) = \left| A\widehat{e_i}(2\omega)\epsilon_{ijk}\hat{\partial}_j\chi_{klm}^{MD}(\phi)\widehat{e_l}(\omega)\widehat{e_m}(\omega) \right|^2 I^\omega I^\omega, \qquad \text{VII.11}$$

where now ϵ_{ijk} is the Levi-Civita tensor, we let $\hat{\partial}_j \to q_j$ for $\vec{q}$ the wave vector of the incident light, and χ_{ijk}^{MD} is the MD susceptibility tensor for $\bar{3}m$, given by

$$\chi^{(2)} = \begin{pmatrix} \begin{pmatrix} xxx \\ 0 \\ 0 \end{pmatrix} & \begin{pmatrix} 0 \\ -xxx \\ xyz \end{pmatrix} & \begin{pmatrix} 0 \\ xyz \\ 0 \end{pmatrix} \\ \begin{pmatrix} 0 \\ -xxx \\ -xyz \end{pmatrix} & \begin{pmatrix} -xxx \\ 0 \\ 0 \end{pmatrix} & \begin{pmatrix} -xyz \\ 0 \\ 0 \end{pmatrix} \\ \begin{pmatrix} 0 \\ 0 \\ 0 \end{pmatrix} & \begin{pmatrix} 0 \\ 0 \\ 0 \end{pmatrix} & \begin{pmatrix} 0 \\ 0 \\ 0 \end{pmatrix} \end{pmatrix}. \qquad \text{VII.12}$$

This yields functional forms for the SHG intensity of

160

$$I^{2\omega}_{p-p}(\phi) = \cos^2(\theta)\left(\cos^4(\theta) + \sin^4(\theta)\right)(2xyz\sin(\theta) + xxx\cos(\theta)\sin(3\phi))^2$$

$$I^{2\omega}_{p-s}(\phi) = (xxx\cos^3(\theta)\cos(3\phi))^2$$

VII.13

$$I^{2\omega}_{s-p}(\phi) = \frac{1}{4}(3 + \cos(4\theta))(xxx\sin(3\phi))^2$$

$$I^{2\omega}_{s-s}(\phi) = (xxx\cos(\theta)\cos(3\phi))^2$$

Yet again, we find that this MD SHG calculation predicts six even lobes for the S-P channel, as shown in Figure VII.7, and so our bulk EQ SHG contribution is identified as the primary source of the SHG signal.
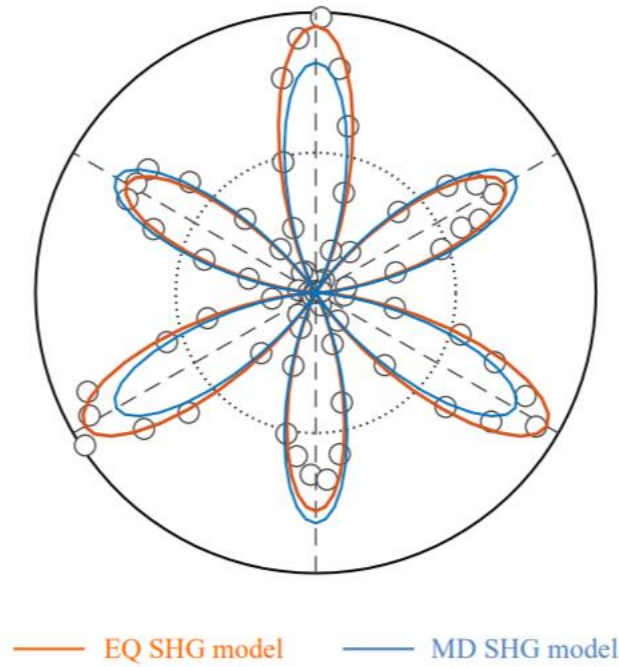
Figure VII.7 – Fits for the room temperature RA-SHG data in the S-P oblique polarization channel using the bulk EQ SHG model of Equation VII.5 and the MD SHG model of Equation VII.13. This figure is adapted from [132].

Having now identified the source of the SHG signal as the bulk EQ SHG of RbFe(MoO$_4$)$_2$, we perform several RA-SHG measurements on RbFe(MoO$_4$)$_2$ in the normal incidence geometry

to select a subset of χ_{ijkl}^{EQ} tensor elements. This data is shown in Figure VII.4 for both the crossed and parallel normal incidence configurations, complete with their fits. As in the oblique incidence geometry, we find that we are sensitive to both the C_3 axis and the three mirror planes enforced by the bulk $\bar{3}m$ point group. However, here, the simulated functional forms of the fits are significantly simpler, given by

$$I_{parallel}^{2\omega}(\phi) = \left(\chi_{yyzy}^{EQ} \cos(3\phi)\right)^2$$

$$I_{crossed}^{2\omega}(\phi) = \left(\chi_{yyzy}^{EQ} \sin(3\phi)\right)^2$$

VII.14

where only the χ_{yyzy}^{EQ} tensor element is relevant. This allows us to extract the value of this tensor element and track its evolution with temperature.

Low-Temperature Symmetries of RbFe(MoO₄)₂

Because of the simplicity of the functional forms of Equation VII.14, and because we are still sensitive to both the C_3 axis and the three mirror planes at normal incidence, we use the normal incidence geometry to obtain RA-SHG patterns on RbFe(MoO$_4$)$_2$ at various temperatures from 200 K to 80 K. A selection of example patterns is shown in Figure VII.8 for the parallel channel. There is a clear demonstration of a phase transition occurring at a T_c between 200 K and 190 K, as evidenced by the sudden appearance of a non-zero background in the RA-SHG patterns as well as by the start of a rotation of the RA-SHG patterns away from the mirror planes of the room temperature phase.
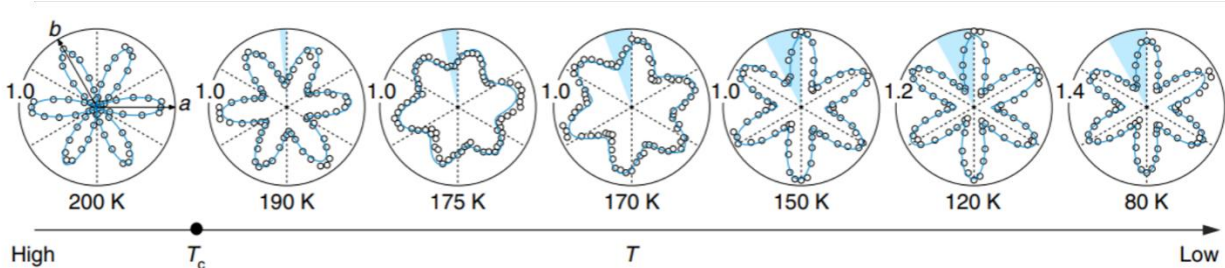
Figure VII.8 – Polar plots of the RA-SHG data in the parallel channel of the normal incidence geometry at selected temperatures above and below T_c. The rotation of each pattern away from the room temperature vertical mirror at $90°$ is highlighted by blue shading. The pattern above T_c is fit to the bulk EQ SHG functional form using $\bar{3}m$ from Equation VII.10, and the patterns below T_c are fit to a weighted two domain state averaged model of the bulk EQ SHG contributions of $\bar{3}$, presented in Equations VII.21 and VII.22. All datasets are plotted on the same intensity scale, with a value of 1.0 corresponding to 22 fW. This figure is adapted from [132].

We first wish to unequivocally pin down the point group of the low temperature phase, which until this point had been debated because previous measurements performed using infrared spectroscopy and Xray diffraction had trouble distinguishing between the subtle differences of point groups $3m$, 32, and $\bar{3}$ [193]. However, our RA-SHG experiment is sensitive to these distinctions between these point groups. We can immediately rule out the $3m$ point group because the RA patterns rotate away from the mirror planes present at room temperature. This rotation indicates that these mirror symmetries are broken below the transition. We can also rule out the 32 point group by looking at the intensity of the SHG response. In particular, the 32 point group is noncentrosymmetric and thus we would expect an ED SHG response, which should be orders of magnitude larger than that seen from the EQ response at room temperature. However, we find that the SHG intensity remains nearly unchanged across T_c, indicating that the low temperature phase is also centrosymmetric and dominated by the bulk EQ SHG response. A comparison of our simulated RA-SHG patterns for the $3m$ and 32 point groups is shown in Figure VII.9. The functional form of these simulations is given by Equation VII.10 for the $3m$ point group. The 32

point group consists of a C_3 axis along the c-axis of the crystal and three C_2 axes aligned with the

C_2 axes of the room temperature $\bar{3}m$ point group. This yields a susceptibility tensor of

$$\chi^{(2)} = \begin{pmatrix} \begin{pmatrix} xxx \\ 0 \\ 0 \end{pmatrix} & \begin{pmatrix} 0 \\ -xxx \\ xyz \end{pmatrix} & \begin{pmatrix} 0 \\ xzy \\ 0 \end{pmatrix} \\ \begin{pmatrix} 0 \\ -xxx \\ -xyz \end{pmatrix} & \begin{pmatrix} -xxx \\ 0 \\ 0 \end{pmatrix} & \begin{pmatrix} -xzy \\ 0 \\ 0 \end{pmatrix} \\ \begin{pmatrix} 0 \\ zxy \\ 0 \end{pmatrix} & \begin{pmatrix} -zxy \\ 0 \\ 0 \end{pmatrix} & \begin{pmatrix} 0 \\ 0 \\ 0 \end{pmatrix} \end{pmatrix}.$$ VII.15

and functional forms for the four polarization channels of

$$I_{p-p}^{2\omega}(\phi) = xxx^2 \cos^6(\theta) \cos^2(3\phi)$$

$$I_{p-s}^{2\omega}(\phi) = \cos^2(\theta) \left((xyz + xzy) \sin(\theta) + xxx \cos(\theta) \sin(3\phi) \right)^2$$

VII.16

$$I_{s-p}^{2\omega}(\phi) = xxx^2 \cos^2(\theta) \cos^2(3\phi)$$

$$I_{s-s}^{2\omega}(\phi) = (xxx \sin(3\phi))^2$$

where, as always, we can get the normal incidence channels by letting $\theta \to 0$.
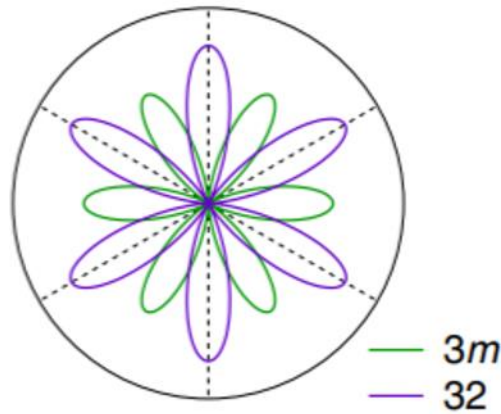
Figure VII.9 – Polar plots of the simulated RA-SHG patterns under point groups $3m$ from Equation VII.10 (green) and 32 from Equation VII.16. This figure is adapted from [132].

This means that the only possible point group remaining for the low temperature phase of

RbFe(MoO₄)₂ is $\bar{3}$. This point group consists of a C_3 axis along the c-axis of the crystal, an S_6 axis

along the c-axis, and inversion symmetry. As such, the EQ susceptibility tensor is

$\chi^{(2)}$

$$
=\left(\begin{array}{ccc}
\left(\begin{array}{ccc}
xyxy+2xyyx & xyyy-\frac{1}{2}(xyyy+yyxy)+yyxy & xzxx \\
-yyxy & xyyx & -yzyy \\
xxzx & -yyzy & yzzy
\end{array}\right) & \left(\begin{array}{ccc}
\frac{xyyy+yyxy}{2} & xyxy & -yzyy \\
xyyx & xyyy & -xzxx \\
-yyzy & -xxzx & xzzy
\end{array}\right) & \left(\begin{array}{ccc}
xzxx & -yzyy & yzyz \\
-yzyy & -xzxx & xzyz \\
yzzy & xzzy & 0
\end{array}\right) \\
\left(\begin{array}{ccc}
-xyyy & xyyx & -yzyy \\
xyxy & -\frac{1}{2}(xyyy+yyxy) & -xzxx \\
-yyzy & -xxzx & -xzzy
\end{array}\right) & \left(\begin{array}{ccc}
xyyx & yyxy & -xzxx \\
-\frac{xyyy+yyxy}{2} & xyxy+2xyyx & yzyy \\
-xxzx & yyzy & yzzy
\end{array}\right) & \left(\begin{array}{ccc}
-yzyy & -xzxx & -xzyz \\
-xzxx & yzyy & yzyz \\
-xzzy & yzzy & 0
\end{array}\right) \\
\left(\begin{array}{ccc}
zxxx & -zyyy & zzyy \\
-zyyy & -zxxx & -zzxy \\
zvzv & 0 & 0
\end{array}\right) & \left(\begin{array}{ccc}
-zyyy & -zxxx & zzxy \\
-zxxx & zyyy & zzyy \\
0 & zvzv & 0
\end{array}\right) & \left(\begin{array}{ccc}
zzyy & zzxy & 0 \\
-zzxy & zzyy & 0 \\
0 & 0 & zzzz
\end{array}\right)
\end{array}\right).
$$

VII.17

and so the functional forms of the SHG intensity are

$$
I^{2\omega}_{p-p}(\phi) = \cos^2(\theta)\Big(\big((xyxy+2xyyx-2yzzy)\cos^2(\theta)\sin(\theta)
$$

$$
+ yzyz\sin^3(\theta) + \cos^3(\theta)\,(xxzx\sin(3\phi)-yyzy\cos(3\phi))
$$

$$
+ 2\cos(\theta)\sin^2(\theta)\,(yyzy\cos(3\phi)-xzxx\sin(3\phi))\big)^2
$$

$$
+ \sin^2(\theta)\big(zyzy\cos^2(\theta)+(zzzz-2zzyy)\sin^2(\theta)
$$

$$
- \cos(\theta)\sin(\theta)\,(zyyy\cos(3\phi)-zxxx\sin(3\phi))\big)^2\Big)
$$

$$
I^{2\omega}_{p-s}(\phi) = \big((xyyy-2xzzy)\cos^2(\theta)\sin(\theta)+xzyz\sin^3(\theta)
$$

VII.18

$$
+ \cos^3(\theta)\,(xxzx\cos(3\phi)+yyzy\sin(3\phi))
$$

$$
- 2\cos(\theta)\sin^2(\theta)\,(xzxx\cos(3\phi)+yzyy\sin(3\phi))\big)^2
$$

$$
I^{2\omega}_{s-p}(\phi) = \cos^2(\theta)\big(xyxy\sin(\theta)+\cos(\theta)\,(yyzy\cos(3\phi)-xxzx\sin(3\phi))\big)^2
$$

$$
+ \sin^2(\theta)\big(zyzy\cos(\theta)
$$

$$
+ \sin(\theta)\,(zyyy\cos(3\phi)-zxxx\sin(3\phi))\big)^2
$$

$$
I^{2\omega}_{s-s}(\phi) = \big(yyxy\sin(\theta)+\cos(\theta)\,(xxzx\cos(3\phi)+yyzy\sin(3\phi))\big)^2
$$

This means that, for the parallel normal incidence channel, we will have a functional form for the

RA-SHG response of

$$I^{2\omega}_{parallel}(\phi) = \left(\chi^{EQ}_{xxx} \sin(3\phi) + \chi^{EQ}_{yyzy} \cos(3\phi) \right)^2,$$ VII.19

which accounts for the rotation, but not the nonzero background, of the RA-SHG patterns below

T_c.

In fact, the only way to account for this nonzero background is to allow for the presence of

two domain states (D1 and D2) in $RbFe(MoO_4)_2$ at low temperatures. As the $I^{2\omega}_{parallel}$ pattern

rotates counterclockwise by an angle

$$\delta = \frac{1}{3} \tan^{-1} \left(\frac{\chi^{EQ}_{xxzx}}{\chi^{EQ}_{yyzy}} \right),$$ VII.20

the other domain, D2, is expected to rotate clockwise by the same angle δ, yielding a functional

form of

$$I^{2\omega}_{parallel,D1}(\phi) = \left(\chi^{EQ}_{xxx} \sin(3\phi) + \chi^{EQ}_{yyzy} \cos(3\phi) \right)^2,$$

$$I^{2\omega}_{parallel,D2}(\phi) = \left(-\chi^{EQ}_{xxx} \sin(3\phi) + \chi^{EQ}_{yyzy} \cos(3\phi) \right)^2.$$ VII.21

These two functions correspond to the two domain states with opposite ferrorotational vectors,

where the FeO_6 octahedra rotate counterclockwise and clockwise, respectively, as depicted in

Figure VII.2 and Figure VII.3 for $T < T_c$. The nonzero background, which cannot be accounted

for by a single-domain state, can be well explained by a weighted linear superposition of

contributions from both domain states, given by

$$I^{2\omega}_{parallel}(\phi) = A \times I^{2\omega}_{parallel,D1}(\phi) + (1 - A) \times I^{2\omega}_{parallel,D2}(\phi),$$ VII.22

where A is the weight of D1.
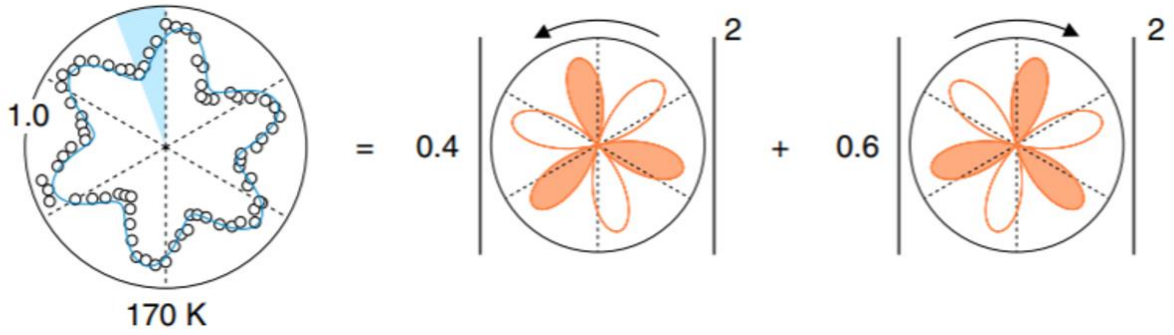
Figure VII.10 – An example of fitting the RA-SHG pattern at 170 K, below T_c, with a weighted average of both domain states using Equation VII.22. The individual patterns (orange) from the two domain states rotate counterclockwise and clockwise, respectively, and their weighting to the total RA-SHG data are indicated by coefficients 0.4 and 0.6, respectively. The filled and open petals represent the phases for the SHG electric fields. This figure is adapted from [132].

This method of weighting the two domains is intricately related to the domain sizes. In particular, when the domain size (l) is smaller than the optical beam size (d), there are two cases to be considered, depending on whether or not the domain size is smaller than the optical diffraction limit (λ). If $l \leq \lambda$, we should use the superposition of the SHG fields from each domain state, rather than their intensities as done in Equation VII.22. If this were to be the case, we would write out the fields from each domain as

$$E^{2\omega}_{parallel,D1}(\phi) = \chi^{EQ}_{xxzx} \sin(3\phi) + \chi^{EQ}_{yyzy} \cos(3\phi)$$

$$E^{2\omega}_{parallel,D2}(\phi) = -\chi^{EQ}_{xxzx} \sin(3\phi) + \chi^{EQ}_{yyzy} \cos(3\phi)$$

VII.23

We could then set the weights of D1 and D2 to be A and $1 - A$, respectively, yielding a superposition of the SHG fields of

$$E^{2\omega}_{parallel}(\phi) = (2A - 1) \cdot \chi^{EQ}_{xxzx} \sin(3\phi) + \chi^{EQ}_{yyzy} \cos(3\phi)$$

VII.24

and a resulting SHG intensity of

$$I^{2\omega}_{parallel}(\phi) = \left((2A - 1) \cdot \chi^{EQ}_{xxzx} \sin(3\phi) + \chi^{EQ}_{yyzy} \cos(3\phi) \right)^2, \qquad\qquad \text{VII.25}$$

up to a constant factor. This can be rewritten as

$$I^{2\omega}_{parallel}(\phi) = C \cdot \cos^2(3\phi - \alpha), \qquad\qquad \text{VII.26}$$

for $C = \left((2A - 1) \cdot \chi^{EQ}_{xxzx} \right)^2 + {\chi^{EQ}_{yyzy}}^2$ and $\alpha = \arctan\left((2A - 1) \cdot \dfrac{\chi^{EQ}_{xxzx}}{\chi^{EQ}_{yyzy}} \right)$. This expression can

account for the RA-SHG pattern rotation below T_c, but cannot account for the nonzero background.

If $l > \lambda$, we should use the superposition of SHG intensities, as in Equation VII.22. Figure VII.10 shows one example of the RA-SHG pattern at 170 K with a good fit using the weighted domain state averaged model. Thus, the appearance of the nonzero background indicates that the domain size must be larger than the optical wavelengths used in this experiment. Moreover, we have taken RA-SHG patterns at multiple location across the sample and found consistent results. This suggests that the domain size is also much smaller than our optical beam diameter of 50 μm. Thus, our estimate of the domain size is between several μm and a couple of tens of μm.

Phase Transition

Now equipped with a good understanding of both the point symmetries of the low temperature phase of RbFe(MoO$_4$)$_2$ and the correct fits for the RA-SHG data based on those symmetries, we can explore the temperature dependence of the fitting parameters − χ^{EQ}_{xxzx}, χ^{EQ}_{yyzy}, domain state weight A, and RA-SHG pattern rotation angle δ. These parameters are plotted as a function of temperature in Figure VII.11. Immediately it is clear that χ^{EQ}_{xxzx} jumps from zero to a finite value at the transition temperature $T_c \approx 195$ K and from there gradually grows larger before saturating at lower temperatures. This behavior suggests that χ^{EQ}_{xxzx} is, to the lowest order, linearly proportional to the ferrorotational order parameter and that the structural phase transition is of

weak first-order character. In contrast, χ_{yyzy}^{EQ} is present above T_c, but experiences a sharp spike at the transition and then slowly decreases below the transition. This suggests that χ_{yyzy}^{EQ} is, to lowest order, proportional to the square of the order parameter.
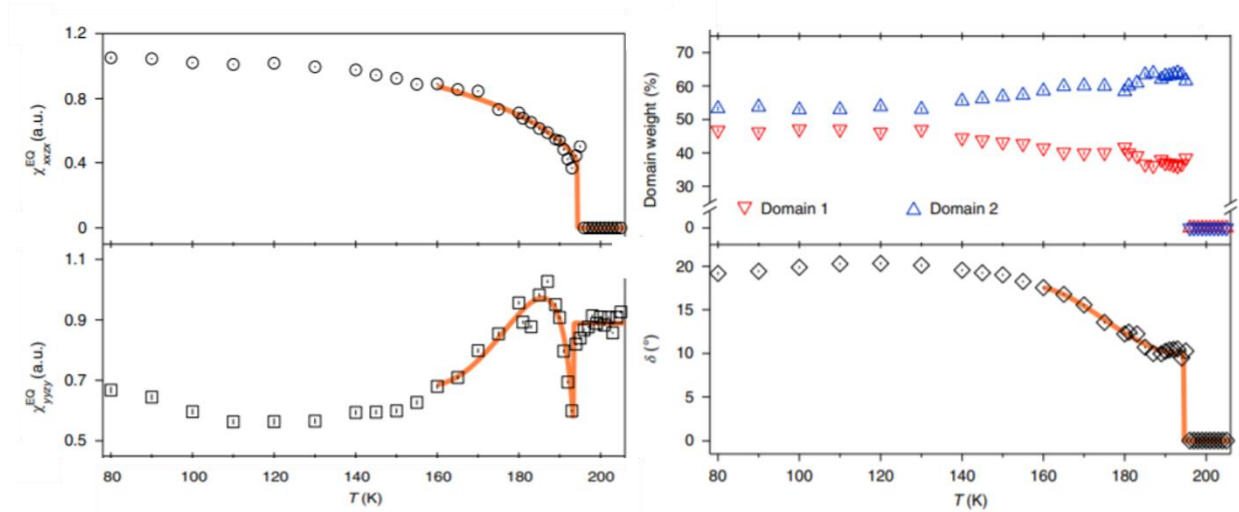
Figure VII.11 – Temperature dependence of the normalized EQ SHG susceptibility tensor elements χ_{xxzx}^{EQ} and χ_{yyzy}^{EQ} as well as the weight A of the domain states and the rotation δ of the RA-SHG patterns. The open shapes are the unique fit values from the RA-SHG data taken at that temperature. The solid orange lines are fits using the Landau theory-based functional forms for the temperature dependence of these parameters. Error bars indicate one standard error in fitting the RA-SHG data with the domain state averaged model. This figure is adapted from [132].

We can take a closer look at the transition by using a group theory analysis to explain the coupling between the EQ SHG fields and the TRS- and SIS-symmetric ferrorotational order parameter. To begin, we can look at the character tables for the $\bar{3}m$ and $\bar{3}$ point groups, shown in Figure VII.12 to see that the order parameter describing the transition between these two structures must transform as the A_{2g} symmetry of $\bar{3}m$. This is because the C_2 and σ_d symmetries lost in the transition from $\bar{3}m$ to $\bar{3}$ are also broken symmetries of the A_{2g} irrep of $\bar{3}m$. Noting that we can

use the plane wave approximation to express the radiated EQ SHG fields in the normal incidence

geometry as

$$\begin{pmatrix} E_x^{2\omega} \\ E_y^{2\omega} \end{pmatrix} \propto \begin{pmatrix} P_x^{2\omega} \\ P_y^{2\omega} \end{pmatrix} = \chi_{xxzx}^{EQ} \begin{pmatrix} (E_x^{\omega})^2 - (E_y^{\omega})^2 \\ -2E_x^{\omega} E_y^{\omega} \end{pmatrix} k_z + \chi_{yyzy}^{EQ} \begin{pmatrix} 2E_x^{\omega} E_y^{\omega} \\ (E_x^{\omega})^2 - (E_y^{\omega})^2 \end{pmatrix} k_z, \quad \text{VII.27}$$

for $E_{x,y}^{\omega}$ ($E_{x,y}^{2\omega}$) the incident (radiated SHG) electric field and k_z the wavevector of the incident

field. Under the $\bar{3}m$ point group, we can identify that the E_x and E_y components will transform as

the E_u irrep, and that the E_z and k_z components will transform as the A_{2u} irrep.

D_{3d} $h=12$	E	$2\,C_3$	$3\,C_2'$	i	$2\,S_6$	$3\,\sigma_d$
A_{1g}	1	1	1	1	1	1
A_{2g}	1	1	−1	1	1	−1
E_g	2	−1	0	2	−1	0
A_{1u}	1	1	1	−1	−1	−1
A_{2u}	1	1	−1	−1	−1	1
E_u	2	−1	0	−2	1	0

S_6 $h=6$	E	$2\,C_3$	i	$2\,S_6$
A_g	1	1	1	1
E_g *	2	−1	2	−1
A_u	1	1	−1	−1
E_u *	2	−1	−2	1

Figure VII.12 – Character table for the $\bar{3}m$ (D_{3d}) and $\bar{3}$ (S_6) point groups, taken from [194].

Because only the electric field is involved in this experiment, we can say with certainty

that no individual component of these fields is the coupling field for the ferrorotational order

because they do not have the correct symmetry properties. However, we can look at the composite

fields present in Equation VII.27 to see if we can construct a field that transforms as the

ferrorotational order parameter using the direct product table of the $\bar{3}m$ point group, shown in

Figure VII.13. In particular, we can look at terms resulting from taking the dot products of terms

in Equation VII.27. doing this, we find that

$$F^{DC} = k_z(E_x^{-2\omega}(E_x^\omega)^2 - E_x^{-2\omega}(E_y)^2 - 2E_x^\omega E_y^\omega E_y^{-2\omega}) \qquad\qquad \text{VII.28}$$

is one DC field with the correct symmetry properties which might serve as a coupling field.

	A_{1g}	A_{2g}	E_g	A_{1u}	A_{2u}	E_u	
A_{1g}	A_{1g}	A_{2g}	E_g	A_{1u}	A_{2u}	E_u	A_{1g}
A_{2g}	A_{2g}	A_{1g}	E_g	A_{2u}	A_{1u}	E_u	A_{2g}
E_g	E_g	E_g	$A_{1g} \oplus [A_{2g}] \oplus E_g$	E_u	E_u	$A_{1u} \oplus A_{2u} \oplus E_u$	E_g
A_{1u}	A_{1u}	A_{2u}	E_u	A_{1g}	A_{2g}	E_g	A_{1u}
A_{2u}	A_{2u}	A_{1u}	E_u	A_{2g}	A_{1g}	E_g	A_{2u}
E_u	E_u	E_u	$A_{1u} \oplus A_{2u} \oplus E_u$	E_g	E_g	$A_{1g} \oplus [A_{2g}] \oplus E_g$	E_u
	A_{1g}	A_{2g}	E_g	A_{1u}	A_{2u}	E_u	

Figure VII.13 – The direct product table of the $\bar{3}m$ point group, taken from [194].

We could imagine other experiments as well involving a magnetic field or a stress field for which we would be interested in identifying a coupling field for the ferrorotational order. A summary of how relevant physical quantities would transform under the $\bar{3}m$ point group is given in Figure VII.14. Using this information, we can see that any coupling field would have the form of eg. $\sigma_{ij}\sigma_{kl}$, $\sigma_{ij}E_kE_l$, $\sigma_{ij}H_kH_l$, $E_iE_jE_kE_l$, $E_iE_jH_kH_l$, etc. That is, it must have a minimum of four sub-indices. This suggests that the lowest rank composite coupling field to this axial vector order parameter under the point group $\bar{3}m$ is of the fourth order, regardless of the choice of constituent fields. This result is consistent with coupling fields obtained using the dichromatic matrix of physical property tensors derived in [185]. Further, this indicates that the lowest order process in which it is possible to observe this ferrorotational order with electric fields is through an EQ SHG process or equivalent.

	Electric field (E)	Magnetic field (H)	Stress (σ_{ij})
TR	+	−	+
SI	−	+	+
$\bar{3}m$ Irrep	$(E_x, E_y) \sim E_u$ $E_z \sim A_{2u}$	$(H_y, H_x) \sim E'_g$ $H_z \sim A'_{2g}$	$(2\sigma_{xy}, \sigma_{xx} - \sigma_{yy}) \sim E_g$ $\sigma_{xx} + \sigma_{yy} \sim A_{1g}$ $(\sigma_{xz}, \sigma_{yz}) \sim E_g$ $\sigma_{zz} \sim A_{1g}$

Figure VII.14 – A summary of how various physical fields transform under the $\bar{3}m$ point group as well as TRS and SIS symmetries. This figure is adapted from [132].

Beyond this symmetry analysis, we can use the relationships between the EQ susceptibility tensor elements and the order parameter as well as the Landau phenomenological theory of phase transitions [180] to derive fits for the temperature evolution of χ^{EQ}_{xxzx} and χ^{EQ}_{yyzy}. In particular, we can expand the Landau free energy in terms of the ferrorotational order parameter, which we will denote η, as

$$F(T) = F_0(T) + \alpha(T - T_c)\eta^2 + \beta\eta^4 + \gamma\eta^6 \qquad \text{VII.29}$$

for $\alpha > 0$, $\beta < 0$, and $\gamma > 0$ constants near T_c for small η near the weak first-order phase transition [181, 195]. We can minimize this free energy to get a functional form for the temperature dependence of η,

$$\eta(T) = \begin{cases} 0, & T > T_c \\ \sqrt{a + b\sqrt{T_d - T}}, & T \leq T_c \end{cases} \qquad \text{VII.30}$$

for $a = -\frac{\beta}{3\gamma}$, $b = \sqrt{\frac{a}{3\gamma}}$, and $T_d = \frac{\beta^2}{3\alpha\gamma} + T_c$ [195]. We know that χ^{EQ}_{xxzx}, like η, obeys the A_{2g}

symmetry of $\bar{3}m$, while χ^{EQ}_{yyzy} obeys the A_{1g} symmetry. We can therefore expand the two tensor

elements as

$$\chi^{EQ}_{xxzx} = a_1\eta + a_3\eta^3 + \cdots$$

$$\chi^{EQ}_{yyzy} = a_0 + a_2\eta^2 + a_4\eta^4 + \cdots$$

VII.31

to arrive at their expected temperature dependences with which to fit the raw data, shown in Figure

VII.11. These fits give an expected value of $T_c = 194.5 \pm 0.9$ K and $T_d = 199.6 \pm 2.1$ K.

Finally, we can look at the temperature dependence as well of the domain weight A to see

that the two domain states show up with uneven populations at T_c and converge to equal

populations with decreasing temperature. And the temperature dependence of the RA-SHG

rotation angle δ exhibits a jump from 0° to 10° at T_c and then gradually approaches a maximum

of 20° at lower temperatures. Because this behavior mimics χ^{EQ}_{xxzx}, we can use the same functional

form to fit δ.

1200 nm RA-SHG Experiments

Importantly, throughout this analysis, we have assumed that the nonlinear optical

susceptibility tensor elements are real, or, at least, have negligible imaginary components. This

would be true if the 800 nm incident and 400 nm reflected SHG wavelengths are not resonant with

any electronic transitions. However, ellipsometry and optical conductivity studies have yet to be

performed on this material, and so it is necessary to validate this assumption. Indeed, in the case

that complex susceptibility tensor elements are warranted, a nonzero background might appear

even at room temperature.

To verify that we are not on resonance, we performed RA-SHG experiments using 1200 nm incident light. In this case, both the incident fundamental and reflected SHG wavelengths are below the absorption edge of $RbFe(MoO_4)_2$. We examined all four polarization combination channels in the oblique incidence geometry as well as the crossed and parallel polarization channels in the normal incidence geometry, shown in Figure VII.15. Qualitatively, it is clear that all patterns lack a nonzero background. Quantitatively, all patterns can still be fit well by the bulk EQ SHG model of Equations VII.4 and VII.5 with real susceptibility tensor elements.
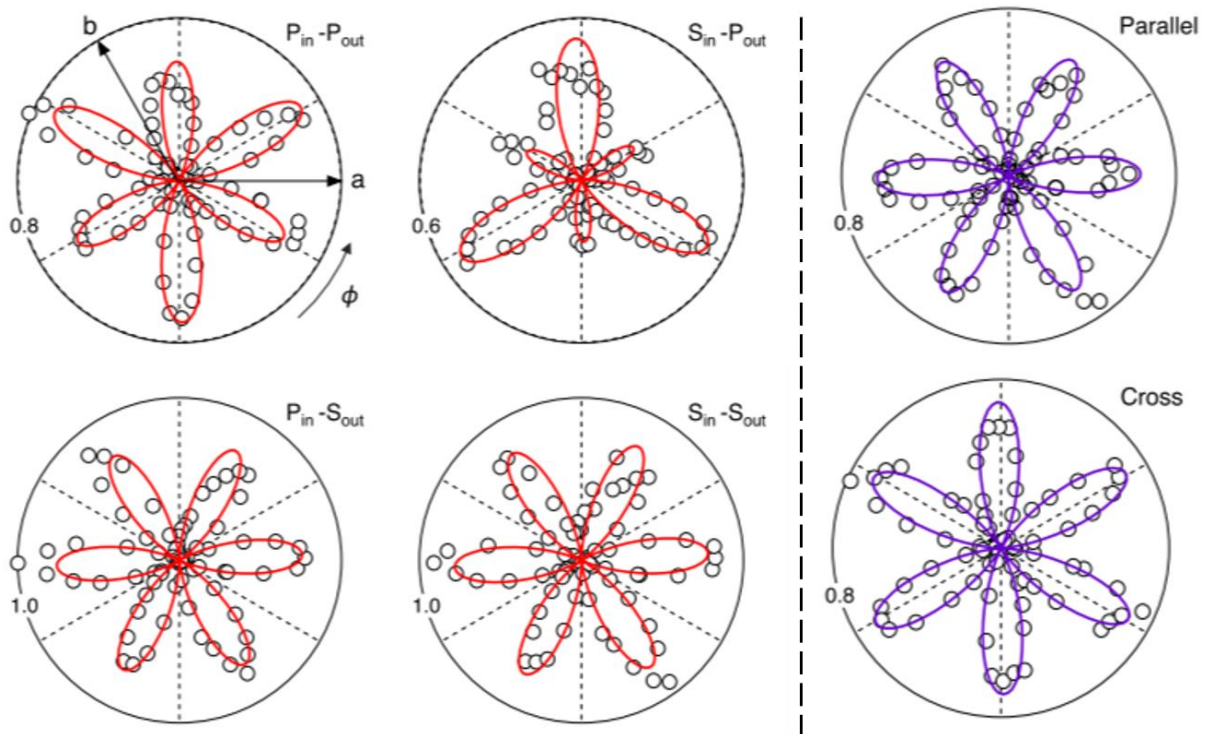
Figure VII.15 – Polar plots of the room temperature ($T = 290$ K) RA-SHG patterns taken with a 1200 nm incident fundamental and 600 nm reflected SHG wavelength in the oblique incidence geometry for all four polarization combination channels (left of dashed line) and at normal incidence in the parallel and crossed polarization channels (right of dashed line). Open circles are the raw RA-SHG data and the solid curves are the fit using the functional forms derived from the bulk EQ SHG susceptibility tensor under point group $\bar{3}m$ from Equation VII.5. The crystalline a- and b-axes are labeled in the oblique P-P channel and omitted for the rest. The three vertical mirror

planes are indicated by the three dashed radial lines in every plot. All data is plotted on the same intensity scale, with a value of 1.0 corresponding to 3 fW. This figure is adapted from [132].

CHAPTER VIII

Summary and Outlook

In this work, we have presented a range of nonlinear optical studies on strongly correlated materials, and particularly on WSMs. In general, we find that these effects are both relatively strong and anisotropic, especially in the topological materials. For example, we were able to add to previous literature on the strength of the SHG response of TaAs with new estimates for the strength of the SHG response in the type-II WSM T_d-WTe$_2$, in thin samples of the type-II WSM T_d-MoTe$_2$, and in the chiral WSM CoSi. A summary of these estimations and how they fit into the current breadth of literature on this topic is included in Table VIII.1.

Material	Susceptibility Estimation (pm/V)	Reference
TaAs (type-I)	$\chi_{zzz}^{ED} \approx 7200$	[14]
T_d-WTe$_2$ (type-II)	$\chi_{xyx}^{ED} \approx 300$ $\chi_{yxx}^{ED} \approx 350$ $\chi_{yyy}^{ED} \approx 200$	Chapter V
T_d-MoTe$_2$ (type-II)	$\chi_{yxx}^{ED} \approx \chi_{yyy}^{ED} \approx 10$	Chapter V
CoSi (chiral)	$\chi_{zyx}^{ED} \approx 1200$	Chapter VI

Table VIII.1 – A table summarizing the estimated strengths of the SHG responses discussed throughout this work and how they fit into the current picture based on previously existing literature on the type-I WSM TaAs.

In addition, we were able to investigate the strong appearance of ISRS in T_d-WTe$_2$ through the use of time-resolved reflectivity measurements. This mechanism of phonon excitation was responsible in particular for the 0.25 THz shear mode, which has been shown to drive a structural

phase transition between the WSM T_d and the non-topological 1T' phase of this material [90]. We also showed that this mode potentially couples to the Weyl fermion quasiparticle excitations in this material through the appearance of a Fano lineshape in the FFT spectrum.

We also studied the photocurrent response of the chiral WSM CoSi. We found that, if we illuminated just the CoSi, the results were consistent with our predictions based on the point symmetries of the CoSi crystal structure. However, the results were highly dependent on symmetry variations on the surface. We found a polarization-dependent response on both the edge of the gold pads and on the bonding location of the wires, which suggests that real photocurrent measurements on WSMs are the most robust when the beam size is small enough that only the material being studied is illuminated by the light.

Finally, we applied our nonlinear optical techniques to another class of strongly correlated materials, the complex oxide $RbFe(MoO_4)_2$, and were able to identify a structural phase transition in this material which was ferrorotational in nature. Through a group symmetry analysis, we were able to not only identify several potential coupling fields, but also to identify that the lowest-order coupling field must be of the same order as the electric quadrupole SHG process we used to make our observations.

These results are interesting in their own right, but also play an important role in opening up potential new research directions for future students and scientists. In this chapter, we will explore a couple of these open questions. We will begin on the experimental side, suggesting several new experimental setups which might help to further the work on nonlinear properties of WSMs. Then, we will move into open questions which arose during our type-II WSM studies and our chiral WSM studies. Finally, we will explore new directions for the ferrorotational ordering

project, including some work which has since been done by our friend and collaborator, Rachel Owen.

Experimental Development

Perhaps the most obvious next step in terms of experimental development is the development of techniques within our lab to look at longer-wavelength effects in the WSM samples. Such techniques allow for the access of the topology of these materials in a more direct way because longer wavelengths, and particularly micron-scale wavelengths, will be able to access the Weyl cone without exciting far above into higher bands. One technique which would allow for such wavelengths would be to use a nonlinear crystal to perform difference frequency generation, described in Chapter III, to decrease the frequency of the light and thus increase the wavelength. By working with two electric field sources of differing wavelengths, one from each NOPA, we could tune the available wavelength within a wide range using this effect, depending on the choice of nonlinear crystal. The resulting longer wavelength light could then be directed to already existing setups after coated optics are appropriately replaced.

Further, we have demonstrated an ability to implement scanning spatial resolution to both our SHG and our photocurrent experiments, but we would very much like to implement time resolution as well. Time-resolved SHG studies are used to observe, among other things, light-induced phase transitions [89, 90]. Our lab does have one setup which can study the time-resolved RA-SHG response of materials, but only for the normal incidence geometry. I have already designed an apparatus which would be able to apply time-resolution to the oblique incidence geometry of the already existing oblique incidence RA-SHG setup using a small D-mirror on a thin post on a manual translation stage to pick up the pump beam (from the other NOPA to allow

wavelength separation) and send it along the normal incidence beam path for an oblique incidence SHG probe and vise-versa. However, due to the COVID shutdowns I was unable to complete the alignment of this apparatus by the time of my graduation.

Implementation of time resolution on the photocurrent setup would also be beneficial, allowing us to measure quantities such as the scattering time of electrons in the material [196]. Implementation of this technique onto the current photocurrent setup detailed in Chapter IV would involve directing light from the other NOPA to this setup and again using a translation stage to implement the time resolution. More so even than this, THz spectroscopy is often used to investigate the photocurrent response of WSMs because this technique follows the same models as the LPGE and CPGE but is a direct optical technique rather than an electronic technique [197]. This eliminates the need for gold pads and wire placement directly on the sample surface [10, 11, 171], which can dramatically affect the measured photocurrent responses as demonstrated in Chapter VI.

Reflections on T_d-WTe$_2$ studies

One of the most apparent features in our WTe$_2$ study presented in Chapter V was the importance of the interlayer shear mode. The nonlinear effect of ISRS was observed through this mode, and the apparent Fano lineshape of this mode in the FFT spectrum suggested possible coupling to the Weyl fermion quasiparticle excitations. Other previous studies have also linked the 0.25 THz shear mode to the Weyl physics in T_d-WTe$_2$ [145]. This mode also exhibited signs of the linear electro-optical effect, observable through a phase difference for different linear polarized probes. Observations of this effect have been previously associated with surface field enhancements of phonon excitations [147-149, 198-200]. Thus, the observation of this effect

through the shear mode suggests the potential for enhancing the shear mode response with the application of some in-plane electric field, either by applying a bias or inducing a photocurrent [72], which might further enhance the nonlinear effects in this material. Therefore, one possible future experiment might be to study this mode more closely by trying to cause such an enhancement and looking at the time-resolved reflectivity or, more appropriately, time-resolved RA-SHG measurements to see if the light-induced phase transition associated with this mode could similarly be driven by these enhancement techniques.

In addition, our time-resolved reflectivity data did illuminate one feature which we could not immediately explain. In particular, we will take a closer look at the TR-MOKE signal. Traditionally, such a signal is obtained by subtracting the R-L signal from the R-R signals and showing that it is equal to subtracting the L-L signal from the L-R signal. That is,

$$(RR - RL) = -(LR - LL).$$ VIII.1

We can rearrange these terms instead to say that

$$(RR - LL) = -(LR - RL).$$ VIII.2

When we compute the relevant quantities for Equation VIII.2, as shown in Figure VIII.1, we find that actually there does seem to be some signal. We are not at the moment sure why this feature shows up in our data for one method of calculation and not the other, but believe that this discrepancy suggests it may be worth investigating T_d-WTe_2 using a TR-MOKE setup which can access the MOKE signal more directly and with better sensitivity using a balanced photodetector.
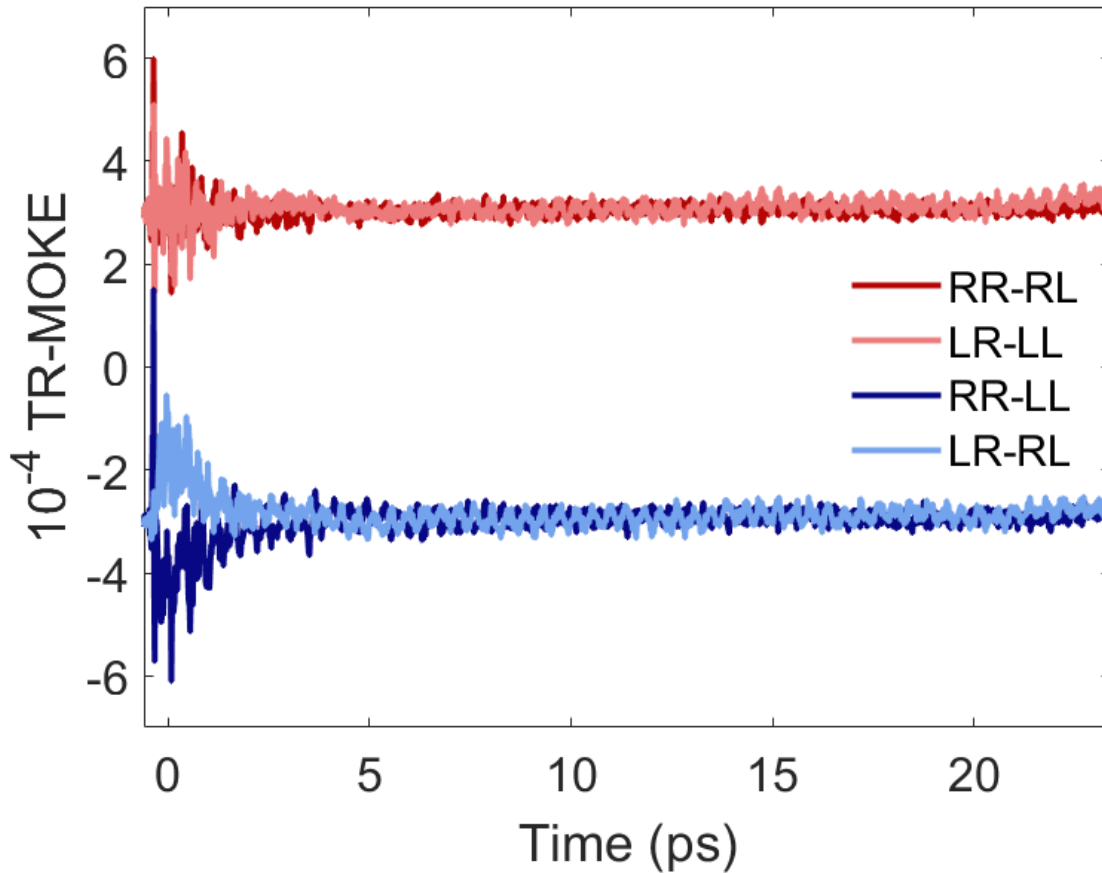
Figure VIII.1 – An illustration of the TR-MOKE signal calculated in the traditional way by subtracting the raw pump-probe data for different circularly polarized probes (red) together with the same calculation done by subtracting different circularly polarized pumps (blue). Although the traditional calculation does not show a TR-MOKE signal, as discussed in Chapter V, it does seem that there is perhaps some MOKE signal around time-zero for calculations performed in the non-traditional way, which might be worthy of further investigation.

Reflections on CoSi Experiments

The most immediate next step for our measurements on the chiral WSM CoSi is to take wavelength-dependent data to search for quantization of the photocurrent response, as predicted in [93] and shown in [10] for THz emission on RhSi. CoSi is predicted to host chiral multifold fermions even at room temperature. Previous DFT calculations have indicated that the inclusion of spin-orbit coupling is vital to correct theoretical predictions of this unique band structure [23,

58-60, 164, 201], as illustrated in Figure VIII.2. In particular, CoSi is predicted to host a threefold fermion of Chern number +2 near the Γ-point and a fourfold fermion of Chern number -2 near the R-point, separated by 0.85 eV [60]. This separation in energy corresponds to a wavelength of 1.46 μm, and so we will be trying to utilize wavelengths longer than this to access the threefold fermion.
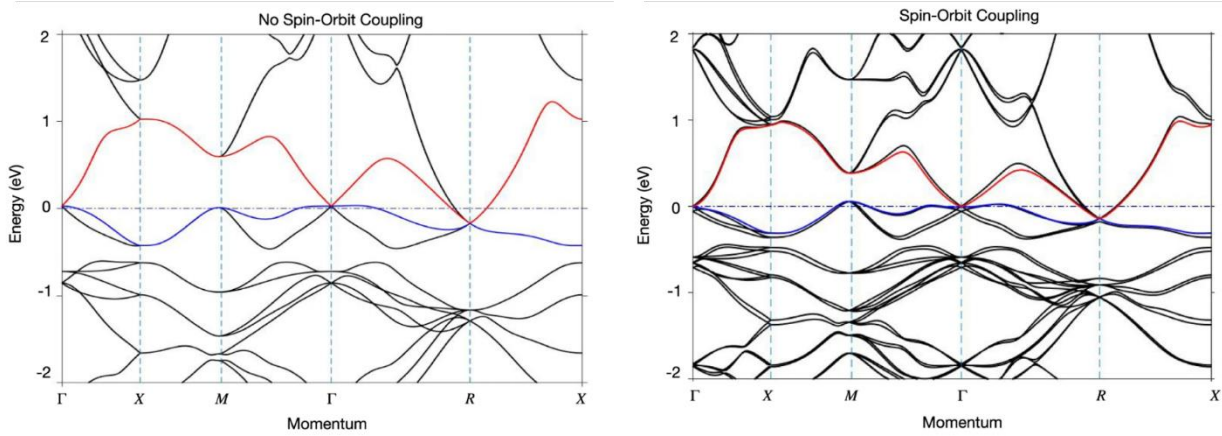
Figure VIII.2 – DFT calculations presented in [60] which illustrate the importance of including spin-orbit coupling to tease out the important topologically protected chiral multifold fermions in the CoSi band structure. The blue band is the highest valence band and the red is the lowest conduction band.

This project is already underway by our collaborator Matthew Day working in Steve Cundiff's group, and we hope to be able to put out a paper combining our analyses in the near future. Given our illustration of the dependence on the lead and pad placement on the sample, however, combined with predictions of scattering effects and defects destroying the quantization effects [202], it seems that this quantization will be very difficult to pin down with electronic measurements. It is possible that direct THz optical measurements, which are electronically cleaner, are necessary to observe these effects.

Further, we would like to confirm the symmetry considerations of our photocurrent data from the (111) crystal facet by designing a method of depositing gold pads which will allow us to

align the pads with the high symmetry directions of this facet. As mentioned in Chapter VI, this is not possible with the square TEM grid used in our experiment.

Reflections on the Ferrorotational Order Studies

Our study presented in Chapter VII and [132] made great strides in the discovery and study of the ferrorotational ordering in RbFe(MoO$_4$)$_2$. However, more work certainly needs to be done. One piece of data which we tried to obtain but were unable to due to the sensitivity of our experiments was to image the ferrorotational domains predicted by our RA-SHG pattern evolution with temperature. The imaging of such domains requires long-time SHG imaging of the EQ SHG response of this material, which is difficult to obtain because the signal level is so low that the acquisition time for such an image would be well beyond what would be reasonable for our laser stability and other experimental limitations.

Further, the identification of ferrorotational ordering in other materials is necessary to continue the study of this field. This torch has already been picked up by Rachel Owen, who has spent over a year working to identify the crystal structure of several other related complex oxides with oxygen cage rotations and to perform absorption measurements on them to identify features within the band structure. Her work has resulted in a further publication in Physical Review B [203].

Conclusion

We believe that the studies presented here are significant in furthering the scientific community's understanding of topological WSMs, illustrating broadly that topological enhancements to the size of nonlinear optical responses can be manifest even at optical

wavelengths, and that the anisotropy of these effects can generally be linked to the point symmetries of the crystalline system under investigation. Every day, theoretical predictions of WSM states in new materials and experimental confirmation of new WSM states are posted to the arXiv. These indicate a vibrant and growing field of study, which can only lead to new exciting properties discovered and applications developed in the future.

APPENDICES

APPENDIX A

Group Theory Formalism

In this appendix, we will present the mathematical formalism of group theory including formal mathematical definitions and theorems. This information, including and especially definitions of terms, is largely taken from [204].

Groups

To begin, a group is a set G together with a law of composition such that the law of composition is associative, G contains an identity element (denoted 1), and every element $a \in G$ has an inverse $b \in G$ such that $ab = ba = 1$. Here, a law of composition is any rule for combining pairs of elements $a, b \in G$ to get another element $p \in G$. We can further define an abelian group as a group whose law of composition is commutative. We say that the order $|G|$ of a group G is the number of elements in G.

The generators of a group are elements of the group which, when multiplied together under certain restrictions (the relations), yield all other elements of the group. All groups can be created via a set of generators and relations. As an illustrative example of this, we can consider the symmetric group S_3. In general, the symmetric group S_n is the group of permutations of the indices $1, 2, \cdots, n$. Because there are $n!$ ways to permute n indices, we must have the order of any symmetric group to be $|S_n| = n!$. We choose S_3 as our example because the order of the group is relatively small ($|S_3| = 3! = 6$), to make it possible to explicitly write out all of the group

properties for the purposes of illustration, but not so small as to be trivial and thus not enlightening.

We will begin by listing the elements of this group:

- $(1,2,3)$ – identity

- $(1,3,2)$ – transpose last two digits

- $(2,1,3)$ – transpose first two digits

- $(2,3,1)$ – one clockwise permutation of identity

- $(3,1,2)$ – two clockwise permutations of identity

- $(3,2,1)$ – transpose the last two digits of the identity, then permute once clockwise

As we can see, there are two main operations we must complete when going from one element to the next – cyclic permutation, which we will call x, and transposition of the first two elements, which we will call y. In S_3, it can be verified that

- $x^3 = 1$

- $y^2 = 1$

- $yx = x^2 y$

Using these restrictions, we can multiply x and y together in every possible combination and, in doing so, find only six distinct elements, which translate directly to the elements of S_3 we have already discussed as permutations on a set of three numbers:

- 1

- x

- x^2

- y

- xy

- $x^2 y$

We thus have that x, y are the generators of S_3, and that $\{x^3 = 1, y^2 = 1, yx = x^2y\}$[14] are the defining relations.[15]

One group operation which will be important to us later is the operation of conjugation. In conjugation, we have elements $x, g \in G$ and are interested in the operation $(g, x) \to gxg^{-1}$. By closure of groups, we must have that $(g, x) \in G$. Conjugation gives us a couple of important group properties. The first is the stabilizer or centralizer of an element $x \in G$, defined as

$$Z(x) = \{g \in G \mid gxg^{-1} = x\} = \{g \in G \mid gx = xg\}. \qquad \text{A.1}$$

That is, the centralizer of x is the set of elements of G which commute with x. From conjugation, we can also look at the orbit, or conjugacy class, of x, defined as

$$C(x) = \{x' \in G \mid x' = gxg^{-1} \text{ for some } g \in G\}. \qquad \text{A.2}$$

From these definitions, it can be proven that

$$|G| = |C(x)| \cdot |Z(x)|. \qquad \text{A.3}$$

Finally, we can talk about the center of a group G, defined as

$$Z = \{z \in G \mid zy = yz \,\forall\, y \in G\}. \qquad \text{A.4}$$

That is, the center of G is the set of all elements of G which commute with all other elements of G. By definition, $1 \in Z$ always.

Representations

We often use representations to describe group operations. Because groups are typically not abelian, it is often convenient to represent group elements as matrices, which are generally not commutative under multiplication. Matrix representations are defined in terms of

---

[14] Actually, the group can be generated using the relations $\{x^3 = 1, y^2 = 1\}$ only, but the $yx = x^2y$ definition is very useful.
[15] Generally, the defining relations are written in the form $r = 1$.

homomorphisms, or maps $\varphi: G \to G'$ from group G to group G' such that, for all elements $a, b \in G$, $\varphi(ab) = \varphi(a)\varphi(b)$. In particular, a matrix representation of a group G is a homomorphism to a particular group, $R: G \to GL_n$, where GL_n is the general nonlinear group[16] for n the size of the matrices we are mapping to. It can be shown that the homomorphism will always map the identity in one group to the identity in another, and inverses in one group to inverses in another.

When we talk about homomorphisms, we frequently discuss the image of the homomorphism. The image of a homomorphism $\varphi: G \to G'$ is defined as

$$\text{im}\varphi = \{x \in G' \mid x = \varphi(a) \text{ for some } a \in G\}. \qquad \text{A.5}$$

We frequently see this denoted as $\text{im}\varphi = \varphi(G)$. We can similarly talk about the image of an individual element $g \in G$ as all of the elements $g' \in G'$ which can be mapped to by g. For the purposes of this discussion, we will denote $\text{im}(g) = R_g$ when discussing the representation homomorphism R.[17]

Perhaps simultaneously the least and most obvious representation of any group is the representation which maps all elements to the identity, known as the trivial representation. More precisely, we are defining a homomorphism $R: G \to GL_1$. That is, we are mapping group elements to scalars (1×1 invertible matrices). In this case, however, we lose all of the uniqueness of the group. For example, any group of six elements will look like S_3 in the trivial representation. Because in the trivial representation all elements of the group are mapped to 1, we have that the trivial representation is abelian for all groups G. This implies that the existence of a trivial representation is not a sufficient requirement to prove that a group is abelian.

---

[16] The general nonlinear group GL_n is the set of all $n \times n$ invertible matrices. We may specifiy the set from which we are drawing elements of these matrices for example as $GL_n(\mathbb{R})$ for real matrices or as $GL_n(\mathbb{C})$ for complex matrices.

[17] That is, R_g is the matrix representation of g.

In contrast, a faithful representation is a representation with a one-to-one correspondence. That is, it is a representation created by an injective, or one-to-one, homomorphism, which satisfies that for all elements $a, b \in G$ such that $a \neq b$ and with representations $\varphi(a), \varphi(b) \in G'$, respectively, we have that $\varphi(a) \neq \varphi(b)$. A faithful representation must then include all of the information about the group and, conversely, any representation which is not faithful must necessarily lose some of the information about the group. In particular, because a faithful representation contains all of the information about the group, we can say that if the faithful representation of a group is abelian, then all representations of a group must be abelian and so the group itself must be abelian.

We typically think of matrices as acting on vectors. Vectors are mathematical objects which live in vector spaces, which are sets of vectors defined over some field F^{18} such that the set is closed under addition and scalar multiplication (multiplication by an element in F) and contains a zero vector (or an identity operator for addition). Thus, we can think about how the matrix representation of group G might transform vectors in some vector space V. In order to do this, we must consider the basis in which we are working. In particular, we can find conjugate representations by using invertible matrices to change bases. That is, when using a matrix P to change bases, we can also use P to get a conjugate representation or equivalent representation $R_g' = P^{-1} R_g P$ of representation R_g of $g \in G$.

In a similar vein, we can define a vector $\vec{v} \in V$ as G-invariant if it remains fixed when acted on by any R_g for $g \in G$. That is, $\vec{v}$ is G-invariant if $R_g \vec{v} = \vec{v} \; \forall \; g \in G$. Further, for any $\vec{v} \in V$, we

---

[18] Here, a field F is a set defined to be abelian under both addition and multiplication satisfying that F (or, more precisely, that the nonzero elements are abelian under multiplication) and satisfying the distributive law, which states that for all elements $a, b, c \in F, a(b + c) = ab + ac$.

can form a G-invariant vector using a process known as averaging over the group. That is, $\forall \vec{v} \in$

$V, \exists \vec{v'}$ such that $\vec{v'}$ is G-invariant. In particular, this G-invariant average vector can be defined as

$$\vec{v'} = \frac{1}{|G|} \sum_{g \in G} R_g \vec{v}. \tag{A.6}$$

Similarly, we can define a subspace $W \subseteq V$ as a G-invariant subspace if $R_g \vec{w} \in W \ \forall \ \vec{w} \in W$ and

$\forall g \in G$.

If we have two spaces $W_1, W_2 \subseteq V$ which are both G-invariant, where $W_1 \neq W_2$, with bases

$B_1 = \{w_1, w_2, \cdots, w_n\}$ and $B_2 = \{u_1, u_2, \cdots, u_m\}$, respectively, and if V has a basis $B_V = B_1 \cup B_2$,

then we say that V is the direct sum of W_1 and W_2, or $V = W_1 \oplus W_2$, and we will be able to find

representations R_g for all $g \in G$ in the block-diagonal form

$$R_g = \begin{pmatrix} A_g & 0 \\ 0 & B_g \end{pmatrix} \tag{A.7}$$

where A_g is a representation of g over W_1 and B_g is a representation of g over W_2. A representation

which cannot be written in this block-diagonal form is said to be irreducible and is known as an

irrep. In other words, the representation of G which acts on vectors in space V is an irrep if V has

no proper G-invariant subspaces.

When using the matrix representations of a group, the most important thing to investigate

is the trace of the matrices, also known as the character χ_R of the matrix of representation R.[19]

Essentially, χ_R is a homomorphism $\chi_R : GL_n \to \mathbb{R}$ mapping elements of the representation to their

traces. There are several important and useful properties of $\chi(g)$:

- $\chi(1)$ is n, the dimension of the matrices in GL_n being used to describe the group G. This

  is true because the representation is by definition a homomorphism, which must map

---

[19] This is not to be confused with the character of the representation of a particular element $g \in G$, which is given by $\chi_R(g) = \text{trace}(R_g)$ and may be denoted $\chi(g)$.

identities to identities, and because the trace of an identity matrix is the dimension of the matrix. This is sometimes also called the dimension of the character.

- The character is constant over conjugacy classes. That is, if elements $g, g' \in G$ are both in the conjugacy class of $h \in G$, then $\chi(g) = \chi(g')$. This comes from the fact that conjugate matrices have the same trace.[20]

- We can define the characteristic polynomial for a representation R_g as $\det(\lambda I - R_g)$. In general, this polynomial will take the form $(x - \gamma_1)^{a_1}(x - \gamma_2)^{a_2} \cdots (x - \gamma_i)^{a_i}$ where $a_k \in \mathbb{N} \, \forall \, 1 \leq k \leq i$, such that the order of the eigenvalue γ_k is a_k. Then, for $g \in G$ with order k, the roots of the characteristic polynomial of R_g are powers of the k-th root of unity $\xi = e^{2\pi i/k}$. Thus, if R_g has dimension d, then $\chi(g)$ is a sum of d powers. This comes from the fact that the trace of a matrix is the sum of its eigenvalues because the trace is independent of the choice of basis, and we can always find a basis where the matrix is diagonal, and its entries are its eigenvalues.

- $\chi(g^{-1}) = \chi(g)^*$ because, as mentioned above, the eigenvalues will be roots of unity. We can imagine working in the basis where R_g is diagonalized. In this case, it is clear that the inverse R_g^{-1} will be the diagonal whose entries are the complex conjugates of the entries of R_g. The character then comes from adding all of these entries.

- If a representation is isomorphic – that is, arising from a homomorphism which is both injective and surjective[21] – then it must have the same character as all other isomorphic representations.

---

[20] Recall, by definition, that if $x' \in C(x)$, then $x' = gxg^{-1}$ for some $g \in G$. Since $\text{trace}(AB) = \text{trace}(BA)$, it must also hold that $\text{trace}(R_{x'}) = \text{trace}(R_g R_x R_{g^{-1}}) = \text{trace}(R_x R_{g^{-1}} R_g)$. Since homomorphisms take inverses to inverses, $R_{g^{-1}} R_g = 1$ and so $\text{trace}(R_{x'}) = \text{trace}(R_g R_x R_{g^{-1}}) = \text{trace}(R_x)$

[21] A surjective homomorphism satisfies that, for all $g' \in G'$, there exists some $g \in G$ such that $\varphi(g) = g'$..

We can define a Hermitian product on characters as

$$\langle \chi, \chi' \rangle = \frac{1}{|G|} \sum_{g \in G} \left(\chi(g) \right)^* \chi'(g). \tag{A.8}$$

Because character is constant on conjugacy classes, this can be rewritten in terms of the orders of the conjugacy classes $|C_i|$ in the group:

$$\langle \chi, \chi' \rangle = \frac{1}{|G|} \sum_{i=1}^{r} |C_i| \left(\chi(g_i) \right)^* \chi'(g_i) \tag{A.9}$$

where g_i is any representative element of the conjugacy class C_i and r is the number of conjugacy classes in the group G.

It can then be shown that all irreducible characters of a finite group G are orthonormal under the Hermitian product and that, for $\rho_1, \rho_2, \cdots, \rho_r$ the isomorphism classes of the irreducible representations of G with characters $\chi_1, \chi_2, \cdots, \chi_r$ and dimensions $d_1, d_2, \cdots, d_r$, we have $|G| = d_1^2 + \cdots d_r^2$.[22] Further, a character is irreducible if and only if $\langle \chi, \chi \rangle = 1$. For example, if $\langle \chi, \chi \rangle = 2$, then χ is the sum of two distinct irreducible characters. If instead $\langle \chi, \chi \rangle = 4$, then either χ is the sum of four distinct irreducible characters or $\chi = 2\chi'$ for some irreducible character χ'.

As an example of the concepts illustrated thus far, we will look again at the group S_3. In addition to the trivial representation, this group has two other unique representations. We will denote the trivial representation Γ_1. The second representation, Γ_2, is known as the sign representation and maps every permutation to the sign of the permutation. That is,

$$\Gamma_{2,x} = 1, \qquad \Gamma_{2,y} = -1. \tag{A.10}$$

This is not a faithful representation, but the third representation, Γ_3, is faithful. In particular, Γ_3 is known as the standard representation and is given by

---

[22] Note that because the trivial representation is a possible representation for all groups, it must be true that at least one $d_i = 1$ in this sum.

$$\Gamma_{3,x} = \begin{pmatrix} \cos\left(\dfrac{2\pi}{3}\right) & -\sin\left(\dfrac{2\pi}{3}\right) \\ \sin\left(\dfrac{2\pi}{3}\right) & \cos\left(\dfrac{2\pi}{3}\right) \end{pmatrix}, \qquad \Gamma_{3,y} = \begin{pmatrix} 1 & 0 \\ 0 & -1 \end{pmatrix}. \tag{A.11}$$

Recall that the character of the representation is the trace. We can thus summarize the characters of these three representations of S_3 in a character table, as shown in Figure A.1. We can immediately see that, in all cases, $\chi(1)$ is the dimension of the representation. Further, we can investigate the Hermitian product defined for characters to look at whether $\Gamma_1, \Gamma_2, \Gamma_3$ are all irreducible and independent. This can be done explicitly:

$$\langle \chi_1, \chi_1 \rangle = \frac{1}{6}(1 \times 1 \times 1 + 2 \times 1 \times 1 + 3 \times 1) = 1$$

$$\langle \chi_1, \chi_2 \rangle = \frac{1}{6}(1 \times 1 \times 1 + 2 \times 1 \times 1 + 3 \times 1 \times -1) = 0$$

$$\langle \chi_1, \chi_3 \rangle = \frac{1}{6}(1 \times 1 \times 2 + 2 \times 1 \times -1 + 3 \times 1 \times 0) = 0$$

$$\langle \chi_2, \chi_2 \rangle = \frac{1}{6}(1 \times 1 \times 1 + 2 \times 1 \times 1 + 3 \times -1 \times -1) = 1$$

$$\langle \chi_2, \chi_3 \rangle = \frac{1}{6}(1 \times 1 \times 2 + 2 \times 1 \times -1 + 3 \times -1 \times 0) = 0$$

$$\langle \chi_3, \chi_3 \rangle = \frac{1}{6}(1 \times 2 \times 2 + 2 \times -1 \times -1 + 3 \times 0 \times 0) = 1$$

Recalling that irreducible representations have $\langle \chi, \chi \rangle = 1$ and non-isomorphic representations have $\langle \chi_1, \chi_2 \rangle = 0$, we have that indeed all three representations of S_3 are irreducible and independent.

S_3	1	x	x^2	y	xy	x^2y
Γ_1	1	1	1	1	1	1
Γ_2	1	1	1	−1	−1	−1
Γ_3	2	−1	−1	0	0	0

Figure A.1 – The character table for S_3.

It is then useful to ask if there are any other irreducible independent representations of S_3. It turns out that we can state definitively that there are not. This is because, as was shown above,

$$|G| = \sum_i d_i^2.$$

A.12

In this case, the dimension of Γ_1 is 1, as is the dimension of Γ_2. Thus, we have

$$|S_3| = d_{\Gamma_1}^2 + d_{\Gamma_2}^2 + d_{\Gamma_3}^2$$

A.13

or $6 = 1^2 + 1^2 + 2^2$. Thus there can be no more independent irreducible representations of S_3.

It may also be useful to mention that we could, for example, define a conjugate representation for Γ_3 by picking our favorite 2×2 invertible matrix and using it to change the basis of the representation. However, the traces of the new representation must be the same as those of the old representation, and so the two representations will be equivalent.

Symmetries and Degeneracies

A degeneracy occurs in a system where two or more eigenstates share the same energy. In general, there are two possible types of degeneracies – accidental and protected. An accidental degeneracy is a degeneracy which exists without any particular physical reason. It is usually lifted once further properties of the system are considered in the mathematical modelling. For example, when we learn about the hydrogen atom in quantum mechanics, we find it is highly degenerate, but many of those degeneracies are lifted when we consider the Zeeman effect or spin-orbit

coupling. In this case, we have not considered a full and complete picture for the hydrogen atom, and so the holes in our model contribute to the appearance of accidental degeneracies. A protected degeneracy, in contrast, is one for which there is a physical reason such that the degeneracy cannot be lifted as long as the reason for the degeneracy remains. It is common that the physical phenomenon causing a protected degeneracy is a symmetry property of the system.

If we have an n-fold degenerate energy level, we can relate two bases for the levels through a unitary matrix – that is, we can perform a change of basis operation. Because this matrix does not change the physics of the system, it must obey the symmetry of the system. That is, the unitary change of basis matrix must be a representation of the point group of the system. If it is a reducible representation, we can make it block diagonal, as discussed above, and thus we see that the full degeneracy of the system is not protected. In contrast, if the representation is irreducible, then the degeneracy is protected.

This leads to a couple of concepts. For one, if the point group has an n-dimensional representation, then it could have an n-fold protected degeneracy. The contrast is also true – if the group does not have an n-dimensional representation, then it cannot have an n-fold protected symmetry, and any such observed symmetry must be accidental. Along with this, we can say that systems modeled by abelian point groups cannot have degeneracies.

APPENDIX B

Crystalline Point Groups

We will now present an overview of crystallographic point groups. Often, when we discuss crystal structures, we use a concept known as the Bravais lattice, which is in a way the most basic lattice describing the crystal. It is formed by looking at the relations between identical points in each of the repeating primitive unit cells. In particular, the Bravais lattice is formed by all points accessible through translations by linear combinations $n_1\overrightarrow{a_1} + n_2\overrightarrow{a_2} + n_3\overrightarrow{a_3}$ for primitive lattice vectors $\overrightarrow{a_1}, \overrightarrow{a_2}, \overrightarrow{a_3}$ and $n_1, n_2, n_3 \in \mathbb{Z}$. There are 14 different Bravais lattices which can occur in seven different crystal systems: orthorhombic (primitive, base-centered, body-centered, face-centered)[23], monoclinic (primitive, base-centered), triclinic, tetragonal (primitive, body/face-centered), hexagonal, trigonal, and cubic (primitive, body-centered, face-centered).

One of the most important Bravais lattice is the reciprocal lattice, which is the set of all wave vectors $\vec{K}$ that yield plane waves with the same periodicity of some other Bravais lattice of the crystal. In particular, for a Bravais lattice spanned by primitive unit vectors $\overrightarrow{a_1}$, $\overrightarrow{a_2}$, $\overrightarrow{a_3}$, we can define primitive vectors for the reciprocal lattice as

---

[23] Each of these describes a different orientation of the Bravais lattice. That is, different locations of the lattice points on the unit cell. For primitive Bravais lattices, lattice points only exist on the corners of the cells. Every Bravais lattice has at least this orientation. Base-centered indicates that there are lattice points on the corners of the cell as well as at the center of one pair of parallel faces. Body-centered indicates lattice points on the corners of the cell and at the center of the cell. Face-centered indicates lattice points on the corners of the cell and at the center of each face of the cell.

$$\vec{b_1} = 2\pi\,\vec{a_2} \times \frac{\vec{a_3}}{\vec{a_1} \cdot (\vec{a_2} \times \vec{a_3})}, \qquad \vec{b_2} = 2\pi\,\vec{a_3} \times \frac{\vec{a_1}}{\vec{a_1} \cdot (\vec{a_2} \times \vec{a_3})},$$

$$\vec{b_3} = 2\pi\,\vec{a_1} \times \frac{\vec{a_2}}{\vec{a_1} \cdot (\vec{a_2} \times \vec{a_3})}.$$

B.1

Because this Bravais lattice is made of wave vectors, it is essentially a visualization of the crystal

structure in momentum space [64].
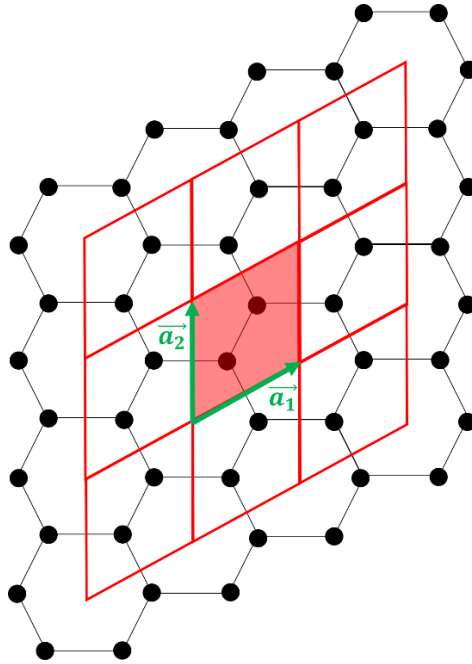
Figure B.1 – As an illustrative example of the Bravais lattice and the symmetry operations involved in creating a full crystal structure, we consider the honeycomb lattice of two-dimensional graphene. The black dots are the locations of the carbon atoms and the hexagonal black lines highlight what we typically think of as the hexagonal crystal structure of graphene. In red, we see that the primitive unit cell is actually a single parallelogram (shaded). The tessellation of that parallelogram defines the Bravais lattice, with primitive lattice vectors $\vec{a_1}$, $\vec{a_2}$ labeled in green.

One oddity which arises from working with real crystals is, because we must have

translational symmetry, we can only have 2-, 3-, 4-, or 6-fold rotational symmetry in any physical

system. The proof of this is fairly straightforward. Referring to Figure B.2, we have that the blue

dots constitute one row of the Bravais lattice, the light blue dots are a rotation by θ, and the dark blue dots are a rotation by $-\theta$. If rotation by θ is a symmetry of the system, then so too must be the rotation by $-\theta$ because all groups are closed under inverses. If these rotations are symmetries of the system, then the light and dark blue dots must also be part of the Bravais lattice and so the distance between any two of these dots must be equal to some integer times the lattice constant a.
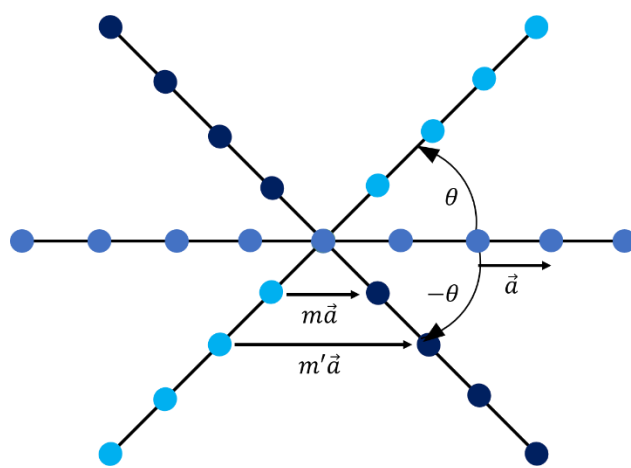
Figure B.2 – An illustration of the portions of a crystal lattice which might be generated using rotations. This image serves as a reference for the proof that a real crystal may only have 2-, 3-, 4-, or 6-fold rotational symmetry. It is adapted from [205].

We can then consider the triangle formed by the central blue dot and the dots connected by vector $m\vec{a}$ in Figure B.2. It must be an isosceles triangle of side lengths a, a, ma, and the top angle must be $\pi - 2\theta$. Using the law of cosines, we must then have that

$$ma = \sqrt{a^2 + a^2 - 2a^2 \cos(\pi - 2\theta)} = 2a \cos(\theta). \qquad \text{B.2}$$

Or $\cos(\theta) = \frac{m}{2}$. Because m is an integer and $-1 \le |\cos(\theta)| \le 1$, we can only have that $m \in \{-2, -1, 0, 1, 2\}$ and so $\theta \in \{\pi, \frac{2\pi}{3}, \frac{\pi}{2}, \frac{\pi}{3}, 0\}$.

Because of the restriction of the degree of rotation, there are only 32 possible point groups in real crystal systems. There are two basic notational conventions used to describe these groups: Schoenflies notation and Hermann-Manguin notation. In Schoenflies notation, the point groups are denoted by a letter symbol with a subscript as follows:

- C_n – the cyclic group which has an n-fold rotational axis

  - C_{nh} has, in addition to the n-fold rotational axis, a mirror plane perpendicular to the axis of rotation

  - C_{nv} has, in addition to the n-fold rotational symmetry, mirror planes parallel to the axis of rotation

- S_{2n} – the Spiegel group has a $2n$-fold rotation-reflection axis

- D_n – the dihedral group has an n-fold rotation axis and n two-fold axes perpendicular to that axis

  - D_{nh} has, in addition to the D_n symmetries, a mirror plane perpendicular to the n-fold axis

  - D_{nv} has, in addition to the D_n symmetries, mirror planes parallel to the n-fold axis

- T – the tetrahedral group has the symmetry of a tetrahedron

  - T_d includes proper rotations

  - T excludes proper rotations

  - T_h has, in addition to the T symmetries, a center of inversion

- O – the octahedral group has the symmetry of an octahedron, or cube

  - O_h includes proper rotations

  - O excludes improper rotations

The Hermann-Manguin notation is the standard notation for point groups. The rotation axes are denoted by a number n such that the angle of rotation is given by $2\pi/n$. Improper rotations are shown with rotoinversion axes as $\bar{n}$. Mirror planes are denoted m. The direction of a symmetry element is dictated by its position in the symbol. Rotations and mirrors in the same direction are denoted as a fraction ($\frac{n}{m}$ or n/m). If the symbol contains three positions, they denote the symmetry elements in the x, y, z spatial coordinates, respectively. The correspondence between the Schoenflies notation and the Hermann-Manguin notation for the various point groups is shown in Table B.1.

Crystal System	Full H-M	Short H-M	Schoenflies	Order
Triclinic	1	1	C_1	1
Triclinic	$\bar{1}$	$\bar{1}$	$C_i = S_2$	2
Monoclinic	2	2	C_2	2
Monoclinic	m	m	$C_s = C_{1h}$	2
Monoclinic	$\dfrac{2}{m}$	$2/m$	C_{2h}	4
Orthohombic	222	222	$D_2 = V$	4
Orthohombic	$mm2$	$mm2$	C_{2v}	4
Orthohombic	$\dfrac{2}{m}\dfrac{2}{m}\dfrac{2}{m}$	mmm	$D_{2h} = V_h$	8
Tetragonal	4	4	C_4	4
Tetragonal	$\bar{4}$	$\bar{4}$	S_4	4
Tetragonal	$\dfrac{4}{m}$	$4/m$	C_{4h}	8

Tetragonal	422	422	D_4	8
Tetragonal	$4mm$	$4mm$	C_{4v}	8
Tetragonal	$\bar{4}2m$	$\bar{4}2m$	$D_{2d} = V_d$	8
Tetragonal	$\dfrac{4}{m}\dfrac{2}{m}\dfrac{2}{m}$	$4/mmm$	D_{4h}	16
Trigonal	3	3	C_3	3
Trigonal	$\bar{3}$	$\bar{3}$	$S_6 = C_{3i}$	6
Trigonal	32	32	D_3	6
Trigonal	$3m$	$3m$	C_{3v}	6
Trigonal	$\bar{3}\dfrac{2}{m}$	$\bar{3}m$	D_{3d}	12
Hexagonal	6	6	C_6	6
Hexagonal	$\bar{6}$	$\bar{6}$	C_{3h}	6
Hexagonal	$\dfrac{6}{m}$	$6/m$	C_{6h}	12
Hexagonal	622	622	D_6	12
Hexagonal	$6mm$	$6mm$	C_{6v}	12
Hexagonal	$\bar{6}m2$	$\bar{6}m2$	D_{3h}	12
Hexagonal	$\dfrac{6}{m}\dfrac{2}{m}\dfrac{2}{m}$	$6/mmm$	D_{6h}	24
Isometric	23	23	T	12
Isometric	$\dfrac{2}{m}\bar{3}$	$m\bar{3}$	T_h	24
Isometric	432	432	O	24
Isometric	$\bar{4}3m$	$\bar{4}3m$	T_d	24

Isometric	$\dfrac{4}{m}\bar{3}\dfrac{2}{m}$	$m\bar{3}m$	O_h	48

Table B.1 - A table of the 32 different point groups for physical crystal systems and how they are denoted using both the Herman-Manguin and Schoenflies notations [64].

APPENDIX C

A Review of Band Structure

Using the Drude model of metallic crystals, we can model electrons in a crystalline material as a gas of otherwise free particles, subject only to the immobile potential caused by the atoms of the crystal [61, 62]. Thus, in effect, modeling crystal energy structures essentially boils down to solving the problem of a free electron in a periodic potential[24]. This requires the use of quantum mechanics.

The first and simplest quantum mechanical problem we are taught in the course of our physics studies is that of the 1d free electron. In this case, the Hamiltonian consists only of a kinetic energy term, and the Schrodinger Equation is

$$-\frac{\hbar^2}{2m}\frac{\partial^2 \psi}{\partial x^2} = E\psi. \qquad \text{C.1}$$

We assume that the solution takes the form $\psi(x) = Ae^{\pm ikx}$. By requiring the wave function be normalized, we find $A = \sqrt{\frac{2}{m}}$. And substituting this into the Schrodinger equation, we get a relationship between E and k of

$$E = \frac{\hbar^2 k^2}{2m}. \qquad \text{C.2}$$

---

[24] Of course, this is certainly not the whole picture for the calculation of band structure, nor even for the modeling of electrons in a metallic state. There are numerous limitations to the Drude model which have come up in countless experiments and have required adjustments to the underlying assumptions, not the least of which is the requirement that electrons obey the Fermi-Dirac distribution rather than the Bose-Einstein distribution, which was not discovered until after the Drude model was first formulated [206, 207]. For a review of some other shortcomings of this model, please see [64].

Here, we call k the wavevector of the wave function $\psi(x)$. The de Broglie relation tells us that k is related to the momentum p of the particle as $p = \hbar k$, so k is frequently used as a stand-in for momentum in discussions of crystalline materials and band structure. In addition, relations between position- and momentum-space are well-established by means of Fourier transformations.

Now we will go to a slightly more complicated setup – that of a free electron in a 1d periodic potential, as shown in Figure C.1b. This translates to a periodic spacing of atoms in a 1d chain providing a periodic and immovable potential which the otherwise free electrons are subject to. Here, we will assume that each atom is a distance a away from each of its nearest neighbors. This chain of atoms yields a periodic potential $U(x) = U(x + a)$, so we must have $\psi(x) = \psi(x + Na)$ for integers N. The solution to this problem is given by Bloch's Theorem as

$$\psi_k(x) = u_{n,k}(x)e^{ikx} \tag{C.3}$$

for $u_{n,k}(x) = u_{n,k}(x + a)$ and where n labels individual bands in the energy structure[25]. This solution is known as a Bloch wave [208]. The requirement of a labeling scheme n arises because for any k there exist multiple solutions of the Schrodinger equation due to the periodic behavior of the potential. Because k is a continuously varying parameter but is subject to periodicity by way of the reciprocal lattice, we can assign the indices n such that, for a given n, the eigenstates and eigenvalues are periodic functions of k in the reciprocal lattice. That is,

$$\psi_{n,k+K}(x) = \psi_{n,k}(x), \qquad E_{n,k+K} = E_{n,k}. \tag{C.4}$$

These functions $E_{n,k}$ then form the band structure of the material.

---

[25] Here keep in mind that here, in the solution to the Bloch equation, k does not actually obey the de Broglie relation. Instead, $\hbar k$ is known as the crystal momentum (though often just referred to haphazardly as the momentum), which is a quantum number characteristic of the translational symmetry of the crystal. The relationship with momentum returns only in the presence of external electromagnetic waves.

Even with a simple 1d chain potential, gaps must open up in the otherwise smooth wavefunction of the free particle. We have already identified the solution to the free particle Schrodinger equation as $\psi(x) = Ae^{\pm iKx}$ for normalization constant A and placeholder variable K, where boundary conditions dictate that $K = \frac{n\pi}{a}$ for some integer n. For this discussion we will restrict ourselves to $n = 1$. If we treat the 1d chain potential as only a small perturbation, we find there must be gaps which open up in the energy spectrum at the edges of the Brillouin zone. To see this, we can construct two linearly independent superpositions of our solution to the free particle Hamiltonian which must be degenerate in energy: $\psi_{\pm}(x) = e^{\frac{i\pi x}{a}} \pm e^{-\frac{i\pi x}{a}}$, or
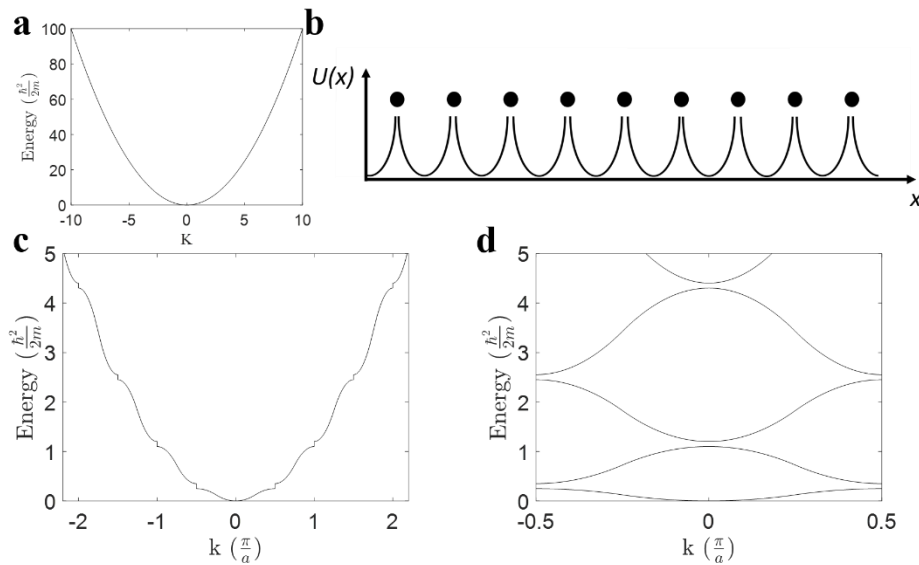
Figure C.1 – Band Diagram Illustrations. (a) The dispersion relation for a free particle. (b) An example periodic potential caused by a 1d ion chain. (c) Gaps are opened up in the free particle potential when it is perturbed by the 1d periodic lattice. Here, calculations assume a potential of the form $U(x) = x^2$ for the area between the ions. (d) An example of folding the dispersion relation in (c) into the first Brillouin zone to get a folded band structure diagram.

$$\psi_{\pm}(x) = \begin{cases} \cos\left(\dfrac{\pi x}{a}\right) \\ \sin\left(\dfrac{\pi x}{a}\right) \end{cases} \tag{C.5}$$

Then we can see that, at the boundary of the Brillouin zone, a gap in the energy opens of size

$$E_g = \left| \int_0^a U(x)\left(\psi_+^2(x) - \psi_-^2(x)\right)dx \right|. \tag{C.6}$$

When we are illustrating this band structure, because we are working with a periodic potential, it is convenient to draw the dispersion relation within a single primitive cell. The primitive cell of the reciprocal lattice typically chosen for this is the first Brillouin zone. For a 1d system, this first Brillouin zone is defined as $-\frac{\pi}{a} \le k \le \frac{\pi}{a}$. Relations outside of this zone are then folded into view. An illustration of this is shown in Figure C.1d for the case of the free particle in the 1d periodic potential. This type of illustration is known as the band diagram of the material [64]. When we are discussing band diagrams, several high symmetry points are considered to be of particular interest. These points are typically defined depending on the crystal structure of the material, but all materials will have a Γ point, which is the center of the Brillouin zone. Other examples of high symmetry points include the X point, which is the center of a square face for a simple or face-centered cubic structure, and the N point, which is the center of a face in a body-centered cubic structure.

Of course, there are always exceptions to pictures we use to model behavior. Band theory works best in systems with minimal interactions between electrons, or when the kinetic energy of the electrons in the material dominates other energy scales of the system. However, some materials have very narrow band gaps or strong electron-electron or electron-impurity interactions which can cause insulating behavior in materials which would otherwise be conducting [209]. In addition, often perturbations of these interactions by doping, temperature, etc. may cause a metal-insulator transition, as for example presented in [210] for $NaOsO_3$.

APPENDIX D

Chirality and Helicity

We know that if we have an electron in a magnetic field, the particle will move in a circular motion. This is because the force on the particle is necessarily perpendicular to both the field and the velocity of the particle. If we were to reverse the time of such a setup, we would see that the particle continues to rotate, but now in the opposite direction. That is, a clockwise rotation would become counterclockwise, and vis versa. This idea of handedness is intimately connected to the properties of helicity and chirality, which will play an important role in our discussion of WSMs below.

Chirality and helicity both have to do with the spin of the electron. Helicity is the sign of the projection of the spin vector onto the momentum vector, as shown in Figure D.1. Chirality is more complicated in that it depends on the point of view of the observer. For massive particles, which must necessarily move at speeds less than the speed of light, chirality depends on whether the motion of the particle appears to be clockwise or counterclockwise in the reference frame of the observer. In our discussion of Weyl semimetals, we will deal with massless particles. Because such particles must move at the speed of light, there is no frame of reference which can change the apparent rotation/spin of the particle, and so chirality and helicity are interchangeable.
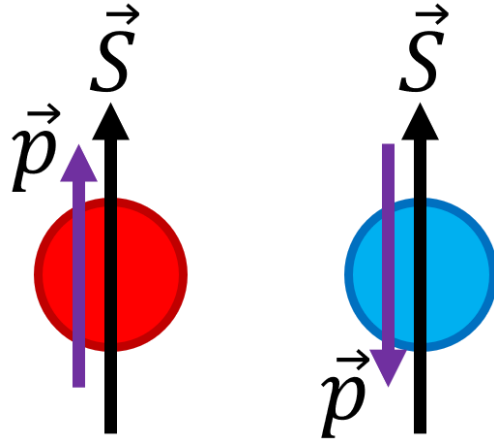
Figure D.1 – An illustration of helicity. For the red electron, the spin and momentum vectors are aligned, so the projection of one onto another is positive. Thus, the red electron is right-handed. For the blue electron, the opposite is true. That is, the spin and momentum vectors are antialigned, so the projection of one onto another is negative – the electron is left-handed. If these electrons were instead photons or some other massless relativistic particle, then their helicity would also determine their chirality.

Example Code for Calculating the Size of the Nonlinear Susceptibility Tensor Elements

The code presented below is used to derive a functional form with which to fit the data obtained

for the WTe$_2$ RA-SHG experiment in order to estimate the size of the susceptibility tensor elements

and thus the strength of the SHG response in this material. This code is written in Mathematica

```
(*Simulate RA-SHG experiments taking the Fresnel corrections into consideration for RFSeO
in normal incidence only*)

ClearAll["Global`*"]

(*Angle of incidence, change to \[Theta]i to do numeric computations*)

Θi = 0;

(*Indices of refraction *)

niω = 1; (*Air*)
ntω = 0.75; (*Fundamental in sample*)
nt2ω = 2; (*SHG in sample*)
κ1 = 9/ntω;
κ2 = 3.1/nt2ω;

(*Experimental parameters*)

Pavg = 0.5*10^-3; (*Average power*)
frep = 200*10^3; (*Rep rate*)
tau = 120*10^-15; (*Pulse duration*)
rFund = 30*10^-6; (*Radius of fundamental beam*)

(*Compute Eiamp*)

Pmax = Pavg/(frep*tau);
```

```
Eiamp = Sqrt[2*Pmax/(Pi*rFund^2*3*10^8*8.854*10^-12)];
```

(*Take absorption scale factor into account*)

```
scaleFactor = 8.854*10^-12;
```

(*Incoming wave vector*)

```
ki = (ωc)*{Sin[Θi], 0, -Cos[Θi]};
```

(*Incoming E-fields*)

```
Eipin = Eiamp*{Cos[Θi], 0, Sin[Θi]};
Eisin = Eiamp*{0, 1, 0};
```

(*Rotation matrix*)

```
Rotz[Φ_] := {{Cos[Φ], -Sin[Φ], 0}, {Sin[Φ], Cos[Φ], 0}, {0, 0, 1}};
```

(*Define the nonlinear susceptibility tensor*)

```
tensor2 = {{{0, xyx, xzx}, {xyx, 0, 0}, {xzx, 0, 0}}, {{yxx, 0, 0}, {0, yyy, yzy}, {0, yzy, yzz}}, {{zxx,
0, 0}, {0, zyy, zzy}, {0, zzy, zzz}}}susu;
```

(*Fundamental angle of incidence = fundamental angle of reflection*)

```
Θr = Θi;
```

(*Snell's law to calculate Θt for fundamental*)

```
temp = Solve[niω*Sin[Θi] == ntω*Sin[Θt], Θt];
Θt = (temp[[1]] /. (x_ -> y_) -> y)[[1]]
```

```
0
```

(*SHG Snell's law equivalents*)

```
Θ2r = Θi;
temp2t = Solve[Sin[Θi]/nt2ω == Sin[Θ2t], Θ2t];
Θ2t = (temp2t[[1]] /. (x_ -> y_) -> y)[[1]];
temps = Solve[Sin[Θi]/ntω == Sin[Θs], Θs];
Θs = (temps[[1]] /. (x_ -> y_) -> y)[[1]];
```

```
Θr = 0;
```

Θs = 0;

(*Compute wave vectors*)

```
kx1r = ki[[1]];
k1rabs = ω/c;
k1r = k1rabs*{Sin[Θr], 0, Cos[Θr]};
kx1t = ki[[1]];
k1tabs = ntω*ω/c;
k1t = k1tabs*{Sin[Θt], 0, -Cos[Θt]};
kxs = 2*kx1t;
ksabs = 2*k1tabs;
ks = ksabs*{Sin[Θs], 0, -Cos[Θs]};
kx2r = 2*ki[[1]];
k2rabs = 2*ω/c;
k2r = k2rabs*{Sin[Θ2r], 0, Cos[Θ2r]};
kx2t = 2*ki[[1]];
k2tabs = 2*nt2ω*ω/c;
k2t = k2tabs*{Sin[Θ2t], 0, -Cos[Θ2t]};
```

(*pin*)

(*Define E0t*)

Etpin = 2*Cos[Θi]*Eipin/(ntω*Cos[Θi] + Cos[Θt]);

(*Define Ert*)

Erpin = (Cos[Θt] - ntω*Cos[Θi])*Eipin/(Cos[Θt] + ntω*Cos[Θi]);

(*Define E0t*)

Etsin = 2*Cos[Θi]*Eisin/(Cos[Θi] + ntω*Cos[Θt]);

(*Define Ert*)

Ersin = (Cos[Θi] - ntω*Cos[Θt])*
  Eisin/(Cos[Θi] + ntω*Cos[Θt]);

(*Simulate experiment by rotating tensor about the z-axis*)

tensor2Rotz = FullSimplify[Transpose[Rotz[Φ - α].Transpose[Rotz[Φ - α]. (tensor2.
Transpose[Rotz[Φ - α]])]]];

(*Calculate PNLS for s-in*)

PxPin = scaleFactor*Sum[tensor2Rotz[[1, i]][[j]] Etpin[[i]] Etpin[[j]], {i, 1, 3}, {j, 1, 3}]
PyPin = scaleFactor*Sum[tensor2Rotz[[2, i]][[j]] Etpin[[i]] Etpin[[j]], {i, 1, 3}, {j, 1, 3}]
PzPin = scaleFactor*Sum[tensor2Rotz[[3, i]][[j]] Etpin[[i]] Etpin[[j]], {i, 1, 3}, {j, 1, 3}]

8.854*10^-12 (0. + 7.24635*10^15 ((2 xyx + yxx) Cos[α - Φ]^2 Sin[α - Φ] + yyy Sin[α - Φ]^3))

8.854*10^-12 (0. + 7.24635*10^15 Cos[α - Φ] (yxx Cos[α - Φ]^2 + (-2 xyx + yyy) Sin[α - Φ]^2))

8.854*10^-12 (0. + 7.24635*10^15 (zxx Cos[α - Φ]^2 + zyy Sin[α - Φ]^2))

(*Calculate PNLS for s-in*)

PxSin = scaleFactor*Sum[tensor2Rotz[[1, i]][[j]] Etsin[[i]] Etsin[[j]], {i, 1, 3}, {j, 1, 3}]
PySin = scaleFactor*Sum[tensor2Rotz[[2, i]][[j]] Etsin[[i]] Etsin[[j]], {i, 1, 3}, {j, 1, 3}]
PzSin = scaleFactor*Sum[tensor2Rotz[[3, i]][[j]] Etsin[[i]] Etsin[[j]], {i, 1, 3}, {j, 1, 3}]

8.854*10^-12 (0. + 7.24635*10^15 Sin[α - Φ] ((-2 xyx + yyy) Cos[α - Φ]^2 + yxx Sin[α - Φ]^2))

8.854*10^-12 (0. + 7.24635*10^15 (yyy Cos[α - Φ]^3 + (2 xyx + yxx) Cos[α - Φ] Sin[α - Φ]^2))

8.854*10^-12 (0. + 7.24635*10^15 (zyy Cos[α - Φ]^2 + zxx Sin[α - Φ]^2))

(*Compute B-fields*)

Bipin = (c/ω)*Cross[ki, Eipin];
Brpin = (c/ω)*Cross[k1r, Erpin];
Btpin = (c/ω)*Cross[k1t, Etpin];

(*Compute B-fields*)

Bisin = (c/ω)*Cross[ki, Eisin];
Brsin = (c/ω)*Cross[k1r, Ersin];
Btsin = (c/ω)*Cross[k1t, Etsin];

(*Compute shg fields*)

E2tpin = FullSimplify[E2tamp*{E2tx, E2ty, E2tz} - 4*Pi*4*ω^2/c^2/(k2tabs^2 - ksabs^2)*({Px, Py, Pz} - ks*(ks.{Px, Py, Pz})/k1tabs^2)];

213

```
B2tpin = FullSimplify[(c/(2*ω))*Cross[k2t, {E2tx, E2ty, E2tz}]*E2tamp - 4*Pi*(4*ω^2/c^2)*c*
Cross[ks, {Px, Py, Pz}]/(2*ω*(k2tabs^2 - ksabs^2))];
E2rpin = E2ramp*{E2rx, E2ry, E2rz};
B2rpin = FullSimplify[(c/(2*ω))*Cross[k2r, E2rpin]];

(*Compute shg fields*)

E2tsin = Simplify[E2tamp*{E2tx, E2ty, E2tz} - 4*Pi*4*ω^2/c^2/(k2tabs^2 - ksabs^2)*({Px, Py,
Pz} - ks*(ks.{Px, Py, Pz})/k1tabs^2)];
B2tsin = Simplify[(c/(2*ω))*Cross[k2t, {E2tx, E2ty, E2tz}]*E2tamp - 4*Pi*(4*ω^2/c^2)*c*
Cross[ks, {Px, Py, Pz}]/(2*ω*(k2tabs^2 - ksabs^2))];
E2rsin = E2ramp*{E2rx, E2ry, E2rz};
B2rsin = Simplify[(c/(2*ω))*Cross[k2r, E2rpin]];

(*Solve for z-components*)

solp1 = Solve[{E2tx^2 + E2ty^2 + E2tz^2 == 1, E2rx^2 + E2ry^2 + E2rz^2 == 1}, {E2tz, E2rz}]

{{E2tz -> -Sqrt[1 - E2tx^2 - E2ty^2], E2rz -> -Sqrt[1 - E2rx^2 - E2ry^2]}, {E2tz -> -Sqrt[1 -
E2tx^2 - E2ty^2], E2rz -> Sqrt[1 - E2rx^2 - E2ry^2]}, {E2tz -> Sqrt[1 - E2tx^2 - E2ty^2], E2rz
-> -Sqrt[1 - E2rx^2 - E2ry^2]}, {E2tz -> Sqrt[1 - E2tx^2 - E2ty^2], E2rz -> Sqrt[1 - E2rx^2 -
E2ry^2]}}

(*Select tz negative and rz positive, solve for E2tx*)

E2tpinx = FullSimplify[E2tpin[[1]] /. solp1[[2]]];
E2rpinx = FullSimplify[E2rpin[[1]] /. solp1[[2]]];
E2tpiny = FullSimplify[E2tpin[[2]] /. solp1[[2]]];
E2rpiny = FullSimplify[E2rpin[[2]] /. solp1[[2]]];
E2tpinz = FullSimplify[E2tpin[[3]] /. solp1[[2]]];
E2rpinz = FullSimplify[E2rpin[[3]] /. solp1[[2]]];
B2rpinx = FullSimplify[B2rpin[[1]] /. solp1[[2]]];
B2tpinx = FullSimplify[B2tpin[[1]] /. solp1[[2]]];
B2rpiny = FullSimplify[B2rpin[[2]] /. solp1[[2]]];
B2tpiny = FullSimplify[B2tpin[[2]] /. solp1[[2]]];
B2rpinz = FullSimplify[B2rpin[[3]] /. solp1[[2]]];(*Fully solved*)
B2tpinz = FullSimplify[B2tpin[[3]] /. solp1[[2]]];(*Fully solved*)

solp2 = Solve[E2rpinx == E2tpinx, E2rx]

{{E2rx -> (0. + 1. E2tamp E2tx - 3.65567 Px)/E2ramp}}

E2tpinx = FullSimplify[E2tpinx /. solp2[[1]]];
E2rpinx = FullSimplify[E2rpinx /. solp2[[1]]];
```

```
E2tpiny = FullSimplify[E2tpiny /. solp2[[1]]];
E2rpiny = FullSimplify[E2rpiny /. solp2[[1]]];
E2tpinz = FullSimplify[E2tpinz /. solp2[[1]]];
E2rpinz = FullSimplify[E2rpinz /. solp2[[1]]];
B2rpinx = FullSimplify[B2rpinx /. solp2[[1]]];
B2tpinx = FullSimplify[B2tpinx /. solp2[[1]]];
B2rpiny = FullSimplify[B2rpiny /. solp2[[1]]];
B2tpiny = FullSimplify[B2tpiny /. solp2[[1]]];

solp3 = Solve[E2rpiny == E2tpiny, E2ry]

{{E2ry -> (0. + 1. E2tamp E2ty - 3.65567 Py)/E2ramp}}

E2tpinx = FullSimplify[E2tpinx /. solp3[[1]]]
E2rpinx = FullSimplify[E2rpinx /. solp3[[1]]]
E2tpiny = FullSimplify[E2tpiny /. solp3[[1]]]
E2rpiny = FullSimplify[E2rpiny /. solp3[[1]]]
E2tpinz = FullSimplify[E2tpinz /. solp3[[1]]]
E2rpinz = FullSimplify[E2rpinz /. solp3[[1]]]
B2rpinx = FullSimplify[B2rpinx /. solp3[[1]]]
B2tpinx = FullSimplify[B2tpinx /. solp3[[1]]]
B2rpiny = FullSimplify[B2rpiny /. solp3[[1]]]
B2tpiny = FullSimplify[B2tpiny /. solp3[[1]]]
```

0. + E2tamp E2tx - 3.65567 Px

0. + 1. E2tamp E2tx - 3.65567 Px

0. + E2tamp E2ty - 3.65567 Py

0. + 1. E2tamp E2ty - 3.65567 Py

-E2tamp Sqrt[1 - E2tx^2 - E2ty^2] + 10.967 Pz

E2ramp Sqrt[1 - (1. (1. E2tamp E2tx - 3.65567 Px)^2)/E2ramp^2 - (1. (1. E2tamp E2ty - 3.65567 Py)^2)/E2ramp^2]

0. - 1. E2tamp E2ty + 3.65567 Py

ConditionalExpression[2 E2tamp E2ty - 2.74175 Py, C[1] \[Element] Integers]

0. + 1. E2tamp E2tx - 3.65567 Px

ConditionalExpression[0. - 2. E2tamp E2tx + 2.74175 Px, C[1] \[Element] Integers]

215

E2tpinx = E2tamp E2tx - 3.656 Px;

E2rpinx = E2tamp E2tx - 3.656 Px;

E2tpiny = E2tamp E2ty - 3.656 Py;

E2rpiny = E2tamp E2ty - 3.656 Py;

E2tpinz = -E2tamp Sqrt[1 - E2tx^2 - E2ty^2] + 10.967 Pz;

E2rpinz = \[Sqrt](E2ramp^2 - (E2tamp E2tx - 3.656 Px)^2 - (E2tamp E2ty - 3.656 Py)^2);

B2rpinx = -E2tamp E2ty + 3.656 Py;

B2tpinx = 2 E2tamp E2ty - 2.742 Py;

B2rpiny = E2tamp E2tx - 3.656 Px;

B2tpiny = -2 E2tamp E2tx + 2.743 Px;

solp4 = FullSimplify[Solve[B2rpinx == B2tpinx, E2tamp]]

{{E2tamp -> (2.13267 Py)/E2ty}}

E2tpinx = FullSimplify[E2tpinx /. solp4[[1]]];
E2rpinx = FullSimplify[E2rpinx /. solp4[[1]]]
E2tpiny = FullSimplify[E2tpiny /. solp4[[1]]];
E2rpiny = FullSimplify[E2rpiny /. solp4[[1]]]
E2tpinz = FullSimplify[E2tpinz /. solp4[[1]]];
E2rpinz = FullSimplify[E2rpinz /. solp4[[1]]]
B2rpinx = FullSimplify[B2rpinx /. solp4[[1]]];
B2tpinx = FullSimplify[B2tpinx /. solp4[[1]]];
B2rpiny = FullSimplify[B2rpiny /. solp4[[1]]];
B2tpiny = FullSimplify[B2tpiny /. solp4[[1]]];

-3.656 Px + (2.13267 E2tx Py)/E2ty

-1.52333 Py

Sqrt[E2ramp^2 - 2.32054 Py^2 - (3.656 Px - (2.13267 E2tx Py)/E2ty)^2]

solp5 = FullSimplify[Solve[B2rpiny == B2tpiny, E2tx]]

{{E2tx -> (1.00016 E2ty Px)/Py}}

```
E2tpinx = FullSimplify[E2tpinx /. solp5[[1]]];
E2rpinx = FullSimplify[E2rpinx /. solp5[[1]]]
E2tpiny = FullSimplify[E2tpiny /. solp5[[1]]];
E2rpiny = FullSimplify[E2rpiny /. solp5[[1]]]
E2tpinz = FullSimplify[E2tpinz /. solp5[[1]]];
E2rpinz = FullSimplify[E2rpinz /. solp5[[1]]]
B2rpinx = FullSimplify[B2rpinx /. solp5[[1]]];
B2tpinx = FullSimplify[B2tpinx /. solp5[[1]]];
B2rpiny = FullSimplify[B2rpiny /. solp5[[1]]];
B2tpiny = FullSimplify[B2tpiny /. solp5[[1]]];
```

-1.523 Px

-1.52333 Py

Sqrt[E2ramp^2 - 2.31953 Px^2 - 2.32054 Py^2]

solp6 = Solve[E2rpinz == nt2\[Omega]*E2tpinz, E2ramp]

{{E2ramp -> -1. \[Sqrt](-15.8792 Px^2 - 15.8725 Py^2 + (18.1931 Py^2)/E2ty^2 - (187.141 Sqrt[0.999687 - 0.999687 E2ty^2 - (1. E2ty^2 Px^2)/Py^2] Py Pz)/E2ty + 481.1 Pz^2)}, {E2ramp -> \[Sqrt](-15.8792 Px^2 - 15.8725 Py^2 + (18.1931 Py^2)/E2ty^2 - (187.141 Sqrt[0.999687 - 0.999687 E2ty^2 - (1. E2ty^2 Px^2)/Py^2] Py Pz)/E2ty + 481.1 Pz^2)}}

```
E2tpinx = FullSimplify[E2tpinx /. solp6[[2]]];
E2rpinx = FullSimplify[E2rpinx /. solp6[[2]]];
E2tpiny = FullSimplify[E2tpiny /. solp6[[2]]];
E2rpiny = FullSimplify[E2rpiny /. solp6[[2]]];
E2tpinz = FullSimplify[E2tpinz /. solp6[[2]]];
E2rpinz = FullSimplify[E2rpinz /. solp6[[2]]];
B2rpinx = FullSimplify[B2rpinx /. solp6[[2]]];
B2tpinx = FullSimplify[B2tpinx /. solp6[[2]]];
B2rpiny = FullSimplify[B2rpiny /. solp6[[2]]];
B2tpiny = FullSimplify[B2tpiny /. solp6[[2]]];
```

```
E2tpinx = FullSimplify[E2tpinx /. {Px -> PxPin, Py -> PyPin, Pz -> PzPin}];
E2rpinx = FullSimplify[E2rpinx /. {Px -> PxPin, Py -> PyPin, Pz -> PzPin}];
E2tpiny = FullSimplify[E2tpiny /. {Px -> PxPin, Py -> PyPin, Pz -> PzPin}];
E2rpiny = FullSimplify[E2rpiny /. {Px -> PxPin, Py -> PyPin, Pz -> PzPin}];
E2tpinz = FullSimplify[E2tpinz /. {Px -> PxPin, Py -> PyPin, Pz -> PzPin}];
E2rpinz = FullSimplify[E2rpinz /. {Px -> PxPin, Py -> PyPin, Pz -> PzPin}];
```

```
B2rpinx = FullSimplify[B2rpinx /. {Px -> PxPin, Py -> PyPin, Pz -> PzPin}];
B2tpinx = FullSimplify[B2tpinx /. {Px -> PxPin, Py -> PyPin, Pz -> PzPin}];
B2rpiny = FullSimplify[B2rpiny /. {Px -> PxPin, Py -> PyPin, Pz -> PzPin}];
B2tpiny = FullSimplify[B2tpiny /. {Px -> PxPin, Py -> PyPin, Pz -> PzPin}];

(*Solve for z-components*)
sols1 = Solve[{E2tx^2 + E2ty^2 + E2tz^2 == 1, E2rx^2 + E2ry^2 + E2rz^2 == 1}, {E2tz, E2rz}]

{{E2tz -> -Sqrt[1 - E2tx^2 - E2ty^2], E2rz -> -Sqrt[1 - E2rx^2 - E2ry^2]}, {E2tz -> -Sqrt[1 -
E2tx^2 - E2ty^2], E2rz -> Sqrt[1 - E2rx^2 - E2ry^2]}, {E2tz -> Sqrt[1 - E2tx^2 - E2ty^2], E2rz
-> -Sqrt[1 - E2rx^2 - E2ry^2]}, {E2tz -> Sqrt[1 - E2tx^2 - E2ty^2], E2rz -> Sqrt[1 - E2rx^2 -
E2ry^2]}}

(*Select tz negative and rz positive, solve for E2tx*)

E2tsinx = Simplify[E2tsin[[1]] /. sols1[[2]]];
E2rsinx = Simplify[E2rsin[[1]] /. sols1[[2]]]
E2tsiny = Simplify[E2tsin[[2]] /. sols1[[2]]];
E2rsiny = Simplify[E2rsin[[2]] /. sols1[[2]]]
E2tsinz = Simplify[E2tsin[[3]] /. sols1[[2]]];
E2rsinz = Simplify[E2rsin[[3]] /. sols1[[2]]]
B2rsinx = Simplify[B2rsin[[1]] /. sols1[[2]]];
B2tsinx = Simplify[B2tsin[[1]] /. sols1[[2]]];
B2rsiny = Simplify[B2rsin[[2]] /. sols1[[2]]];
B2tsiny = Simplify[B2tsin[[2]] /. sols1[[2]]];
B2rsinz = Simplify[B2rsin[[3]] /. sols1[[2]]];(*Already solved*)
B2tsinz = Simplify[B2tsin[[3]] /. sols1[[2]]];(*Already solved*)

E2ramp E2rx

E2ramp E2ry

E2ramp Sqrt[1 - E2rx^2 - E2ry^2]

sols2 = Solve[E2tsinx == E2rsinx, E2rx]

{{E2rx -> -((1. (0. - E2tamp E2tx + 3.65567 Px))/E2ramp)}}

(*Solve for E2ty*)

E2tsinx = Simplify[E2tsinx /. sols2[[1]]];
E2rsinx = Simplify[E2rsinx /. sols2[[1]]]
E2tsiny = Simplify[E2tsiny /. sols2[[1]]];
E2rsiny = Simplify[E2rsiny /. sols2[[1]]]
```

218

E2tsinz = Simplify[E2tsinz /. sols2[[1]]];
E2rsinz = Simplify[E2rsinz /. sols2[[1]]]
B2rsinx = Simplify[B2rsinx /. sols2[[1]]];
B2tsinx = Simplify[B2tsinx /. sols2[[1]]];
B2rsiny = Simplify[B2rsiny /. sols2[[1]]];
B2tsiny = Simplify[B2tsiny /. sols2[[1]]];

0. + 1. E2tamp E2tx - 3.65567 Px

E2ramp E2ry

E2ramp Sqrt[1 - E2ry^2 - (1. (E2tamp E2tx - 3.65567 Px)^2)/E2ramp^2]

sols3 = Solve[E2tsiny == E2rsiny, E2ry]

{{E2ry -> -((1. (0. - E2tamp E2ty + 3.65567 Py))/E2ramp)}}

E2tsinx = Simplify[E2tsinx /. sols3[[1]]]
E2rsinx = Simplify[E2rsinx /. sols3[[1]]]
E2tsiny = Simplify[E2tsiny /. sols3[[1]]]
E2rsiny = Simplify[E2rsiny /. sols3[[1]]]
E2tsinz = Simplify[E2tsinz /. sols3[[1]]]
E2rsinz = Simplify[E2rsinz /. sols3[[1]]]
B2rsinx = Simplify[B2rsinx /. sols3[[1]]]
B2tsinx = Simplify[B2tsinx /. sols3[[1]]]
B2rsiny = Simplify[B2rsiny /. sols3[[1]]]
B2tsiny = Simplify[B2tsiny /. sols3[[1]]]

0. + E2tamp E2tx - 3.65567 Px

0. + 1. E2tamp E2tx - 3.65567 Px

0. + E2tamp E2ty - 3.65567 Py

0. + 1. E2tamp E2ty - 3.65567 Py

-E2tamp Sqrt[1 - E2tx^2 - E2ty^2] + 10.967 Pz

E2ramp Sqrt[1 - (1. (E2tamp E2tx - 3.65567 Px)^2)/E2ramp^2 - (1. (E2tamp E2ty - 3.65567 Py)^2)/E2ramp^2]

0. - 1. E2tamp E2ty + 3.65567 Py

ConditionalExpression[2 E2tamp E2ty - 2.74175 Py, C[1] \[Element] Integers]

0. + 1. E2tamp E2tx - 3.65567 Px

ConditionalExpression[0. - 2. E2tamp E2tx + 2.74175 Px, C[1] \[Element] Integers]

E2tsinx = E2tamp E2tx - 3.656 Px;

E2rsinx = E2tamp E2tx - 3.656 Px;

E2tsiny = E2tamp E2ty - 3.656 Py;

E2rsiny = E2tamp E2ty - 3.656 Py;

E2tsinz = -E2tamp Sqrt[1 - E2tx^2 - E2ty^2] + 10.967 Pz;

E2rsinz = \[Sqrt](E2ramp^2 - (E2tamp E2tx - 3.656 Px)^2 - (E2tamp E2ty - 3.656 Py)^2);

B2rsinx = - E2tamp E2ty + 3.656 Py;

B2tsinx = 2 E2tamp E2ty - 2.742 Py;

B2rsiny = E2tamp E2tx - 3.656 Px;

B2tsiny = -2 E2tamp E2tx + 2.742 Px;

sols4 = FullSimplify[Solve[B2rsinx == B2tsinx, E2tamp]]

{{E2tamp -> (2.13267 Py)/E2ty}}

E2tsinx = Simplify[E2tsinx /. sols4[[1]]];
E2rsinx = Simplify[E2rsinx /. sols4[[1]]]
E2tsiny = Simplify[E2tsiny /. sols4[[1]]];
E2rsiny = Simplify[E2rsiny /. sols4[[1]]]
E2tsinz = Simplify[E2tsinz /. sols4[[1]]];
E2rsinz = Simplify[E2rsinz /. sols4[[1]]]
B2rsinx = Simplify[B2rsinx /. sols4[[1]]];
B2tsinx = Simplify[B2tsinx /. sols4[[1]]];
B2rsiny = Simplify[B2rsiny /. sols4[[1]]];
B2tsiny = Simplify[B2tsiny /. sols4[[1]]];

-3.656 Px + (2.13267 E2tx Py)/E2ty

-1.52333 Py

Sqrt[E2ramp^2 - 2.32054 Py^2 - (3.656 Px - (2.13267 E2tx Py)/E2ty)^2]

sols5 = FullSimplify[Solve[B2rsiny == B2tsiny, E2tx]]

{{E2tx -> (1. E2ty Px)/Py}}

E2tsinx = Simplify[E2tsinx /. sols5[[1]]];
E2rsinx = Simplify[E2rsinx /. sols5[[1]]]
E2tsiny = Simplify[E2tsiny /. sols5[[1]]];
E2rsiny = Simplify[E2rsiny /. sols5[[1]]]
E2tsinz = Simplify[E2tsinz /. sols5[[1]]];
E2rsinz = Simplify[E2rsinz /. sols5[[1]]]
B2rsinx = Simplify[B2rsinx /. sols5[[1]]];
B2tsinx = Simplify[B2tsinx /. sols5[[1]]];
B2rsiny = Simplify[B2rsiny /. sols5[[1]]];
B2tsiny = Simplify[B2tsiny /. sols5[[1]]];

-1.52333 Px

-1.52333 Py

Sqrt[E2ramp^2 - 2.32054 Px^2 - 2.32054 Py^2]

sols6 = Solve[E2rsinz == nt2ω*E2tsinz, E2ramp]

{{E2ramp -> -1. \[Sqrt](-15.8725 Px^2 - 15.8725 Py^2 + (18.1931 Py^2)/E2ty^2 - (187.112 Sqrt[1. - 1. E2ty^2 - (1. E2ty^2 Px^2)/Py^2] Py Pz)/E2ty + 481.1 Pz^2)}, {E2ramp -> \[Sqrt](-15.8725 Px^2 - 15.8725 Py^2 + (18.1931 Py^2)/E2ty^2 - (187.112 Sqrt[1. - 1. E2ty^2 - (1. E2ty^2 Px^2)/Py^2] Py Pz)/E2ty + 481.1 Pz^2)}}

E2tsinx = Simplify[E2tsinx /. sols6[[2]]];
E2rsinx = Simplify[E2rsinx /. sols6[[2]]]
E2tsiny = Simplify[E2tsiny /. sols6[[2]]];
E2rsiny = Simplify[E2rsiny /. sols6[[2]]]
E2tsinz = Simplify[E2tsinz /. sols6[[2]]];
E2rsinz = Simplify[E2rsinz /. sols6[[2]]]
B2rsinx = Simplify[B2rsinx /. sols6[[2]]];
B2tsinx = Simplify[B2tsinx /. sols6[[2]]];
B2rsiny = Simplify[B2rsiny /. sols6[[2]]];
B2tsiny = Simplify[B2tsiny /. sols6[[2]]];

-1.52333 Px

-1.52333 Py

\[Sqrt](-18.1931 Px^2 + (-18.1931 + 18.1931/E2ty^2) Py^2 - (187.112 Sqrt[1. + E2ty^2 (-1. - (1. Px^2)/Py^2)] Py Pz)/E2ty + 481.1 Pz^2)

E2tsinx = Simplify[E2tsinx /. {Px -> PxSin, Py -> PySin, Pz -> PzSin}];
E2rsinx = Simplify[E2rsinx /. {Px -> PxSin, Py -> PySin, Pz -> PzSin}]
E2tsiny = Simplify[E2tsiny /. {Px -> PxSin, Py -> PySin, Pz -> PzSin}];
E2rsiny = Simplify[E2rsiny /. {Px -> PxSin, Py -> PySin, Pz -> PzSin}]
E2tsinz = Simplify[E2tsinz /. {Px -> PxSin, Py -> PySin, Pz -> PzSin}];
E2rsinz = Simplify[E2rsinz /. {Px -> PxSin, Py -> PySin, Pz -> PzSin}]
B2rsinx = Simplify[B2rsinx /. {Px -> PxSin, Py -> PySin, Pz -> PzSin}];
B2tsinx = Simplify[B2tsinx /. {Px -> PxSin, Py -> PySin, Pz -> PzSin}];
B2rsiny = Simplify[B2rsiny /. {Px -> PxSin, Py -> PySin, Pz -> PzSin}];
B2tsiny = Simplify[B2tsiny /. {Px -> PxSin, Py -> PySin, Pz -> PzSin}];

-97735.9 Sin[α - Φ] ((-2 xyx + yyy) Cos[α - Φ]^2 + yxx Sin[α - Φ]^2)

-97735.9 (yyy Cos[α - Φ]^3 + (2 xyx + yxx) Cos[α - Φ] Sin[α - Φ]^2)

\[Sqrt](-7.489*10^10 Sin[α - Φ]^2 ((-2 xyx + yyy) Cos[α - Φ]^2 + yxx Sin[α - Φ]^2)^2 + 1.9804*10^12 (zyy Cos[α - Φ]^2 + zxx Sin[α - Φ]^2)^2 + 4.1164*10^9 (-18.1931 + 18.1931/E2ty^2) (yyy Cos[α - Φ]^3 + (2 xyx + yxx) Cos[α - Φ] Sin[α - Φ]^2)^2 - 1/E2ty 7.70227*10^11 Cos[α - Φ] (yyy Cos[α - Φ]^2 + (2. xyx + yxx) Sin[α - Φ]^2) (zyy Cos[α - Φ]^2 + zxx Sin[α - Φ]^2) \[Sqrt](1. + E2ty^2 (-1. - (1. ((-2. xyx + yyy) Cos[α - Φ]^2 + yxx Sin[α - Φ]^2)^2 Tan[α - Φ]^2)/(yyy Cos[α - Φ]^2 + (2. xyx + yxx) Sin[α - Φ]^2)^2)))

(*Generate models*)

pinsout = FullSimplify[(E2rpiny)^2]

9.5523*10^9 Cos[α - Φ]^2 (yxx Cos[α - Φ]^2 + (-2 xyx + yyy) Sin[α - Φ]^2)^2

sinpout = (E2rsinx*Cos[θi])^2 + (E2rsinz*Sin[θi])^2

9.5523*10^9 Sin[α - Φ]^2 ((-2 xyx + yyy) Cos[α - Φ]^2 + yxx Sin[α - Φ]^2)^2

sinsout = FullSimplify[E2rsiny^2]

9.5523*10^9 (yyy Cos[α - Φ]^3 + (2 xyx + yxx) Cos[α - Φ] Sin[α - Φ]^2)^2

BIBLIOGRAPHY

[1] G. Kotliar, D. Vollhardt, Physics Today, 57 53-59 (2004).

[2] J.G. Rau, E.K.-H. Lee, H.-Y. Kee, Annual Review of Condensed Matter Physics, 7 195-221 (2016).

[3] X. Wan, A.M. Turner, A. Vishwanath, S.Y. Savrasov, Physical Review B, 83 205101 (2011).

[4] A.A. Burkov, Nature Materials, 15 1145-1148 (2016).

[5] S. Jia, S.-Y. Xu, M.Z. Hasan, Nature Materials, 15 1140 (2016).

[6] B.Q. Lv, H.M. Weng, B.B. Fu, X.P. Wang, H. Miao, J. Ma, P. Richard, X.C. Huang, L.X. Zhao, G.F. Chen, Z. Fang, X. Dai, T. Qian, H. Ding, Physical Review X, 5 031013 (2015).

[7] S.-Y. Xu, I. Belopolski, N. Alidoust, M. Neupane, G. Bian, C. Zhang, R. Sankar, G. Chang, Z. Yuan, C.-C. Lee, S.-M. Huang, H. Zheng, J. Ma, D.S. Sanchez, B. Wang, A. Bansil, F. Chou, P.P. Shibayev, H. Lin, S. Jia, M.Z. Hasan, Science, 349 613-617 (2015).

[8] A.A. Soluyanov, D. Gresch, Z. Wang, Q. Wu, M. Troyer, X. Dai, B.A. Bernevig, Nature, 527 495-498 (2015).

[9] Q. Ma, S.-Y. Xu, C.-K. Chan, C.-L. Zhang, G. Chang, Y. Lin, W. Xie, T. Palacios, H. Lin, S. Jia, P.A. Lee, P. Jarillo-Herrero, N. Gedik, Nature Physics, 13 842-847 (2017).

[10] D. Rees, K. Manna, B. Lu, T. Morimoto, H. Borrmann, C. Felser, J. Moore, D. Torchinsky, J. Orenstein, Quantized Photocurrents in the Chiral Multifold Fermion System RhSi, 2019.

[11] D. Rees, K. Manna, B. Lu, T. Morimoto, H. Borrmann, C. Felser, J.E. Moore, D.H. Torchinsky, J. Orenstein, Science Advances, 6 (2020).

[12] S. Chi, Z. Li, Y. Xie, Y. Zhao, Z. Wang, L. Li, H. Yu, G. Wang, H. Weng, H. Zhang, J. Wang, Ultra-broadband photodetection of Weyl semimetal TaAs up to infrared 10 μm range at room temperature, arXiv:1705.05086, 2017.

[13] G. Oktay, M. Sarısaman, M. Tas, Scientific Reports, 10 3127 (2020).

[14] L. Wu, S. Patankar, T. Morimoto, N.L. Nair, E. Thewalt, A. Little, J.G. Analytis, J.E. Moore, J. Orenstein, Nature Physics, 13 350 (2016).

[15] C.-K. Chan, N.H. Lindner, G. Refael, P.A. Lee, Physical Review B, 95 041104(R) (2017).

[16] N. Sirica, R.I. Tobey, L.X. Zhao, G.F. Chen, B. Xu, R. Yang, B. Shen, D.A. Yarotski, P. Bowlan, S.A. Trugman, J.X. Zhu, Y.M. Dai, A.K. Azad, N. Ni, X.G. Qiu, A.J. Taylor, R.P. Prasankumar, Physical review letters, 122 197401 (2019).

[17] Q. Ma, S.-Y. Xu, H. Shen, D. MacNeill, V. Fatemi, T.-R. Chang, A.M. Mier Valdivia, S. Wu, Z. Du, C.-H. Hsu, S. Fang, Q.D. Gibson, K. Watanabe, T. Taniguchi, R.J. Cava, E. Kaxiras, H.-Z. Lu, H. Lin, L. Fu, N. Gedik, P. Jarillo-Herrero, Nature, 565 337-342 (2019).

[18] I. Sodemann, L. Fu, Physical review letters, 115 216806 (2015).

[19] M.Z. Hasan, S.-Y. Xu, I. Belopolski, S.-M. Huang, Annual Review of Condensed Matter Physics, 8 289-309 (2017).

[20] P. Li, Y. Wen, X. He, Q. Zhang, C. Xia, Z.-M. Yu, S.A. Yang, Z. Zhu, H.N. Alshareef, X.-X. Zhang, Nature Communications, 8 2150 (2017).

[21] P.K. Das, D. Di Sante, F. Cilento, C. Bigi, D. Kopic, D. Soranzio, A. Sterzi, J.A. Krieger, I. Vobornik, J. Fujii, T. Okuda, V.N. Strocov, M.B.H. Breese, F. Parmigiani, G. Rossi, S. Picozzi, R. Thomale, G. Sangiovanni, R.J. Cava, G. Panaccione, Electronic Structure, 1 014003 (2019).

[22] K. Deng, G. Wan, P. Deng, K. Zhang, S. Ding, E. Wang, M. Yan, H. Huang, H. Zhang, Z. Xu, J. Denlinger, A. Fedorov, H. Yang, W. Duan, H. Yao, Y. Wu, S. Fan, H. Zhang, X. Chen, S. Zhou, Nature Physics, 12 1105-1110 (2016).

[23] D.A. Pshenay-Severin, Y.V. Ivanov, A.A. Burkov, A.T. Burkov, Journal of Physics: Condensed Matter, 30 135501 (2018).

[24] Z. Rao, H. Li, T. Zhang, S. Tian, C. Li, B. Fu, C. Tang, L. Wang, Z. Li, W. Fan, J. Li, Y. Huang, Z. Liu, Y. Long, C. Fang, H. Weng, Y. Shi, H. Lei, Y. Sun, T. Qian, H. Ding, Nature, 567 496-499 (2019).

[25] D. Takane, Z. Wang, S. Souma, K. Nakayama, T. Nakamura, H. Oinuma, Y. Nakata, H. Iwasawa, C. Cacho, T. Kim, K. Horiba, H. Kumigashira, T. Takahashi, Y. Ando, T. Sato, Physical review letters, 122 076402 (2019).

[26] H. Weyl, Zeitschrift für Physik, 56 330-352 (1929).

[27] S.-M. Huang, S.-Y. Xu, I. Belopolski, C.-C. Lee, G. Chang, B. Wang, N. Alidoust, G. Bian, M. Neupane, C. Zhang, S. Jia, A. Bansil, H. Lin, M.Z. Hasan, Nature Communications, 6 7373 (2015).

[28] H. Weng, C. Fang, Z. Fang, B.A. Bernevig, X. Dai, Physical Review X, 5 011029 (2015).

[29] J.N. J. J. Sakurai, Modern Quantum Mechanics, 2 ed., Pearson Education, Inc., 1301 Sansome Street, San Francisco, CA 94111, 1994.

[30] E. Wigner, Nachrichten von der Gesellschaft der Wissenschaften zu Göttingen, Mathematisch-Physikalische Klasse, 1932 13 (1932).

[31] M.V. Berry, Proceedings of the Royal Society of London. A. Mathematical and Physical Sciences, 392 45-57 (1984).

[32] S. Lang, Complex Analysis, 4 ed., Springer, 1998.

[33] Y. Aharonov, D. Bohm, Physical Review, 115 485-491 (1959).

[34] D. Xiao, M.-C. Chang, Q. Niu, Reviews of Modern Physics, 82 1959-2007 (2010).

[35] M.Z. Hasan, C.L. Kane, Reviews of Modern Physics, 82 3045-3067 (2010).

[36] S.A. Yang, SPIN, 06 1640003 (2016).

[37] B.-J. Yang, T. Morimoto, A. Furusaki, Physical Review B, 92 165120 (2015).

[38] G. Cao, X.-G. Huang, Physics Letters B, 757 1-5 (2016).

[39] S.A. Parameswaran, T. Grover, D.A. Abanin, D.A. Pesin, A. Vishwanath, Physical Review X, 4 031035 (2014).

[40] G. Sharma, P. Goswami, S. Tewari, Physical Review B, 96 045112 (2017).

[41] H.B. Nielsen, M. Ninomiya, Physics Letters B, 105 219-223 (1981).

[42] N.B.M. Schröter, D. Pei, M.G. Vergniory, Y. Sun, K. Manna, F. de Juan, J.A. Krieger, V. Süss, M. Schmidt, P. Dudin, B. Bradlyn, T.K. Kim, T. Schmitt, C. Cacho, C. Felser, V.N. Strocov, Y. Chen, Nature Physics, 15 759-765 (2019).

[43] G. Chen, M. Hermele, Physical Review B, 86 235129 (2012).

[44] H. Weng, Y. Liang, Q. Xu, R. Yu, Z. Fang, X. Dai, Y. Kawazoe, Physical Review B, 92 045108 (2015).

[45] S. Borisenko, D. Evtushinsky, Q. Gibson, A. Yaresko, K. Koepernik, T. Kim, M. Ali, J. van den Brink, M. Hoesch, A. Fedorov, E. Haubold, Y. Kushnirenko, I. Soldatov, R. Schäfer, R.J. Cava, Nature Communications, 10 3424 (2019).

[46] A.A. Burkov, L. Balents, Physical review letters, 107 127205 (2011).

[47] M. Shuichi, New Journal of Physics, 9 356-356 (2007).

[48] S.-Y. Xu, I. Belopolski, D.S. Sanchez, C. Zhang, G. Chang, C. Guo, G. Bian, Z. Yuan, H. Lu, T.-R. Chang, P.P. Shibayev, M.L. Prokopovych, N. Alidoust, H. Zheng, C.-C. Lee, S.-M. Huang, R. Sankar, F. Chou, C.-H. Hsu, H.-T. Jeng, A. Bansil, T. Neupert, V.N. Strocov, H. Lin, S. Jia, M.Z. Hasan, Science Advances, 1 e1501092 (2015).

[49] N. Xu, H.M. Weng, B.Q. Lv, C.E. Matt, J. Park, F. Bisti, V.N. Strocov, D. Gawryluk, E. Pomjakushina, K. Conder, N.C. Plumb, M. Radovic, G. Autès, O.V. Yazyev, Z. Fang, X. Dai, T. Qian, J. Mesot, H. Ding, M. Shi, Nature Communications, 7 11006 (2016).

[50] S.-Y. Xu, N. Alidoust, I. Belopolski, Z. Yuan, G. Bian, T.-R. Chang, H. Zheng, V.N. Strocov, D.S. Sanchez, G. Chang, C. Zhang, D. Mou, Y. Wu, L. Huang, C.-C. Lee, S.-M. Huang, B. Wang, A. Bansil, H.-T. Jeng, T. Neupert, A. Kaminski, H. Lin, S. Jia, M. Zahid Hasan, Nature Physics, 11 748-754 (2015).

[51] D.-F. Xu, Y.-P. Du, Z. Wang, Y.-P. Li, X.-H. Niu, Q. Yao, D. Pavel, Z.-A. Xu, X.-G. Wan, D.-L. Feng, Chinese Physics Letters, 32 107101 (2015).

[52] N. Xu, Z.J. Wang, A.P. Weber, A. Magrez, P. Bugnon, H. Berger, C.E. Matt, J.Z. Ma, B.B. Fu, B.Q. Lv, N.C. Plumb, M. Radovic, E. Pomjakushina, K. Conder, T. Qian, J.H. Dil, J. Mesot, H. Ding, M. Shi, Discovery of Weyl semimetal state violating Lorentz invariance in MoTe2, arXiv, 2016.

[53] A. Liang, J. Huang, S. Nie, Y. Ding, Q. Gao, C. Hu, S. He, Y. Zhang, C. Wang, B. Shen, J. Liu, P. Ai, L. Yu, X. Sun, W. Zhao, S. Lv, D. Liu, C. Li, Y. Zhang, Y. Hu, Y. Xu, L. Zhao, G. Liu, Z. Mao, X. Jia, F. Zhang, S. Zhang, F. Yang, Z. Wang, Q. Peng, H. Weng, X. Dai, Z. Fang, Z. Xu, C. Chen, X.J. Zhou, Electronic Evidence for Type II Weyl Semimetal State in MoTe2, arXiv, 2016.

[54] J. Sánchez-Barriga, M.G. Vergniory, D. Evtushinsky, I. Aguilera, A. Varykhalov, S. Blügel, O. Rader, Physical Review B, 94 161401 (2016).

[55] Y. Wu, D. Mou, N.H. Jo, K. Sun, L. Huang, S.L. Bud'ko, P.C. Canfield, A. Kaminski, Physical Review B, 94 121113 (2016).

[56] C. Wang, Y. Zhang, J. Huang, S. Nie, G. Liu, A. Liang, Y. Zhang, B. Shen, J. Liu, C. Hu, Y. Ding, D. Liu, Y. Hu, S. He, L. Zhao, L. Yu, J. Hu, J. Wei, Z. Mao, Y. Shi, X. Jia, F. Zhang, S. Zhang, F. Yang, Z. Wang, Q. Peng, H. Weng, X. Dai, Z. Fang, Z. Xu, C. Chen, X.J. Zhou, Physical Review B, 94 241119 (2016).

[57] S.-Y. Xu, N. Alidoust, G. Chang, H. Lu, B. Singh, I. Belopolski, D.S. Sanchez, X. Zhang, G. Bian, H. Zheng, M.-A. Husanu, Y. Bian, S.-M. Huang, C.-H. Hsu, T.-R. Chang, H.-T. Jeng, A. Bansil, T. Neupert, V.N. Strocov, H. Lin, S. Jia, M.Z. Hasan, Science Advances, 3 e1603266 (2017).

[58] G. Chang, S.-Y. Xu, B.J. Wieder, D.S. Sanchez, S.-M. Huang, I. Belopolski, T.-R. Chang, S. Zhang, A. Bansil, H. Lin, M.Z. Hasan, Physical review letters, 119 206401 (2017).

[59] P. Tang, Q. Zhou, S.-C. Zhang, Physical review letters, 119 206402 (2017).

[60] D.S. Sanchez, I. Belopolski, T.A. Cochran, X. Xu, J.-X. Yin, G. Chang, W. Xie, K. Manna, V. Süß, C.-Y. Huang, N. Alidoust, D. Multer, S.S. Zhang, N. Shumiya, X. Wang, G.-Q. Wang, T.-R. Chang, C. Felser, S.-Y. Xu, S. Jia, H. Lin, M.Z. Hasan, Nature, 567 500-505 (2019).

[61] P. Drude, Annalen der Physik, 306 566-613 (1900).

[62] P. Drude, Annalen der Physik, 308 369-402 (1900).

[63] J.H.d. Boer, E.J.W. Verwey, Proceedings of the Physical Society, 49 59-71 (1937).

[64] N.W. Ashcroft, N.D. Mermin, Solid State Physics, Holt, Rinehart and Winston, 1976.

[65] N.F. Mott, Reviews of Modern Physics, 40 677-683 (1968).

[66] M. Imada, A. Fujimori, Y. Tokura, Reviews of Modern Physics, 70 1039-1263 (1998).

[67] W. Witczak-Krempa, G. Chen, Y.B. Kim, L. Balents, Annual Review of Condensed Matter Physics, 5 57-82 (2014).

[68] P. Santini, S. Carretta, G. Amoretti, R. Caciuffo, N. Magnani, G.H. Lander, Reviews of Modern Physics, 81 807-863 (2009).

[69] R.W. Boyd, Nonlinear Optics (Third Edition), Academic Press, Burlington, 2008.

[70] S. Patankar, L. Wu, B. Lu, M. Rai, J.D. Tran, T. Morimoto, D.E. Parker, A.G. Grushin, N.L. Nair, J.G. Analytis, J.E. Moore, J. Orenstein, D.H. Torchinsky, Physical Review B, 98 165113 (2018).

[71] Y. Chen, B. Peng, C. Cong, J. Shang, L. Wu, W. Yang, J. Zhou, P. Yu, H. Zhang, Y. Wang, C. Zou, J. Zhang, S. Liu, Q. Xiong, H. Shao, Z. Liu, H. Zhang, W. Huang, T. Yu, Advanced Materials, 31 1804979 (2019).

[72] M. Chen, K. Lee, J. Li, L. Cheng, Q. Wang, K. Cai, E.E.M. Chia, H. Chang, H. Yang, ACS Nano, 14 3539-3545 (2020).

[73] G. Chang, J.-X. Yin, T. Neupert, D.S. Sanchez, I. Belopolski, S.S. Zhang, T.A. Cochran, Z. Chéng, M.-C. Hsu, S.-M. Huang, B. Lian, S.-Y. Xu, H. Lin, M.Z. Hasan, Physical review letters, 124 166404 (2020).

[74] J.W. McIver, D. Hsieh, H. Steinberg, P. Jarillo-Herrero, N. Gedik, Nature Nanotechnology, 7 96-100 (2012).

[75] S.-Y. Xu, Q. Ma, H. Shen, V. Fatemi, S. Wu, T.-R. Chang, G. Chang, A.M.M. Valdivia, C.-K. Chan, Q.D. Gibson, J. Zhou, Z. Liu, K. Watanabe, T. Taniguchi, H. Lin, R.J. Cava, L. Fu, N. Gedik, P. Jarillo-Herrero, Nature Physics, 14 900-906 (2018).

[76] Y. Araki, Scientific Reports, 8 15236 (2018).

[77] T. Morimoto, N. Nagaosa, Science Advances, 2 e1501524 (2016).

[78] A.A. Zyuzin, A.A. Burkov, Physical Review B, 86 115133 (2012).

[79] M. He, Y. Chen, L. Zhu, H. Wang, X. Wang, X. Xu, Z. Ren, Photon. Res., 7 1493-1500 (2019).

[80] C.-L. Zhang, S.-Y. Xu, I. Belopolski, Z. Yuan, Z. Lin, B. Tong, G. Bian, N. Alidoust, C.-C. Lee, S.-M. Huang, T.-R. Chang, G. Chang, C.-H. Hsu, H.-T. Jeng, M. Neupane, D.S. Sanchez, H. Zheng, J. Wang, H. Lin, C. Zhang, H.-Z. Lu, S.-Q. Shen, T. Neupert, M. Zahid Hasan, S. Jia, Nature Communications, 7 10735 (2016).

[81] D. Kumar, C.-H. Hsu, R. Sharma, T.-R. Chang, P. Yu, J. Wang, G. Eda, G. Liang, H. Yang, Nature Nanotechnology, (2021).

[82] G.B. Osterhoudt, L.K. Diebel, M.J. Gray, X. Yang, J. Stanco, X. Huang, B. Shen, N. Ni, P.J.W. Moll, Y. Ran, K.S. Burch, Nature Materials, 18 471-475 (2019).

[83] Z. Ji, G. Liu, Z. Addison, W. Liu, P. Yu, H. Gao, Z. Liu, A.M. Rappe, C.L. Kane, E.J. Mele, R. Agarwal, Nature Materials, 18 955-962 (2019).

[84] E.H. Hall, American Journal of Mathematics, 2 287-292 (1879).

[85] S. Nandy, I. Sodemann, Physical Review B, 100 195117 (2019).

[86] D.J. Thouless, Physical Review B, 27 6083-6087 (1983).

[87] J.-S. You, S. Fang, S.-Y. Xu, E. Kaxiras, T. Low, Physical Review B, 98 121109 (2018).

[88] Symmetry Gallery @ Otterbein, 2019.

[89] M.Y. Zhang, Z.X. Wang, Y.N. Li, L.Y. Shi, D. Wu, T. Lin, S.J. Zhang, Y.Q. Liu, Q.M. Liu, J. Wang, T. Dong, N.L. Wang, Physical Review X, 9 021036 (2019).

[90] E.J. Sie, C.M. Nyby, C.D. Pemmaraju, S.J. Park, X. Shen, J. Yang, M.C. Hoffmann, B.K. Ofori-Okai, R. Li, A.H. Reid, S. Weathersby, E. Mannebach, N. Finney, D. Rhodes, D. Chenet, A. Antony, L. Balicas, J. Hone, T.P. Devereaux, T.F. Heinz, X. Wang, A.M. Lindenberg, Nature, 565 61-66 (2019).

[91] G.E. Pikus, E.L. Ivchenko, Photogalvanic effects in noncentrosymmetric semiconductors: W. Zawadzki (Ed.) Narrow Gap Semiconductors Physics and Applications, Springer Berlin Heidelberg, Berlin, Heidelberg, pp. 388-406, 1980.

[92] A. Yariv, P. Yeh, Optical waves in crystals : propagation and control of laser radiation, Hoboken, 2003.

[93] F. de Juan, A.G. Grushin, T. Morimoto, J.E. Moore, Nature Communications, 8 15995 (2017).

[94] T. Gaumnitz, A. Jain, Y. Pertot, M. Huppert, I. Jordan, F. Ardana-Lamas, H.J. Worner, Opt. Express, 25 27506-27518 (2017).

[95] A. Weiner, Ultrafast Optics, Wiley, 2009.

[96] Spirit-NOPA-VISIR User's Manual, Light Conversion, Spectra Physics.

[97] D.H. Torchinsky, H. Chu, T. Qi, G. Cao, D. Hsieh, Review of Scientific Instruments, 85 (2014).

[98] J.W. Harter, L. Niu, A.J. Woss, D. Hsieh, Opt. Lett., 40 4671-4674 (2015).

[99] F.E. Neumann, Annalen der Physik, 101 418-454 (1832).

[100] Andor iXon Ultra 897 Users Manual, Oxford Instruments.

[101] Personal Communication from Liuyan Zhao.

[102] N. Bloembergen, P.S. Pershan, Physical Review, 128 606-622 (1962).

[103] K.S. Novoselov, D. Jiang, F. Schedin, T.J. Booth, V.V. Khotkevich, S.V. Morozov, A.K. Geim, Proceedings of the National Academy of Sciences of the United States of America, 102 10451 (2005).

[104] J.R. Brent, N. Savjani, P. O'Brien, Progress in Materials Science, 89 411-478 (2017).

[105] Y. Cao, V. Fatemi, S. Fang, K. Watanabe, T. Taniguchi, E. Kaxiras, P. Jarillo-Herrero, Nature, 556 43-50 (2018).

[106] D.J. Trainer, A.V. Putilov, B. Wang, C. Lane, T. Saari, T.-R. Chang, H.-T. Jeng, H. Lin, X. Xi, J. Nieminen, A. Bansil, M. Iavarone, Journal of Physics and Chemistry of Solids, 128 325-330 (2019).

[107] K.S. Novoselov, A. Mishchenko, A. Carvalho, A.H. Castro Neto, Science, 353 aac9439 (2016).

[108] J. Jiang, Z.K. Liu, Y. Sun, H.F. Yang, C.R. Rajamathi, Y.P. Qi, L.X. Yang, C. Chen, H. Peng, C.C. Hwang, S.Z. Sun, S.K. Mo, I. Vobornik, J. Fujii, S.S.P. Parkin, C. Felser, B.H. Yan, Y.L. Chen, Nature Communications, 8 13973 (2017).

[109] M.N. Ali, J. Xiong, S. Flynn, J. Tao, Q.D. Gibson, L.M. Schoop, T. Liang, N. Haldolaarachchige, M. Hirschberger, N.P. Ong, R.J. Cava, Nature, 514 205-208 (2014).

[110] D. Kang, Y. Zhou, W. Yi, C. Yang, J. Guo, Y. Shi, S. Zhang, Z. Wang, C. Zhang, S. Jiang, A. Li, K. Yang, Q. Wu, G. Zhang, L. Sun, Z. Zhao, Nature Communications, 6 7804 (2015).

[111] X.-C. Pan, X. Chen, H. Liu, Y. Feng, Z. Wei, Y. Zhou, Z. Chi, L. Pi, F. Yen, F. Song, X. Wan, Z. Yang, B. Wang, G. Wang, Y. Zhang, Nature Communications, 6 7805 (2015).

[112] P. Villars, WTe2 Crystal Structure: Datasheet from "PAULING FILE Multinaries Edition – 2012" in SpringerMaterials (online database), Springer-Verlag Berlin Heidelberg & Material Phases Data System (MPDS), Switzerland & National Institute for Materials Science (NIMS), Japan.

[113] J. Jiang, F. Tang, X.C. Pan, H.M. Liu, X.H. Niu, Y.X. Wang, D.F. Xu, H.F. Yang, B.P. Xie, F.Q. Song, P. Dudin, T.K. Kim, M. Hoesch, P.K. Das, I. Vobornik, X.G. Wan, D.L. Feng, Physical review letters, 115 166601 (2015).

[114] Y. Wu, N.H. Jo, M. Ochi, L. Huang, D. Mou, S.L. Bud'ko, P.C. Canfield, N. Trivedi, R. Arita, A. Kaminski, Physical review letters, 115 166602 (2015).

[115] P.K. Das, D. Di Sante, I. Vobornik, J. Fujii, T. Okuda, E. Bruyer, A. Gyenis, B.E. Feldman, J. Tao, R. Ciancio, G. Rossi, M.N. Ali, S. Picozzi, A. Yadzani, G. Panaccione, R.J. Cava, Nature Communications, 7 10847 (2016).

[116] F.-X. Xiang, M. Veldhorst, S.-X. Dou, X.-L. Wang, EPL (Europhysics Letters), 112 37009 (2015).

[117] I. Belopolski, S.-Y. Xu, Y. Ishida, X. Pan, P. Yu, D.S. Sanchez, H. Zheng, M. Neupane, N. Alidoust, G. Chang, T.-R. Chang, Y. Wu, G. Bian, S.-M. Huang, C.-C. Lee, D. Mou, L. Huang, Y. Song, B. Wang, G. Wang, Y.-W. Yeh, N. Yao, J.E. Rault, P. Le Fèvre, F. Bertran, H.-T. Jeng, T. Kondo, A. Kaminski, H. Lin, Z. Liu, F. Song, S. Shin, M.Z. Hasan, Physical Review B, 94 085127 (2016).

[118] F.Y. Bruno, A. Tamai, Q.S. Wu, I. Cucchi, C. Barreteau, A. de la Torre, S. McKeown Walker, S. Riccò, Z. Wang, T.K. Kim, M. Hoesch, M. Shi, N.C. Plumb, E. Giannini, A.A. Soluyanov, F. Baumberger, Physical Review B, 94 121112 (2016).

[119] Q. Zhang, Z. Liu, Y. Sun, H. Yang, J. Jiang, S.-K. Mo, Z. Hussain, X. Qian, L. Fu, S. Yao, M. Lu, C. Felser, B. Yan, Y. Chen, L. Yang, physica status solidi (RRL) – Rapid Research Letters, 11 1700209 (2017).

[120] I. Belopolski, D.S. Sanchez, Y. Ishida, X. Pan, P. Yu, S.-Y. Xu, G. Chang, T.-R. Chang, H. Zheng, N. Alidoust, G. Bian, M. Neupane, S.-M. Huang, C.-C. Lee, Y. Song, H. Bu, G. Wang, S. Li, G. Eda, H.-T. Jeng, T. Kondo, H. Lin, Z. Liu, F. Song, S. Shin, M.Z. Hasan, Nature Communications, 7 13643 (2016).

[121] D. Di Sante, P.K. Das, C. Bigi, Z. Ergönenc, N. Gürtler, J.A. Krieger, T. Schmitt, M.N. Ali, G. Rossi, R. Thomale, C. Franchini, S. Picozzi, J. Fujii, V.N. Strocov, G. Sangiovanni, I. Vobornik, R.J. Cava, G. Panaccione, Physical review letters, 119 026403 (2017).

[122] B. Feng, Y.-H. Chan, Y. Feng, R.-Y. Liu, M.-Y. Chou, K. Kuroda, K. Yaji, A. Harasawa, P. Moras, A. Barinov, W. Malaeb, C. Bareille, T. Kondo, S. Shin, F. Komori, T.-C. Chiang, Y. Shi, I. Matsuda, Physical Review B, 94 195134 (2016).

[123] C.-L. Lin, R. Arafune, R.-Y. Liu, M. Yoshimura, B. Feng, K. Kawahara, Z. Ni, E. Minamitani, S. Watanabe, Y. Shi, M. Kawai, T.-C. Chiang, I. Matsuda, N. Takagi, ACS Nano, 11 11459-11465 (2017).

[124] Y. Sun, S.-C. Wu, M.N. Ali, C. Felser, B. Yan, Physical Review B, 92 161107 (2015).

[125] H.P. Hughes, R.H. Friend, Journal of Physics C: Solid State Physics, 11 L103-L105 (1978).

[126] R. Clarke, E. Marseglia, H.P. Hughes, Philosophical Magazine B, 38 121-126 (1978).

[127] R. He, S. Zhong, H.H. Kim, G. Ye, Z. Ye, L. Winford, D. McHaffie, I. Rilak, F. Chen, X. Luo, Y. Sun, A.W. Tsen, Physical Review B, 97 041410 (2018).

[128] L. Huang, T.M. McCormick, M. Ochi, Z. Zhao, M.-T. Suzuki, R. Arita, Y. Wu, D. Mou, H. Cao, J. Yan, N. Trivedi, A. Kaminski, Nature Materials, 15 1155-1160 (2016).

[129] A. Tamai, Q.S. Wu, I. Cucchi, F.Y. Bruno, S. Riccò, T.K. Kim, M. Hoesch, C. Barreteau, E. Giannini, C. Besnard, A.A. Soluyanov, F. Baumberger, Physical Review X, 6 031021 (2016).

[130] high-temperature MoTe2 (MoTe2 ht) Crystal Structure: Datasheet from "PAULING FILE Multinaries Edition – 2012" in SpringerMaterials (https://materials.springer.com/isp/crystallographic/docs/sd_1250845), Springer-Verlag Berlin Heidelberg & Material Phases Data System (MPDS), Switzerland & National Institute for Materials Science (NIMS), Japan.

[131] C.-H. Lee, E.C. Silva, L. Calderin, M.A.T. Nguyen, M.J. Hollander, B. Bersch, T.E. Mallouk, J.A. Robinson, Scientific Reports, 5 10013 (2015).

[132] W. Jin, E. Drueke, S. Li, A. Admasu, R. Owen, M. Day, K. Sun, S.-W. Cheong, L. Zhao, Nature Physics, 16 42-46 (2020).

[133] B. Rahman Rano, I.M. Syed, S.H. Naqib, Results in Physics, 19 103639 (2020).

[134] H. Padmanabhan, Y. Park, D. Puggioni, Y. Yuan, Y. Cao, L. Gasparov, Y. Shi, J. Chakhalian, J.M. Rondinelli, V. Gopalan, Applied Physics Letters, 113 122906 (2018).

[135] K. Markey, T. Putzeys, P. Horcajada, T. Devic, N. Guillou, M. Wübbenhorst, S.V. Cleuvenbergen, T. Verbiest, D.E. De Vos, M.A. van der Veen, Dalton Transactions, 45 4401-4406 (2016).

[136] C.C. Homes, M.N. Ali, R.J. Cava, Physical Review B, 92 161109 (2015).

[137] W.D. Kong, S.F. Wu, P. Richard, C.S. Lian, J.T. Wang, C.L. Yang, Y.G. Shi, H. Ding, Applied Physics Letters, 106 081906 (2015).

[138] M.K. Jana, A. Singh, D.J. Late, C.R. Rajamathi, K. Biswas, C. Felser, U.V. Waghmare, C.N.R. Rao, Journal of Physics: Condensed Matter, 27 285401 (2015).

[139] Y.C. Jiang, J. Gao, L. Wang, Scientific Reports, 6 19624 (2016).

[140] Q. Song, X. Pan, H. Wang, K. Zhang, Q. Tan, P. Li, Y. Wan, Y. Wang, X. Xu, M. Lin, X. Wan, F. Song, L. Dai, Scientific Reports, 6 29254 (2016).

[141] Y.M. Dai, J. Bowlan, H. Li, H. Miao, S.F. Wu, W.D. Kong, P. Richard, Y.G. Shi, S.A. Trugman, J.X. Zhu, H. Ding, A.J. Taylor, D.A. Yarotski, R.P. Prasankumar, Physical Review B, 92 161104(R) (2015).

[142] H.J. Zeiger, J. Vidal, T.K. Cheng, E.P. Ippen, G. Dresselhaus, M.S. Dresselhaus, Physical Review B, 45 768-778 (1992).

[143] Y.X. Yan, E.B. Gamble, K.A. Nelson, The Journal of Chemical Physics, 83 5391-5399 (1985).

[144] T. Fukuda, K. Makino, Y. Saito, P. Fons, A.V. Kolobov, K. Ueno, M. Hase, Applied Physics Letters, 116 093103 (2020).

[145] P. Hein, S. Jauernik, H. Erk, L. Yang, Y. Qi, Y. Sun, C. Felser, M. Bauer, Nature Communications, 11 2613 (2020).

[146] T.E. Stevens, J. Kuhl, R. Merlin, Physical Review B, 65 144304 (2002).

[147] G.C. Cho, W. Kütt, H. Kurz, Physical review letters, 65 764-766 (1990).

[148] T. Dekorsy, T. Pfeifer, W. Kütt, H. Kurz, Physical Review B, 47 3842-3849 (1993).

[149] W.A. Kutt, W. Albrecht, H. Kurz, IEEE Journal of Quantum Electronics, 28 2434-2444 (1992).

[150] T.K. Cheng, J. Vidal, H.J. Zeiger, G. Dresselhaus, M.S. Dresselhaus, E.P. Ippen, Applied Physics Letters, 59 1923-1925 (1991).

[151] M.-C. Lee, C.H. Kim, I. Kwak, J. Kim, S. Yoon, B.C. Park, B. Lee, F. Nakamura, C. Sow, Y. Maeno, T.W. Noh, K.W. Kim, Physical Review B, 98 161115 (2018).

[152] A.Q. Wu, X. Xu, Applied Surface Science, 253 6301-6304 (2007).

[153] R.A. Bartels, S. Backus, M.M. Murnane, H.C. Kapteyn, Postconference Digest Quantum Electronics and Laser Science, 2003. QELS., 2.

[154] P.B. Allen, Physical review letters, 59 1460-1463 (1987).

[155] L. Cheng, C. La-o-vorakiat, C.S. Tang, S.K. Nair, B. Xia, L. Wang, J.-X. Zhu, E.E.M. Chia, Applied Physics Letters, 104 211906 (2014).

[156] R.H.M. Groeneveld, R. Sprik, A. Lagendijk, Physical Review B, 51 11433-11445 (1995).

[157] A. Slachter, Time resolved Kerr rotation and reflectance on 2D and 1D confined electron spins in an AlGaAs/GaAs heterojunction, University of Groningen, pp. 171, 2006.

[158] J. Lee, J.R. Challa, D.W. McCamant, Journal of Raman Spectroscopy, 44 1263-1272 (2013).

[159] B. Xu, Y.M. Dai, L.X. Zhao, K. Wang, R. Yang, W. Zhang, J.Y. Liu, H. Xiao, G.F. Chen, S.A. Trugman, J.X. Zhu, A.J. Taylor, D.A. Yarotski, R.P. Prasankumar, X.G. Qiu, Nature Communications, 8 14933 (2017).

[160] M. Kotur, D. Guénot, Á. Jiménez-Galán, D. Kroon, E.W. Larsen, M. Louisy, S. Bengtsson, M. Miranda, J. Mauritsson, C.L. Arnold, S.E. Canton, M. Gisselbrecht, T. Carette, J.M. Dahlström, E. Lindroth, A. Maquet, L. Argenti, F. Martín, A. L'Huillier, Nature Communications, 7 10566 (2016).

[161] C. Ott, A. Kaldun, P. Raith, K. Meyer, M. Laux, J. Evers, C.H. Keitel, C.H. Greene, T. Pfeifer, Science, 340 716 (2013).

[162] R. Beams, L.G. Cançado, S. Krylyuk, I. Kalish, B. Kalanyan, A.K. Singh, K. Choudhary, A. Bruma, P.M. Vora, F. Tavazza, A.V. Davydov, S.J. Stranick, ACS Nano, 10 9626-9636 (2016).

[163] M. Droth, G. Burkard, V.M. Pereira, Physical Review B, 94 075404 (2016).

[164] C. Shekhar, Nature Materials, 17 953-954 (2018).

[165] F. Flicker, F. de Juan, B. Bradlyn, T. Morimoto, M.G. Vergniory, A.G. Grushin, Physical Review B, 98 155145 (2018).

[166] J.L. Mañes, Physical Review B, 85 155118 (2012).

[167] B. Bradlyn, J. Cano, Z. Wang, M.G. Vergniory, C. Felser, R.J. Cava, B.A. Bernevig, Science, 353 aaf5037 (2016).

[168] B.J. Wieder, Y. Kim, A.M. Rappe, C.L. Kane, Physical review letters, 116 186402 (2016).

[169] T.M. Project, Materials Data on CoSi by Materials Project, United States, 2020.

[170] B. Xu, Z. Fang, M.-Á. Sánchez-Martínez, J.W.F. Venderbos, Z. Ni, T. Qiu, K. Manna, K. Wang, J. Paglione, C. Bernhard, C. Felser, E.J. Mele, A.G. Grushin, A.M. Rappe, L. Wu, Proceedings of the National Academy of Sciences, 117 27104 (2020).

[171] Z. Ni, K. Wang, Y. Zhang, O. Pozo, B. Xu, X. Han, K. Manna, J. Paglione, C. Felser, A.G. Grushin, F. de Juan, E.J. Mele, L. Wu, Nature Communications, 12 154 (2021).

[172] W.M.H. Sachtler, G.J.H. Dorgelo, A.A. Holscher, Surface Science, 5 221-229 (1966).

[173] S.S. Ullah, M. Robinson, J. Hoey, M.S. Driver, A.N. Caruso, D.L. Schulz, Semiconductor Science and Technology, 27 065012 (2012).

[174] Q. Wang, J. Zheng, Y. He, J. Cao, X. Liu, M. Wang, J. Ma, J. Lai, H. Lu, S. Jia, D. Yan, Y. Shi, J. Duan, J. Han, W. Xiao, J.-H. Chen, K. Sun, Y. Yao, D. Sun, Nature Communications, 10 5736 (2019).

[175] J.S. White, C. Niedermayer, G. Gasparovic, C. Broholm, J.M.S. Park, A.Y. Shapiro, L.A. Demianets, M. Kenzelmann, Physical Review B, 88 060409 (2013).

[176] K. Aizu, Physical Review B, 2 754-772 (1970).

[177] B.B. Van Aken, J.-P. Rivera, H. Schmid, M. Fiebig, Nature, 449 702-705 (2007).

[178] A.S. Nicola, F. Manfred, M. Maxim, Journal of Physics: Condensed Matter, 20 1-15 (2008).

[179] A.S. Zimmermann, D. Meier, M. Fiebig, Nature Communications, 5 1-6 (2014).

[180] L. Landau, Nature, 138 840-841 (1936).

[181] J.C. Tolédano, P. Tolédano, The Landau Theory of Phase Transitions, WORLD SCIENTIFIC, 1987.

[182] A. Kiss, Y. Kuramoto, Journal of the Physical Society of Japan, 75 103704 (2006).

[183] S.-W. Cheong, D. Talbayev, V. Kiryukhin, A. Saxena, npj Quantum Materials, 3 (2018).

[184] V. Gopalan, D.B. Litvin, Nature Materials, 10 376-381 (2011).

[185] J. Hlinka, J. Privratska, P. Ondrejkovic, V. Janovec, Physical review letters, 116 (2016).

[186] A.K. Yadav, C.T. Nelson, S.L. Hsu, Z. Hong, J.D. Clarkson, C.M. Schlepütz, A.R. Damodaran, P. Shafer, E. Arenholz, L.R. Dedon, D. Chen, A. Vishwanath, A.M. Minor, L.Q. Chen, J.F. Scott, L.W. Martin, R. Ramesh, Nature, 530 198-201 (2016).

[187] R.D. Johnson, L.C. Chapon, D.D. Khalyavin, P. Manuel, P.G. Radaelli, C. Martin, Physical review letters, 108 067201 (2012).

[188] M. Kenzelmann, G. Lawes, A.B. Harris, G. Gasparovic, C. Broholm, A.P. Ramirez, G.A. Jorge, M. Jaime, S. Park, Q. Huang, A.Y. Shapiro, L.A. Demianets, Physical review letters, 98 (2007).

[189] A. Waskowska, L. Gerward, J.S. Olsen, W. Morgenroth, M. Maczka, K. Hermanowicz, Journal of physics. Condensed matter : an Institute of Physics journal, 22 10 (2010).

[190] R.D. Johnson, S. Nair, L.C. Chapon, A. Bombardi, C. Vecchini, D. Prabhakaran, A.T. Boothroyd, P.G. Radaelli, Physical review letters, 107 (2011).

[191] T. Inami, Journal of Solid State Chemistry, 180 2075-2079 (2007).

[192] A.J. Hearmon, F. Fabrizi, L.C. Chapon, R.D. Johnson, D. Prabhakaran, S.V. Streltsov, P.J. Brown, P.G. Radaelli, Physical review letters, 108 237201 (2012).

[193] S.A. Klimin, M.N. Popova, B.N. Mavrin, P.H.M. van Loosdrecht, L.E. Svistov, A.I. Smirnov, L.A. Prozorova, H.A.K. von Nidda, Z. Seidov, A. Loidl, A.Y. Shapiro, L.N. Demianets, Physical Review B, 68 (2003).

[194] G. Katzer, Character Tables for Point Groups used in Chemistry.

[195] A.F. Devonshire, Advances in Physics, 3 85-130 (1954).

[196] C.P. Weber, Journal of Applied Physics, 129 070901 (2021).

[197] T. Kampfrath, M. Battiato, P. Maldonado, G. Eilers, J. Nötzold, S. Mährlein, V. Zbarsky, F. Freimuth, Y. Mokrousov, S. Blügel, M. Wolf, I. Radu, P.M. Oppeneer, M. Münzenberg, Nature Nanotechnology, 8 256-260 (2013).

[198] J.P. Heritage, J.G. Bergman, A. Pinczuk, J.M. Worlock, Chemical Physics Letters, 67 229-232 (1979).

[199] T. Pfeifer, T. Dekorsy, W. Kütt, H. Kurz, Applied Physics A, 55 482-488 (1992).

[200] G.A. Garrett, T.F. Albrecht, J.F. Whitaker, R. Merlin, Physical review letters, 77 3661-3664 (1996).

[201] G. Chang, B.J. Wieder, F. Schindler, D.S. Sanchez, I. Belopolski, S.-M. Huang, B. Singh, D. Wu, T.-R. Chang, T. Neupert, S.-Y. Xu, H. Lin, M.Z. Hasan, Nature Materials, 17 978-985 (2018).

[202] A. Avdoshkin, V. Kozii, J.E. Moore, Physical review letters, 124 196603 (2020).

[203] R. Owen, E. Drueke, C. Albunio, A. Kaczmarek, W. Jin, D. Obeysekera, S.-W. Cheong, J. Yang, S. Cundiff, L. Zhao, Physical Review B, 103 054104 (2021).

[204] M. Artin, Algebra, Second Edition ed., Pearson Education, Inc., 501 Boylston Street, Suite 900, Boston, MA 02116, 1991.

[205] K. Sun, Physics 520 Notes, 2017.

[206] E. Fermi, Rendiconti Lincei, 145 (1926).

[207] P.A.M. Dirac, R.H. Fowler, Proceedings of the Royal Society of London. Series A, Containing Papers of a Mathematical and Physical Character, 112 661-677 (1926).

[208] F. Bloch, Zeitschrift für Physik, 52 555-600 (1929).

[209] V. Dobrosavljevic, Conductor-Insulator Quantum Phase Transitions, (2012).

[210] S. Dobrovits, B. Kim, M. Reticcioli, A. Toschi, S. Khmelevskyi, C. Franchini, Journal of Physics: Condensed Matter, 31 244002 (2019).